Bulk and supported mixed (Ni)MoW sulfide catalysts based on mixed H4SiMonW12-nO40 Keggin heteropolyacids for deep hydrotreating

Aleksandr Kokliukhin

THESE

Co-tutelle these
Université de Lille / Samara State Technical University

Ecole Doctorale
Sciences de la Matière du Rayonnement et de l'Environnement

Pour obtenir le titre de

Docteur en Chimie

Chimie-Physique chimie

Catalyseurs sulfures (Ni)MoW massiques et supportés, préparés à partir d'hétéropolyacides mixtes de Keggin $H_4SiMo_nW_{12-n}O_{40}$, pour l'hydrotraitement des coupes lourdes

présenté par

Aleksandr Kokliukhin

Date de la soutenance de thèse: 24 juin 2021

Prof. Carole LAMONIER, Université de Lille, France	**Superviseuse**
Dr. Pavel NIKULSHIN, All-Russian Research Institute of Oil Refining, Russia	**Superviseur**
Dr. Christine LANCELOT, Université de Lille, France	**Co-superviseuse**
Prof. Jean-François PAUL, Université de Lille, France	**Président du jury**
Prof. Xavier CARRIER, Sorbonne Université, Paris, France	**Rapporteur**
Dr. Andrey POPOV, Lomonosov Moscow State University, Russia	**Rapporteur**
Dr. Darya ISHUTENKO, Samara State Technical University, Russia	**Examinatrice**
Dr. Frederic RICHARD, Université de Poitiers, France	**Examinateur**

THESIS

Co-tutelle thesis Lille University / Samara State Technical University

Ecole Doctorale
Sciences de la Matière du Rayonnement et de l'Environnement

for the degree of

Doctor in Chemistry

Chemistry-Physical chemistry

Bulk and supported mixed (Ni)MoW sulfide catalysts based on mixed $H_4SiMo_nW_{12-n}O_{40}$ Keggin heteropolyacids for deep hydrotreating

presented by

Aleksandr Kokliukhin

Date of the thesis defence: June 24th, 2021

Prof. Carole LAMONIER, Université de Lille, France	**Supervisor**
Dr. Pavel NIKULSHIN, All-Russian Research Institute of Oil Refining, Russia	**Supervisor**
Dr. Christine LANCELOT, Université de Lille, France	**Co-supervisor**
Prof. Jean-François PAUL, Université de Lille, France	**President of the jury**
Prof. Xavier CARRIER, Sorbonne Université, Paris, France	**Referee**
Dr. Andrey POPOV, Lomonosov Moscow State University, Russia	**Referee**
Dr. Darya ISHUTENKO, Samara State Technical University, Russia	**Examiner**
Dr. Frederic RICHARD, Université de Poitiers, France	**Examiner**

Acknowledgement

Firstly, I would like to express the deepest appreciation to my supervisors Prof. Carole Lamonier, Dr. Pavel Nikulshin and co-supervisor Dr.Christine Lancelot for their emphatic guidance and support in steering my thesis towards completion. I am deeply affected by their scientific method and attitude. I am very grateful to them for their patience and mutual understanding**,** as well as for the knowledge and experience that they were able to convey to me.

I also would like to thank Dr. Pascal Blanchard for the help, valuable discussions, ideas and pieces of advice during my research work and, of course, for your friendly support.

I am also thankful to Prof. Xavier Carrier and Dr. Andrey Popov for accepting the role of Referees for my thesis as well as Dr. Frederic Richard and Dr. Darya Ishutenko for examining the thesis. I also express my gratitude to Prof. Jean-François Paul for the execution of the role of the president of the examination committee.

I would also like to express my gratitude to the *Unité de Catalyse et Chimie du Solide* (UCCS, UMR 8181) research team, and especially Dr. Olivier Mentré and Dr. Nicolas Nuns, for their assistance in my research. I owe my gratitude to Dr. Aram Bugaev (*The Smart Materials Research Institute, Southern Federal University*), Dr. Valerie Briois (*Synchrotron SOLEIL*), and Dr. Maya Marinova(*Institut Michel-Eugène Chevreul*) for their invaluable help in interpreting the results and assisting with the articles.

I also owe the successful completion of my thesis to the research group of the laboratory "Chemical technology of oil and gas processing" of the Samara State Technical University. *I would especially like* to thank Dr. Alexander Mozhaev and Dr. Maria Nikulshina for their support in my research work, as well as for skills and experience.

It is impossible to complete the work without help of our teams.

I should not forget to thank all of my friends in Samara and Lille for their helping hands. You have given me support and helped me succeed in my work.

And finally, I would like to express special thanks to my parents and, of course, my wife for their love, continued support and care throughout my studies.

Thanks to all of you!

"... a constant desire to do everything right, and complete unawareness of what exactly is right." ©

Table of contents

General Introduction 6

Chapter 1

1. Literature review 12

1.1 Introduction 12
1.2 The development of hydrotreating processes 12
1.2.1 The role and purpose of hydrogenation processes in oil refining 12
1.2.2 Main compounds and target reactions of hydrotreating 14
1.3 Hydrotreating sulfide catalysts 17
1.3.1 The composition and structure of the active phase 17
1.3.2 On active phase and active sites of unpromoted hydrotreating catalysts 19
1.3.3 Relations between active phase composition and catalytic properties 20
1.3.4 The influence of the support on the catalytic activity 21
1.3.5 Mesostructured silica as a promising support for hydrotreating catalysts 22
1.4 Supported MoWS catalysts 23
1.4.1 Methods for the synthesis of supported mixed MoWS hydrotreating catalysts 23
1.4.2 Heteropolyanions as effective precursors of hydrotreating catalysts 25
1.4.2.1 Type, composition and structures of heteropolyanions 25
1.4.2.2 Heteropolyanions as precursor for hydrotreating catalysts 25
1.4.2.3 Mixed MoW-heteropolyanions as interesting precursors for hydrotreating catalysts 26
1.5 Unsupported (bulk) sulfide hydrotreating catalysts 28
1.5.1 Methods for the synthesis of unsupported sulfide hydrotreating catalysts 28
1.5.2 Promoted unsupported sulfide catalysts 31
1.5.3 Unsupported mixed (Ni)MoW catalysts 35
1.5.4 The bulk catalysts: from science to industry 37
1.6 Conclusion 39
References 40

Chapter 2

2. Unpromoted MoWS hydrotreating catalysts supported on alumina 50

2.1 Introduction 51
2.2 Synthesis and characterization of $H_4SiMo_nW_{12-n}O_{40}$ Keggin-type heteropolyacids 52
2.2.1 Synthesis of $H_4SiMo_nW_{12-n}O_{40}$ Keggin-type heteropolyacids 52
2.2.1.1 Synthesis of monometallic $H_4SiMo_{12}O_{40}$ and $H_4SiW_{12}O_{40}$ heteropolyacids 52
2.2.1.2 Synthesis of mixed $H_4SiMo_nW_{12-n}O_{40}$ (n = 1 and 3) heteropolyacids using lacunar salts 52
2.2.1.3 One-step synthesis of mixed $H_4SiMo_nW_{12-n}O_{40}$ (n = 6 and 9) heteropolyacids 53
2.2.2 Characterization of $H_4SiMo_nW_{12-n}O_{40}$ Keggin-type heteropolyacids 54
2.2.2.1 IR and Raman analysis 54
2.2.2.2 Single-crystal XRD analysis 56

Table of contents

2.3 Preparation and characterization of the supported oxidic precursors 59
2.4 Characterization of supported Mo(W)/Al_2O_3 sulfide catalysts 61
2.4.1 Transmission electron microscopy (TEM) 61
2.4.2 High-angle annular dark-field scanning transmission electron microscopy (HAADF-STEM) 63
2.4.3 X-ray photoelectron spectroscopy (XPS) 65
2.5 Influence of the Mo/(Mo+W) atomic ratio in the active phase on the catalytic properties 68
2.6 Conclusion 71
References 73

Chapter 3

3. Ni-promoted MoWS hydrotreating catalysts supported on alumina 76

3.1 Introduction 77
3.2 Synthesis of NiMo(W)/Al_2O_3 catalysts 78
3.3 Characterization of sulfided NiMo(W)/Al_2O_3 catalysts 78
3.3.1 Transmission electron microscopy (TEM) 79
3.3.2 X-ray photoelectron spectroscopy (XPS) 81
3.4 Determination of the composition and structure of the active phase 86
3.4.1 HAADF characterization of gas phase sulfided Ni(Mo)W/Al_2O_3 catalysts 86
3.4.2 EXAFS characterization of gas phase sulfided Ni(Mo)W/Al_2O_3 catalysts 87
3.5 Catalytic tests in hydrotreating of model and real feeds 92
3.5.1 NiMo(W)/Al_2O_3 catalysts in hydrotreating of DBT and naphthalene 92
3.5.2 NiMo(W)/Al_2O_3 catalysts in co-hydrotreating of DBT, naphthalene and quinoline 94
3.5.3 Hydrotreating of SRGO 98
3.6 Conclusions 101
References 103

Chapter 4
4. Bulk mixed MoWS hydrotreating catalysts 106

Introduction 107
Full Published Article 108
Supporting Information for Chapter 4 121

Chapter 5
5. Mixed MoW catalysts supported on mesostructured silica 124

5.1 Introduction 125
5.2 Comparison of the catalytic properties of supported mixed MoW catalysts based on alumina and mesostructured silica (SBA-15 and COK-12). 126
5.2.1 Supports and catalysts preparation 126
5.2.2 Characterization of MoW/Sup catalysts 127
5.2.3 Transmission electron microscopy (TEM) 128

Table of contents

5.2.4 X-ray photoelectron spectroscopy (XPS) of MoW/Sup catalysts 130
5.2.5 MoW/Sup catalysts in hydrotreating of mixture of DBT and naphthalene. 132
5.3 Influence of the Mo/W ratio on the catalytic activity of mixed SBA-15 based catalysts 134
5.3.1 Preparation and characterization of the Mo(W)/SBA-15 catalysts 134
5.3.2 Transmission electron microscopy (TEM) 134
5.3.3 X-ray photoelectron spectroscopy (XPS) 136
5.3.4 Mo(W)/SBA-15 catalysts in hydrotreating of DBT and naphthalene 136
5.4 Conclusions 140
References 141

General Conclusion 143

Annex 148

1. Physicochemical methods of analysis 149
1.1 Raman spectroscopy 149
1.2 IR- spectroscopy 150
1.3 Single-crystal X-ray diffraction (XRD) 150
1.4. Powder XRD 151
1.5 Low-temperature adsorption of nitrogen 151
1.6 High-resolution transmission electron microscopy (HRTEM) 154
1.7. High resolution high-angle annular dark-field scanning transmission electron microscopy (HR HAADF-STEM) 155
1.8 X-ray photoelectron spectroscopy (XPS) 156
1.9 ToF-SIMS measurements 157
1.10 EXAFS spectroscopy 159
1.11 Evaluation of catalytic activities in model reactions 161
1.12 Evaluation of catalytic activities in hydrotreating of SRGO 163
References 166

General introduction

Recently, much attention has been paid to the quality of the produced fuel, especially diesel and gasoline. As the world demand for these types of fuel increases every year, environmental standards for diesel fuel have noticeably tightened, especially concerning the content of total sulfur (≤10 ppm) and polyaromatic hydrocarbons (≤11 wt.%). At the same time, the period of light oil is coming to an end and lately oil refining has been paying more and more attention to the use of heavy viscous sour oil sources, with an increase of the volume of heavy sulfur and high-sulfur oils to be treated [1]. In this regard, hydrotreating process is still one of the most important catalytic processes in oil refining. Deep hydrotreating of petroleum fractions to produce ultra-clean fuels is possible only in the presence of highly efficient catalysts.

For more than a century, academic and industrial hydrotreating catalysts have been based on a general composition - Co(Ni)Mo(W)S/Al_2O_3. The development of researches on sulfide catalysis has made possible to increase the activity of catalysts tenfold and to create hundreds of brands of industrial hydrotreating catalysts. Recently, there has been a growing interest in the use of mixed metal sulfides for hydrotreating catalysts, which may include two or more structural-forming metals, such as molybdenum [2, 3], tungsten [4] and niobium [5].

The development of the trimetallic NiMoWS bulk catalyst «Nebula» from Albemarle was a real breakthrough in oil refining. This catalyst exhibits activity at least three times higher than the best conventional supported hydrotreating catalyst used in industry [6]. According to the results of many studies, it was found that the specific catalytic activity of bulk catalysts is several times higher than the supported one [4, 7, 8]. However, bulk catalysts are much more expensive than supported ones and are used only in batch loading together with supported ones, which should also have high activity.

In addition to the modification of the active phase, research is underway on the use of new materials for support, such as mesostructured silica (MCM-48(41), SBA-15(16), etc), carbon, zeolites and their alumina composite materials (Al_2O_3-B_2O_3, Al_2O_3-TiO_2, Al_2O_3-SBA-15, etc). Among them, mesostructured silica have been explored as support for hydrotreating catalysts, their main advantage being their high thermal stability and well-developed texture [9, 10].

But even now, most of the developed catalytic systems do not cope with modern tasks, such as the deterioration of the quality of raw materials and the tightening of environmental standards. Therefore, the development of new highly active catalysts for hydrofining petroleum fractions is a real challenge for both science and industry.

The aim of this work is the development of (Ni)MoW catalysts prepared from mixed Keggin-type $SiMo_nW_{12-n}$ heteropolyacids as precursors, with a large range of Mo/W ratio, ranging from 1/11 to 9/3. The effect of the Mo/(Mo +W) molar ratio on the activity of the prepared MoW and NiMoW bulk and supported catalysts in hydrotreating of model and real feedstocks will be explored.

The thesis consists of five chapters. Chapter I provides an overview of the literature on the role of hydrotreatment in oil refinery, main compounds and target reactions of hydrotreating. The composition and structure of supported and bulk hydrotreating catalysts are described in detail, as well as methods for their preparation, the structure of the active phase and active sites. The advantages and potential of using mixed MoW sulfided systems are considered. The use of heteropolyanions as promising oxide precursors is described.

Chapter II focuses on a new method for the synthesis of mixed $H_4SiMo_nW_{12-n}O_{40}$ heteropolyacids (HPA) with high molybdenum content (Mo/W=6/6 and 9/3), as well as advanced physico-chemical characterization of starting precursors and corresponding prepared catalysts supported on alumina. The catalysts were tested in model hydrotreating reactions (DBT HDS and naphthalene HYD). The composition of the active phase was studied by X-ray photoelectron spectroscopy (XPS) and the crystallite structure was analyzed by high-angle annular dark-field scanning transmission electron microscopy (HAADF-STEM). The influence of the Mo/W ratio together with the nature of the precursors (mixed HPA or mixture of monometallic HPAs) on the active phase and catalytic activity is considered.

Chapter III presents studies of the influence of the atomic Mo/W ratio on the catalytic activity of Ni-promoted MoW/Al_2O_3 catalysts tested in hydrodesulfurization of dibenzothiophene and naphthalene hydrogenation with the addition of nitrogen-containing compound and hydrotreating of a straight-run diesel fraction. Catalyst samples were analyzed by TEM and XPS, and the composition and structure of the active phase were studied by extended X-ray absorption fine structure (EXAFS), and HAADF. The main goal of this section is to select the optimal catalyst composition for the process of hydrotreating diesel fractions, taking into account the effect of inhibition by nitrogen-containing components.

Chapter IV is devoted to the preparation of unsupported MoW catalysts by HF acid etching of the support and the investigation of their physicochemical and catalytic properties in hydrodesulfurization of dibenzothiophene and naphthalene hydrogenation. This chapter presented the results of a study of the composition and structure of non-supported catalysts by EXAFS and ToF-SIMS.

Chapter V examined the possibility of replacing traditional alumina with a more promising support, such as mesostructured silica, in order to improve catalytic properties. The obtained samples were tested in the reactions of DBT HDS and HYD of naphthalene.

References

[1] A. Stanislaus, A. Marafi, and M. S. Rana, "Recent advances in the science and technology of ultra low sulfur diesel (ULSD) production," *Catal. Today*, vol. 153, no. 1–2, pp. 1–68, 2010, doi: 10.1016/j.cattod.2010.05.011.

[2] J. Hein, O. Y. Gutiérrez, S. Albersberger, J. Han, A. Jentys, and J. A. Lercher, "Towards Understanding Structure–Activity Relationships of Ni–Mo–W Sulfide Hydrotreating Catalysts," *ChemCatChem*, vol. 9, no. 4, pp. 629–641, 2017, doi: 10.1002/cctc.201601281.

[3] L. Zhang, X. Long, D. Li, and X. Gao, "Study on high-performance unsupported Ni-Mo-W hydrotreating catalyst," *Catal. Commun.*, vol. 12, no. 11, pp. 927–931, 2011, doi: 10.1016/j.catcom.2011.03.004.

[4] C. Yin, Y. Wang, S. Xue, H. Liu, H. Li, and C. Liu, "Influence of sulfidation conditions on morphology and hydrotreating performance of unsupported Ni-Mo-W catalysts," *Fuel*, vol. 175, pp. 13–19, Jul. 2016, doi: 10.1016/j.fuel.2016.02.029.

[5] V. Gaborit *et al.*, "Hydrotreating properties of mixed $Nb_xMo_{1-x}S_2$ alumina supported catalysts," *Catal. Today*, vol. 78, no. 1-4 SPEC., pp. 499–505, 2003, doi: 10.1016/S0920-5861(02)00336-X.

[6] F. L. Plantenga *et al.*, "'NEBULA': A hydroprocessing catalyst with breakthrough activity," *Stud. Surf. Sci. Catal.*, vol. 145, pp. 407–410, 2003, doi: 10.1016/s0167-2991(03)80246-x.

[7] D. Genuit, P. Afanasiev, and M. Vrinat, "Solution syntheses of unsupported Co(Ni)-Mo-S hydrotreating catalysts," *J. Catal.*, vol. 235, no. 2, pp. 302–317, 2005, doi: 10.1016/j.jcat.2005.08.016.

[8] L. Wang, Y. Y. Zhang, Y. Y. Zhang, Z. Jiang, and C. Li, "Ultra-deep hydrodesulfurization of diesel fuels on trimetallic NiMoW sulfide catalysts," *Chem. - A Eur. J.*, vol. 15, no. 46, pp. 12571–12575, Nov. 2009, doi: 10.1002/chem.200901997.

[9] T. Klimova, J. Reyes, O. Gutiérrez, and L. Lizama, "Novel bifunctional NiMo/Al-SBA-15 catalysts for deep hydrodesulfurization: Effect of support Si/Al ratio," *Appl. Catal. A Gen.*, vol. 335, no. 2, pp. 159–171, 2008, doi: 10.1016/j.apcata.2007.11.008.

[10] T. E. Klimova, D. Valencia, J. A. Mendoza-Nieto, and P. Hernández-Hipólito, "Behavior of NiMo/SBA-15 catalysts prepared with citric acid in simultaneous hydrodesulfurization of dibenzothiophene and 4,6-dimethyldibenzothiophene," *J. Catal.*, vol. 304, pp. 29–46, 2013, doi: 10.1016/j.jcat.2013.03.027.

Chapter 1

Literature review

1.1 Introduction

The first chapter provides an analysis of the scientific literature as well as the general context of the present study. The beginning of the section is devoted to general problems of oil refining and, in particular, the process of hydrotreating. The main aspects of the hydrotreating are considered, such as the purpose of the process, the main reactions and the role of the catalyst. The composition and structure of traditional catalysts, as well as the main directions of their modernization, such as the introduction of additives, replacement of the support and the use of new precursors of the active phase are described. The second part of this chapter deals with the development of mixed MoW catalytic systems, studies of mixed active phase including simultaneously two structure-forming metals (Mo and W) together with the synthesis of mixed MoW precursors such as heperopolyacids. Finally, the main methods of promoted and non-promoted unsupported catalysts synthesis as well as successful attempts to introduce bulk catalysts in industry, are then reported. The main conclusions obtained from the state of the art are summarized and allow to draw the objectives of the thesis devoted to the development of (Ni)MoW supported and bulk sulfide catalysts for hydrotreatment.

1.2 The development of hydrotreating processes

1.2.1 The role and purpose of hydrogenation processes in oil refining

Hydrotreating is the most used process for refining of components of crude oil over the last 60 years [1]. The constant growth in the consumption of liquid hydrocarbons and the tightening of environmental standards are the main reasons for the high rates of development of the hydrotreating process. According to the U.S. Energy Information Administration for 2018, global liquid fuels demand will increase more than 20% in 2050 [2] (**Fig. 1.1**), and the demand for motor fuels will reach 107 million barrels per day [3].

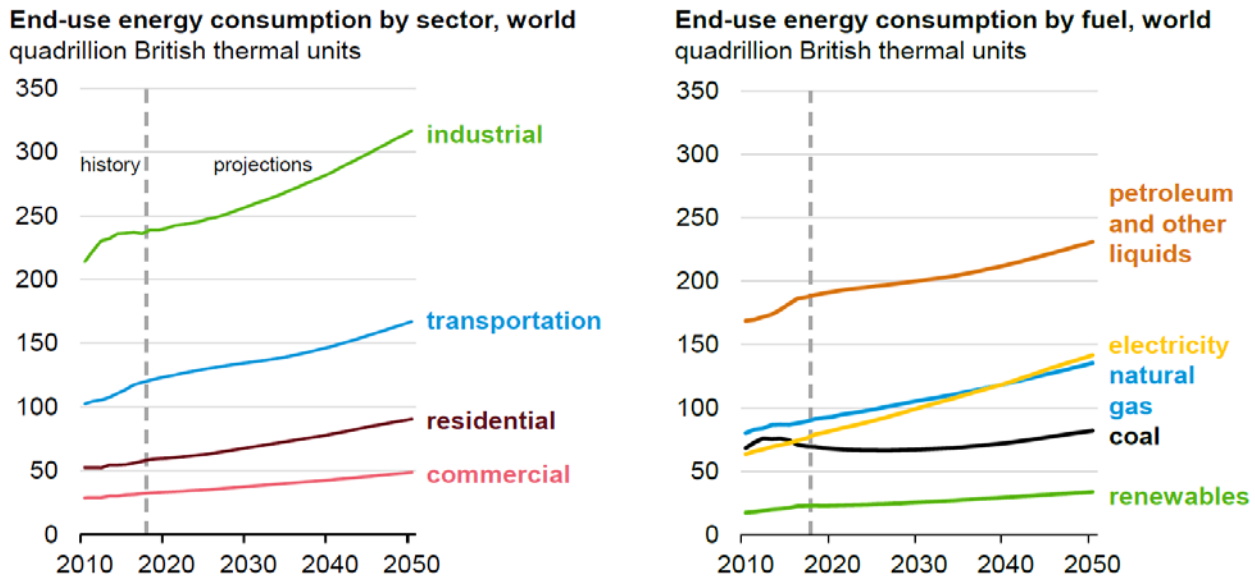

Fig. 1.1 Projected consumption of energy sources by various sectors [adapted from 11]

Analysts predict an increase in consumption of diesel fuel, which means that the hydrotreating process will be in demand in the future. Straight-run distillates such as kerosene and gas oil cannot be used directly as motor fuels due to several technical and chemical limitations such as high amounts of impurities (sulfur, nitrogen, and aromatics) and low cetane numbers in the case of diesel fuels. According to the worldwide refining survey for 2010, hydrotreatment has the largest processing capacity among all refining operations (45, 4 mil. barrels per calendar day) [4]. In the structure of the refinery, this process plays a key role in the production of all types of liquid fuel (**Fig. 1.2**). Usually, the hydrotreating process can be split into two major areas: (i) postprocessing of distillates and (ii) feed pretreatment for conversion processes such as isomerization, catalytic reforming, catalytic cracking.

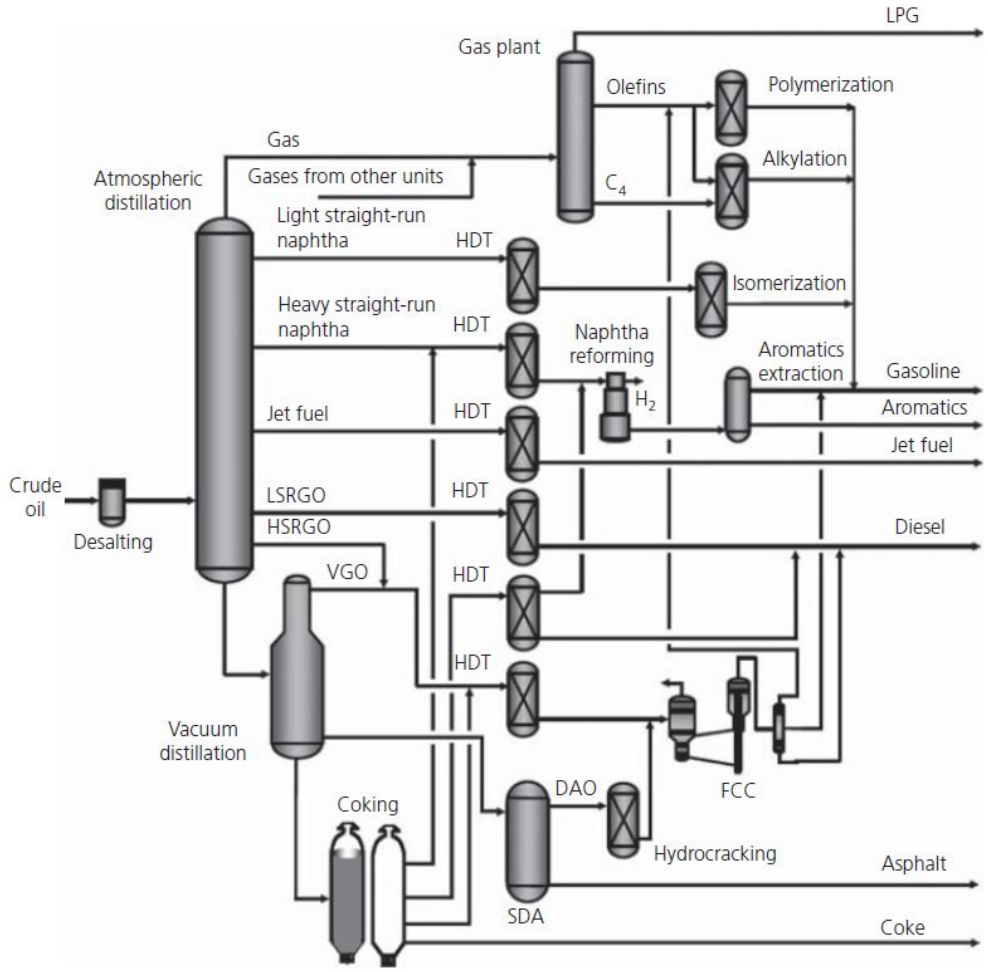

Fig. 1.2 Process scheme of a typical petroleum refinery. [adapted from 10]

At the same time, there has been a steady trend towards the involvement of heavy secondary fractions in the hydrorefining process. Light cycle oil, thermal cracking gas oil, gasoline and light delayed coking gas oil, as well as heavy straight-run fractions are widely involved in hydrotreating of diesel fractions for the last 15–20 years [5]. This trend is due to the fact that plants are seeking to increase the production of light petroleum products. Secondary distillates are subjected to more difficult hydrotreating than that of straight-run fractions due to the presence of a large content of

unsaturated hydrocarbons (aromatic, olefinic, diolefinic, etc.), polynuclear aromatics (PNA), asphalt-resinous substances, heavy sulfur compounds of cyclic structure [16, 17]. The sulfur removal and hydrogenation of polynuclear aromatics (PNA) are of primary concern because these compounds are among the major targets of environmental regulations.

1.2.2 Main compounds and target reactions of hydrotreating

The content of organic sulfur and polyaromatic compounds primarily depends on the composition and type of raw materials. Many studies of the composition of organic sulfur compounds, including the content of organic sulfur compounds in straight-run gas oils, have been carried out. **Fig. 1.3** shows the various types of sulfur containing compounds present in a typical Kuwait straight-run light gas oil analyzed by GC-SCD.

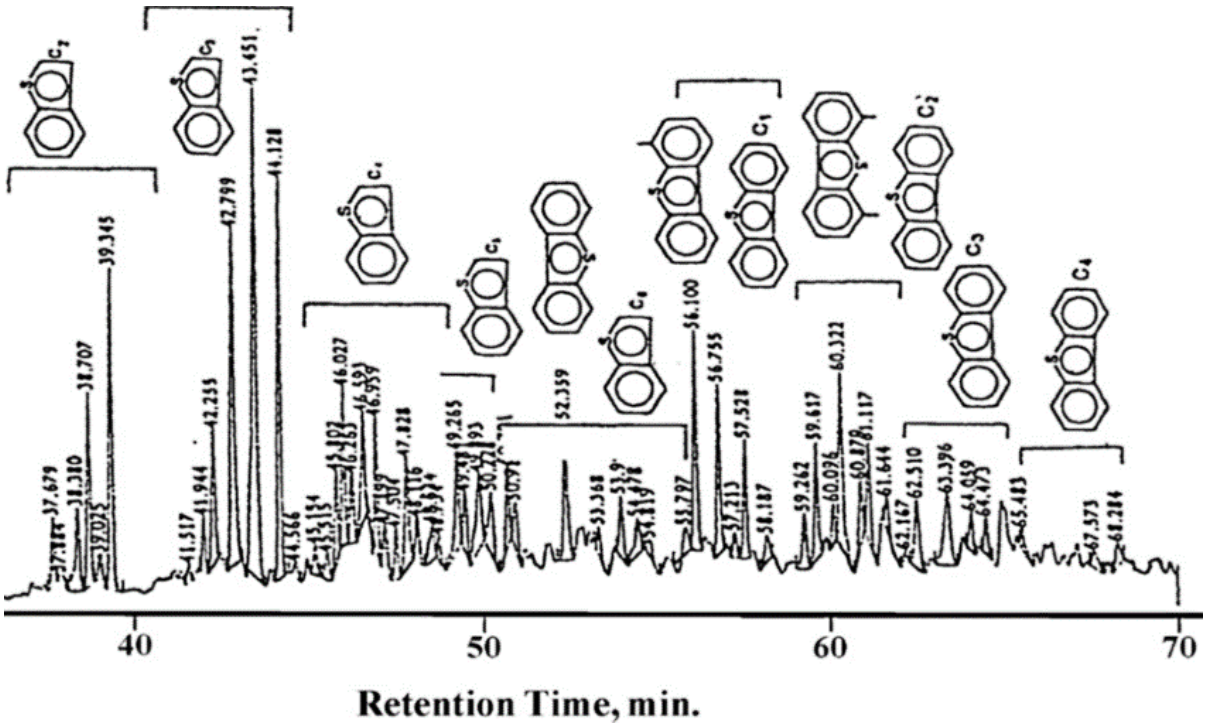

Fig. 1.3 GC–SCD chromatograms of sulfur compounds distribution in Kuwait straight-run light gas oil [8]

It was found that for the kerosene and gas oil middle distillate fractions, thiophenic compounds containing benzo- and dibenzothiophene structures dominate. Increasing the molecular weight and the number of aromatic rings in the structure reduces the reactivity in the HDS reaction (**Table 1.1**) as evidenced by the decrease of the pseudo-first-rate constant, because the aromatic structures become more stable increasingly [9]. Among the numerous reactions occurring during HDS, the slowest are the hydrogenolysis reactions of DBT and its derivatives.

Table 1.1 The reactivities of the different types of S-compounds [10]

Reactant	Structure	Pseudo first-order rate constant (l/(g of catalyst s^{-1}))
Thiophene		1.38×10^{-3}
Benzothiophene	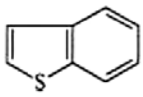	8.11×10^{-4}
Dibenzothiophene	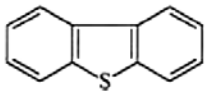	6.11×10^{-5}
Benzo[b]naphtho[2,3-d]thiophene	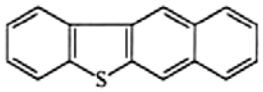	1.61×10^{-4}
7,8,9,10-tetrahydro-benzo[b]naphtho[2,3-d]thiophene	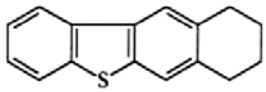	7.78×10^{-5}

*Catalyst: Co/Mo/Al_2O_3 (CoO, 3.7%; MoO_3, 13%; SiO_2, 1.8%); LHSV: 6 h^{-1}; reactor type: trickle bed; feed: 10 wt.% sulfur in tetralin.

The transformation of S-containing molecules with aromatic rings occurs through two parallel reactions (**Fig. 1.4.**): for HYD route, the primary stage is the hydrogenation of one of the aromatic rings of dibenzothiophene, and then hydrogenolysis of the C – S bond to form cyclohexylbenzene (CHB); during DDS route the hydrogenolysis of C-S-C bonds occurs, leading to the formation of biphenyl (BP) [21–23]. The HYD pathway is the predominant one for unpromoted catalysts in DBT HDS, while the DDS pathway is the predominant one for promoted catalysts.

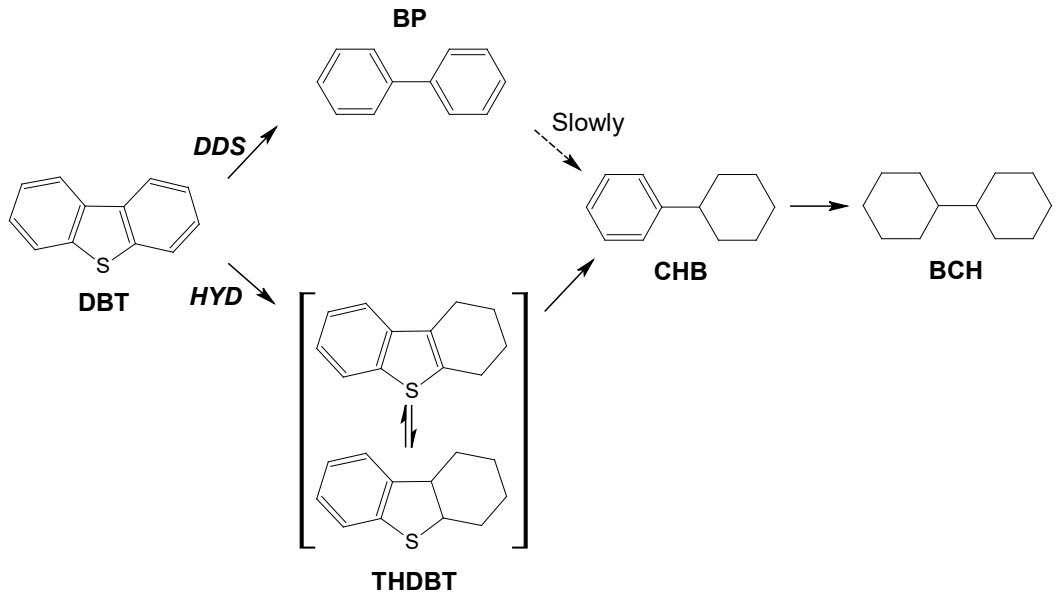

Fig. 1.4. Reaction network of the HDS of DBT adapted from Ref.

The greatest attention should be paid to dibenzothiophene (DBT) with alkyl substituents, which can reduce the reactivity in the HDS reaction, especially when they are adjacent to the S-atom in the dibenzothiophene core, due to steric effects. [16, 24, 25]. As the alkyl substituents approach the sulfur heteroatom, the reactivity of the component decreases (**Fig 1.5**).

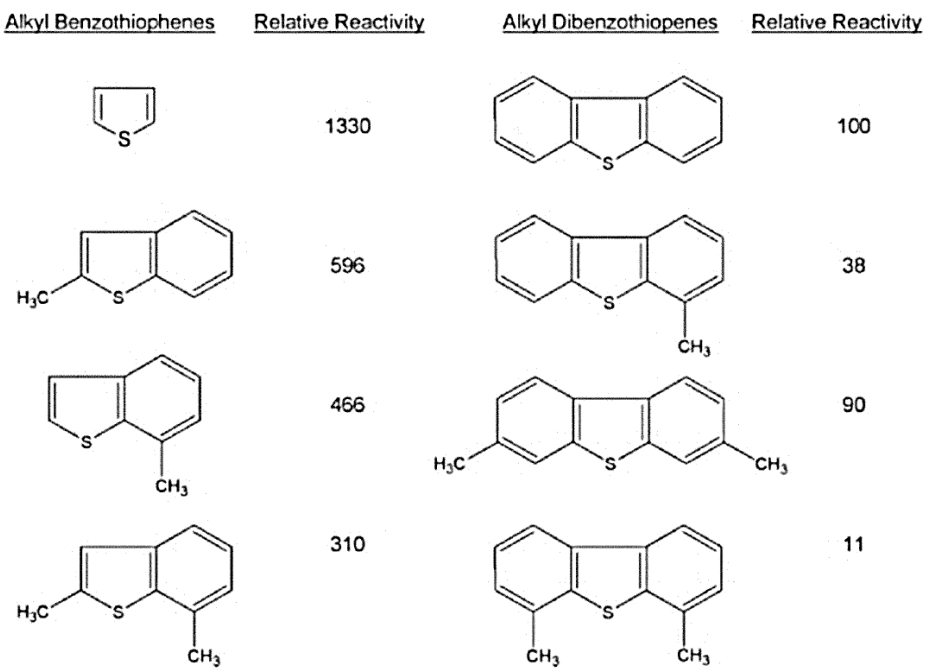

Fig. 1.5 Relative reactivity of alkyl-substituted BTs and DBTs [9]

Sulfur compounds with alkyl substituents at the 4- and 6- positions are the most resistant to desulfurization due to the steric hindrance around the sulfur atom. Such structure makes the σ-type interaction between the sulfur and the vacancy difficult [16]. In contrast, 2,8- and 3,6-alkyldibenzothiophenes are almost as reactive as dibenzothiophenes, and some of the alkyl-substituted ones are even more reactive, an effect attributed to increased electron density on the S atom (inductive effect) [23, 27, 28].

As mentioned earlier, another important indicator of the quality of the resulting fuels is the content of polycyclic aromatic hydrocarbons. Moreover, the presence of aromatic hydrocarbons has a negative effect on the hydrodesulfurization reaction due to competitive adsorption [1, 29]. The content of aromatic hydrocarbons in straight-run gas oil is approximately 25-30% and depends on the composition of the oil itself [21]. The involvement of secondary fractions in hydroprocessing significantly increases the content of aromatic hydrocarbons in the feed. For example, light cycle oil (LCO) from the FCC can contain up to 70% aromatic hydrocarbons [1, 24, 30]. Hydrogenation of PNA compounds (**Fig. 1.6**) [22] proceeds sequentially, from ring to ring.

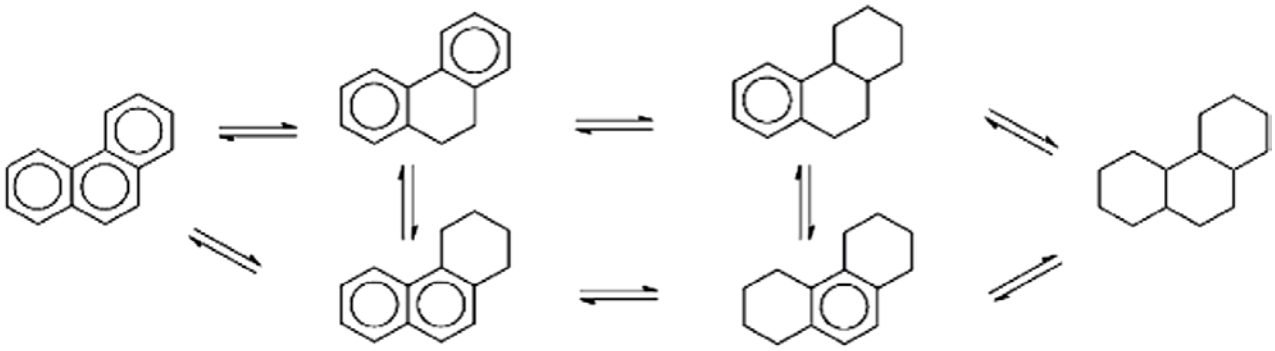

Fig. 1.6 Directions of phenanthrene hydrogenation reactions.

The kinetic study showed that each subsequent ring is much more difficult to hydrogenate than the previous one [30, 32]. The arrangement of the rings also affects the hydrogenation activity of aromatic hydrocarbons. The hydrogenation rate increases in the following order:

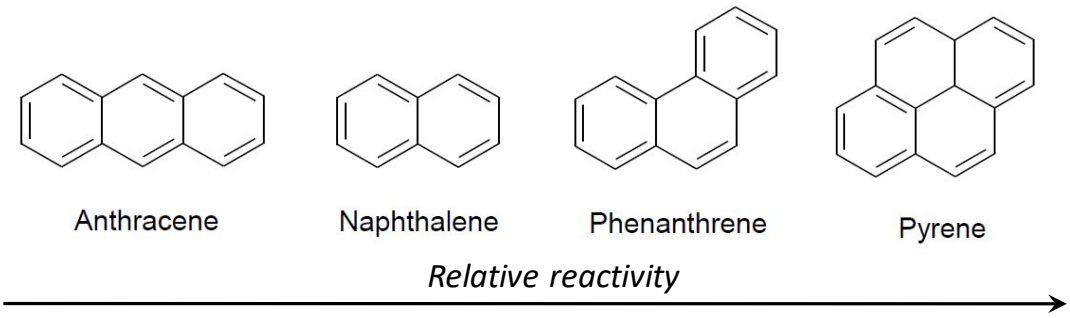

It was found that the presence of alkyl substituents on the rings of aromatics hardly affects the strength of adsorption [24]. In addition, PNAs are able to undergo polycondensation reactions, which lead to the formation of coke on the catalyst surface. Coking of the catalyst is one of the main reasons for the decrease in its activity.

Nitrogen-containing organic compounds have a strong influence on both HDS and HYD reactions. Interest in the study of the inhibitory effect of nitrogen-containing compounds increased when the need arose for the production of fuels with ultra-low sulfur content. The straight-run diesel fraction can contain up to 300 ppm of nitrogen [19], but when secondary processes are involved in gas oil hydrotreating, this content can significantly increase [25]. At the moment, the nitrogen content in fuel is not regulated by standards, but the presence of even a small amount (~30 ppm) of N-containing compounds in the feed significantly reduces the depth of sulfur removal [23]. Basic nitrogen compounds such as quinoline and acridine have the greatest inhibitory effect [35, 36]. In many works it was noted that hydrogenation reactions are mainly inhibited by nitrogen compounds due to their stronger adsorption [36–38]. In addition, the study of model compounds showed that hydrodenitrogenation of various cyclic nitrogen-containing compounds proceeds along the path of preliminary hydrogenation of the nitrogen-containing ring, and only then the cleavage of the C-N bond with the formation of an aliphatic amine, which is rapidly converted into ammonia and hydrocarbon [24, 39, 40]. For this reason, it is necessary to consider not only the HYD and HDS activity, but also to take into account the effect of nitrogen-containing inhibitors in the development and research of hydrotreating catalysts.

1.3 Hydrotreating sulfide catalysts

1.3.1 The composition and structure of the active phase

The active phase of hydrotreating sulfide catalysts consist in small MoS_2 (WS_2) crystallites (**Fig. 1.7**) with a layered structure. Several structural models for promoted and unpromoted Mo(W)S_2 were proposed and described in the literature [41–44].

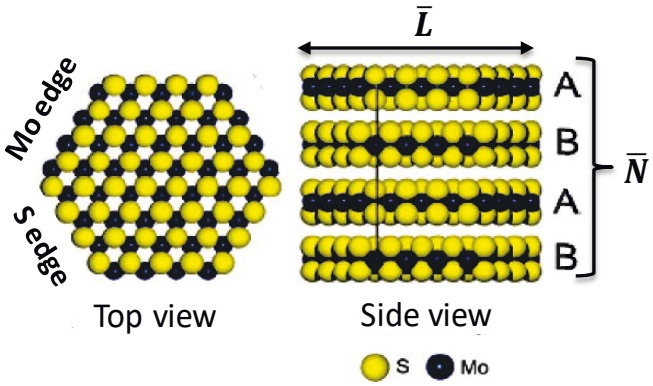

Fig. 1.7 Ball model of a MoS2

For Co and Ni promoted sulfided catalysts, Voorhoeve and Stuiver [35] proposed the "intercalation model" of the MoS_2 (WS_2) structure. The promoter Co(Ni) ions occupy octahedral intercalation positions in the van der Waal's gap between the slabs. Later Farragher and Cossee [36] and Farragher [37] proposed a modified model (pseudointercalation model) in which intercalation is supposed to occur only at the edges of the crystals. Delmon and co-workers [47, 48] studying unsupported catalysts found that the Co_9S_8 and MoS_2 phases can be in contact with each other (the contact synergy model). This contact synergism is explained by spill-over of hydrogen from Co_9S_8 and MoS_2.

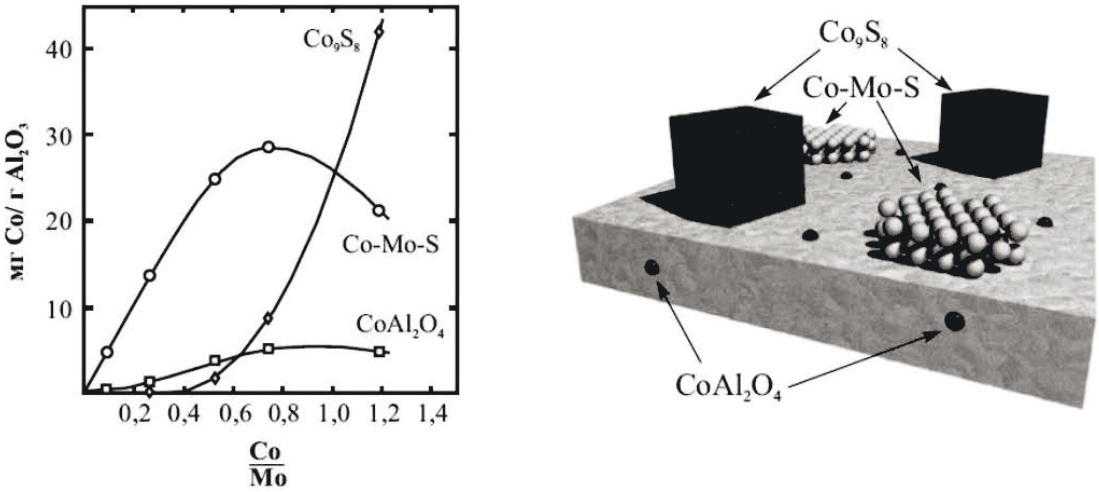

Fig. 1.8 Distribution of Co particles depending on the Co/Mo ratio (left) and the composition of individual Co particles on the carrier surface (right). Adapted from [24, 43]

Using Mössbauer spectroscopy, Topsøe et al. found that there were new replicas in the spectrum, apart from some previously known cobalt phases as $CoAl_2O_4$ and Co_9S_8 (**Fig. 1.8**), which the authors identified as the CoMoS phase [24, 42] The Co-Mo-S phase is MoS_2-like structures with the Co atoms located at the edges of the S–Mo–S layers. The Ni-Mo-S phase has a similar structure, using Ni as a promoter [40].

Two types of "Co-Mo-S type" phase (I and II type) with different catalytic properties were found depending on conditions of preparation. Harris and Chianelli [41] explained the differences in the properties of CoMoS phases of type I and II, based on the concept of the decisive role of metal-

sulfur covalent bonds on catalytic activity. In the type I "CoMoS phase", substantial interaction with the support was observed. This interaction decreases in type II "CoMoS phase", and the nature of the metal-sulfur bonds becomes more covalent, leading to an increase in catalyst activity in the HDS reaction.

1.3.2 On active phase and active sites of unpromoted hydrotreating catalysts

Each Mo atom is surrounded by six sulfur atoms in trigonal-prismatic coordination inside the crystallite (**Fig. 1.9**), where each sulfur atom is strongly bonded to three Mo atoms [14]. It is known that active centers are located on the edges of the MoS_2 (WS_2) slabs and contain coordination unsaturated molybdenum atoms and sulfur atoms. In **Fig. 1.9**, the structure of molybdenum disulfide in the bonds form allow to present in detail the surface atoms of sulfur and molybdenum. On the metallic edge (Me edge), each Mo atom is coordinated to four sulfur atoms, and on the sulfur edge (S edge), each S atom is coordinated to two Mo atoms.

It was found that under the reaction conditions, these edges are unstable [51–53]: hydrogen can react with sulfur located on S edges, forming anion vacancies or coordination-unsaturated sites (CUS) - molybdenum atoms, and hydrogen sulfide can dissociate after adsorption on the CUS on Me edges.

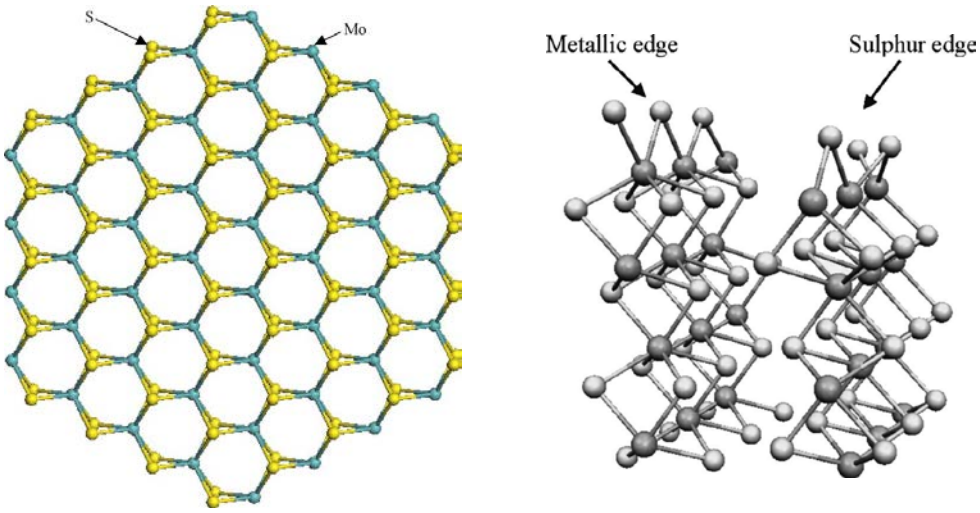

Fig. 1.9 Hexagonal MoS_2 crystallite exposing Mo- and S-edges (left) [45] and Cell showing the MoS_2 surface, stable upon classical reaction conditions (right) [46]

First, it was assumed that the centers of hydrogenation and direct desulfurization were the same [47]. Then, two different types of active centers were involved in HDS reactions. According to the "rim-edge" model [48] (**Fig. 1.10**) developed for bulk catalysts and later adapted for supported catalysts, the centers of the HDS and HYD reactions have a similar structure, but a different location: the HDS and HYD active centers are on the rim edges and the HDS centers are located on the edges of the MoS_2 crystallites. Salmeron et al. [49] found that sulfides of the basal plane do not participate in hydrogenation and hydrogenolysis reactions and are almost inactive.

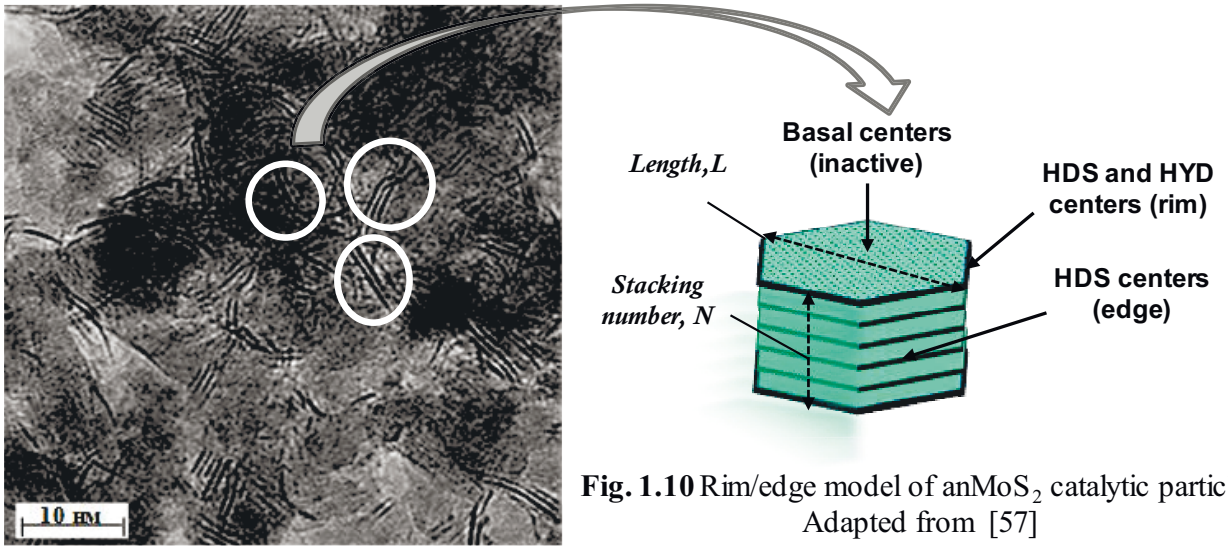

Fig. 1.10 Rim/edge model of anMoS_2 catalytic particle. Adapted from [57]

However, further studies showed that the centers of hydrogenation and hydrodesulfurization have different structures. Thus, for example, nitrogen-containing compounds primarily inhibit the hydrogenation reaction, while they have almost no effect on HDS activity, which in turn indicates the presence of two different active centers [59, 60]. Ma and Song [52] suggested that the hydrogenation sites are multiple vacant sites at the edges of Mo where planar π-adsorption occurs. Based on the data from scanning tunnel microscopy (STM) study and DFT calculations, it was found that the hydrogenation and ring opening of thiophenic compounds occurs on fully sulfur-saturated Mo $(10\bar{1}0)$ edges of MoS_2, sites with metallic character - the so-called "BRIM" center [53]. These centers can bind S-containing molecules, and if there are hydrogen on the adjacent edge centers in the form of SH-groups, they are able to transfer hydrogen and carry out HYD reactions due to metallic properties.

1.3.3 Relations between active phase composition and catalytic properties

The introduction of a metallic promoter significantly affects the structure and reactivity of active sites. According to the "CoMoS phase" model, promoter atoms are located on the edges of MoS_2crystallites. Replacement of Mo(W) by cobalt or nickel changes the binding energy of sulfur atoms located on the edges. For example, the removal of S atoms from a promoted edge site(Co-promoted) is an exothermic process, while the removal of sulfur from the surface of a slab of unpromoted MoS_2 is an endothermic process [54]. It can be said that the influence of the promoter is related to the optimization of the metal-sulfur bond strength. According to the Sabatier principle, the optimization of the strength of the adsorption of an organic sulfur compound (or desorption of H_2S) increases the catalytic activity of catalysts of this type (**Fig. 1.11**) [55]. It was found that Co and Ni atoms can provide optimal binding energies.

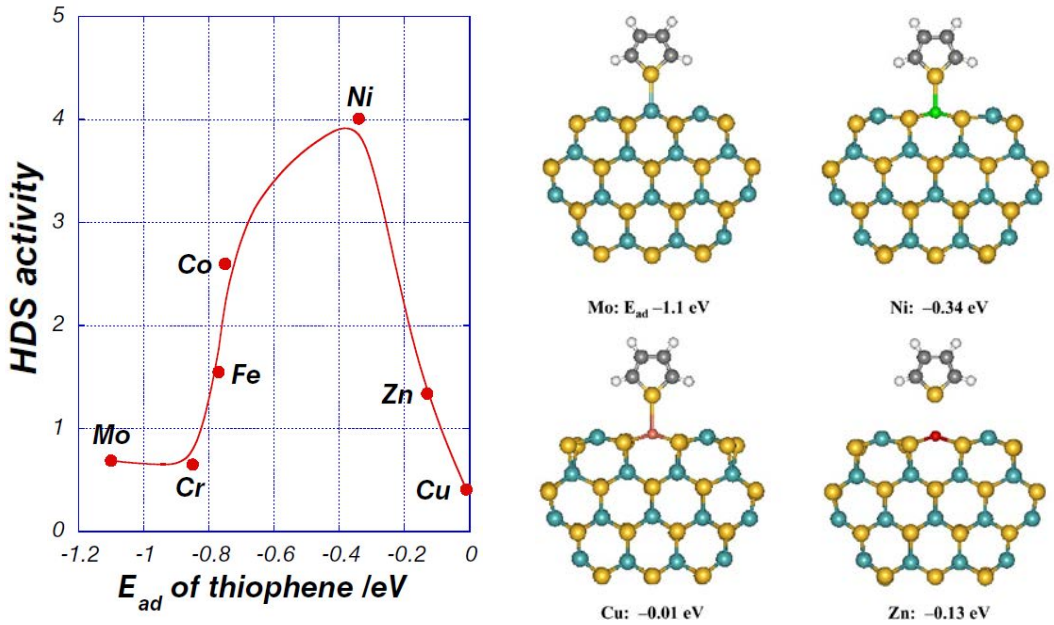

Fig. 1.11 Experimental HDS activity of X-MoS_2 catalysts vs. adsorption energy of thiophene. Adapted from [55]

Toulhoat and Raybaud [56] also reported that for HDT reactions the sulfur–metal bond energy (E_{MS}), correlates well with the activity via a volcano curve. Nikulshin et al. [57] obtained similar dependences not only for the reaction of the HDS reaction, but also for the HYD reaction in the presence of supported $XMo_6(S)/Al_2O_3$ (where X= Cr, Mn, Fe, Ni, Co, Cu, Zn, Ga) catalysts. It was found that the Co and Ni atoms can optimize the electron density on the anti-bonding d-orbital of Mo that results in improved catalytic activity. A further increase in electron density enhances the interaction between the products and the catalyst, which leads to a decrease in catalytic activity.

1.3.4 The influence of the support on the catalytic activity

The nature of the support has a great influence on the dispersion of the oxide and sulfide phases of catalysts, the sulfidation of the deposited precursor, the composition of particles on the surface, the morphology of active phase particles, catalytic properties and selectivity, deactivation, etc. There are numerous types of supports reported in literature: carbon, simple oxides (Al_2O_3, SiO_2, TiO_2, ZrO_2), binary oxides (TiO_2-Al_2O_3, TiO_2-ZrO_2, etc.), silica-alumina, zeolites and clays used in hydroprocessing. However, most of them did not find industrial application [58], because of impairing drawbacks. For example, most mesoporous carbons have poor crushing strengths, low bulk density or low surface area [59] .

It was recognized very early that TiO_2 and ZrO_2 could impart four to five times higher activities in Mo(W) catalysts in comparison to alumina. But at the same time these supports systematically lose their advantages over alumina for the promoted catalysts [67, 69].

Silica-alumina is promising support for HDS as their Brønsted acidity can improve HDS conversion of refractory compounds such as 4,6-DMDBT by enhancing the hydrogenation activity

of the active phase or by suppressing the steric hindrance brought by the alkyl groups, through previous isomerization [60]. On the other hand, the high acid properties of these catalysts tend to accelerate the formation of coke on the surface of the catalysts leading to deactivation [61]. Moreover, the presence of strong Brønsted sites also induces significant cracking [58]. The difficulty in obtaining well dispersed active phase species of HDS catalysts supported on zeolites and the small size of the zeolite pores will impede the application of zeolites as support for hydrotreatment [62].

The absolute leader among hydrotreating catalyst carriers is γ-Al_2O_3, which has a developed surface, the possibility to control the porous structure, high bulk density, thermal resistance and strength and ability to undergo regeneration [63].

1.3.5 Mesostructured silica as a promising support for hydrotreating catalysts

In more and more works of researchers, various meso-structured silica materials are proposed as support [73–76].

Trong On et al. [67] divided all the most well-known mesostructured silica (MSS) into three large groups obtained following different synthetic procedures. The first one is so-called M41S family of silica and aluminosilicates, prepared using ionic surfactants, such as cetyltrimethylammonium bromide (CTAB) as structuring agents. The second group (HMS and MSU) was developed by Pinnavaia and co-workers, who produced these materials using two neutral routes based on hydrogen bonding and self-assembly of non-ionic primary amines such as hexadecyl amine or polyethylene oxide (EO) surfactants and neutral oligomeric silica precursors S_0I_0 [77–79]. Finally, the third group of silicates (such as SBA-15 and COK-12) was developed by Stucky et al. [71] and Jammaer et al. [72] respectively, using di- and tri-block copolymers as organic structuring agents. These materials, with hexagonal (p6mm) structure, have long-range order and thick walls (typically between 3 and 9 nm) which make them thermally and hydrothermally more stable than previous materials.

Dhar et al. [73] conducted a comparative analysis of the hydrotreating (HDT) catalytic activity of Ni(Co)MoS supported on SBA-15 and Al_2O_3 for thiophene HDS and cyclohexene HYD. It was found that catalysts based on SBA-15 are more active in these reactions than alumina supported catalysts. A similar comparison was made by [74]. CoMo supported catalysts based on Co_2Mo_{10}HPA and different supports (γ-Al_2O_3, SBA-15, SiO_2) with Mo loading equal to 4 at·nm^{-2} were evaluated in HDT of the model feed containing dibenzothiophene (DBT) and naphthalene. It was found that CoMo/SBA-15 catalysts had the highest TOF numbers in DBT HDS and naphthalene HYD reactions. These findings were attributed to the optimal morphology of sulfide particles and the Co/Mo promotion degree due to the more suitable interaction between the active phase species and the support resulting in an increase of the stacking number and decrease of the average slab length of the CoMoS species located inside of mesoporous silicate channels as compared to the SiO_2 supported

samples. Ordered mesoporous materials, modified or not by incorporation of different heteroatoms (Al, Ti or Zr), were shown to present attractive properties (high surface area, large pore volume and thermal stability) leading to high performance HDT catalysts [84–87].

1.4 Supported MoWS catalysts

Recently, in the field of sulfide catalysis the attention of researchers was paid to the creation of mixed catalytic systems including two structure-forming atoms, such as molybdenum and tungsten. However, on the way of designing such systems, many obstacles arise, such as the stronger interaction of W species with the support than that of molybdenum [79] or lower sulfidation degree of tungsten oxide than that of molybdenum oxide, due to the stronger W-O bond strength [80]. But research is ongoing and first results have already been achieved.

1.4.1 Methods for the synthesis of supported mixed MoWS hydrotreating catalysts

Thomazeau et al. [81] conducted a study of catalytic systems prepared by incipient wetness coimpregnation of the support with solutions of ammonium heptamolybdate (AHM) ($(NH_4)_6Mo_7O_{24}\cdot 4H_2O$), ammonium metatungstate (AMT) ($(NH_4)_6H_2W_{12}O_{40}\cdot xH_2O$) and $Co(Ni)(NO_3)_2\cdot 6H_2O$ with the expected optimal ratio Ni(Co)/(Ni(Co) + Mo + W) = 0.3. Before impregnation, the pH of the solutions was adjusted to 9.5 with diluted ammonia for monomeric species (WO_4^{2-} or MoO_4^{2-}) to be predominant. After co-impregnation, catalysts were oven-dried overnight at 393 K and calcined in air at 773 K during 2 h. It was found that the promoted Mo-W-S solid exhibits a new synergy effect in thiophene HDS when Ni was used as a promoter: $NiMo_{0.5}W_{0.5}S_2$ catalyst reveals higher intrinsic HDS activity than bimetallic NiMoS and NiWS due to optimum metal-sulfur bond energy (**Fig. 1.12**). But at the same time, the $CoMo_{0.5}W_{0.5}S_2$ catalyst led to catalytic results without synergetic effect corresponding to a linear combination of the HDS activities of the two CoWS and CoMoS reference systems.

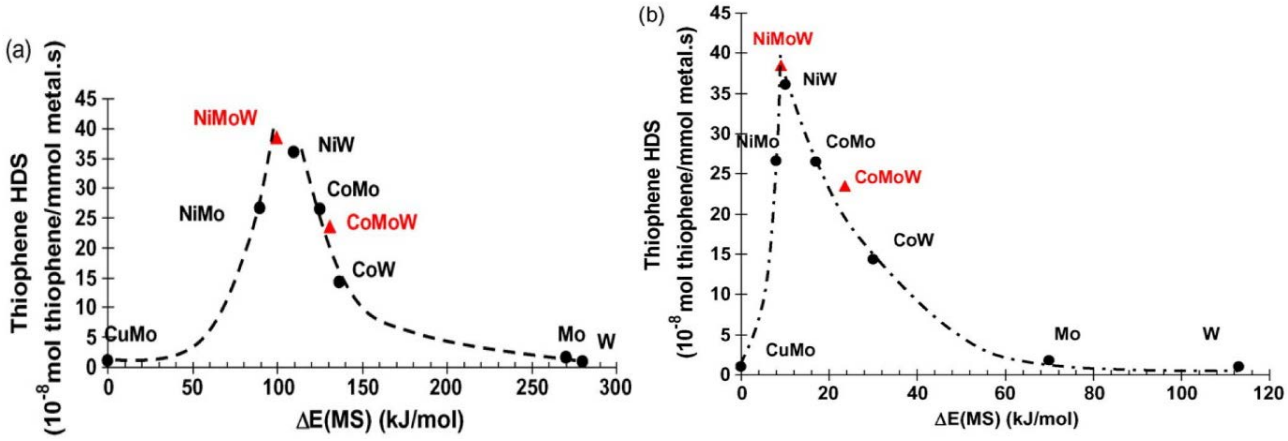

Fig. 1.12 Thiophene HDS activity as a function of the sulfur metal bond energy calculated on the (a) Mo(W)-edge and (b) S-edge. The reference in energy is chosen for the CuMoS active phase. Dashed volcano curves are only guide for the eyes [81]

Vázquez-Salas et al. [82] used the same method of synthesis to obtain NiMoW catalysts based on HMS modified with Ti (HMS-Ti) and conducted a comparative analysis of activities with Ni(Co)Mo/Al_2O_3 catalysts. All synthetized Ni-promoted MoW catalysts exhibited improved specific activities in the HDS of DBT compared to that of two commercial NiMo/γ-Al_2O_3 and NiW/γ-Al_2O_3 catalysts. Moreover, NiMoW/HMS-Ti catalysts showed a high enhancement of dibenzothiophene conversion via hydrogenation route with respect to their Ti-free counterpart.

The study of the genesis of NiMoW catalysts based on γ-Al_2O_3 was also developed by Hensen and co-workers [83]. All catalysts were synthetized by pore volume impregnation with aqueous solution of AHM ($(NH_4)_6Mo_7O_{24}\cdot 4H_2O$), AMT ($(NH_4)_6H_2W_{12}O_{40}\cdot xH_2O$) and nickel nitrate. It was found that the presence of Mo atoms does not affect the rate of sulfidation of tungsten under gas-phase conditions (H_2/H_2S (10%), 400ºC). However, it was found that increasing the pressure during sulfidation to 15 bar helps to reduce the temperature of tungsten sulfidation and in this case mixed slabs with a random distribution of Mo and W atoms are formed, while at atmospheric pressure slabs with a core-shell structure are formed, where Mo is mainly located in the core, and W in the shell (**Fig. 1.13**).

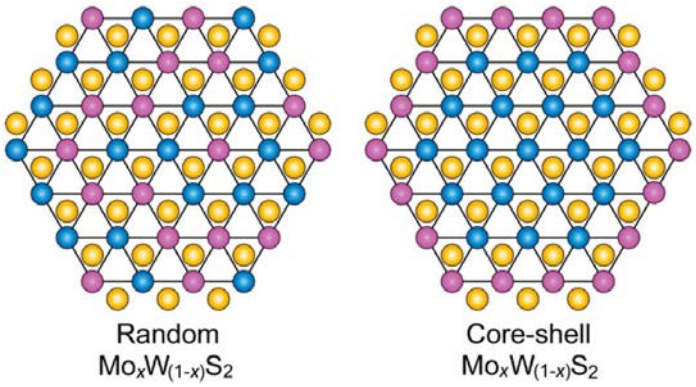

Fig. 1.13 Possible structures of the active phase in Ni-promoted $Mo_xW_{(1-x)}$ catalysts ($x \leq 1$) [83]

Moreover, the temperature of the sulfidation increase also contributes to the formation of slabs with a random distribution of atoms, which was explained by the sintering of particles together with the formation of slabs of greater length. Each structure was evaluated in only one reaction: the core-shell structure in the thiophene HDS reaction, the random structure – in the DBT HDS reaction, but in both cases, no pronounced synergistic effect between Mo and W was observed. More interesting data were obtained in in HDS of gas oil, according to the results of which it was found that mixed $NiMo_{0.75}W_{0.25}$ was the most active, which shows the potential of mixed systems [83].

Sigurdson et al. [84] reported that the catalytic activity in HDN and HDS reactions increases when phosphorus is added to NiMoW/Al_2O_3 as a promoter thanks to the P doping improving the dispersion and number of surface-active sites. A series of P-doped catalysts with different amount of P (0–2.5 wt.%) were prepared by impregnation of alumina with aqueous solution (pH ~ 4) containing

ammonium heptamolybdate, ammonium tungstate, nickel nitrate. and phosphoric acid. The catalysts were tested under conditions of industrial hydrotreatment of light coking gas oil in a trickle bed reactor. The phosphorous content of 1.6 wt.% is optimal and the trimetallic catalyst exhibits better hydrotreating activity than bimetallic and commercial catalysts.

Various types of studies of mixed MoW systems can be found in the literature, and most of them are related to synthesis using traditional precursors of the active phase, such as AHM, AHT, AMT and ammonium tungstate [94–96].

1.4.2 Heteropolyanions as effective precursors of hydrotreating catalysts

1.4.2.1 Type, composition and structures of heteropolyanions

Works concerning synthesis of hydrotreating catalysts via heteropolyanions (HPAs) have been known since the middle of 1980s. Instead of the use of traditional Mo and W precursors as AHM, AHT, AMT and others inorganic heteropolyanions are more and more common in the literature as precursor of active phase [90, 97, 98]. For hydrotreating catalysts preparation, HPAs with the Keggin [67, 99] and Anderson [100–103] structures and their derivatives [104, 105] (**Fig. 1.14**) are the most frequently used.

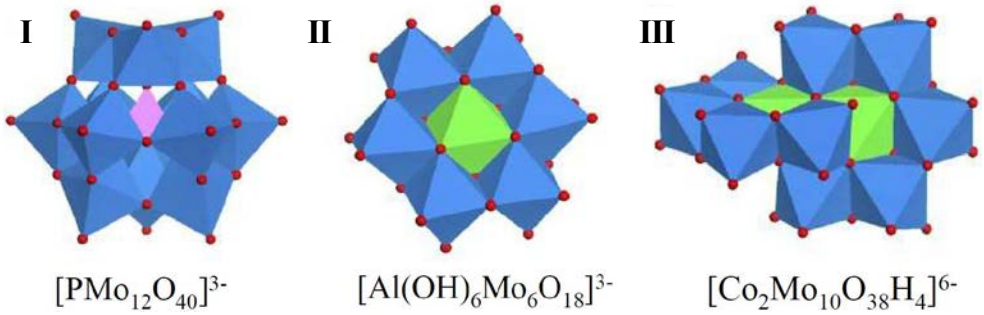

Fig. 1.14 The most commonly used heteropolyanions (I – Keggin structure; II - Anderson structure; III - substituted Anderson derivative) for a synthesis of HDT catalysts. Color scheme: Mo (blue); O (red); P (pink); Co (green) [91]

Heteropolyanions are complex inorganic compounds, which composition can be described as an assembly of oxygen polyhedra (octahedra and tetrahedra) of limited extent obtained by sharing one or more oxo (or hydroxo) ligands, the polyhedra being joined at their corners, edges or faces [97]. The stability of the HPA is influenced primarily by the composition of the ligand sphere: HPA with W is much more stable than HPA with Mo [98].

1.4.2.2 Heteropolyanions as precursor for hydrotreating catalysts

Hetoropolyanions can be derived from the acids (heteropoly acids) and corresponding salts (Co, Ni, etc.) (heteropoly compounds). Heteropolyanions are favorable for the preparation of catalysts because of the uniform adsorption of HPA on the surface of the support [100, 103], the possibility to

avoid the calcination step due to the absence of NH_4^+, NO_3^- counterions (if metallic salts of heteropolyanions are used for example) and a higher sulfidation degree of metals, which contributes to an increase in catalytic activity.

The main advantage of Anderson HPA is the presence of the 3d-metal as heteroatom in the composition of the HPA, including the traditional promoters of Ni (Co) or Fe [98]. The literature data [67, 101, 104] shows that the activity of catalysts synthesized from HPA in the thiophene HDS depends on the molar ratio of promoter/molybdenum [67, 101]. Using HPA with Anderson structure, this ratio is 1/6, which is suboptimal. For this reason, the derived dimeric form $[Co_2Mo_{10}O_{38}H_4]^{6-}$ from the Anderson structure is more preferable as a precursor of the active phase, since it has a Co/Mo molar ratio in this structure equal to 1/5, which is much closer to the optimum value of 1/2. In addition, the lack of a promoter is compensated by using Co(Ni) salts of HPA type $(Ni)_2[Ni(OH)_6Mo_6O_{18}] \times nH_2O$ or $(Co)_3[Co_2Mo_{10}O_{38}H_4] \times nH_2O$.

In turn, the Keggin type HPA and its derivatives (**Fig. 14 I**) are more stable than Anderson HPC, accessible and important for catalysis [108, 109]. In the Keggin-type heteropolyanions, one non-metallic atom, such as P, Si, As, B, etc., exists in a regular tetrahedron, combined with 12 MO_6 octahedra (where M is Mo^{VI}, W^{VI}, V^V), which are connected by shared edges to form trimetallic M_3O_{13} groups joined together by their vertices [101]. Depending on the synthesis conditions, various isomers (α, β, etc) can be isolated.

It has been shown that supported phosphomolybdic heteropolyacid ($H_3PMo_{12}O_{40}$) and its Co and Ni salts are efficient oxide precursors for thiophene HDS [102]. Moreover, Ni promoted molybdenum and tungsten HPA-based catalysts showed better performance in deep HDS of 4,6-DMDBT [103] and diesel hydrotreating [104] than the counterparts prepared from traditionally used Mo(W) ammonium salts.

Blanchard et al. have shown that catalysts obtained from the PMo-HPA with Keggin structure are more active in the thiophene HDS than those prepared from AHM and H_3PO_4 due to a better metal dispersion and the absence of ammonium counterions [91]. Griboval et al. [92] showed by using of $SiMo_{12}$ and PMo_{12}HPAs that the nature of the heteroatom (Si or P) of these HPAs does not affect the thiophene HDS catalytic activity of the obtained catalysts.

1.4.2.3 Mixed MoW-heteropolyanions as interesting precursors for hydrotreating catalysts

The literature also describes the synthesis of mixed HPA with Keggin structure, containing two structure-forming metals at once. Mixed heteropolyanions, such as $[PV_xMo_{12-x}O_{40}]^{(3+x)-}$ where (x= 1-3) [98], $[PV_xW_{12-x}O_{40}]^{(3+x)-}$ where (x= 1-4) [114, 115], were described and prepared for different applications. Mixed $PMo_{(12-x)}V_xO_{40}^{(3+x)-}$ generally used in the field of mild oxidation catalysis have been prepared for hydrodemetallation catalysis [107]. Spojakina et al. [108] also reported that catalyst

based on $(NH_4)_5[PMo_{11}V^{IV}O_{40}]$ are more active in thiophene HDS than a sample prepared from PMo_{12}HPA.

Concerning mixed HPA containing molybdenum and tungsten, the method of synthesis and catalytic properties in hydrotreating of two $SiMo_nW_{n-12}$ HPA (n = 1 and 3) were described in detail by Nikulshina et al [109]. Mixed heteropolyacids were synthesized via intermediate lacunary salts of the corresponding acids. The lacunary Keggin structure corresponds to a Keggin structure, in which one or more sites previously occupied by molybdenum or tungsten atoms are vacant (**Fig 1.15**).

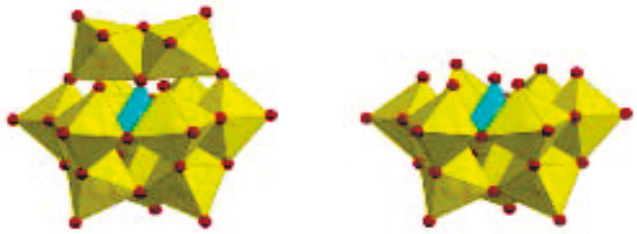

$[SiW_{11}O_{39}]^{8-}$ $[SiW_9O_{34}H]^{9-}$

Fig 1.15 The "lacunary" Keggin structure

These monovacant $[SiW_{11}O_{39}]^{8-}$ or polyvacant $[SiW_9O_{34}]^{9-}$ heteropolyanions can be synthesized directly depending on the pH medium. Further free vacancies are filled with molybdenum atoms and the corresponding mixed salts $[SiMo_1W_{11}O_{40}]^{4-}$ and $[SiMo_3W_9O_{40}]^{4-}$ respectively with the Keggin structure are formed. The literature describes methods for the synthesis of mixed $SiMo_nW_{n-12}$HPA with only a Mo/W ratio of 1/11 and 3/9. In the HDS of DBT and HYD of naphthalene, after activation under H_2S, catalysts prepared by incipient wetness impregnation of alumina using $SiMo_nW_{n-12}$HPAs as precursor were more efficient than their counterparts obtained by a mixture of monometallic HPAs with the same Mo/W ratio, which was related to the formation of a mixed $MoWS_2$ phase when using mixed HPA as precursor [109]. This phase was evidenced by HAADF. The arrangement of atoms of molybdenum and tungsten within the cluster depends on the method of sulfidation. According to the data published by Nikulshina et al. [110], [111] in the case of gas-phase sulfidation molybdenum atoms are located in the center of particles and surrounded by tungsten atoms (core-shell structure) **(Fig 1.16 a)**, while smaller islands of Mo surrounding by W atoms were observed in the liquid-phase sulfidation **(Fig 1.16 b)**. Moreover, it was found that with an increase of Mo/W ratio from 1/11 to 3/9 in a mixed phase, the catalytic activity also increases [110].

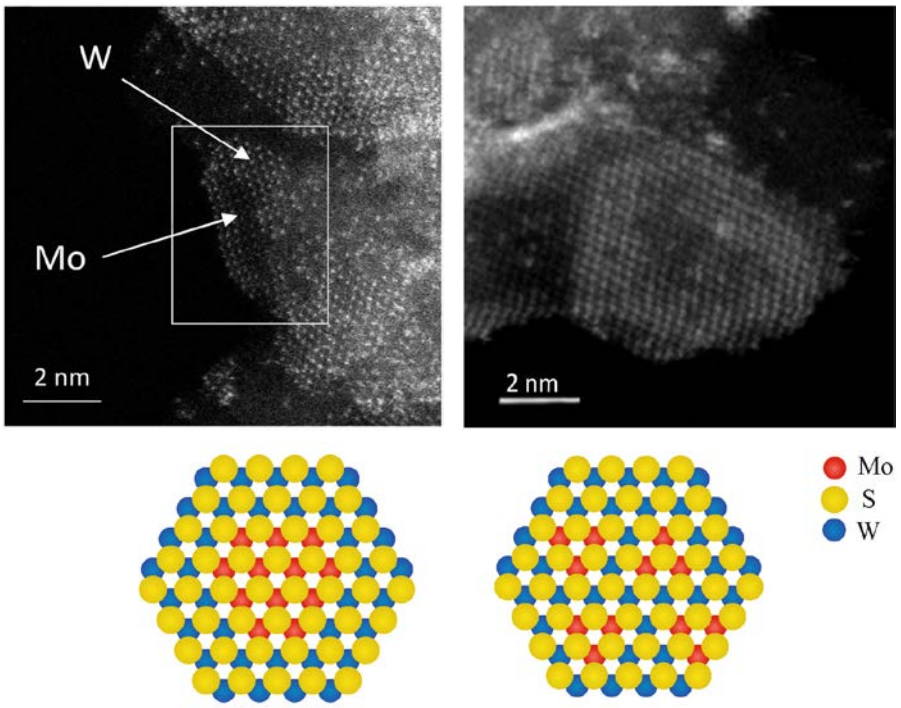

Fig. 1.16. HAADF images of sulfide Mo_3W_9-GS (a), Mo_3W_9-LS (b) catalysts (adapted from [119, 120]) (GS -gas phase sulfidation; LS - liquid phase sulfidation)

1.5 Unsupported (bulk) sulfide hydrotreating catalysts

Recently, the number of studies aimed at the development of unsupported sulfide hydrotreating catalysts has significantly increased. Currently, new catalysts appeared in the market, which contains very large amounts of active components and can be considered as bulk catalysts. The metal composition of the active phase in bulk catalysts is the same than that in the supported one, but at the same time, their hydrotreating volume activity may exceed two or more times that of supported catalysts [112]. The concentration of the active component can vary from 80% (if various additives and modifiers are used or if the role of the support is played by inactive sulfide) to 100% (pure bulk catalyst).

1.5.1 Methods for the synthesis of unsupported sulfide hydrotreating catalysts

The literature has described various methods for preparing bulk catalysts. One of the first methods for growing nano-sized MoS_2 particles inside inverse micellar cages in nonaqueous solvents was proposed more than 20 years ago and described by Wilcoxon and Samara [113]. The MoS_2 clusters are formed by first dissolving a molybdenum (IV) halide salt in solution with micellar cages and then combining this solution with another inverse micelle solution containing a sulfiding agent (e.g., metal sulfide or H_2S). The authors managed to get MoS_2 nanoparticles ranging in size from 2 to 15 nm. The size of the particles depends on the size of the initial micelles containing salt of Mo(IV).

Methods of hydrothermal [122, 123] and solvothermal [124, 125] processes for the synthesis of bulk catalysts have also been described. Devers et al. [114] synthesized unsupported MoS_2 by

hydrothermal method using $(NH_4)_2MoS_4$ (ATTM) as Mo source. The catalysts consisted in multi-layered slabs with an average length of 5 to 50 nm and a surface area (from 50 to 100 m^2/g) depending on the synthesis conditions (temperature and acidity of the reaction mixture). It was found that samples with a large particle length exhibit a higher activity in hydrogenation (HYD), while samples with a low particle length are more active in hydrodesulfurization (HDS). Vrinat and co-workers [117] investigated bulk molybdenum disulfide obtained by the solvothermal method using molybdenum naphthenate as precursor and n-hexadecane or 1-methylnaphthalene as hydrocarbon solution. The samples had a high surface area (more than 200 m^2/g) and showed higher catalytic activity in thiophene HDS than the sample obtained by the hydrothermal method. A variable amount of a carbonaceous phase was detected in catalysts (6-8 wt.% of the total solids). It has been suggested that the coke phase originates from the organic-molybdenum precursor, while the organic solvent is not involved in the formation of a carbonaceous phase. The authors did not establish a direct dependence of the catalytic activity on the surface area. However, changes in the texture of coke can affect the accessibility of reagents to the MoS_2 surface and, therefore, the catalytic activity can depend on the interface between coke and molybdenum sulfide [117].

Polyakov et al. [118] reported the method of high temperature decomposition of ATTM. The catalysts were tested in the model reactions of hydrogenation and isomerization of alkenes, as well as deuterium exchange. It was found that MoS_2 microcrystalline obtained at high-temperature was completely inactive in hydrocarbon transformations (isomerization of alkenes and ethylene hydrogenation) and H_2/D_2 scrambling, but after high-energy ball milling was transformed into an active catalyst. The activity of MoS_2 correlates with the degree of structural defects such as split nanoslab projecting from an aggregation of bent nanoslabs and stepwise truncations of the layers (**Fig 1.17.**).

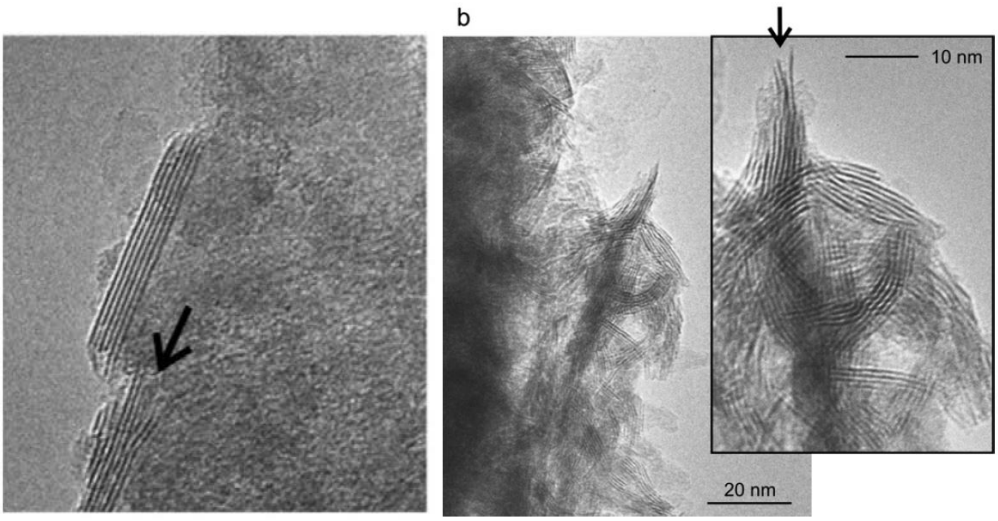

Fig. 1.17 structural defects of MoS_2 crystallites. Adapted from [118]

The direct method of producing WS_2 and MoS_2 nanoplates in one stage in environmentally friendly conditions was also described in [119]. The process was realized in stainless steel reactor at room temperature in a nitrogen filled glovebox using elemental sulfur, tungsten and molybdenum powders (all micrometer sized). The temperature of the tube furnace was raised to 750 °C at a rate of 15°C/min and the temperature maintained at 750°C for 1–3 h. The sizes (diameter) of the WS_2 and MoS_2 particles were 1–5 μm and 3-10 μm respectively.

A different interesting method for the synthesis of unsupported catalysts has also been described [128, 129]. The catalysts were prepared from purified molybdenite MoS_2 mineral in an activation mill. The grinding conditions were as follows: the raw MoS_2 and the grinding media with a diameter of 1 mm in the ratio of 1/75, butanol as the milling additive, at an agitating rate of 2600 rpm for 10 h in an argon atmosphere. The ground MoS_2 powder containing a high concentration of crystalline defects, dislocations or discontinuities in the random layer structure, can make it more active in the hydrodesulfurization reaction. The catalysts were evaluated in the model reaction of hydrogenolysis of dibenzothiophene, as well as hydrotreatment of heavy oil fraction. It was found that bulk MoS_2 catalyzed the desulfurization of 4,6-DMDBT more than the industrial catalyst under the equivalent molybdenum weight, while as for DBT HDS it was inferior to the industrial sample [121].

Li et al [122] used the HF etching for MoS_2 structural studies removing Al_2O_3 from supported MoS_2 catalysts. The application of HF etching may affect the size distribution of the slabs and change the size distribution of the MoS_2 phase to more stacking and longer particle size, no matter what kind of metal loading or precursors is used.

Varakin et al. [123] used the same method to prepare bulk catalysts (Et-MoS_2 and Et-MoS_2/C) by removal of alumina using HF etching (Et) from supported MoS_2/Al_2O_3 and $MoS_2/C/Al_2O_3$. These bulk systems had greater catalytic activity in DBT HDS than the samples obtained by decomposition of ATTM (Ref-MoS_2), solvothermal synthesis using a hexadecane/water mixture in the volume ratio of 1/3 at 350 °C and under 4 or 14 MPa of hydrogen (4-MoS_2, 14-MoS_2) and hydrothermal synthesis with surfactants Triton X114 (Trit-MoS_2) and chitosan (Chit-MoS_2). In bulk catalysts, as in supported catalysts, the morphology of the active phase particles plays an important role. The authors, using the 3D diagram for rate constant k_{HDS} as a function of average length and average stacking number (**Fig 1.18**), demonstrated that the maximum HDS activity is achieved with a good dispersion of the active phase (the shortest length and the largest stacking), which corresponds to the catalysts obtained by etching the support.

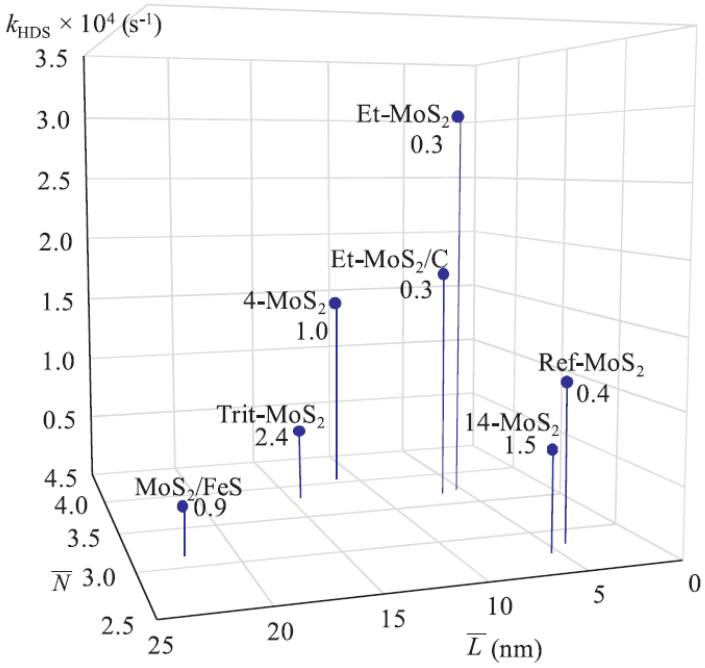

Fig. 1.18. 3D diagram for rate constant k_{HDS} as a function of average length and average stacking number. (The values near the catalyst marker show the nitrogen content wt. %) [123].

It was also found that nitrogen content in bulk catalysts, which the samples acquired during synthesis, strongly impacted catalytic activity. The authors suggested that incomplete removal or presence of ammonium from ATTM during the activation process had led to the nitrogen incorporation into the MoS_2 crystallite and, as a result, inhibited activity in DBT HDS. In the case of Et-MoS_2 and Et-MoS_2/C samples, it was assumed that nitrogen comes from the support after its peptization in nitric acid.

1.5.2 Promoted unsupported sulfide catalysts

Introduction of the promoter always represents a delicate procedure in order to form a good composite of MoS_2/WS_2 and Co/Ni salt to obtain high active multi-metal unsupported catalysts with high surface area [112]. For this reason, more and more researches are aimed at creating bi- and polymetallic unsupported catalysts.

More than thirty years ago, Richardson [124] proposed a method for the preparation of promoted unsupported sulfide catalysts. Unsupported molybdenum sulfide was obtained by precipitation of ammonium heptamolybdate $(NH_4)_6Mo_7O_{24}$, which was then air-dried and cobalt acetate solution was further added to impregnate the samples with the desired compositions. It was found that the HDS activity of the samples is directly dependent on the concentration of cobalt.

The Co(Ni)MoS_2 catalyst without carrier was proposed in [125] by hydrothermal synthesis using water and organic solvent. The samples showed a higher activity in hydrodesulfurization of 4,6-dibenzothiophene in comparison with the supported analogs. The catalysts had a good pore volume (V_P = 0.72 m^3/g) and a high specific surface area (S_{BET} = 320 m^2/g), while most bulk catalysts

traditionally have a low specific surface area, not exceeding 100 m^2/g [7, 133, 134]. For this reason, various organic additives and surfactants are added during the synthesis of bulk catalysts [126]. Later Yoosuk et al. [128] showed effects of preparation conditions in hydrothermal synthesis of highly active unsupported NiMo sulfide catalysts for simultaneous hydrodesulfurization of dibenzothiophene and 4,6-dimethyldibenzothiophene. Studies were carried out in the temperature range from 300 to 375ºC and pressures from 1.4 MPa to 3.4 MPa. The highest temperature and highest H_2 pressure in the preparation led to an increase in surface area and pore volume of NiMo bulk catalysts, as well as to highest activity of the resulting catalyst in simultaneous HDS of DBT and 4,6-DMDBT.

Genuit et al [126] described the methods for preparing Ni(Co)Mo bulk catalysts by solution reactions. In this work, different variations of the initial reagents and their influence on the catalytic activity were examined in detail. For the preparation of bulk promoted Ni(Co)Mo catalyst, ammonium thiodimolybdate $(NH_4)_2Mo_2S_{12}$ (TDM), $Co(NO_3)_2$ and acetylacetonate $(Co(acac)_2)$ and ethylene glycol (EG) as organic agent were used. Several surfactants of the same family (Triton X114, Triton X100, Tergitol NPX and Imbentin N 60) were tested as textural promoters. It was observed that impregnation of dispersed unsupported MoS_2 catalysts with aqueous Co nitrate led to a poor promoting effect. The negative influence of Co nitrate was explained by the oxidative reaction of MoS_2 by nitrate anions. The use of $Co(acac)_2$ contributed to the improvement of the promoting effect. It was also found that carbonaceous species formed through the decomposition of EG during the sulfiding treatment of the catalyst precursors disperse well over the sulfide particles, preventing MoS_2 slabs from sintering. Earlier, Rueda et al. [117] showed that the use of organic additives, which are a source of carbon for catalysts, contributes to an increase in the surface area of unsupported catalysts, thereby increasing their HDS activity.

Pollack and co-workers [129] first proposed the HF etching for structural studies of Ni-MoS_2/Al_2O_3 supported catalysts. At that time, there were almost no ideas about the formation of a mixed NiMoS phase. Therefore, the authors suggested that only MoS_2 and Ni_9S_8 is formed. Using the TEM analysis method, authors have established that molybdenum disulfide can form multilayer particles with an average length of 3 to 5 nm.

De la Rosa et al. [130] proposed the HF etching for structural studies of alumina and silica supported CoMo catalysts. HF can react and dissolve not only alumina, but also silica for eliminating the support. However, in their study, De la Rosa et al. found that the dissolution of the support by HF solution led to a reorganization of the MoS_2 particles into less stacked slabs and partial destruction of the active phase with loss of cobalt [130].

Delvaux et al. [138, 139] conducted a large series of experiments devoted to the research of the promoting effect in unsupported CoMo catalysts obtained by the so-called “co-maceration method”.

Molybdenum oxide (MoO_3) and cobalt oxide (Co_3O_4) were co-digested in an aqueous ammonium sulfide solution for 6 h at 70°C. The compounds obtained were subsequently heated under an H_2S-Ar atmosphere for 4 h at 400°C before evacuation [131].

In the same time, several groups of researchers were studying the promoting effect in Ni-W bulk systems in the reactions of hydrogenation of unsaturated hydrocarbons and the hydrogenolysis of sulfur compounds [44, 140]. The studies of the promoting effect in unsupported Ni-W and Co-Mo catalysts carried out by Delvaux et al. [132] and Delmon et al. [134] were systemized by Grange [133] and are summarized in **Fig 1.19**.

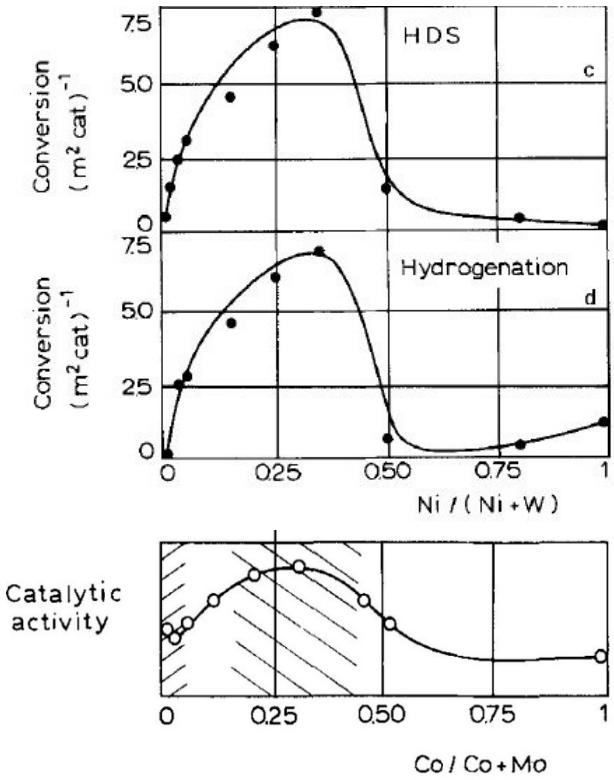

Fig. 1.19 Variation of the catalytic properties of unsupported fully sulfided CoMo and NiW catalyst [133].

It was found that the optimum HDS activity for bulk catalysts based on Mo and W is achieved with the addition of a promoting metal (Me) corresponding to an atomic ratio Me/(Me + Mo(W))] ≈ 0.3. Later similar dependencies were published by Inamura et al. [135]. Inamura and Prins discovered interesting dependencies in the study of the promotion of bulk molybdenum disulfide. Promoted MoS_2 were prepared by impregnation of pure MoS_2 with solution of $Co(NO_3)_2 \cdot 6H_2O$ in acetone. The HDS of thiophene and the consecutive hydrogenation of butene properties indicated that the Co ions are preferentially situated at the edges of the MoS_2 crystallites below Co/(Co + Mo) ≈ 0.08 and promote the HDS reaction. Further addition of Co leads to the segregation of Co_9S_8, which acts as a support for highly dispersed Co-promoted MoS_2 crystallites. As a result of this structural effect, the Co-MoS_2 crystallites become better accessible and the catalytic activity increases again above Co/(Co + Mo) ≈ 0.2. Structural models have been proposed for various Co/(Co + Mo) ratio (**Fig 1.20**).

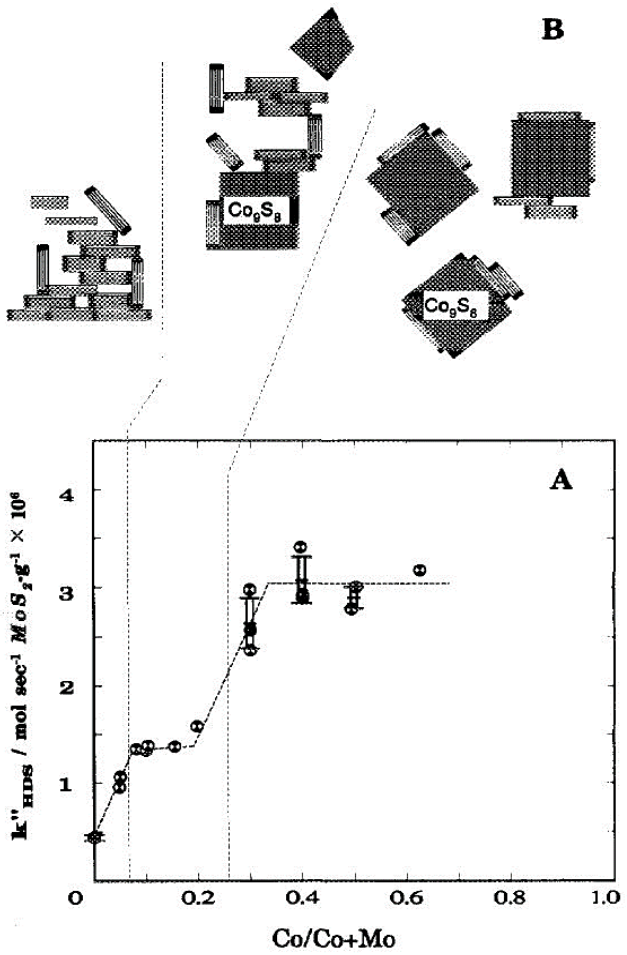

Fig. 1.20 (a) the rate constant *k*"$_{hds}$ normalized to the mos$_2$ content versus the co/(co+mo) atomic ratio, with standart deviations given by error bars. (b) schematic models for the co sulfide and the mos$_2$ crystallite phases [135]

At low cobalt concentrations, a layered structure is formed, the same as that of bulk MoS_2. The first increase in *k*"$_{HDS}$ was attributed to the decoration of the MoS_2 edges by the Co ions. Similar concepts have been proposed by Halbert et al. [136] In their work, they suggested that the addition of cobalt has two effects. In the first case "electronic promotion," meaning that Co and Mo act together to create sites or vacancies that are more active than sites on either single component (pseudo-binary). The second concept implies that when Co is added, there is a "structural stimulation" by the interaction of Co and Mo, which increases the phase dispersion, thereby increasing the activity.

The explanation for the second promotion effect for Co/(Co+Mo) = 0.2÷0.4 might be related to the formation of Co_9S_8 crystallites. Delmon and co-workers [38] found that the unsupported catalysts, which had simultaneously MoS_2 and Co_9S_8 phases present were able to work together by being in close contact and the hydrodesulfurization occurred at the interface between these two bulk sulfide phases, but there was no insight how these two bulk phases interacted to produce a synergistic effect.

Based on the correlation between the energy of the metal-sulfur bond calculated by DFT (density functional theory) and HDS performances evaluated in DBT HDS, Ramos et al. [137] showed the model of the surface contact region between the two bulk Co_9S_8/MoS_2 phases (**Fig 1.21)**.

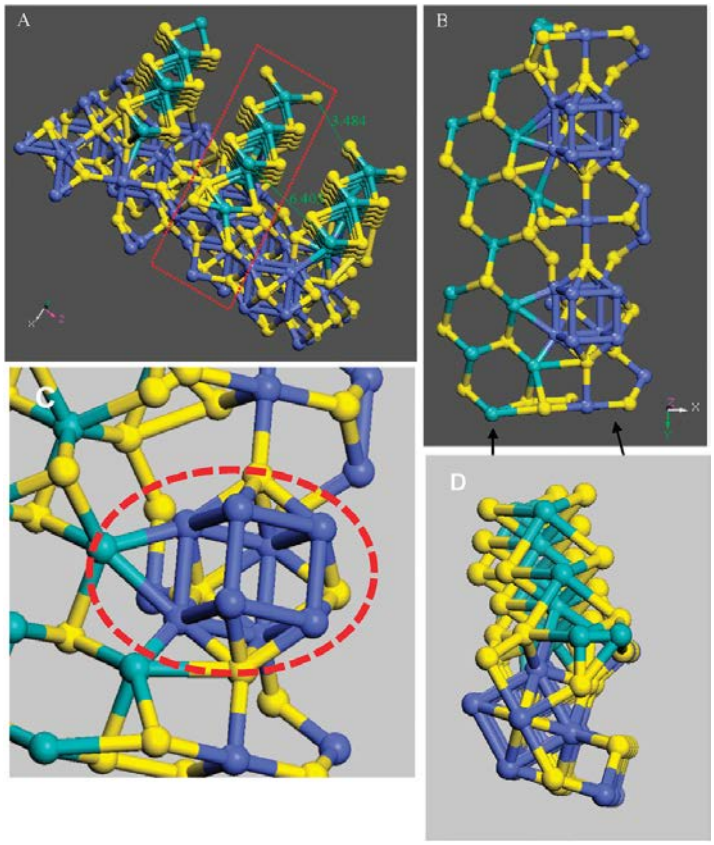

Fig. 1.21 (A) The resulting model interface between the layered MoS_2 (010) plane and the Co_9S_8 (111) plane. The atoms are colored as follows: cobalt (blue), sulfur (yellow) and molybdenum (green), (B) portion of the interface called "seed" (red dashed line) used for DFT calculations, (C) zoom on a cobalt cubic cluster arrangement connected to Mo atoms, (D) another view of (B) [137].

Modeling of the interface showed the creation of open latent vacancy sites on half of the Mo atoms interacting with cobalt and formation of Co–Mo bonds. Strong electron donation from Co to Mo also occurs through the intermediate sulfur atom bonded to both metals [137].

The same synergistic effect was found for unsupported NiW catalysts. Le and co-workers [138] also supposed that the catalyst is represented by core shell of NiS particles covered by curved WS_2 layers. But at the same time, Olivas et al. [139] reported that a NiW catalyst containing mainly nanorods has a higher catalytic activity compared to a NiW catalyst containing nanoparticles.

1.5.3 Unsupported mixed (Ni)MoW catalysts

A new trimetallic NiMoW bulk catalyst was synthesized by Wang et al. [140]. It was found that the NiMoW sulfide catalyst has a high HDS activity which is achieved mainly by forming a unique multilayered structure of the NiMoW sulfide, in which the Ni_7S_6 species with layered structure act as a support for Mo, W, or MoW sulfide particles. Furthermore, the formation of Mo-W composite species was confirmed by EXAFS. The Mo-W composite species could interact with Ni species to form Ni-Mo-W-S active species [140]. Mixed Mo-W particles were formed only on the surface of

Ni_7S_6, while monometallic MoS and WS species were located in the interlayer space (**Fig. 1.22**).

Wang and co-workers [141] used the bulk NiMoWS in hydrodeoxygenation of p-cresol. The catalysts with W/Mo molar ratio from 0 to 0.7 were prepared by one step hydrothermal method. Among these, the MoW catalyst with W/Mo=0.5 exhibited the highest activity in the HDO of p-cresol. The reaction rate constant was almost twice higher than that of the bimetallic NiMo analog.

Thanks to the Extended Hückel calculations, Olivas et al. [142] discovered a synergistic effect in a three-metal NiMoW system. A higher synergistic effect of Ni in $(MoW)S_2$ than in $Ni(MoS_2)$ and $Ni(WS_2)$ was found. The authors explain this by the fact that the combination of Mo and W atoms in forming binary $(Mo\text{-}W)S_2$ compounds changes the semiconductor character of MoS_2 or WS_2 increasing the metallic character and addition of Ni increases the availability of electrons over the Fermi level.

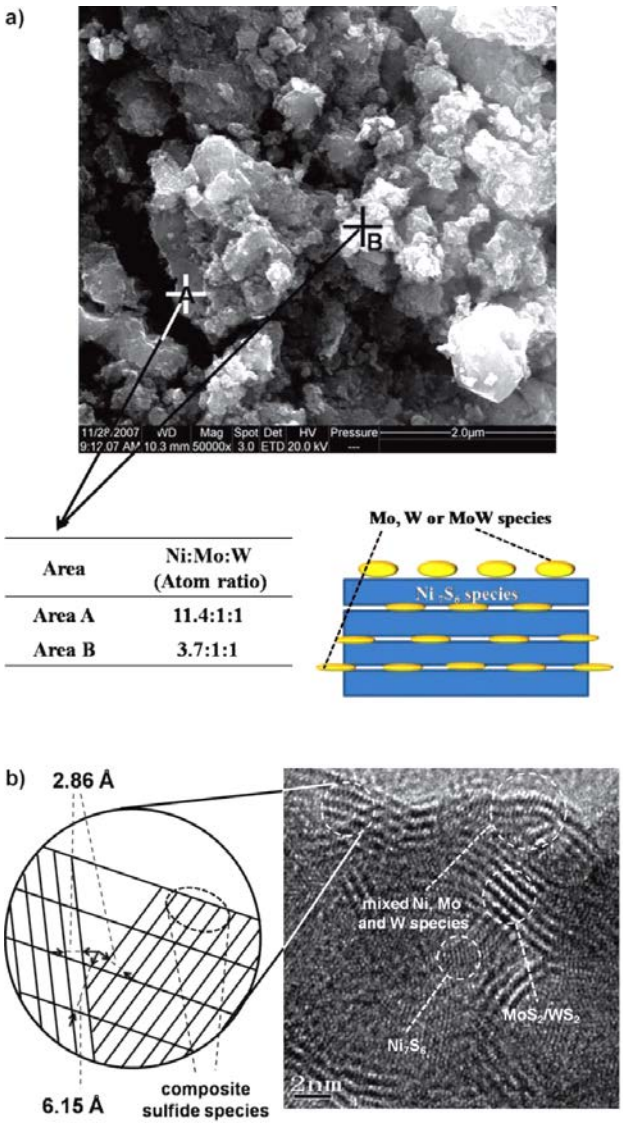

Fig. 1.22 SEM image and elemental analysis by EDX of the NiMoW sulfide catalyst and b) HRTEM image of the NiMoW sulfide catalyst.

At the same time, two research groups, Huirache-Acunã et al. [143] and Nava et al. [144], studied the effect of *ex situ* and *in situ* activation, respectively, for trimetallic (Ni – Mo – W) precursors containing alkyl fragments. Results obtained by Nava et al. showed that, after *in situ* decomposition of alkylthiometallates with the production of unsupported NiMoW catalysts, they had large specific surface areas (33.8-108.1 m^2/g), whereas after *ex situ* activation of tetraalkylammonium thiometallates $(R_4N)_2Mo(W)S_4$, the materials had lower SSA values (3.9–11.3 m^2/g). By *ex situ* activation no clear relationship could be observed between the alkyl group length, specific surface areas and the catalytic activity. But the opposite situation was observed in the case of *in-situ* activation. The alkyl group present in the tetraalkylammonium precursor has a direct influence on specific area and HDS activity [144].

1.5.4 The bulk catalysts: from science to industry

Akzo Nobel and ExxonMobil jointly developed a new bulk trimetallic NiMoW catalyst, known as NEBULA. This series of catalysts was significantly superior in activity to the supported STARS series. Eijsbouts et al. [6, 151, 152] showed a comparative analysis of the HDS, HDN and HDA activity of catalysts from the STARS and NEBULA series. Nippon Ketjen Co., Ltd and Albemarle developed industrial technology for producing hydroprocessing catalyst that could deliver 100% Type II active sites – STARS. Ni-Mo KF848-STARS and Co-Mo KF757-STARS, the first catalysts in the STARS portfolio, were launched shortly before the introduction of clean fuels regulations in Japan, Europe and North America [6, 153]. By all indications, NEBULA exceeded its predecessor. Already with the move to STARS, a new development S-curve was started (**Fig. 1.23**). At present time, the end point of the graph is NEBULA, a catalyst with breakthrough activity that reaches four times the activity of the conventional catalysts [145].

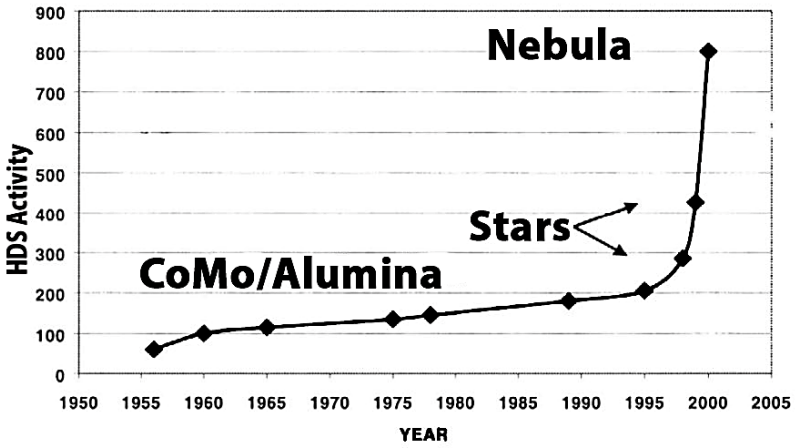

Fig. 1.23 Hydroprocessing catalyst development history [145]

The NEBULA's catalysts line was adapted not only for the diesel hydrotreatment process, but also for hydrocracking of heavy oil fractions (**Fig. 1.24**) [149].

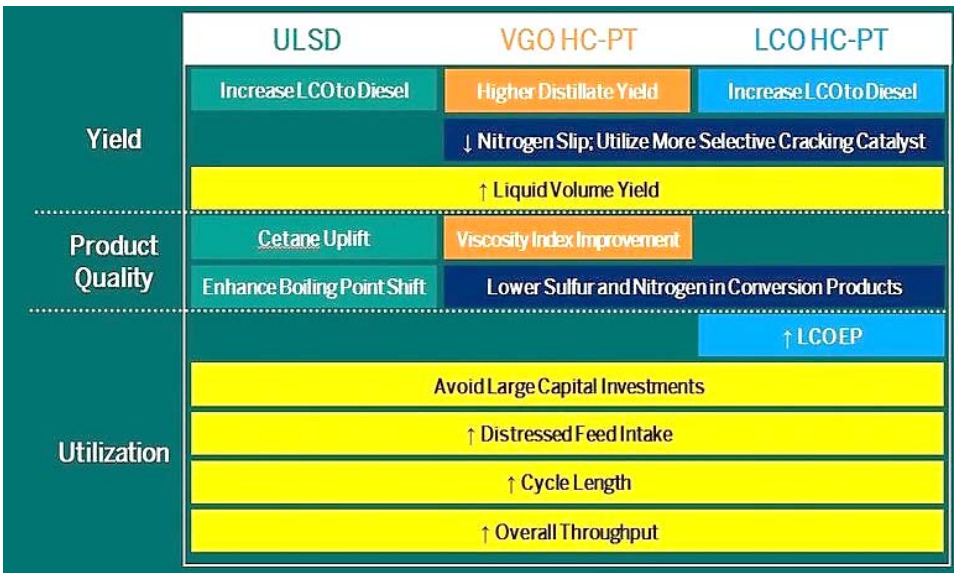

Fig. 1.24 The positive aspects of using catalyst NEBULA.

Of course, this development was a breakthrough in oil refining. Nebula is a commercially proven catalytic solution, with over 5.000 MT sold to over 60 individual users since its initial commercialization. The use of Nebula catalysts allows to avoid large investments and increases the operating cycle length and overall throughput.

In the middle of 2018, the ExxonMobil jointly with Albemarle renewed the new bulk catalyst Celestia™. According to data published on the Albemarle website [150], the Celestia™ catalyst has higher HDN, HDS and especially HYD activity than its predecessor Nebula (**Fig 1.25**). The Celestia catalyst was adapted for batch loading with other series of catalysts for processes such as hydrotreatment of light gas oil and pretreatment for the hydrocracking.

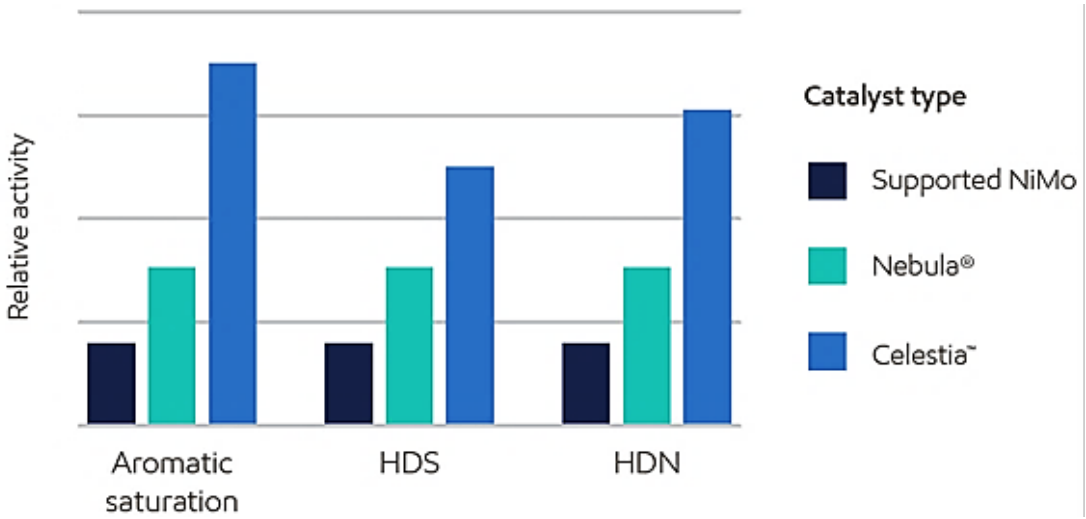

Fig. 1.25 Relative activity of Nebula, Celestia and supported NiMo catalysts [150]

The question of the cost of bulk catalysts and the method of their regeneration remains open. It is assumed that the bulk catalysts will have a high cost, since a large amount of precursor is consumed for synthesis in comparison with supported catalysts. However, as reported by manufacturers, bulk catalysts will have a short payback period, which makes them competitive.

After analyzing all the available information, we can conclude that the development of catalysts does not stand still, in particular the development of bulk catalysts. For this reason, the search, development and improvement of catalytic systems is an important task.

1.6 Conclusion

Literature review has shown that mixed MoW supported and unsupported sulfides are efficient catalysts that revealed most of the time better catalytic performances than that of their monometallic Mo or W counterparts. Most of previously reported MoW mixed supported and bulk catalysts were prepared using as precursors (together or sequentially) ammonium heptamoybdate and ammonium metatungstate or ammonium thiomolybdate $(NH_4)_2MoS_4$ and ammonium thiotungstate $(NH_4)_2WS_4$. The efficiency of mixed MoW supported catalysts was generally proven in HDS using alumina as the most choosen support. Particular attention was paid to the use of mesostructured silica. As noted in literature, mesostructured silica has several advantages over traditional Al_2O_3, such as high surface area, monomodal distribution of pore size and thermal stability. Moreover, sulfide catalysts based on mesostructured silica showed higher catalytic activity in the reactions of HDS and HYD.

Our work will be focused on MoW catalysts synthesized from mixed $H_4SiMo_nW_{12-n}O_{40}$ heteropolyacids (HPA). Talking into account previous catalytic study showing that the increase of Mo/W ratio in mixed HPA leads to improved catalytic activity, we proposed to extend the known MoW series (with molar Mo/W ratio equal to 1/11 and 3/9) to new mixed HPA using Mo/W ratio equal to 9/3 and 6/6, which synthesis is not described in the literature. The use of MoW HPAs will allow to start from a single molecular entity to introduce together Mo and W. As suggested by literature, this initial nanoscale proximity of Mo and W could induce and facilitate after sulfidation the formation of the mixed $(MoW)S_2$ phase which formation was claimed to explain better catalytic performances of MoW catalysts.

Taking into account the advantages and potential of using mixed MoW systems for hydrotreating of petroleum feedstock, MoW catalysts supported on mesostructured silica will be investigated. Special attention will be also paid to bulk catalysts, which have already found industrial application and have shown excellent results. The literature describes many methods for the synthesis of bulk catalysts. In the present work, new bulk mixed MoWS catalysts will be synthesized using the HF etching method. The physico-chemical properties of the catalysts obtained will be investigated by advanced characterization methods and their catalytic performances will be investigated in HDS and hydrogenation reactions under the conditions of a fixed-bed microreactor.

References

[1] J. Ancheyta, A. Alvarez-Majmutov, and C. Leyva, "Hydrotreating of oil fractions," in *Multiphase Catalytic Reactors: Theory, Design, Manufacturing, and Applications*, 2016, pp. 295–329.

[2] International Energy Outlook, "Internaltional Energy Outlook 2019," *U.S. Energy Inf. Adm.*, vol. September, no. 09, pp. 25–150, 2019.

[3] C. Perego and A. Bosetti, "Biomass to fuels: The role of zeolite and mesoporous materials," *Microporous Mesoporous Mater.*, vol. 144, no. 1–3, pp. 28–39, 2011, doi: 10.1016/j.micromeso.2010.11.034.

[4] "Worldwide Refineries-Capacities as of January 1, 2011 | Oil & Gas Journal." https://www.ogj.com/ogj-survey-downloads/worldwide-refining/document/17299937/worldwide-refineriescapacities-as-of-january-1-2011 (accessed Apr. 08, 2021).

[5] D. J. Podratz, K. Kleemeier, W. J. Turner, and B. M. Moyse, "Mixed-distillate hydrotreating reduces costs," *Oil Gas J.*, vol. 97, no. 20, pp. 41–43, 1999.

[6] J. Il Park, I. Mochida, A. M. J. Marafi, and A. Al-Mutairi, "Modern Approaches to Hydrotreating Catalysis," in *Springer Handbooks*, 2017, pp. 675–712.

[7] S. Bezergianni, A. Dimitriadis, O. Kikhtyanin, and D. Kubička, "Refinery co-processing of renewable feeds," *Progress in Energy and Combustion Science*, vol. 68. pp. 29–64, 2018, doi: 10.1016/j.pecs.2018.04.002.

[8] H. Qabazard, F. Abu-Seedo, A. Stanislaus, M. Andari, and M. Absi-Halabi, "Comparison Between the Performance of Conventional and High-Metal Co-Mo and Ni-Mo Catalysts in Deep Desulfurization of Kuwait Atmospheric Gas Oil," *Fuel Sci. Technol. Int.*, vol. 13, no. 9, pp. 1135–1151, 1995, doi: 10.1080/08843759508947728.

[9] D. D. Whitehurst, T. Isoda, and I. Mochida, "Present State of the Art and Future Challenges in the Hydrodesulfurization of Polyaromatic Sulfur Compounds," in *Advances in Catalysis*, vol. 42, no. C, Academic Press Inc., 1998, pp. 345–471.

[10] R. Shafi and G. J. Hutchings, "Hydrodesulfurization of hindered dibenzothiophenes: an overview," *Catal. Today*, vol. 59, no. 3, pp. 423–442, 2000, doi: 10.1016/S0920-5861(00)00308-4.

[11] I. A. Van Parijs, L. H. Hosten, and G. F. Froment, "Kinetics of the Hydrodesulfurization on a CoMo/γ-Al_2O_3 Catalyst. 2. Kinetics of the Hydrogenolysis of Benzothiophene," *Ind. Eng. Chem. Prod. Res. Dev.*, vol. 25, no. 3, pp. 437–443, 1986, doi: 10.1021/i300023a012.

[12] D. H. Broderick, G. C. A. Schuit, and B. C. Gates, "The sulfided CoMo/γ-Al_2O_3 catalyst: Evidence of structural changes during hydrodesulfurization of dibenzothiophene," *J. Catal.*, vol. 54, no. 1, pp. 94–97, 1978, doi: 10.1016/0021-9517(78)90030-1.

[13] P. Michaud, J. L. Lemberton, and G. Pérot, "Hydrodesulfurization of dibenzothiophene and 4,6-dimethyldibenzothiophene: Effect of an acid component on the activity of a sulfided NiMo on alumina catalyst," *Appl. Catal. A Gen.*, vol. 169, no. 2, pp. 343–353, 1998, doi: 10.1016/S0926-860X(98)00021-0.

[14] H. Topsøe, B. S. Clausen, and F. E. Massoth, "Hydrotreating Catalysis," *Catalysis*, pp. 1–269, 1996, doi: 10.1007/978-3-642-61040-0_1.

[15] B. Pawelec, R. M. Navarro, J. M. Campos-Martin, and J. L. G. Fierro, "Towards near zero-sulfur liquid fuels: A perspective review," *Catal. Sci. Technol.*, vol. 1, no. 1, pp. 23–42, 2011, doi: 10.1039/c0cy00049c.

[16] X. Ma, K. Sakanishi, and I. Mochida, "Hydrodesulfurization Reactivities of Various Sulfur Compounds in Diesel Fuel," *Ind. Eng. Chem. Res.*, vol. 33, no. 2, pp. 218–222, 1994, doi: 10.1021/ie00026a007.

[17] M. Houalla *et al.*, "Hydrodesulfurization of methyl-substituted dibenzothiophenes catalyzed by sulfided CoMo/γ-Al_2O_3," *J. Catal.*, vol. 61, no. 2, pp. 523–527, 1980, doi: 10.1016/0021-9517(80)90400-5.

[18] V. Meille, E. Schulz, M. Lemaire, and M. Vrinat, "Hydrodesulfurization of alkyldibenzothiophenes over a NiMo/Al_2O_3 catalyst: Kinetics and mechanism," *J. Catal.*, vol. 170, no. 1, pp. 29–36, 1997, doi: 10.1006/jcat.1997.1732.

[19] A. Stanislaus, A. Marafi, and M. S. Rana, "Recent advances in the science and technology of ultra low sulfur diesel (ULSD) production," *Catal. Today*, vol. 153, no. 1–2, pp. 1–68, 2010, doi: 10.1016/j.cattod.2010.05.011.

[20] J. Quartararo, S. Mignard, and S. Kasztelan, "Trends for mono-aromatic compounds hydrogenation over sulfided Ni, Mo and NiMo hydrotreating catalysts," *Catal. Letters*, vol. 61, no. 3–4, pp. 167–172, 1999, doi: 10.1023/a:1019093410354.

[21] A. Stanislaus and H. C. Barry, "Aromatic hydrogenation catalysis: A review," *Catal. Rev.*, vol. 36, no. 1, pp. 75–123, 1994, doi: 10.1080/01614949408013921.

[22] T. Koltai *et al.*, "Comparative inhibiting effect of polycondensed aromatics and nitrogen compounds on the hydrodesulfurization of alkyldibenzothiophenes," *Appl. Catal. A Gen.*, vol. 231, no. 1–2, pp. 253–261, 2002, doi: 10.1016/S0926-860X(02)00063-7.

[23] F. Van Looij, P. Van Der Laan, W. H. J. Stork, D. J. DiCamillo, and J. Swain, "Key parameters in deep hydrodesulfurization of diesel fuel," *Appl. Catal. A Gen.*, vol. 170, no. 1, pp. 1–12, 1998, doi: 10.1016/S0926-860X(98)00028-3.

[24] C. Aubert, R. Durand, P. Geneste, and C. Moreau, "Factors affecting the hydrogenation of substituted benzenes and phenols over a sulfided $NiOMoO_3/\gamma$-Al_2O_3 catalyst," *J. Catal.*, vol. 112, no. 1, pp. 12–20, Jul. 1988, doi: 10.1016/0021-9517(88)90116-9.

[25] G. C. Laredo, S. Leyva, R. Alvarez, M. T. Mares, J. Castillo, and J. L. Cano, "Nitrogen compounds characterization in atmospheric gas oil and light cycle oil from a blend of Mexican crudes," *Fuel*, vol. 81, no. 10, pp. 1341–1350, 2002, doi: 10.1016/S0016-2361(02)00047-9.

[26] B. Temel *et al.*, "Atomic-scale insight into the origin of pyridine inhibition of MoS_2-based hydrotreating catalysts," *J. Catal.*, vol. 271, no. 2, pp. 280–289, 2010, doi: 10.1016/j.jcat.2010.02.007.

[27] G. C. Laredo, E. Altamirano, and J. A. De los Reyes, "Inhibition effects of nitrogen compounds on the hydrodesulfurization of dibenzothiophene: Part 2," *Appl. Catal. A Gen.*, vol. 243, no. 2, pp. 207–214, 2003, doi: 10.1016/S0926-860X(02)00321-6.

[28] M. S. Rana, R. Navarro, and J. Leglise, "Competitive effects of nitrogen and sulfur content on activity of hydrotreating CoMo/Al_2O_3 catalysts: A batch reactor study," *Catal. Today*, vol. 98, pp. 67–74, 2004, doi: 10.1016/j.cattod.2004.07.020.

[29] M. Egorova and R. Prins, "Competitive hydrodesulfurization of 4,6-dimethyldibenzothiophene, hydrodenitrogenation of 2-methylpyridine, and hydrogenation of naphthalene over sulfided NiMo/γ-Al_2O_3," *J. Catal.*, vol. 224, no. 2, pp. 278–287, 2004, doi: 10.1016/j.jcat.2004.03.005.

[30] M. J. Girgis, B. C. Gates, and M. J. Girgis, "Reactivities, Reaction Networks, and Kinetics in High-Pressure Catalytic Hydroprocessing," *Ind. Eng. Chem. Res.*, vol. 30, no. 9, pp. 2021–2058, 1991, doi: 10.1021/ie00057a001.

[31] J. F. Cocchetto and C. N. Satterfield, "Thermodynamic Equilibria of Selected Heterocyclic Nitrogen Compounds with Their Hydrogenated Derivatives," *Ind. Eng. Chem. Process Des. Dev.*, vol. 15, no. 2, pp. 272–277, 1976, doi: 10.1021/i260058a011.

[32] T. C. Ho, "Hydrodenitrogenation Catalysis," *Catal. Rev.*, vol. 30, no. 1, pp. 117–160, 1988, doi: 10.1080/01614948808078617.

[33] H. Topsøie, R. Candia, N. -Y Topsøe, B. S. Clausen, and H. Topsøe, "On The State of the Co-MO-S Model," *Bull. des Sociétés Chim. Belges*, vol. 93, no. 8–9, pp. 783–806, Sep. 1984, doi: 10.1002/bscb.19840930820.

[34] H. Topsøe, "The role of Co-Mo-S type structures in hydrotreating catalysts," *Appl. Catal. A Gen.*, vol. 322, pp. 3–8, 2007, doi: 10.1016/j.apcata.2007.01.002.

[35] R. J. H. Voorhoeve and J. C. M. Stuiver, "The mechanism of the hydrogenation of cyclohexene and benzene on nickel-tungsten sulfide catalysts," *J. Catal.*, vol. 23, no. 2, pp. 243–252, Nov. 1971, doi: 10.1016/0021-9517(71)90046-7.

[36] P. Farragher, A L, Cossee, "Proceedings, 5th International Congress on Catalysis," 1977.
[37] A. L. Farragher, "Symposium on the Role of Solid State Chemistry in Catalysis," 1977.
[38] G. Hagenbach, P. Courty, and B. Delmon, "Physicochemical investigations and catalytic activity measurements on crystallized molydbenum sulfide-cobalt sulfide mixed catalysts," *J. Catal.*, vol. 31, no. 2, pp. 264–273, Nov. 1973, doi: 10.1016/0021-9517(73)90333-3.
[39] P. Grange and B. Delmon, "The role of cobalt and molybdenum sulphides in hydrodesulphurisation catalysts: A review," *J. Less-Common Met.*, vol. 36, no. 1–2, pp. 353–360, 1974, doi: 10.1016/0022-5088(74)90119-2.
[40] N. Y. Topsøe and H. Topsøe, "Characterization of the structures and active sites in sulfided $CoMo/Al_2O_3$ and $NiMo/Al_2O_3$ catalysts by NO chemisorption," *J. Catal.*, vol. 84, no. 2, pp. 386–401, 1983, doi: 10.1016/0021-9517(83)90010-6.
[41] S. Harris and R. R. Chianelli, "Catalysis by transition metal sulfides: A theoretical and experimental study of the relation between the synergic systems and the binary transition metal sulfides," *J. Catal.*, vol. 98, no. 1, pp. 17–31, 1986, doi: 10.1016/0021-9517(86)90292-7.
[42] S. Eijsbouts, J. J. L. Heinerman, and H. J. W. Elzerman, "MoS_2 structures in high-activity hydrotreating catalysts. I. Semi-quantitative method for evaluation of transmission electron microscopy results. Correlations between hydrodesulfurization and hydrodenitrogenation activities and MoS_2 dispersion," *Appl. Catal. A, Gen.*, vol. 105, no. 1, pp. 53–68, 1993, doi: 10.1016/0926-860X(93)85133-A.
[43] J. F. Paul and E. Payen, "Vacancy formation on MoS_2 hydrodesulfurization catalyst: DFT study of the mechanism," *J. Phys. Chem. B*, vol. 107, no. 17, pp. 4057–4064, 2003, doi: 10.1021/jp027668f.
[44] S. Cristol, J. F. Paul, E. Payen, D. Bougeard, J. Hafner, and F. Hutschka, "Theoretical study of benzothiophene hydrodesulfurization on MoS_2," *Stud. Surf. Sci. Catal.*, vol. 127, pp. 327–334, 1999, doi: 10.1016/s0167-2991(99)80424-8.
[45] M. Sun, J. Adjaye, and A. E. Nelson, "Theoretical investigations of the structures and properties of molybdenum-based sulfide catalysts," *Appl. Catal. A Gen.*, vol. 263, no. 2, pp. 131–143, 2004, doi: 10.1016/j.apcata.2003.12.011.
[46] S. Cristol, J. F. Paul, E. Payen, D. Bougeard, S. Clémendot, and F. Hutschka, "Theoretical study of the MoSi (100) surface: A chemical potential analysis of sulfur and hydrogen coverage," *J. Phys. Chem. B*, vol. 104, no. 47, pp. 11220–11229, 2000, doi: 10.1021/jp0023819.
[47] U. Zeuthen, P, Stolze, P, Pedersen, "Kinetics for simultaneous HDS, HDN and hydrogenation model reactions on a $Co-Mo/Al_2O_3$ catalyst," *Bull. Des Soc. Chim. Belges*, vol. 96, no. 11–12, pp. 985–995, 1987.
[48] M. Daage and R. R. Chianelli, "Structure-function relations in molybdenum sulfide catalysts: The 'Rim-Edge' model," *Journal of Catalysis*, vol. 149, no. 2. pp. 414–427, 1994, doi: 10.1006/jcat.1994.1308.
[49] M. Salmeron, G. A. Somorjai, A. Wold, R. Chianelli, and K. S. Liang, "The adsorption and binding of thiophene, butene and H_2S on the basal plane of MoS_2 single crystals," *Chem. Phys. Lett.*, vol. 90, no. 2, pp. 105–107, 1982, doi: 10.1016/0009-2614(82)83620-8.
[50] M. Nagai and T. Kabe, "Selectivity of molybdenum catalyst in hydrodesulfurization, hydrodenitrogenation, and hydrodeoxygenation: Effect of additives on dibenzothiophene hydrodesulfurization," *J. Catal.*, vol. 81, no. 2, pp. 440–449, 1983, doi: 10.1016/0021-9517(83)90182-3.
[51] M. Nagai, T. Sato, and A. Aiba, "Poisoning effect of nitrogen compounds on dibenzothiophene hydrodesulfurization on sulfided $NiMo/Al_2O_3$ catalysts and relation to gas-phase basicity," *J. Catal.*, vol. 97, no. 1, pp. 52–58, 1986, doi: 10.1016/0021-9517(86)90036-9.
[52] C. Song and X. Ma, "New design approaches to ultra-clean diesel fuels by deep desulfurization and deep dearomatization," in *Applied Catalysis B: Environmental*, 2003, vol. 41, no. 1–2, pp. 207–238, doi: 10.1016/S0926-3373(02)00212-6.
[53] P. G. Moses, B. Hinnemann, H. Topsøe, and J. K. Nørskov, "The hydrogenation and direct

desulfurization reaction pathway in thiophene hydrodesulfurization over MoS_2 catalysts at realistic conditions: A density functional study," *J. Catal.*, vol. 248, no. 2, pp. 188–203, 2007, doi: 10.1016/j.jcat.2007.02.028.

[54] P. Raybaud, J. Hafner, G. Kresse, S. Kasztelan, and H. Toulhoat, "Structure, Energetics, and Electronic Properties of the Surface of a Promoted MoS_2 Catalyst: An ab Initio Local Density Functional Study," *J. Catal.*, vol. 190, no. 1, pp. 128–143, 2000, doi: 10.1006/jcat.1999.2743.

[55] H. Orita, K. Uchida, and N. Itoh, "A volcano-type relationship between the adsorption energy of thiophene on promoted MoS_2 cluster-model catalysts and the experimental HDS activity: Ab initio density functional study," *Appl. Catal. A Gen.*, vol. 258, no. 1, pp. 115–120, 2004, doi: 10.1016/j.apcata.2003.08.016.

[56] H. Toulhoat and P. Raybaud, "Kinetic interpretation of catalytic activity patterns based on theoretical chemical descriptors," in *Journal of Catalysis*, 2003, vol. 216, no. 1–2, pp. 63–72, doi: 10.1016/S0021-9517(02)00118-5.

[57] P. A. Nikulshin, N. N. Tomina, A. A. Pimerzin, A. Y. Stakheev, I. S. Mashkovsky, and V. M. Kogan, "Effect of the second metal of Anderson type heteropolycompounds on hydrogenation and hydrodesulphurization properties of $XMo_6(S)/Al_2O_3$ and Ni_3-$XMo_6(S)/Al_2O_3$ catalysts," *Appl. Catal. A Gen.*, vol. 393, no. 1–2, pp. 146–152, 2011, doi: 10.1016/j.apcata.2010.11.033.

[58] M. Breysse, C. Geantet, P. Afanasiev, J. Blanchard, and M. Vrinat, "Recent studies on the preparation, activation and design of active phases and supports of hydrotreating catalysts," *Catal. Today*, vol. 130, no. 1, pp. 3–13, 2008, doi: 10.1016/j.cattod.2007.08.018.

[59] J. P. R. Vissers, F. P. M. Mercx, S. M. A. M. Bouwens, V. H. J. de Beer, and R. Prins, "Carbon-covered alumina as a support for sulfide catalysts," *J. Catal.*, vol. 114, no. 2, pp. 291–302, Dec. 1988, doi: 10.1016/0021-9517(88)90033-4.

[60] F. Sánchez-Minero, J. Ramírez, R. Cuevas-Garcia, A. Gutierrez-Alejandre, and C. Fernández-Vargas, "Kinetic study of the HDS of 4,6-DMDBT over $NiMo/Al_2O_3$-$SiO_2(x)$ catalysts," *Ind. Eng. Chem. Res.*, vol. 48, no. 3, pp. 1178–1185, 2009, doi: 10.1021/ie8005808.

[61] G. Muralidhar, F. E. Massoth, and J. Shabtai, "Catalytic functionalities of supported sulfides. I. Effect of support and additives on the CoMo catalyst," *J. Catal.*, vol. 85, no. 1, pp. 44–52, Jan. 1984, doi: 10.1016/0021-9517(84)90108-8.

[62] F. Richard, T. Boita, and G. Pérot, "Reaction mechanism of 4,6-dimethyldibenzothiophene desulfurization over sulfided $NiMoP/Al_2O_3$-zeolite catalysts," *Appl. Catal. A Gen.*, vol. 320, pp. 69–79, 2007, doi: 10.1016/j.apcata.2006.12.014.

[63] M. S. Rana, J. Ancheyta, P. Rayo, and S. K. Maity, "Effect of alumina preparation on hydrodemetallization and hydrodesulfurization of Maya crude," in *Catalysis Today*, 2004, vol. 98, no. 1-2, pp. 151–160, doi: 10.1016/j.cattod.2004.07.029.

[64] A. Corma, A. Martínez, V. Martínez-Soria, and J. B. Montón, "Hydrocracking of vacuum gasoil on the novel mesoporous MCM-41 aluminosilicate catalyst," *J. Catal.*, vol. 153, no. 1, pp. 25–31, Apr. 1995, doi: 10.1006/jcat.1995.1104.

[65] C. Song and K. M. Reddy, "Mesoporous molecular sieve MCM-41 supported Co-Mo catalyst for hydrodesulfurization of dibenzothiophene in distillate fuels," *Appl. Catal. A Gen.*, vol. 176, no. 1, pp. 1–10, 1999, doi: 10.1016/S0926-860X(98)00230-0.

[66] T. Klimova, J. Ramírez, M. Calderón, and J. M. Domínguez, "New Mo and NiMo catalysts supported on MCM-41/Alumina for thiophene hydrodesulfurization," *Stud. Surf. Sci. Catal.*, vol. 117, pp. 493–500, 1998, doi: 10.1016/s0167-2991(98)81029-x.

[67] D. Trong On, D. Desplantier-Giscard, C. Danumah, and S. Kaliaguine, "Perspectives in catalytic applications of mesostructured materials," *Appl. Catal. A Gen.*, vol. 222, no. 1–2, pp. 299–357, 2001, doi: 10.1016/S0926-860X(01)00842-0.

[68] P. T. Tanev, M. Chibwe, and T. J. Pinnavaia, "Titanium-containing mesoporous molecular sieves for catalytic oxidation of aromatic compounds," *Nature*, vol. 368, no. 6469, pp. 321–323, 1994, doi: 10.1038/368321a0.

[69] S. A. Bagshaw, E. Prouzet, and T. J. Pinnavaia, "Templating of mesoporous molecular sieves by nonionic polyethylene oxide surfactants," *Science*, vol. 269, no. 5228, pp. 1242–1244,

1995, doi: 10.1126/science.269.5228.1242.
[70] T. J. Pinnavaia and W. Zhang, "Catalytic properties of mesoporous molecular sieves prepared by neutral surfactant assembly," *Stud. Surf. Sci. Catal.*, vol. 117, pp. 23–36, 1998, doi: 10.1016/s0167-2991(98)80974-9.
[71] D. Zhao *et al.*, "Triblock copolymer syntheses of mesoporous silica with periodic 50 to 300 angstrom pores," *Science*, vol. 279, no. 5350, pp. 548–552, 1998, doi: 10.1126/science.279.5350.548.
[72] J. Jammaer, A. Aerts, J. D'Haen, J. W. Seo, and J. A. Martens, "Convenient synthesis of ordered mesoporous silica at room temperature and quasi-neutral pH," *J. Mater. Chem.*, vol. 19, no. 44, pp. 8290–8293, 2009, doi: 10.1039/b915273c.
[73] G. M. Dhar *et al.*, "Physico-chemical characterization and catalysis on SBA-15 supported molybdenum hydrotreating catalysts," *Catal. Today*, vol. 99, no. 3–4, pp. 309–314, 2005, doi: 10.1016/j.cattod.2004.10.005.
[74] A. Kokliukhin, M. Nikulshina, A. Sheldaisov-Meshcheryakov, A. Mozhaev, and P. Nikulshin, "CoMo Hydrotreating Catalysts Supported on Al_2O_3, SiO_2 and SBA-15 Prepared from Single Co_2Mo_{10}-Heteropolyacid: In Search of Self-Promotion Effect," *Catal. Letters*, vol. 148, no. 9, pp. 2869–2879, Sep. 2018, doi: 10.1007/s10562-018-2480-7.
[75] A. Wang, Y. Wang, T. Kabe, Y. Chen, A. Ishihara, and W. Qian, "Hydrodesulfurization of dibenzothiophene over siliceous MCM-41-supported catalysts: I. Sulfided Co-Mo catalysts," *J. Catal.*, vol. 199, no. 1, pp. 19–29, 2001, doi: 10.1006/jcat.2000.3148.
[76] J. A. Mendoza-Nieto, F. Robles-Méndez, and T. E. Klimova, "Support effect on the catalytic performance of trimetallic NiMoW catalysts prepared with citric acid in HDS of dibenzothiophenes," *Catal. Today*, vol. 250, pp. 47–59, 2015, doi: 10.1016/j.cattod.2014.05.002.
[77] L. Vradman *et al.*, "High loading of short WS_2 slabs inside SBA-15: Promotion with nickel and performance in hydrodesulfurization and hydrogenation," *J. Catal.*, vol. 213, no. 2, pp. 163–175, 2003, doi: 10.1016/S0021-9517(02)00012-X.
[78] O. Y. Gutiérrez, G. A. Fuentes, C. Salcedo, and T. Klimova, "SBA-15 supports modified by Ti and Zr grafting for NiMo hydrodesulfurization catalysts," *Catal. Today*, vol. 116, no. 4, pp. 485–497, 2006, doi: 10.1016/j.cattod.2006.06.035.
[79] T. A. Saleh, "Applying Nanotechnology to the Desulfurization Process in Petroleum Engineering," in *Applying Nanotechnology to the Desulfurization Process in Petroleum Engineering*, vol. i, T. A. Saleh, Ed. IGI Global, 2016, pp. 378–389.
[80] A. J. Van der Vlies, R. Prins, and T. Weber, "Chemical principles of the sulfidation of tungsten oxides," *J. Phys. Chem. B*, vol. 106, no. 36, pp. 9277–9285, 2002, doi: 10.1021/jp020961v.
[81] C. Thomazeau, C. Geantet, M. Lacroix, M. Danot, V. Harlé, and P. Raybaud, "Predictive approach for the design of improved HDT catalysts: γ-Alumina supported (Ni, Co) promoted $Mo_{1-x}W_xS_2$ active phases," *Appl. Catal. A Gen.*, vol. 322, pp. 92–97, 2007, doi: 10.1016/j.apcata.2007.01.016.
[82] P. J. Vázquez-Salas *et al.*, "Enhancement of dibenzothiophene hydrodesulphurization via hydrogenation route on NiMoW catalyst supported on HMS modified with Ti," *Catal. Today*, vol. 305, pp. 65–74, 2018, doi: 10.1016/j.cattod.2017.10.005.
[83] L. Van Haandel, M. Bremmer, P. J. Kooyman, J. A. R. Van Veen, T. Weber, and E. J. M. Hensen, "Structure-Activity Correlations in Hydrodesulfurization Reactions over Ni-Promoted $Mo_xW_{(1-x)}S_2/Al_2O_3$ Catalysts," *ACS Catal.*, vol. 5, no. 12, pp. 7276–7287, 2015, doi: 10.1021/acscatal.5b01806.
[84] S. Sigurdson, V. Sundaramurthy, A. K. Dalai, and J. Adjaye, "Phosphorus promoted trimetallic NiMoW/γ-Al_2O_3 sulfide catalysts in gas oil hydrotreating," *J. Mol. Catal. A Chem.*, vol. 291, no. 1–2, pp. 30–37, 2008, doi: 10.1016/j.molcata.2008.05.011.
[85] G. An, C. Liu, C. Xiong, and C. Lu, "A study on the morphology of unsupported Ni-Mo-W sulfide hydrotreating catalysts through high-resolution transmission electron microscopy," *Pet. Sci. Technol.*, vol. 30, no. 15, pp. 1599–1608, 2012, doi: 10.1080/10916466.2010.509065.

[86] R. Huirache-Acuña *et al.*, "Comparison of the morphology and HDS activity of ternary Ni(Co)-Mo-W catalysts supported on Al-HMS and Al-SBA-16 substrates," *Appl. Catal. B Environ.*, vol. 125, pp. 473–485, 2012, doi: 10.1016/j.apcatb.2012.05.034.

[87] J. A. Mendoza-Nieto, O. Vera-Vallejo, L. Escobar-Alarcón, D. A. Solís-Casados, and T. Klimova, "Development of new trimetallic NiMoW catalysts supported on SBA-15 for deep hydrodesulfurization," *Fuel*, vol. 110, pp. 268–277, 2013, doi: 10.1016/j.fuel.2012.07.057.

[88] J. C. Mogica-Betancourt *et al.*, "Interaction effects of nickel polyoxotungstate with the Al_2O_3-MgO support for application in dibenzothiophene hydrodesulfurization," *J. Catal.*, vol. 313, pp. 9–23, 2014, doi: 10.1016/j.jcat.2014.02.009.

[89] H. Topsoe, B. S. Clausen, and H. Topsbe, "Catalysis Reviews Science and Engineering Importance of Co-Mo-S Type Structures in Hydrodesulfurization Importance of Co-Mo-S Type Structures in H ydrodesulfurization," vol. 26, no. 4, pp. 395–420, 1984, doi: 10.1080/01614948408064719.

[90] E. Kraleva, A. Spojakina, K. Jiratova, and L. Petrov, "Support effect on the properties of iron-molybdenum hydrodesulfurization catalysts," *Catal. Letters*, vol. 112, no. 3–4, pp. 203–212, 2006, doi: 10.1007/s10562-006-0204-x.

[91] P. Blanchard, C. Lamonier, A. Griboval, and E. Payen, "New insight in the preparation of alumina supported hydrotreatment oxidic precursors: A molecular approach," *Appl. Catal. A Gen.*, vol. 322, pp. 33–45, 2007, doi: 10.1016/j.apcata.2007.01.018.

[92] A. Griboval, P. Blanchard, E. Payen, M. Fournier, and J. L. Dubois, "Alumina supported HDS catalysts prepared by impregnation with new heteropolycompounds. Comparison with catalysts prepared by conventional Co-Mo-P coimpregnation," 1998. doi: 10.1016/S0920-5861(98)00230-2.

[93] C. I. Cabello, I. L. Botto, and H. J. Thomas, "Anderson type heteropolyoxomolybdates in catalysis: 1. $(NH_4)_3[CoMo_6O_{24}H_6]\cdot 7H_2O/\gamma\text{-}Al_2O_3$ as alternative of $Co\text{-}Mo/\gamma\text{-}Al_2O_3$ hydrotreating catalysts," *Appl. Catal. A Gen.*, vol. 197, no. 1, pp. 79–86, 2000, doi: 10.1016/S0926-860X(99)00535-9.

[94] C. I. Cabello, M. Muñoz, E. Payen, and H. J. Thomas, "Influence of cobalt content on the hydrotreatment catalytic activity of $CoMo_6/\gamma\text{-}Al_2O_3$ heteropolyoxomolybdate-based catalyst," *Catal. Letters*, vol. 92, no. 1–2, pp. 69–73, 2004, doi: 10.1023/b:catl.0000011090.71716.6e.

[95] C. I. Cabello, F. M. Cabrerizo, A. Alvarez, and H. J. Thomas, "Decamolybdodicobaltate(III) heteropolyanion: Structural, spectroscopical, thermal and hydrotreating catalytic properties," *J. Mol. Catal. A Chem.*, vol. 186, no. 1–2, pp. 89–100, 2002, doi: 10.1016/S1381-1169(02)00043-2.

[96] C. Lamonier, C. Martin, J. Mazurelle, V. Harlé, D. Guillaume, and E. Payen, "Molybdocobaltate cobalt salts: New starting materials for hydrotreating catalysts," *Appl. Catal. B Environ.*, vol. 70, no. 1–4, pp. 548–556, 2007, doi: 10.1016/j.apcatb.2005.12.027.

[97] H. Toulhoat and P. Raybaud, "Prediction of optimal catalysts for a given chemical reaction," *Catal. Sci. Technol.*, vol. 10, no. 7, pp. 2069–2081, 2020, doi: 10.1039/c9cy02196e.

[98] M. T. Pope, "Heteropoly and isopoly oxometalates," *Angew. Chemie*, vol. 96, no. 9, p. 730, 1984.

[99] I. V. Kozhevnikov, "Heterogeneous acid catalysis by heteropoly acids: Approaches to catalyst deactivation," *J. Mol. Catal. A Chem.*, vol. 305, no. 1–2, pp. 104–111, 2009, doi: 10.1016/j.molcata.2008.11.029.

[100] I. V Kozhevnikov, "Catalysis by heteropoly acids and multicomponent polyoxometalates in liquid-phase reactions," *Chem. Rev.*, vol. 98, no. 1, pp. 171–198, 1998, doi: 10.1021/cr960400y.

[101] J. F. Keggin, "The structure and formula of 12-phosphotungstic acid," *Proc. R. Soc. London. Ser. A, Contain. Pap. a Math. Phys. Character*, vol. 144, no. 851, pp. 75–100, 1934, doi: 10.1098/rspa.1934.0035.

[102] S. Damyanova and J. L. G. Fierro, "Surface properties of titania-supported 12-molybdophosphoric acid hydrodesulphurization catalysts," *Appl. Catal. A Gen.*, vol. 144, no.

1–2, pp. 59–77, 1996, doi: 10.1016/0926-860X(96)00104-4.
[103] L. Lizama and T. Klimova, "Highly active deep HDS catalysts prepared using Mo and W heteropolyacids supported on SBA-15," *Appl. Catal. B Environ.*, vol. 82, no. 3–4, pp. 139–150, 2008, doi: 10.1016/j.apcatb.2008.01.018.
[104] N. N. Tomina, P. A. Nikul'shin, and A. A. Pimerzin, "Influence of Anderson and Keggin heteropoly compounds as precursors of oxide phases in hydrotreating catalysts on their performance," *Pet. Chem.*, vol. 48, no. 2, pp. 92–99, 2008, doi: 10.1134/s0965544108020035.
[105] G. A. Tsigdinos, "Heteropoly compounds of molybdenum and tungsten," in *Topics in Current Chemistry*, Springer-Verlag, 2006, pp. 1–64.
[106] D. P. Smith and M. T. Pope, "Heteropoly 12-Metallophosphates Containing Tungsten and Vanadium. Preparation, Voltammetry, and Properties of Mono-, Di-, Tetra- and Hexavanado Complexes1,2," *Inorg. Chem.*, vol. 12, no. 2, pp. 331–336, Feb. 1973, doi: 10.1021/ic50120a018.
[107] D. Soogund *et al.*, "New Mo-V based oxidic precursor for the hydrotreatment of residues," *Appl. Catal. B Environ.*, vol. 98, no. 1–2, pp. 39–48, 2010, doi: 10.1016/j.apcatb.2010.04.024.
[108] A. A. Spojakina, N. G. Kostova, B. Sow, M. W. Stamenova, and K. Jiratova, "Thiophene conversion and ethanol oxidation on SiO_2-supported 12-PMoV-mixed heteropoly compounds," *Catal. Today*, vol. 65, no. 2–4, pp. 315–321, 2001, doi: 10.1016/S0920-5861(00)00585-X.
[109] M. S. Nikulshina *et al.*, "Molecular approach to prepare mixed MoW alumina supported hydrotreatment catalysts using $H_4SiMo_nW_{12-n}O_{40}$ heteropolyacids," *Catal. Sci. Technol.*, vol. 8, no. 21, pp. 5557–5572, 2018, doi: 10.1039/c8cy00672e.
[110] M. Nikulshina *et al.*, "MoW synergetic effect supported by HAADF for alumina based catalysts prepared from mixed $SiMonW_{12-n}$ heteropolyacids," *Appl. Catal. B Environ.*, vol. 224, no. July 2017, pp. 951–959, 2018, doi: 10.1016/j.apcatb.2017.11.049.
[111] M. Nikulshina *et al.*, "Enhancing the hydrodesulfurization of 4,6-dimethyldibenzothiophene through the use of mixed $MoWS_2$ phase evidenced by HAADF," *Catal. Today*, vol. 329, no. September 2018, pp. 24–34, 2019, doi: 10.1016/j.cattod.2018.11.051.
[112] L. Zhang, X. Long, D. Li, and X. Gao, "Study on high-performance unsupported Ni-Mo-W hydrotreating catalyst," *Catal. Commun.*, vol. 12, no. 11, pp. 927–931, 2011, doi: 10.1016/j.catcom.2011.03.004.
[113] J. P. Wilcoxon and G. A. Samara, "Strong quantum-size effects in a layered semiconductor: MoS2 nanoclusters," *Phys. Rev. B*, vol. 51, no. 11, pp. 7299–7302, 1995, doi: 10.1103/PhysRevB.51.7299.
[114] E. Devers, P. Afanasiev, B. Jouguet, and M. Vrinat, "Hydrothermal syntheses and catalytic properties of dispersed molybdenum sulfides," *Catal. Letters*, vol. 82, no. 1–2, pp. 13–17, 2002, doi: 10.1023/A:1020512320773.
[115] W. J. Li, E. W. Shi, J. M. Ko, Z. Z. Chen, H. Ogino, and T. Fukuda, "Hydrothermal synthesis of MoS_2 nanowires," *J. Cryst. Growth*, vol. 250, no. 3–4, pp. 418–422, 2003, doi: 10.1016/S0022-0248(02)02412-0.
[116] Y. Peng, Z. Meng, C. Zhong, J. Lu, Z. Yang, and Y. Qian, "Tube- and ball-like amorphous MoS2 prepared by a solvothermal method," *Mater. Chem. Phys.*, vol. 73, no. 2–3, pp. 327–329, 2002, doi: 10.1016/S0254-0584(01)00364-9.
[117] N. Rueda, R. Bacaud, and M. Vrinat, "Highly dispersed, nonsupported molybdenum sulfides," *J. Catal.*, vol. 169, no. 1, pp. 404–406, 1997, doi: 10.1006/jcat.1997.1669.
[118] M. Polyakov *et al.*, "Mechanochemical activation of MoS_2-Surface properties and catalytic activities in hydrogenation and isomerization of alkenes and in H_2/D_2 exchange," *J. Catal.*, vol. 260, no. 2, pp. 236–244, 2008, doi: 10.1016/j.jcat.2008.10.005.
[119] V. G. Pol, S. V. Pol, and A. Gedanken, "Micro to nano conversion: A one-step, environmentally friendly, solid state, bulk fabrication of WS_2 and MoS_2 nanoplates," *Cryst. Growth Des.*, vol. 8, no. 4, pp. 1126–1132, 2008, doi: 10.1021/cg0700972.
[120] K. Uchida *et al.*, "Preparation of MoS_2 Catalyst for Ultra-deep Desulfurization of Diesel Oil

by a Media Agitation Mill. Effect of Media Filling Ratio.," *J. Soc. Powder Technol. Japan*, vol. 39, no. 9, pp. 679–684, 2002, doi: 10.4164/sptj.39.679.

[121] M. Kouzu, K. Uchida, Y. Kuriki, and F. Ikazaki, "Micro-crystalline molybdenum sulfide prepared by mechanical milling as an unsupported model catalyst for the hydrodesulfurization of diesel fuel," *Appl. Catal. A Gen.*, vol. 276, no. 1–2, pp. 241–249, 2004, doi: 10.1016/j.apcata.2004.08.010.

[122] Y. Li, A. Li, F. Li, D. Liu, Y. Chai, and C. Liu, "Application of HF etching in a HRTEM study of supported MoS_2 catalysts," *J. Catal.*, vol. 317, pp. 240–252, 2014, doi: 10.1016/j.jcat.2014.06.007.

[123] A. N. Varakin, A. V. Mozhaev, A. A. Pimerzin, and P. A. Nikulshin, "Comparable investigation of unsupported MoS_2 hydrodesulfurization catalysts prepared by different techniques: Advantages of support leaching method," *Appl. Catal. B Environ.*, vol. 238, pp. 498–508, 2018, doi: 10.1016/j.apcatb.2018.04.003.

[124] J. T. Richardson, "Electronic properties of unsupported cobalt-promoted molybdenum sulfide," *J. Catal.*, vol. 112, no. 1, pp. 313–319, 1988, doi: 10.1016/0021-9517(88)90143-1.

[125] Y. E. Licea, R. Grau-Crespo, L. A. Palacio, and A. C. Faro, "Unsupported trimetallic Ni(Co)-Mo-W sulphide catalysts prepared from mixed oxides: Characterisation and catalytic tests for simultaneous tetralin HDA and dibenzothiophene HDS reactions," *Catal. Today*, vol. 292, pp. 84–96, 2017, doi: 10.1016/j.cattod.2016.11.031.

[126] D. Genuit, P. Afanasiev, and M. Vrinat, "Solution syntheses of unsupported Co(Ni)-Mo-S hydrotreating catalysts," *J. Catal.*, vol. 235, no. 2, pp. 302–317, 2005, doi: 10.1016/j.jcat.2005.08.016.

[127] L. Alvarez *et al.*, "Comparative study of MoS_2 and Co/MoS_2 catalysts prepared by ex situ/in situ activation of ammonium and tetraalkylammonium thiomolybdates," *J. Mol. Catal. A Chem.*, vol. 210, no. 1–2, pp. 105–117, 2004, doi: 10.1016/j.molcata.2003.09.002.

[128] B. Yoosuk, C. Song, J. H. Kim, C. Ngamcharussrivichai, and P. Prasassarakich, "Effects of preparation conditions in hydrothermal synthesis of highly active unsupported NiMo sulfide catalysts for simultaneous hydrodesulfurization of dibenzothiophene and 4,6-dimethyldibenzothiophene," *Catal. Today*, vol. 149, no. 1–2, pp. 52–61, 2010, doi: 10.1016/j.cattod.2009.05.001.

[129] S. S. Pollack, J. V. Sanders, and R. E. Tischer, "High-reflectance and single layer MoS_2: two new forms," *Appl. Catal.*, vol. 8, no. 3, pp. 383–388, 1983, doi: 10.1016/0166-9834(83)85008-8.

[130] M. P. De La Rosa *et al.*, "Structural studies of catalytically stabilized model and industrial-supported hydrodesulfurization catalysts," *J. Catal.*, vol. 225, no. 2, pp. 288–299, 2004, doi: 10.1016/j.jcat.2004.03.039.

[131] G. Delvaux, P. Grange, and B. Delmon, "X-ray photoelectron spectroscopic study of unsupported cobalt-molybdenum sulfide catalysts," *J. Catal.*, vol. 56, no. 1, pp. 99–109, 1979, doi: 10.1016/0021-9517(79)90093-9.

[132] G. Delvaux, P. Grange, and B. Delmon, "Influence of the preparation temperature on the physicochemical characteristics and catalytic properties of unsupported sulfided cobalt/molybdenum catalysts" *Bull. Soc. Chim. Fr.*, vol. 1–2, 1979.

[133] P. Grange, "Catalytic Hydrodesulfurization," *Catal. Rev.*, vol. 21, no. 1, pp. 135–181, 1980, doi: 10.1080/03602458008068062.

[134] D. S. Thakur, P. Grange, and B. Delmon, "A comparison of some catalytic, structural and textural properties of unsupported MoS_2 and WS_2 hydrodesulfurization catalysts promoted by Group VIII metals," *J. Less-Common Met.*, vol. 64, no. 2, pp. 201–211, 1979, doi: 10.1016/0022-5088(79)90171-1.

[135] K. Inamura and R. Prins, "The role of Co in unsupported Co-Mo sulfides in the hydrodesulfurization of thiophene," *Journal of Catalysis*, vol. 147, no. 2. pp. 515–524, 1994, doi: 10.1006/jcat.1994.1168.

[136] T. R. Halbert, T. C. Ho, E. I. Stiefel, R. R. Chianelli, and M. Daage, "Synthesis and activity of

hydrotreating catalysts prepared via promotion by low-valent transition-metal complexes," *J. Catal.*, vol. 130, no. 1, pp. 116–129, 1991, doi: 10.1016/0021-9517(91)90096-M.

[137] M. Ramos, G. Berhault, D. A. Ferrer, B. Torres, and R. R. Chianelli, "HRTEM and molecular modeling of the MoS_2-Co_9S_8 interface: Understanding the promotion effect in bulk HDS catalysts," *Catal. Sci. Technol.*, vol. 2, no. 1, pp. 164–178, 2012, doi: 10.1039/c1cy00126d.

[138] Z. Le, P. Afanasiev, D. Li, X. Long, and M. Vrinat, "Solution synthesis of the unsupported Ni-W sulfide hydrotreating catalysts," *Catal. Today*, vol. 130, no. 1, pp. 24–31, 2008, doi: 10.1016/j.cattod.2007.07.002.

[139] A. Olivas, G. Alonso, and S. Fuentes, "The catalytic activity of Ni/W bimetallic sulfide nanostructured catalysts in the hydrodesulfurization of dibenzothiophene," *Top. Catal.*, vol. 39, no. 3–4, pp. 175–179, 2006, doi: 10.1007/s11244-006-0054-1.

[140] L. Wang, Y. Y. Zhang, Y. Y. Zhang, Z. Jiang, and C. Li, "Ultra-deep hydrodesulfurization of diesel fuels on trimetallic NiMoW sulfide catalysts," *Chem. A Eur. J.*, vol. 15, no. 46, pp. 12571–12575, 2009, doi: 10.1002/chem.200901997.

[141] W. Wang, K. Zhang, Z. Qiao, L. Li, P. Liu, and Y. Yang, "Hydrodeoxygenation of p-cresol on unsupported Ni-W-Mo-S catalysts prepared by one step hydrothermal method," *Catal. Commun.*, vol. 56, pp. 17–22, 2014, doi: 10.1016/j.catcom.2014.06.024.

[142] A. Olivas, D. H. Galván, G. Alonso, and S. Fuentes, "Trimetallic NiMoW unsupported catalysts for HDS," *Appl. Catal. A Gen.*, vol. 352, no. 1–2, pp. 10–16, 2009, doi: 10.1016/j.apcata.2008.09.022.

[143] R. Huirache-Acuña *et al.*, "Synthesis of Ni-Mo-W sulphide catalysts by ex situ decomposition of trimetallic precursors," *Appl. Catal. A Gen.*, vol. 304, no. 1–2, pp. 124–130, 2006, doi: 10.1016/j.apcata.2006.02.032.

[144] H. Nava, F. Pedraza, and G. Alonso, "Nickel-molybdenum-tungsten sulphide catalysts prepared by in situ activation of tri-metallic (Ni-Mo-W) alkylthiomolybdotungstates," *Catal. Letters*, vol. 99, no. 1–2, pp. 65–71, 2005, doi: 10.1007/s10562-004-0777-1.

[145] F. L. Plantenga *et al.*, "'NEBULA': A hydroprocessing catalyst with breakthrough activity," *Stud. Surf. Sci. Catal.*, vol. 145, pp. 407–410, 2003, doi: 10.1016/s0167-2991(03)80246-x.

[146] S. Eijsbouts, S. W. Mayo, and K. Fujita, "Unsupported transition metal sulfide catalysts: From fundamentals to industrial application," *Appl. Catal. A Gen.*, vol. 322, pp. 58–66, 2007, doi: 10.1016/j.apcata.2007.01.008.

[147] S. Eijsbouts, F. Plantenga, B. Leliveld, Y. Inoue, and K. Fujita, "STARS and NEBULA - New Generations of Hydroprocessing Catalysts for the Production of Ultra Low Sulfur Diesel," *ACS Div. Fuel Chem. Prepr.*, vol. 48, no. 2, pp. 494–495, 2003.

[148] "Catalysts | STARS Technology | Albemarle." https://www.albemarle.com/businesses/catalysts/hydroprocessing-catalysts/hydrotreating/stars-technology (accessed Apr. 09, 2021).

[149] "Catalytic Hydrotreating | Nebula | Albemarle." https://www.albemarle.com/businesses/catalysts/hydroprocessing-catalysts/hydrotreating/nebula (accessed Apr. 09, 2021).

[150] "Celestia | Hydroprocessing Catalysts | Albemarle." https://www.albemarle.com/businesses/catalysts/hydroprocessing-catalysts/hydrotreating/celestia (accessed Apr. 09, 2021).

Chapter 2

Unpromoted MoWS hydrotreating catalysts supported on alumina

2.1 Introduction

The literature review allows concluding that the use of mixed MoW catalysts is a promising method for improving the hydrotreating process. Various types of mixed MoW systems can be found in the literature, which preparation mostly involves traditional precursors of the active phase, such as ammonium heptamolybdate (AHM), ammonium paratungstate (APT), ammonium metatungstate (AMT) and ammonium tungstate [1–3]. Heteropolycompounds, such as Keggin and Keggin-derivated heteropolymolybdate and heteropolytungstate structures, can be used as starting oxidic precursor for highly active hydrotreating catalysts [4–7].

A method was previously proposed to synthesize MoW catalysts using mixed $H_4[SiMo_1W_{11}O_{40}]$ and $H_4[SiMo_3W_9O_{40}]$ Keggin-type heteropolyacids (HPA) prepared from corresponding lacunar salts, allowing to introduce both Mo and W metals in a catalyst from a single molecular precursor [8]. It was found that such catalysts are more efficient in DBT HDS and naphthalene HYD than their counterparts obtained from a mixture of monometallic $H_4SiMo_{12}O_{40}$ and $H_4SiW_{12}O_{40}$ HPAs with the same Mo/(Mo+W) ratio. The use of mixed HPAs as a precursor led to the formation of mixed $MoWS_2$ sulfides, the composition and structure of which were studied in detail by HAADF and EXAFS analysis. [9, 10]. Moreover, it was found that when increasing the Mo/W atomic ratios from 1/11 to 3/9, the catalytic activity also increases.

We thus intended to synthetize HPA with higher Mo/W ratio than the one previously studied, as we assumed that it may have a strong effect on the structure of the active phase and thus on the catalytic activity. Various mixed polyanions are mentioned in the literature, but most of synthesis cannot provide a high yield of the product and/or lead to the formation of a mixture of various mixed anions, which are almost impossible to separate. In this chapter, a new one-stage method was proposed for the synthesis of mixed HPAs with Mo/W ratio 6/6 and 9/3, based on monometallic $H_4SiMo_{12}O_{40}$ and $H_4SiW_{12}O_{40}$ HPAs without prior formation of lacunar salts. The structure of the obtained compounds was identified by single-crystalline XRD, IR and Raman spectroscopy. Catalysts with different Mo/(Mo+W) atomic ratio were synthesized using corresponding mixed HPAs, characterized by advanced analysis methods and tested under the conditions of a micro-flow unit in model reactions of DBT HDS and naphthalene HYD.

2.2 Synthesis and characterization of $H_4SiMo_nW_{12-n}O_{40}$ Keggin-type heteropolyacids

2.2.1 Synthesis of $H_4SiMo_nW_{12-n}O_{40}$ Keggin-type heteropolyacids

2.2.1.1 Synthesis of monometallic $H_4SiMo_{12}O_{40}$ and $H_4SiW_{12}O_{40}$ heteropolyacids

$H_4SiMo_{12}O_{40}$ ($SiMo_{12}$) HPA was obtained according to the method described by Sanchez et al. [11]. Sodium molybdate dihydrate (58.1 g) was dissolved in 240 ml of distilled water (1 mol L^{-1} ions MoO_4^{2-}) and then 74 ml of concentrated nitric acid (HNO_3) was added to the solution under stirring. After that, 100 ml of sodium silicate solution (0.2 mol L^{-1} SiO_3^{2-}) was added dropwise under stirring. To transform the polyanion from β to α form, the solution was heated and kept at 80°C for 40 min. Then the solution was cooled down to room temperature and extraction was performed with ether [12, 13]. The cooled solution was transfused into a 500 ml separatory funnel. Then, in equal portions (30 ml each), concentrated hydrochloric acid and diethyl ether were added. The mixture was stirred, the pressure being periodically released. The heavy phase containing the ether-polymolybdate complex was isolated piece by piece by addition of new portion of acid and ether. The isolated ether complex was mixed with distilled water in a ratio of 2/1 and poured into a Petri dish. The resulting solution was placed in a fume hood to remove ether vapors and transferred to a fridge for crystallization at a temperature of 4°C.

$H_4[SiW_{12}O_{40}]$ (SiW_{12}) HPA was prepared according to [12]. 182 g of sodium tungstate dihydrate was dissolved in 300 ml of hot distilled water. 240 ml of 3 M aqueous HCl were added by fractions under vigorous stirring in order to redissolve the local precipitate of tungstic acid. Then, in a separating funnel, 100 ml of sodium silicate solution (0.5 M) was added by dropping and following by 50 ml of hydrochloric acid solution. The resulting mixture was heated and kept at 90°C for 1 h. The acid was isolated from the solution by the ethereal method, similar to that used in the synthesis of $H_4SiMo_{12}O_{40}$ acid.

2.2.1.2 Synthesis of mixed $H_4SiMo_nW_{12-n}O_{40}$ (n = 1 and 3) heteropolyacids using lacunar salts

Mixed $H_4SiMo_3W_9O_{40}$ and $H_4SiMo_1W_{11}O_{40}$ HPAs were prepared by multistage synthesis using the corresponding lacunar structures [9]. The lacunar salt α-$K_8[SiW_{11}O_{39}]$ was obtained by the following procedure: 11 g of sodium silicate pentahydrate was dissolved in 100 ml of distillate water followed by the addition of 4 M solution of hydrochloric acid (50 ml); the second solution was prepared by dissolving 182 g of sodium tungstate dihydrate in 230 ml of distilled water followed by the addition of 4 M solution of hydrochloric acid (145 ml). Then, the previously obtained sodium silicate solution was added dropwise to the second solution with stirring. The final solution was boiled at 65°C for 1 h and then potassium chloride (75 g) was added to precipitate $K_8[SiW_{11}O_{39}]$ separated by filtration [14]. The corresponding mixed α-$K_4[SiMo_1W_{11}O_{40}]$ salt was obtained according to the

method described in reference [11]. 6 ml of solution of nitric acid (13 M) was added dropwise to 10 ml of sodium molybdate dihydrate solution (1 M), and then the dried $K_8[SiW_{11}O_{39}]$ salt was added in small portions with stirring. After 3 h stirring, the salt was isolated by filtration.

The mixed $H_4[SiMo_3W_9O_{40}]$ HPA was obtained in almost the same way using the corresponding lacunar β-$Na_9[SiW_9O_{34}H]$ salt obtained by dissolving sodium metasilicate pentahydrate (12 g) and sodium tungstate dihydrate (150 g) in 250 mL of cold water [15]. Then, 95 ml of hydrochloric acid solution (6 M) was slowly added dropwise into the vigorously stirred solution. If a suspension of silica is formed, the solution must be filtered. The purified solution was stirred for 1 hour and then transferred to a refrigerator (4°C) for 48 hours to crystallize the β-$Na_9[SiW_9O_{34}H]$ salt. The mixed potassium salt β-$K_8[SiMo_3W_9O_{39}]$ was prepared following ref. [11]. 60 ml of hydrochloric acid (12 M) was added into 40 ml of sodium molybdate dihydrate solution (1 M) with stirring, and then β-$Na_9[SiW_9O_{34}H]$ salt (27 g) was added in small portions. The resulting solution was stirred for 1 hour. The mixed β-$K_8[SiMo_3W_9O_{39}]$ salt was precipitated by the addition of potassium chloride (5 g) followed by filtration.

The corresponding mixed α-$K_4[SiMo_1W_{11}O_{40}]$ and β-$K_8[SiMo_3W_9O_{39}]$ salts were dissolved in distilled water and isolated by the "ether" extraction (described in section 2.1.1). HPAs were crystallized from an aqueous solution at a temperature of 4°C.

2.2.1.3 One-step synthesis of mixed $H_4SiMo_nW_{12-n}O_{40}$ (n = 6 and 9) heteropolyacids

The synthesis of polyvacant lacunar compounds of molybdenum or tungsten with a large number of vacant positions (more than three) with Si as a heteroatom did not appear possible to consider as a starting step to prepare the desired mixed compounds. The main problem lies in the isolation of pure high-lacunar W or Mo based compounds from solution for further synthesis of the corresponding mixed ones. To prepare mixed MoW heteropolyacids with high Mo/W ratio, we had to develop a new synthesis route. Several methods of preparation have been proposed in the literature. In 1942, Brown and Frazer [16] proposed a method for the synthesis of mixed $SiMo_nW_{12-n}$HPAs from sodium molybdate, sodium tungstate, sodium silicate and followed by the stepwise addition of hydrochloric acid. However, the work did not present any data confirming the formation of a "mixed" structure. In this study, attempts were made to reproduce this technique and analyze the compounds. It was found that, a mixture of two HPA forms in the crystal, as was also observed when the corresponding monometallic $H_4SiMo_{12}O_{40}$ and $H_4SiW_{12}O_{40}$ HPAs were boiled. This section thus presents a one-step protocol for the synthesis of two new $SiMo_nW_{12-n}$ HPAs with Mo/W ratio equal to 6/6 and 9/3 using monometallic $H_4[SiMo_{12}O_{40}]$ and $H_4[SiW_{12}O_{40}]$ HPAs as starting materials:

- for Mo/W = 6/6: 4.12 g of $SiMo_{12}$ and 6.21 g of SiW_{12} acids were dissolved in 40 ml of distilled water;

- for Mo/W = 9/3: 6.62 g of $SiMo_{12}$ and 3.44 g of SiW_{12} acids were dissolved in 48 ml of distilled water.

Yellow solutions were obtained in both cases. The acid solutions were heated to 80°C and kept for 1 h. After that, potassium hydroxide was added to each solution in small portions until pH reaches 4. After the addition of alkali, the solution became slightly greenish. Both solutions were boiled for another 30 min at 80°C and then cooled down to room temperature. It was noticed that the mixed acid was sufficiently stable to be crystallized from aqueous solution by using the etherate method. The extraction and the crystallization were carried out according to the procedure described in section 2.1.1.

The elemental composition and structures of the mixed heteropolyacids were confirmed by XRD, IR and Raman spectroscopy.

2.2.2 Characterization of $H_4SiMo_nW_{12-n}O_{40}$ Keggin-type heteropolyacids

2.2.2.1 IR and Raman analysis

IR and Raman spectra of all synthesized HPAs are presented in **Figs. 2.1** and **2.2**, respectively.

IR spectra of monometallic and mixed HPAs are very close and present the typical peaks of Keggin structure. For all samples, characteristic peaks assigned to the Keggin structure are observed at 913-930 and 957-982 cm^{-1} for Si-O and Mo(W)-O_t vibrations stretching mode respectively together with lines at 867-882 and 773-780 cm^{-1} corresponding to Mo(W)-O_b-Mo(W) and Mo(W)-O_c-Mo(W) vibrations. The increase of the Mo content in $SiMo_nW_{12-n}O_{40}^{4-}$ is reflected by a slight shift to lower wavenumbers for Mo(W)-O_t and Mo(W)-O_b-Mo(W) lines [12, 17].

Raman spectra of monometallic and mixed MoW HPAs (**Fig. 2.2**) are dominated by a main peak corresponding to symmetric ν_s(Mo(W)-O_t) terminal vibration [12, 18, 19]. For the high W content mixed HPA, $SiMo_1W_{11}$ and $SiMo_3W_9$ HPAs, the position of this line (1005 cm^{-1}) is similar to that observed for $SiW_{12}O_{40}$ while a more important shift towards low wavenumbers is observed with the increase of Mo content, which, possibly, can be associated to a change in the bond strength between oxygen and metal. Previously, a similar effect was found in a work devoted to the synthesis of mixed potassium salt K_4[β-$SiMo_3W_9O_{40}$] [20]. An important difference is observed for vibrations ν_s(W-O_c-W) and ν_s(Mo-O_c-Mo), which correspond to peaks at 552 and 638 cm^{-1}. In the case of spectra for mixed HPAs, a weak peak is observed, which lies between 552 and 638 cm^{-1}, which may indicate the presence of different ν_s(Mo(W)-O_c-W(Mo)) vibrations.

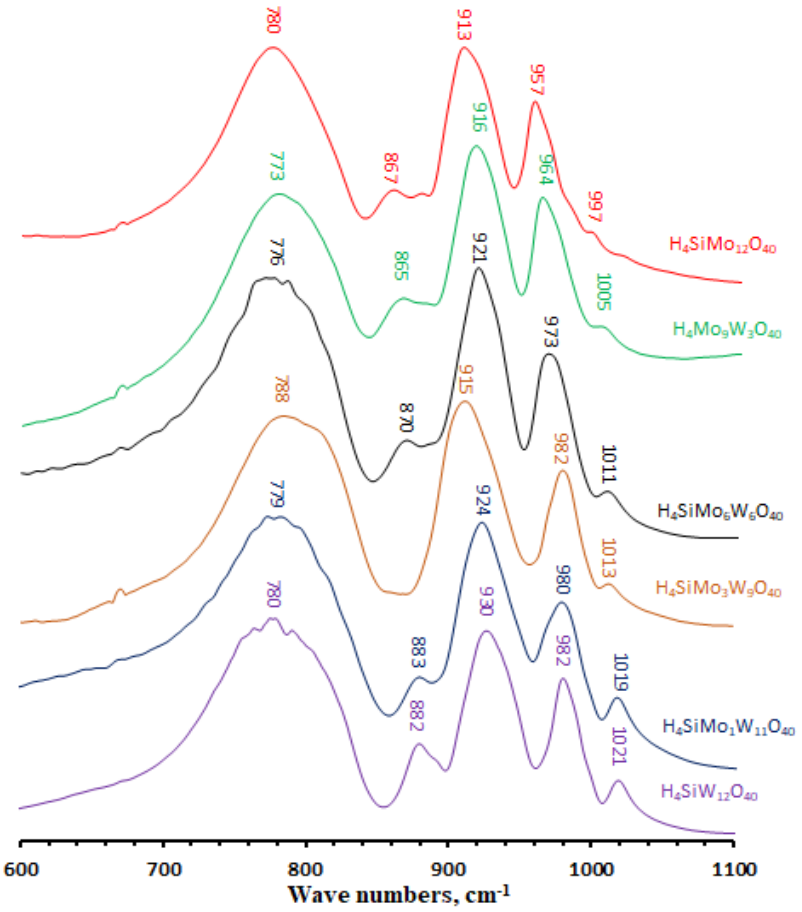

Fig. 2.1. IR-spectra for $SiMo_nW_{12-n}HPAs$.

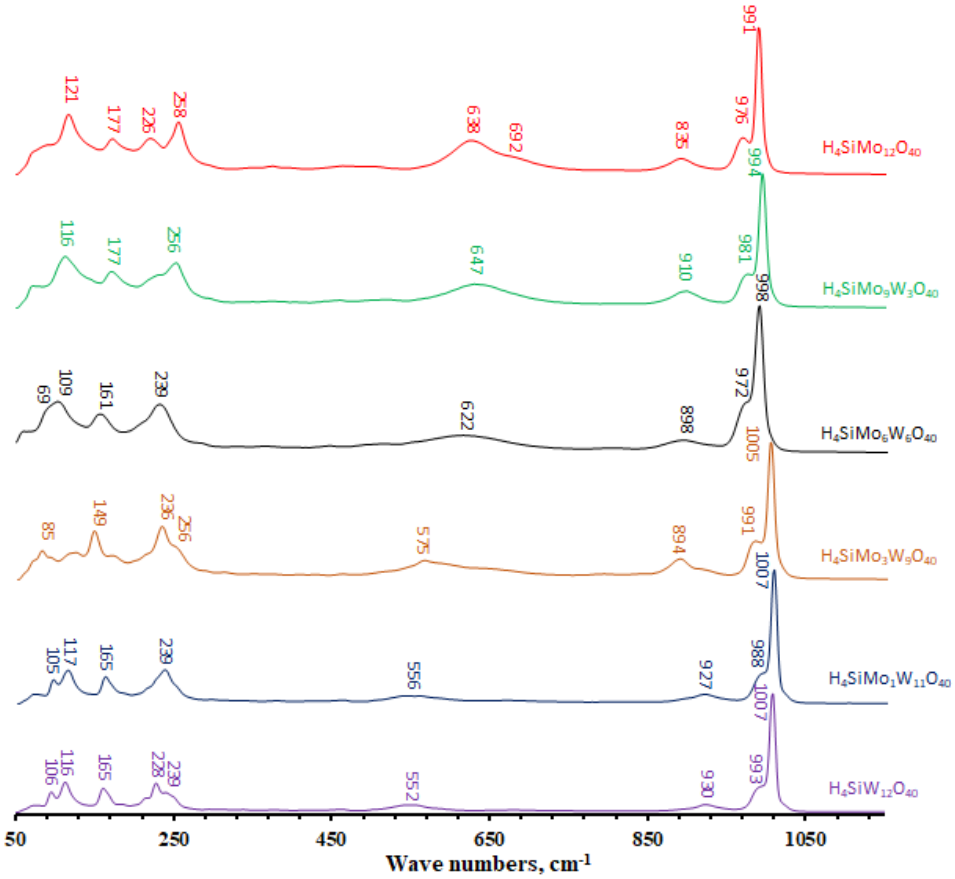

Fig. 2.2 Raman spectra for $SiMo_nW_{12-n}HPAs$.

To complete this study, a hydrated single crystal was obtained by crystallization from a solution of a mixture of two monometallic $H_4SiMo_{12}O_{40}$ and $H_4SiW_{12}O_{40}$ HPAs with a corresponding ratio Mo/W = 9/3 without adding potassium hydroxide. For this crystal, Raman analysis was also carried out (**Fig. 2.3**) and revealed the presence of two main peaks at 991 and 1006 cm^{-1} corresponding to ν_s(Mo-O_t) and ν_s(W-O_t) terminal vibrations, respectively, indicating that this single crystal is a mixture of two heteropolyacids. Contrariwise, for the mixed HPAs, the presence of a single peak at 994 cm^{-1} in the HPA spectrum confirms the formation of a mixed compound in which Mo and W oxygen vibrational mods cannot be observed separately [9]. Due to the similarity between molybdenum and tungsten, Mo-O_t and W-O_t cannot be distinguished with a complete making of Mo-O_t and W-O_t vibrations.

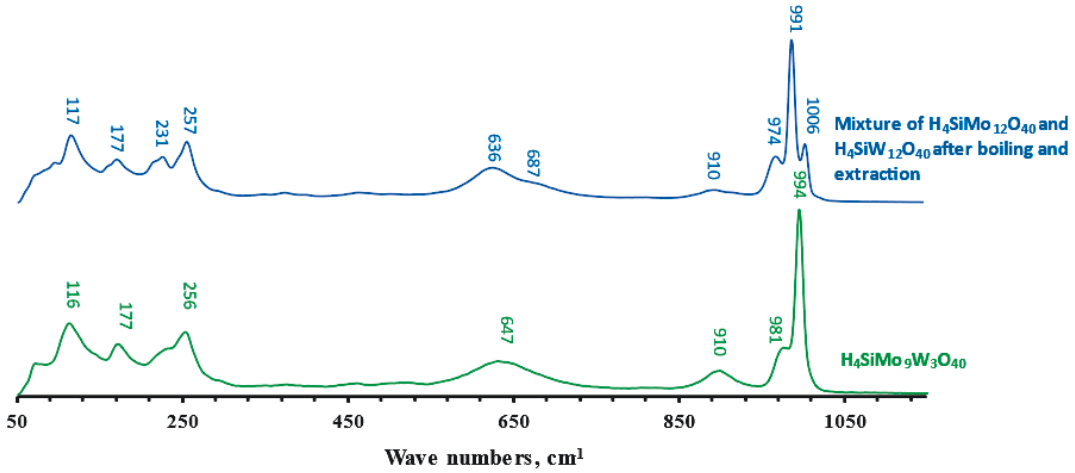

Fig. 2.3 Raman spectra for $SiMo_9W_3$HPA and the mixture of $H_4SiMo_{12}O_{40}$ and $H_4SiW_{12}O_{40}$ HPAs.

Both Raman and IR analysis are consistent with the formation of a mixed Keggin structure for the newly synthesized mixed heteropolyacids $SiMo_6W_6$ and $SiMo_9W_3$.

2.2.2.2 Single-crystal XRD analysis

$H_4[SiMo_3W_9O_{40}]$ HPA was previously studied in detail by single-crystal XRD analysis [9]. It was found that in the β-$H_4[SiMo_3W_9O_{40}]$ structure where one W_3O_{13} is rotated by 60° (main difference from α structure), the X-Ray structure resolution testifies the ordered W substitution by Mo in each of the three other W_3O_{13} groups. These results showed that this HPA has an ordered structure in which the molybdenum octahedra have a strict position (**Fig. 2.4**).

To determine the structure of the new $H_4[SiMo_6W_6O_{40}]$ and $H_4[SiMo_9W_3O_{40}]$ HPAs, single crystal XRD was also performed. The crystal data and the structure refinement parameters for the obtained crystals are given in **Table 2.1.**

Both heteropolyacids $SiMo_6W_6$ and $SiMo_9W_3$ structures are isomorphs and crystallize in the tetragonal space group P-42_1c. The number of hydration water molecules determined during the

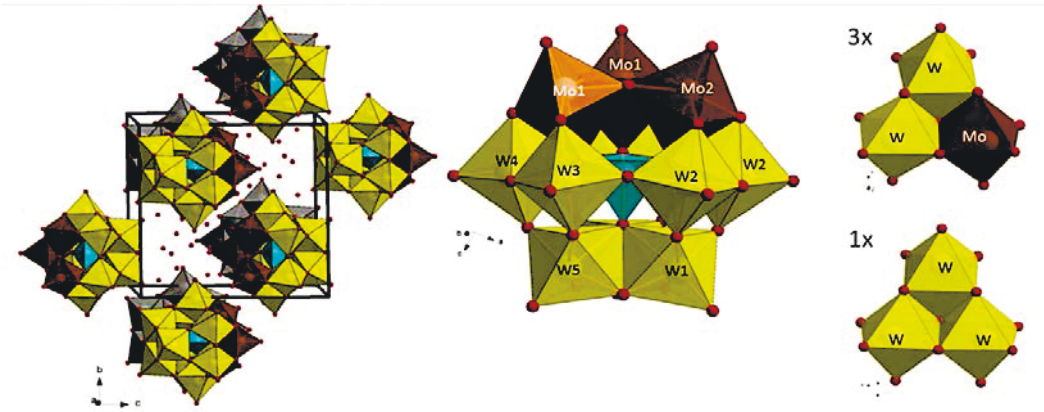

Fig. 2.4 Crystals and detailed heteropolyanion structures and formation of $H_4[SiMo_3W_9O_{40}]\cdot 10H_2O$* (adapted from [9])

structural refinement corresponds to 36 molecules per $H_4[SiMo_nW_{12-n}O_{40}]$ cluster for the two compounds, in agreement with their nearly identical refined lattice parameters. Before going into the structural details, one should note the poor stability of the crystals in air at ambient temperature, even more pronounced for the $H_4[SiMo_6W_6O_{40}]$ polycation for which a single crystal had to be isolated very rapidly and collected at 100K in a cold nitrogen flow to prevent from degradation by moisture into an amorphous solid. For the $H_4[SiMo_9W_3O_{40}]$ hydrate a simple protection of the crystals by vacuum grease allowed full data collection at room temperature. The two crystal structures are similar and show a distribution of HPA (two per unit cell) separate by ca.12.75Å (d(Si-Si)) (**Fig. 2.5**) surrounded by water molecules. For both compounds, the Mo/W occupancy and the scale factor parameters are strongly correlated which complicates the determination of the real Mo/W ratio during refinement. However, it was checked that fixing the ratio to the preparation stoichiometry leads to best R% values together with most reasonable thermal parameters for all atoms. No evidence was found that Mo/W are ordered, contrarily to what was obtained for $H_4[SiMo_3W_9O_{40}]$.

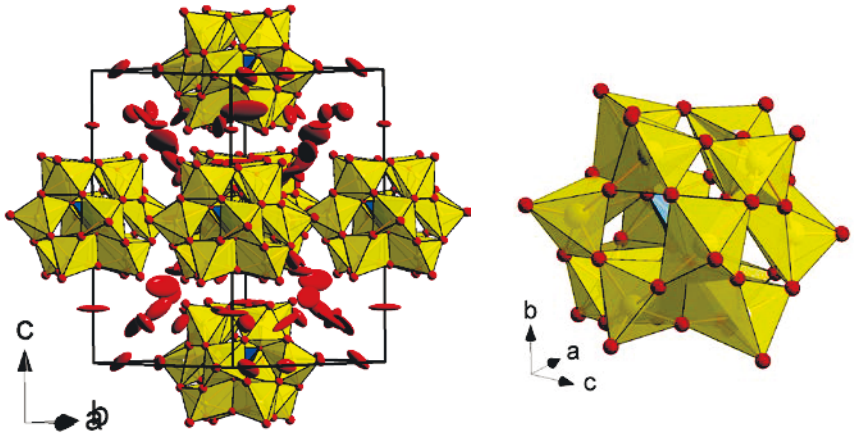

Fig. 2.5 Crystals and detailed heteropolyanion structures of synthesized $H_4[SiMo_6W_6O_{40}]\cdot 36H_2O$ (similarly for $H_4[SiMo_9W_3O_{40}]\cdot 36H_2O$)

Single-crystal XRD of $SiMo_6W_6$ and $SiMo_9W_3$ HPA allows to conclude that mixed heteropolyanions containing both W and Mo atoms with disordered positions were formed.

Table 2.1 Crystal data, data collection and structure refinement parameters for $H_4[SiMo_6W_6O_{40}]\cdot 36H_2O$ and $H_4[SiMo_9W_3O_{40}]$ $36H_2O$

Crystal data		
Cluster formula	$H_4[SiMo_6W_6O_{40}]$	$H_4[SiMo_9W_3O_{40}]$
Crystal symmetry	Tetragonal	
Space group	$P\text{-}42_1c$	
Working temp. (K)	100	293
Unit cell (Å)	a = 12.732(2) c = 18.0525(6)	12.7447(3) 18.0632(9)
Volume (Å^3)	2926.38	2933.96
Z, Mw	2, 2994.8	2, 2761.02
Calculated density (g/cm^3)	3.40	3.12
Data collection		
Equipment	Bruker Apex Duo	
Radiation MoKα (Å)	0.71073	
Scan mode	ω/φ - scan	
Recorded angular range θ (°)	1.96 – 33.13	1.96 – 31.69
Recording reciprocal space	-15 ≤ h ≤19 -19 ≤ k ≤ 16 -27 ≤ l ≤ 27	-18 ≤ h ≤18 -18 ≤ k ≤ 18 -26 ≤ l ≤ 26
N. ind. Ref.	2656	2672
N. ind. Ref. [I>3σ(I)]	2465	2222
μ (cm^{-1}) (λ = MoKα)	131.1	78.8
Absorption correction	analytical (Sadabs)	
R merging factor (%)	4.12	4.22
Refinement parameters		
Software	Jana 2000	
Number of refined parameters	106	107
R_1 (F) all , [I>3σ(I)] = $\sum\|\|F_O\| - \|F_C\|\|/\sum\|F_O\|$ (%)	3.62, 4.01	3.45, 4.67
wR_2 (F^2) all, [I>3σ(I)] = $[\sum w(F_O^2 - F_C^2)^2 / \sum w(F_O^2)]^{1/2}$ (%)	3.85, 4.14	5.27, 5.21
Weight	unit	$1/(\sigma^{2\wedge}(F)+0.0001F^2)$
Isotropic secondary extinction	none	none
Max / Min Δρ e/Å^3	-1.37/1.95	-1.05/1.81

2.3 Preparation and characterization of the supported oxidic precursors

The bimetallic Mo_nW_{12-n} catalysts were prepared by using the corresponding mixed $H_4[SiMo_nW_{n-12}O_{40}]$ HPAs and will be referred to as Mo_nW_{12-n}/Al_2O_3. Reference catalysts were also prepared using the impregnating solutions obtained by mixing $SiMo_{12}$ and SiW_{12} in an aqueous solution with the same Mo/W ratio than the corresponding mixed HPAs and were denoted as Mo_n+W_{12-n}/Al_2O_3. The catalysts with surface density of the metals d(Mo + W) equal to 3.9 at nm^{-2} were prepared by incipient wetness impregnation of alumina support [γ-Al_2O_3 (Norton), specific area: 240 $m^2\ g^{-1}$, pore volume: 0.9 mL g^{-1}]. The oxidic catalyst precursors after maturation were dried at 60°C (4 h), 80°C (2 h) and 100°C (4 h) in air atmosphere without further calcination. The chemical compositions of the prepared catalysts are given in **Table 2.2**. All the obtained samples had approximately the same textural characteristics, regardless of the type of precursor.

Table 2.2 Composition and textural characteristics of sulfided Mo(W) catalysts.

Catalyst	*d*(Me) at nm^{-2}	Content (wt. %)		Textural characteristics		
		Mo	W	S_{BET}[a] ($m^2\ g^{-1}$)	V_p[b] ($cm^3\ g^{-1}$)	D[c] (nm)
Mo_{12}/Al_2O_3*	3.9	18.0	-	215	0.53	7.6
Mo_9W_3/Al_2O_3		13.1	7.1	204	0.56	7.7
Mo_9+W_3/Al_2O_3				210	0.59	7.5
Mo_6W_6/Al_2O_3		8.5	13.8	191	0.58	7.9
Mo_6+W_6/Al_2O_3				204	0.59	7.8
Mo_3W_9/Al_2O_3*		4.2	20.1	210	0.53	7.6
Mo_3+W_9/Al_2O_3*				206	0.53	7.6
Mo_1W_{11}/Al_2O_3		1.4	24.2	205	0.53	7.5
Mo_1+W_{11}/Al_2O_3				208	0.55	7.6
W_{12}/Al_2O_3*		-	26.2	208	0.54	7.6

[a]S_{BET} is the surface area, [b]V_p is the pore volume, and [c]D is the pore diameter. * adapted from [10]

To evidence the behavior of the HPAs after deposition on the support, Raman analysis was performed and obtained Raman spectra of the oxidic catalysts are shown in **Fig. 2.6.** For comparison purposes, Raman spectra of the oxidic precursors prepared from a mixture of monometallic HPA $SiMo_{12}$ and SiW_{12} are also reported.

For precursors prepared from a mixture of HPAs, the main Raman line observed around 970 cm^{-1} and corresponding to Mo(W)-O terminal vibrations presents an important shoulder at 950 cm^{-1}, increasing with Mo content, witnessing the presence of Keggin entities with other species. Mo_{12}/Al_2O_3 presents the Raman spectrum of $AlMo_6O_{24}H_6^{3-}$ ($AlMo_6$) Anderson species in agreement with results previously reported [21, 22], with a main peak at 944 cm^{-1}. For oxidic catalysts prepared

from a mixture of SiW_{12} and $SiMo_{12}$ HPAs, the shoulder noticed at 950 cm^{-1} is then due to the $AlMo_6$ formation from instable $SiMo_{12}$ species when deposited on alumina due to the "buffer effect" of alumina and Al^{3+} extraction from the support [23, 24]. Raman lines at 550, 350 and 215 cm^{-1} are also clearly observed, which are unambiguously assigned to the formation of the well-known Anderson heteropolyanion species.

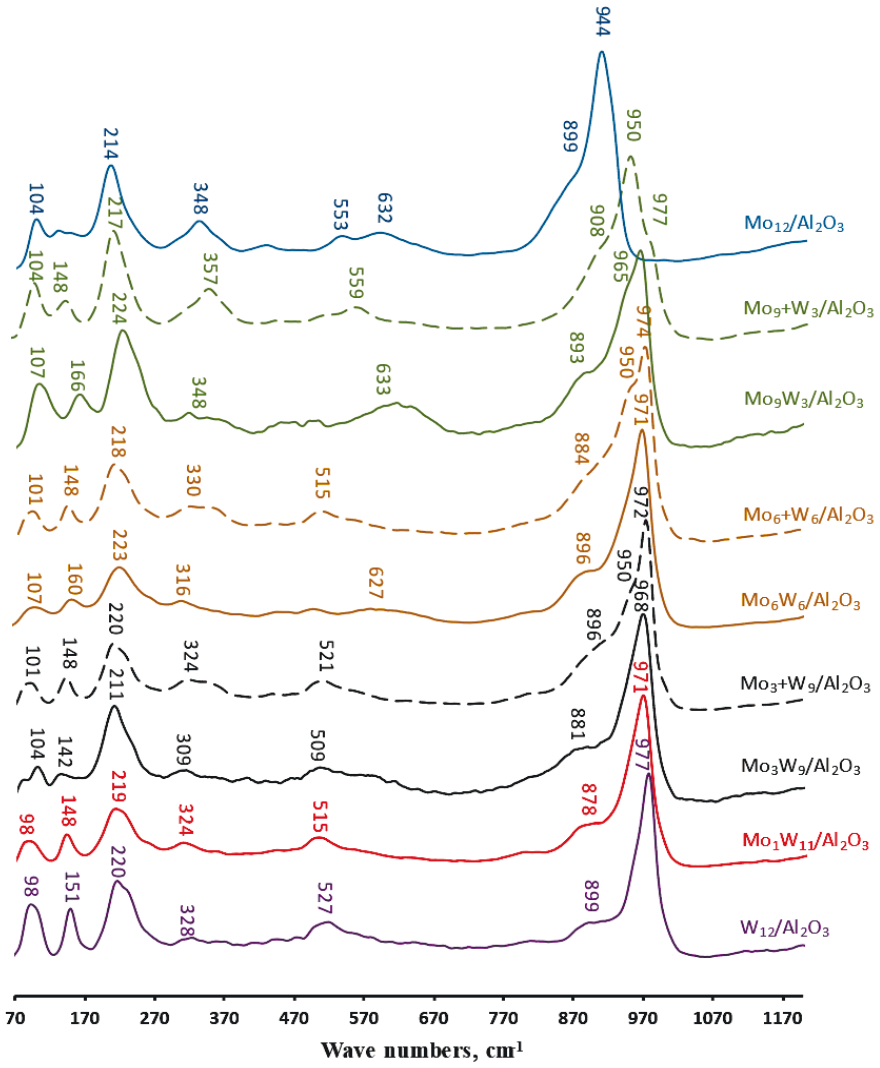

Fig. 2.6. Raman spectra for oxidic MoW catalysts dried at 110 ºC.

For the corresponding catalysts prepared from mixed HPAs ($SiMo_9W_3$, $SiMo_6W_6$ and $SiMo_3W_9$) the shoulder is not observed. It is in agreement with the use of a mixed $SiMo_nW_{12-n}$ HPA more stable on alumina support than the $SiMo_{12}$ one. A shift of the main peaks is also observed with the increase of molybdenum content, as was previously noted on Raman and IR spectra of bulk HPAs. Moreover, analysis of the low Raman shift region (below 230 cm^{-1}) shows lines similar in shape and position for the bulk and the corresponding Keggin W-based HPA catalysts [12], except for Mo_9W_3/Al_2O_3 and Mo_9+W_3/Al_2O_3 ones, in which the proportion of molybdenum is much higher. In this case, all peaks are shifted to the low wavenumbers. As already noted, for the W-based catalysts, after drying, a shift from 1007 to 977 cm^{-1} of the main line (W-O_t vibration) towards lower

wavenumbers due to interaction with the support is observed [9]. According to the obtained spectral data, it can be assumed that the mixed MoW structure is preserved even after maturation and drying.

2.4 Characterization of supported Mo(W)/Al_2O_3 sulfide catalysts

Before characterization, the catalysts were sulfided in a flow of H_2S/H_2 (10 vol. %) at atmospheric pressure and 400 °C for 2 h. For characterization of the active phase, sulfided catalysts were unloaded from the reactor for analysis in a glove box in an inert gas atmosphere (argon).

2.4.1 Transmission electron microscopy (TEM)

All catalysts were characterized by TEM to obtain more information about the dispersion of Mo(W)S_2 active phase. The TEM micrographs are shown in **Fig. 2.7**. The observed black thread-like slabs correspond to Mo(W)S_2 crystallites with 0.65 nm interplanar distances matching characteristic (002) basal planes of crystalline MoS_2. In TEM, only the slabs parallel to the electron beam can be visualized and the observed contrast does not allow to distinguish MoS_2, WS_2 or $MoWS_2$ particles. Only global morphological information will be obtained, through the distributions in stacking degree and length of the Mo(W)S_2 slabs, presented together with the corresponding average values in **Table 2.3**.

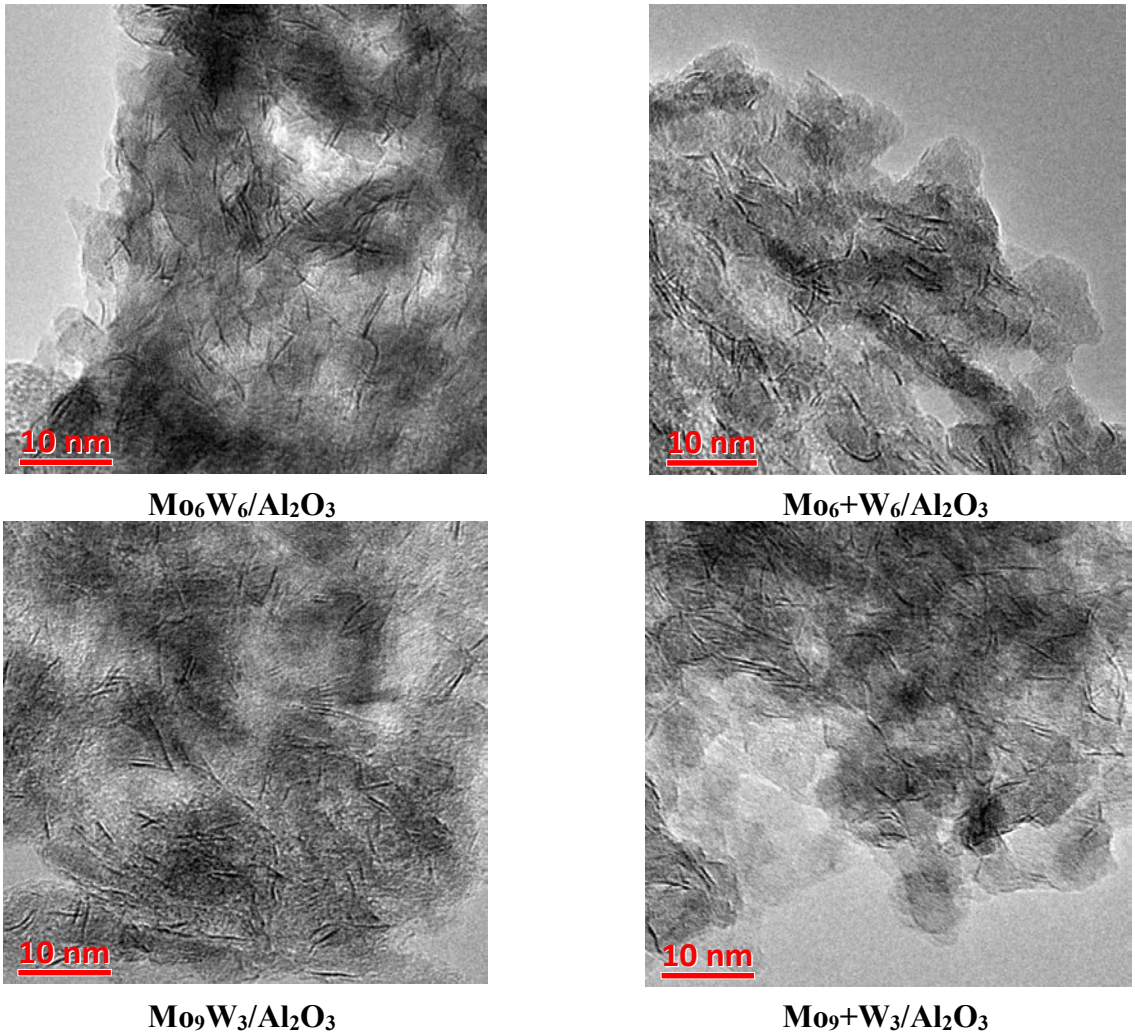

Mo_6W_6/Al_2O_3 **Mo_6+W_6/Al_2O_3**

Mo_9W_3/Al_2O_3 **Mo_9+W_3/Al_2O_3**

Fig. 2.7. TEM micrographs of sulfided MoW catalysts.

Table 2.3. Morphological characteristics of sulfided Mo(W) catalysts.

Catalyst	Average length $\bar{L}$ (nm)	Average stacking number $\bar{N}$	Dispersion of MoS_2 particles D	Distribution of slab length (rel. %)					Distribution of stacking number (rel. %)			
				<2 nm	2-4 nm	4-6 nm	6-8 nm	>8 nm	1	2	3	>4
Mo_{12}/Al_2O_3	3.8	1.2	0.31	3	61	30	5	1	79	18	2	1
Mo_9W_3/Al_2O_3	4.0	1.5	0.29	2	49	40	8	1	57	37	4	2
Mo_9+W_3/Al_2O_3	3.6	1.2	0.32	6	62	29	2	1	82	15	2	1
Mo_6W_6/Al_2O_3	3.9	1.4	0.30	3	57	34	5	1	70	24	5	1
Mo_6+W_6/Al_2O_3	3.8	1.3	0.31	3	58	31	6	2	73	24	2	1
Mo_3W_9/Al_2O_3	3.8	2.0	0.33	4	56	36	3	1	34	42	14	10
Mo_3+W_9/Al_2O_3	3.5	2.3	0.29	6	68	23	2	1	29	29	30	12
Mo_1W_{11}/Al_2O_3	3.9	2.1	0.30	3	56	37	4	1	32	44	19	5
Mo_1+W_{11}/Al_2O_3	4.1	2.2	0.29	2	51	40	7	2	31	43	22	4
W_{12}/Al_2O_3	4.2	1.2	0.28	2	46	42	8	2	84	14	2	-

[a] MoS_2 dispersion calculated from HRTEM results.

The average particle length and stacking number ranged from 3.6 to 4.2 nm and from 1.2 to 2.3, respectively. The average length appears to be similar regardless of the Mo/W ratio, between 3.5 and 3.8 nm for Mo_n+W_{n-12}/Al_2O_3 catalysts and between 3.8 and 4.0 nm for Mo_nW_{n-12}/Al_2O_3 catalysts, the highest value (4.2 nm) being observed on W_{12}/ Al_2O_3 catalyst. The highest stacking value corresponds to Mo_3+W_9/Al_2O_3 catalyst (2.3). The increase in molybdenum percentage led to a decrease of the stacking number of $Mo(W)S_2$ particles, from 2.3 to 1.2 for Mo_n+W_{n-12}/Al_2O_3 catalysts, from 2.0 to 1.5 for Mo_nW_{n-12}/Al_2O_3 catalysts. The dispersion of the active phase varies between 0.28 and 0.34. Moreover, the dispersion of the active phase of mixed Mo_nW_{12-n} catalysts decreased from 0.33 to 0.29 with an increasing Mo/W ratio from 3/9 to 9/3, while it increased from 0.29 to 0.32 for the ones based on the mixture of HPAs counterparts.

2.4.2 High-angle annular dark-field scanning transmission electron microscopy (HAADF-STEM)

The TEM method does not allow to determine the structure and arrangement of metals in the composition of the active phase, but gives only general morphological information about the sulfided phase. Contrariwise, HAADF allows visualization of the basal planes of the sulfide phase, where the Z-contrast between Mo and W atoms facilitates their discrimination. Typical HAADF images of sulfided Mo_3W_9/Al_2O_3, Mo_6W_6/Al_2O_3, Mo_9W_3/Al_2O_3 and W_{12}/Al_2O_3 catalysts are presented in **Fig. 2.7.**

The overwhelming majority of clusters, both in the case of a monometallic W_{12}/Al_2O_3 catalyst and in the case of mixed Mo_nW_{12-n}/Al_2O_3 samples, have an irregular shape, which may be associated to the interaction of the active phase with an inhomogeneous support surface. In the micrographs of the catalysts, apart from the main clusters, isolated metal atoms and groups of atoms (less than 1 nm in size) are observed, which are not observed in the TEM images.

Most attention was paid to the monolayer particles and their structure. For the monometallic W_{12}/Al_2O_3 catalyst, particles with a homogeneous structure are observed in all images. For MoW catalysts, difference in contrast of the atoms in the slabs are clearly observed. The intensity in HAADF images, for a given thickness and density and depending on the collection angles, is a function of the atomic number (Z-number), being approximately proportional to $Z^{1.7}$ [25], as a result of which W atoms (Z=74) appear brighter than Mo atoms (Z= 42) in HAADF images (**Fig 2.8**). This is confirmed by the intensity profiles obtained in a row of atoms, as illustrated for Mo_3W_9 sample in **Fig. 2.8**, where the ratio in intensities corresponds to the ratio of $Z^{1.7}$. We can thus conclude that, as previously observed for Mo_3W_9/Al_2O_3 [10], the use of mixed $SiMo_6W_6$ and $SiMo_9W_3$ HPAs promotes the formation of particles with a mixed structure after gas-phase sulfidation. In catalysts prepared from a mixture of two monometallic $SiMo_{12}$ and SiW_{12} HPAs, like for Mo_3+W_9 [10], a majority of monometallic particles is observed, together with very few mixed clusters.

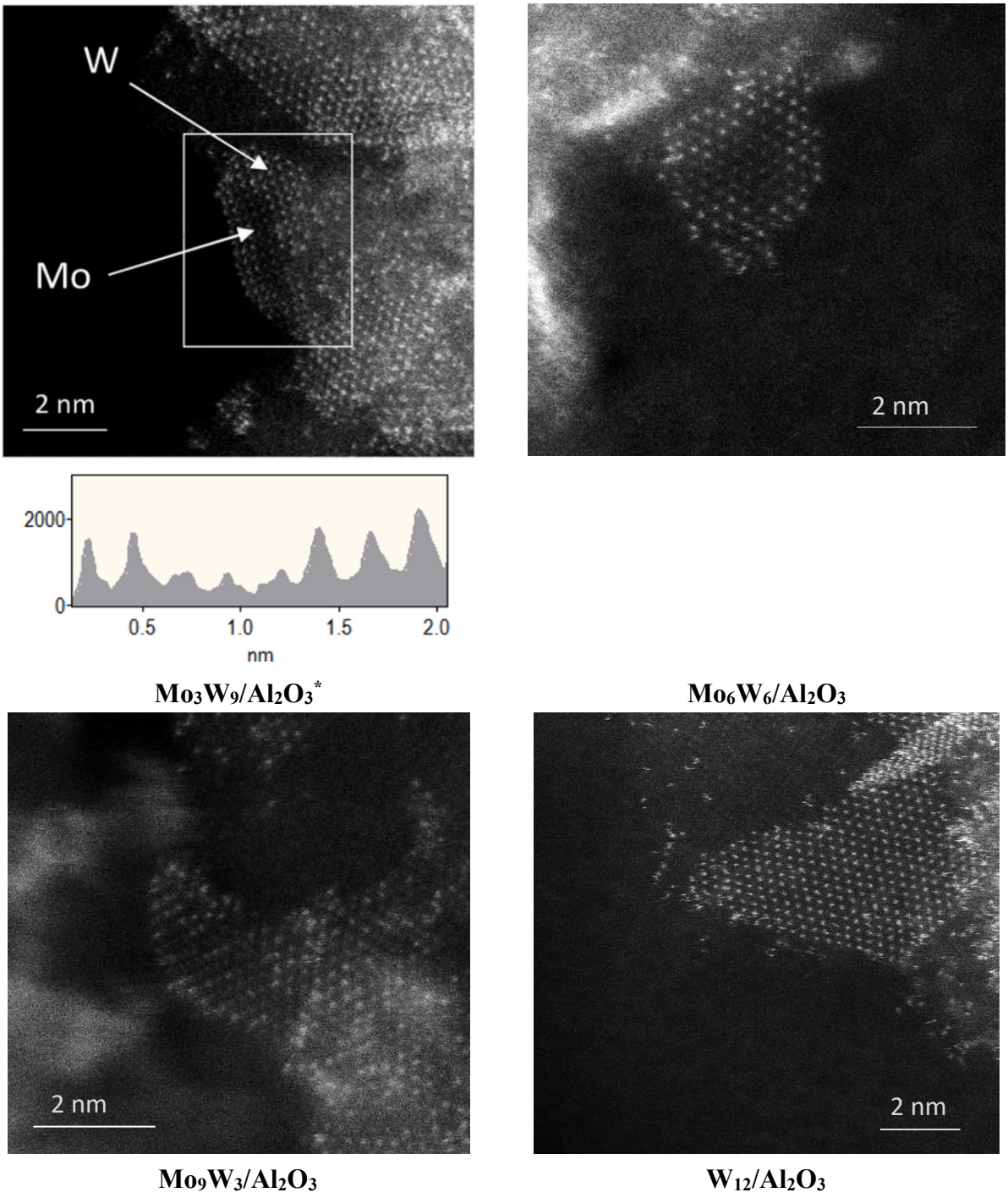

Fig. 2.8. HAADF images of sulfided MoW catalysts, with intensity profile corresponding to the row of atoms identified by the arrow on mixed Mo_3W_9/Al_2O_3. * adapted from [10].

Moreover, as HAADF allows discriminating Mo and W atoms, it is possible to visualize their relative positions inside the slabs. In the case of the Mo_6W_6/Al_2O_3 sample, as for the Mo_3W_9/Al_2O_3, mixed slabs are formed in which the molybdenum atoms are concentrated in a core, surrounded by tungsten atoms. The Mo_9W_3/Al_2O_3 sample was characterized by a disordered structure of Mo and W atoms inside the slabs, where the two-dimensional foils can be represented as MoS_2 particles with small inclusions of W atoms. Perhaps this can be explained by the different kinetics of sulfidation of Mo and W atoms and an excess of the former in the structure. According to the data obtained by

HAADF imaging, it can be concluded that mixed $MoWS_2$ particles are observed for all mixed MoW samples but that the distribution of the atoms depends on the ratio of molybdenum and tungsten in the structure. Therefore, when the content of Mo increases from 50 (in Mo_6W_6/Al_2O_3 catalyst) to 75 at % (in Mo_9W_3/Al_2O_3), a transition occurs from an ordered core-shell structure to a disordered structure in which tungsten atoms are randomly located.

2.4.3 X-ray photoelectron spectroscopy (XPS)

Information about the composition of sulfide particles on the surface of the synthesized catalysts was obtained in detail by XPS. The XPS spectra of Mo_nW_{12-n}/Al_2O_3 and Mo_n+W_{12-n}/Al_2O_3 were decomposed according to previous works [9, 10] using the appropriate oxide and sulfided references as supported monometallic catalysts (**Fig. 2.9**). The Mo3d spectra contain three doublets: 229.0 eV and 232.0 eV correspond to $Mo3d_{5/2}$ and $Mo3d_{3/2}$ of Mo^{4+} (MoS_2 species), doublet at about 230.0 and 233.5 eV is related to Mo^{5+} (MoO_xS_y species) and doublet at 232.5 and 235.7 eV is associated with Mo^{6+} oxide species.

Tungsten oxide sulfides at higher temperatures than molybdenum due to thermodynamics and lower reactivity [26]. For W analysis, as shown in **Fig 2.9,** $W5p_{3/2}$ and Mo4p ranges (non splitted level) overlap the W4f levels. The contributions of these peaks were excluded when calculating the true content of W4f fractions.

The spectral characteristics of $W5p_{3/2}$, $W4f_{5/2}$, $W4f_{7/2}$ are interdependent and simulated by doublets corresponding to $W4f_{5/2}$, $W4f_{7/2}$ core levels, using constraints in area, full width at half maximum (FWHM) and binding energies (BE). The W4f spectra contain three 4f doublets: the doublet with binding energies (BE) at 32.1 and 34.3 eV is associated to $W4f_{7/2}$ and $W4f_{5/2}$ of W^{4+} species of the WS_2 phase, the doublet with binding energies at 33.0 and 35.2 eV to W^{5+} species of a WS_xO_y oxysulfide species, and finally the doublet with binding energies at 36.0 and 37.9 eV is correlated with W^{6+} oxide species.

The results of the XPS decomposition for the metal fractions of molybdenum and tungsten species of the sulfided Mo_nW_{12-n}/Al_2O_3 and Mo_n+W_{12-n}/Al_2O_3 are reported in **Table 2.4**. In all bimetallic catalysts, the sulfidation degree of molybdenum was found higher than in the monometallic Mo_{12} sample: from 70% in Mo_{12} to higher than 80% in all bimetallic samples. Replacing a quarter of the Mo atoms with W made it possible to increase the sulfidation degree by more than 20 rel. % compared to Mo_{12}/Al_2O_3 catalyst. In parallel with this, tungsten sulfidation occurs, only 51% in W_{12}/Al_2O_3, which is associated with a stronger interaction with the support and is consistent with the literature data [27–29]. Increase in the molybdenum content contributed to an increase in the degree of sulfidation of both metals in mixed Mo_nW_{12-n}/Al_2O_3 catalysts, the highest values for both Mo (91%) and W (85%) being obtained for Mo_9W_3/Al_2O_3 catalyst.

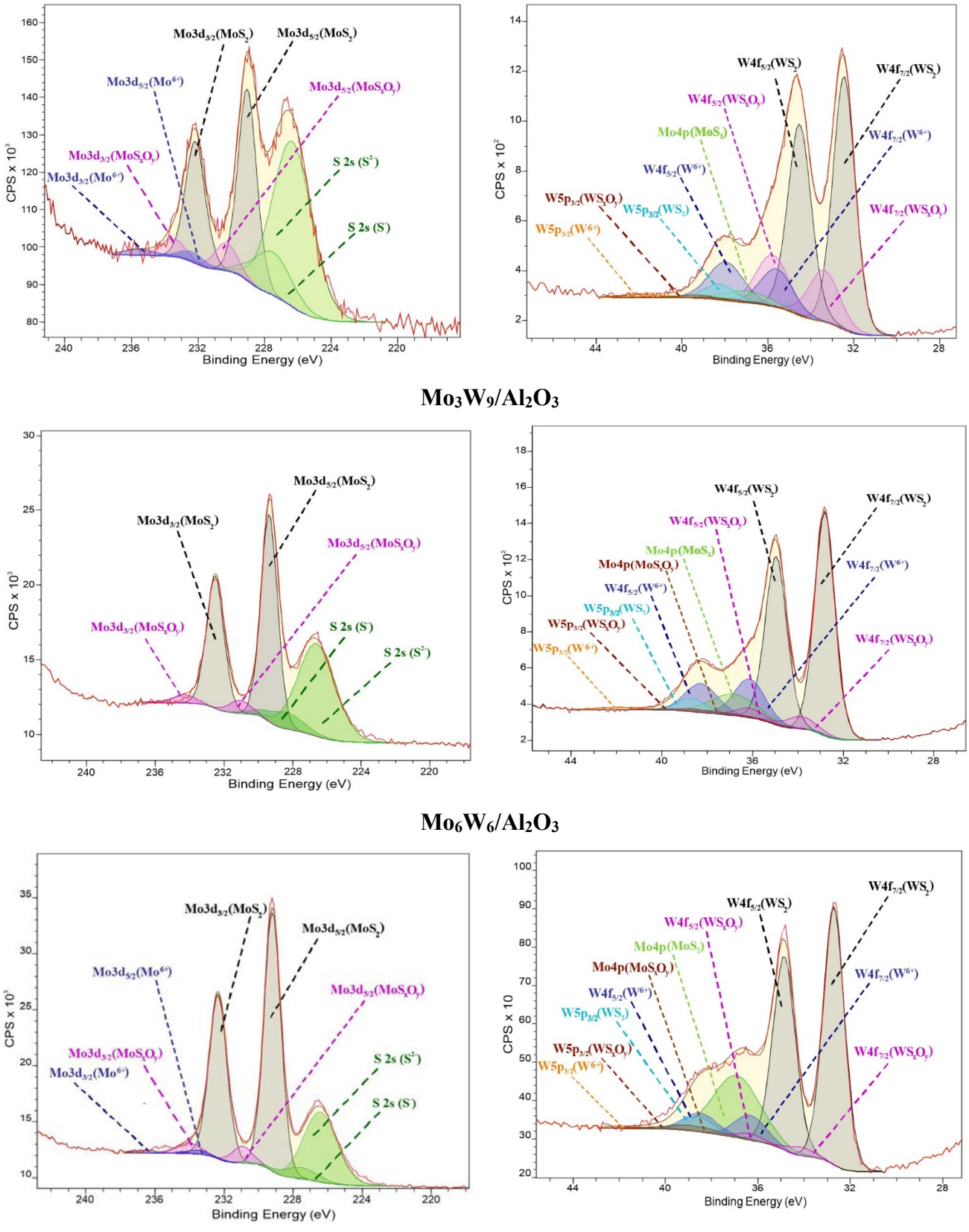

Fig. 2.9 XPS Mo 3d and W 4f spectra recorded for sulfided Mo_3W_9/Al_2O_3, Mo_6W_6/Al_2O_3 and Mo_9W_3/Al_2O_3 catalysts; in blue: $Mo(W)^{6+}$ oxide contributions; in pink: $Mo(W)S_xO_y$ contributions; in black: $Mo(W)S_2$ contributions: in green S contributions.

Table 2.4. Metal distribution for Mo and W species present at the surface of sulfided Mo(W) catalysts.

Catalyst	Mo percentage (rel. %)			W percentage (rel. %)			Number of edge sites (10^{20} at g^{-1})		
	MoS_2	MoS_xO_y	Mo^{6+}	WS_2	WS_xO_y	W^{6+}	Mo^{IV}_{edge}	W^{IV}_{edge}	$\sum Mo^{IV}_{edge} + W^{IV}_{edge}$
Mo_{12}/Al_2O_3*	70	15	15	-	-	-	0.88	-	0.88
Mo_9W_3/Al_2O_3	91	7	2	85	3	12	0.82	0.60	1.42
Mo_9+W_3/Al_2O_3	83	11	6	71	6	23	0.87	0.59	1.46
Mo_6W_6/Al_2O_3	91	7	1	76	5	19	0.61	0.80	1.40
Mo_6+W_6/Al_2O_3	81	16	3	62	23	23	0.63	0.80	1.43
Mo_3W_9/Al_2O_3*	81	14	5	64	18	18	0.23	0.94	1.17
Mo_3+W_9/Al_2O_3*	90	8	2	77	11	12	0.48	0.74	1.22
Mo_1W_{11}/Al_2O_3*	85	13	2	51	7	42	0.10	1.02	1.12
Mo_1+W_{11}/Al_2O_3*	89	2	9	57	8	35	0.11	0.98	1.09
W_{12}/Al_2O_3*	-	-	-	51	16	33	-	0.98	0.98

* - Adapted from [10]

It should also be noted that the sulfidation degree of Mo in mixed Mo_nW_{12-n}/Al_2O_3 catalysts was higher than in bimetallic Mo_n+W_{12-n}/Al_2O_3 samples prepared from mixture of HPAs. Using *in situ* time-resolved characterizations of the sulfidation by H_2S/H_2 of the catalysts by Quick-XAS associated with MCR-ALS chemometric method, differences were revealed in sulfidation pathways and formation of intermediates between monometallic and mixed bimetallic Keggin HPAs based catalysts [30]. Previously, the authors suggested that the sulfidation of Mo_3W_9/Al_2O_3 catalysts begins with the formation of MoS_2 nuclei, which contribute to the activation of H_2S, which allows increasing the sulfidation degree of WO_3 and raising the number of active sites [8] . According to XAS analysis, it was found that the proximity of metals in the $H_4[SiMo_3W_9O_{40}]$ has a significant effect and changes the sulfidation kinetics of both tungsten (lowering the sulfiding temperature and increasing sulfidation degree) and molybdenum (the formation of intermediate products occurs at a higher temperature in comparison with the monometallic Mo_{12}/Al_2O_3).

2.5 Influence of the Mo/(Mo+W) atomic ratio in the active phase on the catalytic properties

The catalytic activities of the sulfided Mo_nW_{12-n}/Al_2O_3 and Mo_n+W_{12-n}/Al_2O_3 catalysts in co-HDT of DBT and naphthalene are presented in **Table 2.5** and **Fig. 2.10**.

Table 2.5. Catalytic properties of MoW/Al_2O_3 catalysts in the hydrotreating of DBT and naphthalene.

Catalyst	Conversion (%)		Reaction rate constant ($\times 10^5$ mol h^{-1} g^{-1})		$S_{HYD/DDS}$
	DBT HDS	Naphthalene HYD	k_{HDS}	k_{HYD}	
Mo_{12}/Al_2O_3*	51.9	40.5	45	157	1.73
Mo_9W_3/Al_2O_3	59.2	55.2	55	244	2.83
Mo_9+W_3/Al_2O_3	44.3	39.6	36	153	2.51
Mo_6W_6/Al_2O_3	61.3	57.3	59	258	3.16
Mo_6+W_6/Al_2O_3	47.6	42.2	40	166	2.33
Mo_3W_9/Al_2O_3*	52.9	47.5	46	195	3.18
Mo_3+W_9/Al_2O_3*	32.1	27.3	24	97	1.76
W_{12}/Al_2O_3*	22.2	23.8	15	82	2.61

* - Adapted from [10]

The reactants conversions varied in a wide range, from 22.2 to 61.3% for HDS of DBT and from 23.8 to 57.3% for HYD of naphthalene over all prepared catalysts. The W_{12}/Al_2O_3 sample demonstrated the lowest activities in DBT HDS (22.2 %) and in naphthalene HYD (23.8 %). Increasing the molybdenum content up to Mo/(Mo+W) = 0.5, by replacing 1, 3 and 6 tungsten atoms by molybdenum ones, led to an increase in activity both in HDS and HYD, whatever the precursor

used (mixed HPAs or mixture of monometallic HPAs). A decrease is then observed for the catalysts with the highest amount of Mo (Mo/(Mo+W) = 0.75). The optimum values are thus obtained for an equal quantity of Mo and W in the active phase (Mo/(Mo+W) = 0.5). A similar result was reported for CoMoW/SBA-15 catalysts prepared from AHT, AMT and cobalt nitrate hexahydrate by Huirache-Acuña et al [31], where the maximum activity in DBT HDS was achieved with a molar ratio of Mo/(Mo+W) equal to 0.6, which almost corresponds to the result obtained in this work. Wang et al. [32], using the density functional theory (DFT) calculations, found that the 50% substitution of Mo by W in unsupported mixed $MoWS_2$ catalysts led to the best hydrogen activation because of the reduction of H adsorption free energy and facilitation of charge transfer.

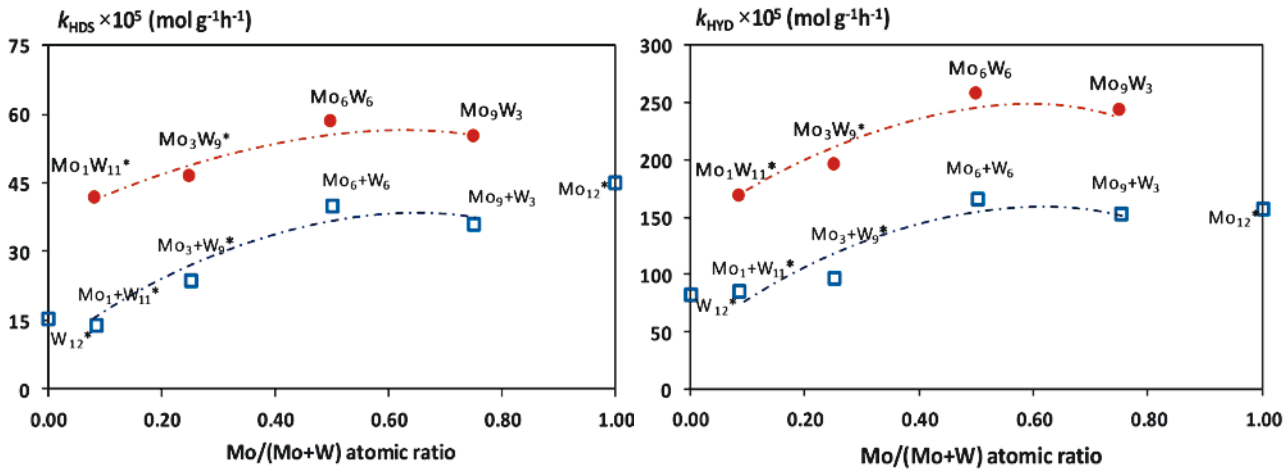

(a) **(b)**

Fig. 2.10. Dependence of reaction rate constants in DBT HDS (a) and naphthalene HYD (b) on Mo/(Mo+W) atomic in MoW/Al_2O_3 catalysts (circles correspond to mixed MoW catalysts prepared from mixed $SiMo_nW_{12-n}$HPA; squares are mixed Mo+W catalysts prepared from a mixture of $SiMo_{12}$ and SiW_{12}HPA). * adapted from [10]

Catalytic properties both in the HDS and HYD reactions were found higher for the catalysts synthesized from mixed $SiMo_nW_{12-n}$ HPAs than those of the catalysts obtained from the mixture of the monometallic HPAs, and this for all studied Mo/W ratios.

The number of edge sites has been calculated taking into account the metal sulfidation determined by XPS as well as the dispersion of the active phase obtained by TEM (**Table 2.4**).

Relative concentrations of each species Mo and W (molybdenum (tungsten) oxide $Mo(W)^{6+}$, oxysulfide $Mo(W)S_xO_y$ and $Mo(W)S_2$) were determined for every sulfided catalyst. The relative amount of Mo(W)S phase was determined by the equation:

$$[\mathrm{Mo(W)S}]\ (\%) = \frac{A_{\mathrm{Mo(W)S}}}{A_{\mathrm{Mo(W)S}} + A_{\mathrm{Mo(W)S}_x O_y} + A_{\mathrm{Mo(W)}^{6+}}} \times 100, \qquad (1)$$

where A_X represents the peak area of the species x.

The effective content of Mo(W)S phase was determined using the equation:

$$C_{\mathrm{Mo(W)S}} = [\mathrm{Mo(W)S}] \times C(Mo(W))_T \quad , \tag{2}$$

where $C(Mo(W))_T$ represents the effective concentration of Mo(W) determined by XPS (at.%).

The number of edge sites of the active phase was calculated as follows:

$$\mathrm{MoWS_{egde}} = W \cdot \left(\frac{C_{\mathrm{WS_2}}}{Ar_W} + \frac{C_{\mathrm{MoS_2}}}{Ar_{Mo}}\right) \cdot D \cdot 3600 \tag{3}$$

where W is the weight of the catalyst (g); $C_{\mathrm{WS_2}}$ and $C_{\mathrm{MoS_2}}$ are the effective content of W and Mo in WS_2 and MoS_2 states, respectively (wt. %); D is the dispersion of $Mo_nW_{12-n}S_2$ species; Ar_W and Ar_{Mo} are the standard atomic weight of tungsten (183.9 g/mol) and molybdenum (95.9 g/mol), respectively.

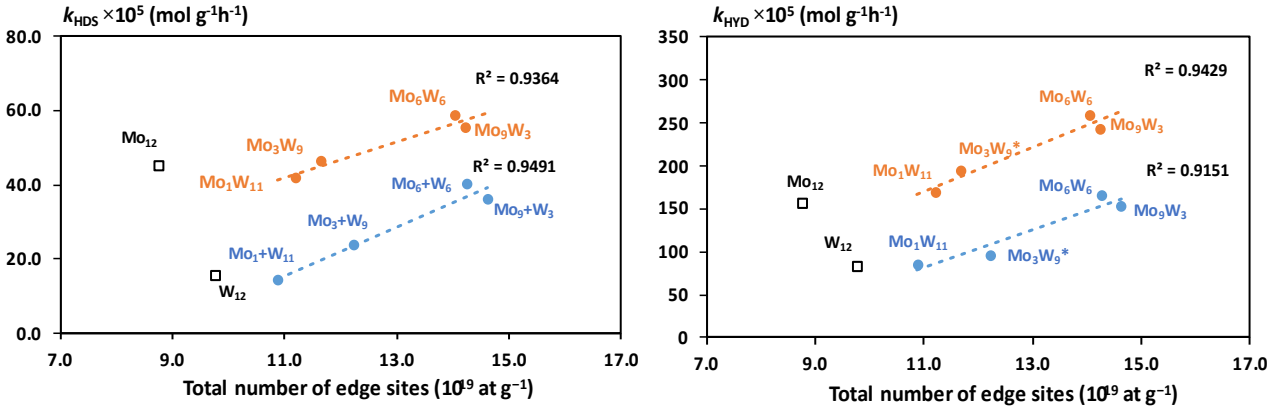

(a) **(b)**

Fig. 2.11. Dependence of DBT HDS (a) and naphthalene HYD (b) rate constants on total number of edge sites

This allows to estimate in a global way the number of active centers without taking into account their nature. Since the values of dispersion of the active phase for all catalysts were approximately equal, the key effect on the number of edge centers was exerted only by the sulfidation degree of metals. An increase in the molybdenum content led to an increase in the content of edge sites for both types of MoW catalysts due to the higher degree of sulfidation of both metals compared to monometallic ones (**Table 2.4**). However, the number of edge sites is similar for MoW catalysts and their Mo+W counterparts for each Mo/(Mo+W) ratio, indicating that the difference in performance between the two series is not related to a different number of active sites but could be due to a difference in the quality of the active sites. As confirmed by HAADF analysis and previously by XAS analysis on Mo_3W_9 catalyst, mixed $MoWS_2$ slabs are observed in samples that have been synthesized from mixed HPAs [30], which was attributed to the close interaction of both metals in the mixed oxide precursor. The presence of this mixed structure in MoW catalysts resulted in higher activity both in HDS and HYD compared to catalysts Mo+W, where mainly monometallic slabs were observed (with an equivalent number of active sites). The structure of the mixed slabs seems to also

have an influence on the catalytic performance: if a core-shell structure with Mo atoms surrounded by W ones is observed on Mo_3W_9 and on Mo_6W_6 catalyst, a more random structure prevails on Mo_9W_3, which results in a decrease in catalytic activity of Mo_9W_3/Al_2O_3.catalyst. The significant increase in conversion for the Mo_6W_6/Al_2O_3 sample could then be explained by the formation of optimal structure of mixed slabs with a high concentration of edge sites. (**Fig 2.11**).

2.6 Conclusion

A new method of single-stage synthesis of mixed Keggin HPAs with a molar Mo/(Mo + W) ratio varying from 0.5 to 0.75 has been proposed. The structure of the obtained compounds was confirmed by Raman, IR and single-XRD methods. Both $H_4[SiMo_6W_6O_{40}]$ $31H_2O$ and $H_4[SiMo_9W_3O_{40}]$ $31H_2O$ HPAs are isomorph and crystallize in the tetragonal space group P-421c. Contrariwise to $H_4[SiMo_3W_9O_{40}]\cdot 10H_2O$ and $H_4[SiMo_1W_{11}O_{40}]\cdot 10H_2O$ obtained from lacunar compounds in which the molybdenum and tungsten atoms had a fixed position, the newly synthetized $H_4[SiMo_6W_6O_{40}]\cdot 36H_2O$ and $H_4[SiMo_9W_3O_{40}]\cdot 36H_2O$ compounds present a disordered arrangement of molybdenum and tungsten atoms in the Keggin structure.

Sulfided MoW on alumina catalysts were prepared from these mixed HPAs, together with reference catalysts obtained from a mixture of monometallic HPAs in the same ratio than in the mixed ones.

HAADF analysis evidenced that the mixed $MoWS_2$ phase with a core of molybdenum surrounded by tungsten atoms, already observed on Mo_3W_9 catalyst, was retained on Mo_6W_6 catalyst. A mixed phase was also present when increasing the molybdenum content in Mo_9W_3 catalyst, however slabs with a random distribution of atoms were formed for this sample (**Fig 2.12**). This mixed sulfide phase is not present or in very small quantities in the reference catalysts.

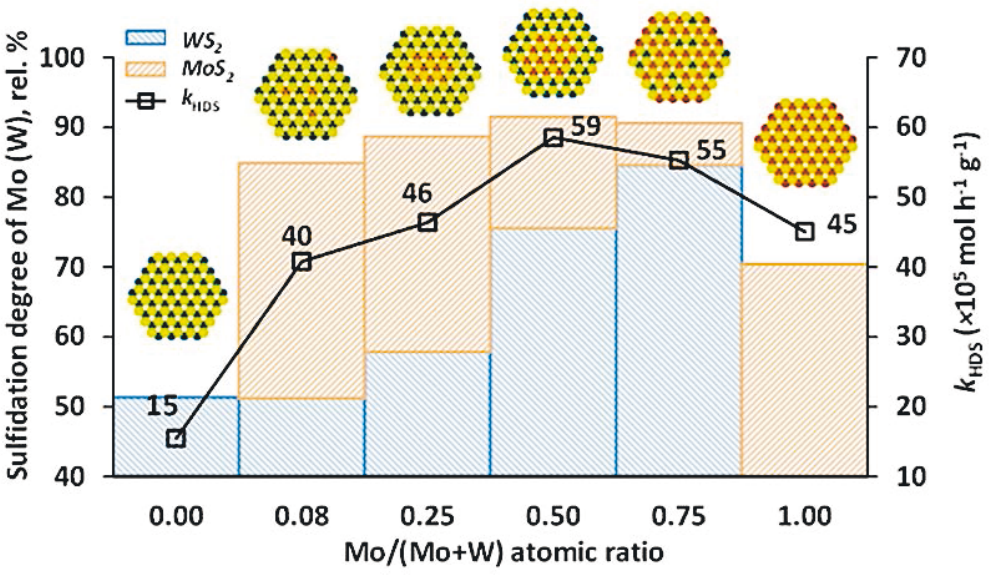

Fig. 2.12. Sulfidation degree of Mo(W) in mixed MoW/Al_2O_3 catalysts, their HDS activity and Mo/(Mo+W) atomic ratio. *The active phase models are based on HAADF.*

XPS data showed that the sulfidation degree in bimetallic catalysts is higher than in monometallic ones. This effect is enhanced by the use of mixed HPAs, which is explained by the closer proximity of metal atoms at the molecular level in the precursor. The simultaneous presence of Mo and W leads to a modification of the metal sulfidation kinetics, according to previously obtained XAS results.

The results of catalytic tests showed that Mo_6W_6 and Mo_9W_3 alumina supported samples were more active in DBT HDS and naphthalene HYD reactions than their Mo+W references prepared using their monometallic counterparts. Similar quantity of edge sites was calculated for both Mo_nW_{12-n} and Mo_n+W_{12-n} catalysts with the same Mo/Mo+W ratio, indicating that the difference in performance is more related to the presence of the mixed $MoWS_2$ active phase in MoW catalysts. The maximum conversion of reagents in the studied reactions was achieved on Mo_6W_6/Al_2O_3 due to the formation of the optimal structure of mixed slabs rich in edge sites.

References

[1] G. An, C. Liu, C. Xiong, and C. Lu, "A study on the morphology of unsupported Ni-Mo-W sulfide hydrotreating catalysts through high-resolution transmission electron microscopy," *Pet. Sci. Technol.*, vol. 30, no. 15, pp. 1599–1608, 2012, doi: 10.1080/10916466.2010.509065.

[2] J. A. Mendoza-Nieto, O. Vera-Vallejo, L. Escobar-Alarcón, D. A. Solís-Casados, and T. Klimova, "Development of new trimetallic NiMoW catalysts supported on SBA-15 for deep hydrodesulfurization," *Fuel*, vol. 110, pp. 268–277, 2013, doi: 10.1016/j.fuel.2012.07.057.

[3] R. Huirache-Acuña *et al.*, "Comparison of the morphology and HDS activity of ternary Ni(Co)-Mo-W catalysts supported on Al-HMS and Al-SBA-16 substrates," *Appl. Catal. B Environ.*, vol. 125, pp. 473–485, 2012, doi: 10.1016/j.apcatb.2012.05.034.

[4] P. Nikulshin, A. Mozhaev, C. Lancelot, P. Blanchard, E. Payen, and C. Lamonier, "Catalyseurs d'hydrotraitement à base de sulfures de métaux de transition préparés à partir des hétéropolyanions d'Anderson et du dimère Co_2Mo_{10}. Une revue," *Comptes Rendus Chim.*, vol. 19, no. 10, pp. 1276–1285, 2016, doi: 10.1016/j.crci.2015.10.006.

[5] R. Shafi, M. R. H. Siddiqui, G. J. Hutchings, E. G. Derouane, and I. V Kozhevnikov, "Heteropoly acid precursor to a catalyst for dibenzothiophene hydrodesulfurization," *Appl. Catal. A Gen.*, vol. 204, no. 2, pp. 251–256, 2000, doi: 10.1016/S0926-860X(00)00530-5.

[6] P. Blanchard, C. Lamonier, A. Griboval, and E. Payen, "New insight in the preparation of alumina supported hydrotreatment oxidic precursors: A molecular approach," *Appl. Catal. A Gen.*, vol. 322, pp. 33–45, 2007, doi: 10.1016/j.apcata.2007.01.018.

[7] C. I. Cabello, F. M. Cabrerizo, A. Alvarez, and H. J. Thomas, "Decamolybdodicobaltate(III) heteropolyanion: Structural, spectroscopical, thermal and hydrotreating catalytic properties," *J. Mol. Catal. A Chem.*, vol. 186, no. 1–2, pp. 89–100, 2002, doi: 10.1016/S1381-1169(02)00043-2.

[8] M. Nikulshina *et al.*, "MoW synergetic effect supported by HAADF for alumina based catalysts prepared from mixed $SiMo_nW_{12-n}$ heteropolyacids," *Appl. Catal. B Environ.*, vol. 224, pp. 951–959, 2018, doi: 10.1016/j.apcatb.2017.11.049.

[9] M. S. Nikulshina *et al.*, "Molecular approach to prepare mixed MoW alumina supported hydrotreatment catalysts using $H_4SiMo_nW_{12-n}O_{40}$ heteropolyacids," *Catal. Sci. Technol.*, vol. 8, no. 21, pp. 5557–5572, 2018, doi: 10.1039/c8cy00672e.

[10] M. Nikulshina *et al.*, "Enhancing the hydrodesulfurization of 4,6-dimethyldibenzothiophene through the use of mixed $MoWS_2$ phase evidenced by HAADF," *Catal. Today*, vol. 329, , pp. 24–34, 2019, doi: 10.1016/j.cattod.2018.11.051.

[11] C. Sanchez, J. Livage, J. P. Launay, M. Fournier, and Y. Jeannin, "Electron Delocalization in Mixed-Valence Molybdenum Polyanions," *J. Am. Chem. Soc.*, vol. 104, no. 11, pp. 3194–3202, 1982, doi: 10.1021/ja00375a044.

[12] C. Rocchiccioli-Deltcheff, M. Fournier, R. Franck, and R. Thouvenot, "Vibrational Investigations of Polyoxometalates. 2. Evidence for Anion-Anion Interactions in Molybdenum(VI) and Tungsten(VI) Compounds Related to the Keggin Structure," *Inorg. Chem.*, vol. 22, no. 2, pp. 207–216, 1983, doi: 10.1021/ic00144a006.

[13] M. T. Pope, "Heteropoly and isopoly oxometalates," *Angew. Chemie*, vol. 96, no. 9, p. 730, 1984.

[14] A. Tézé and G. Hervé, "Formation et isomerisation des undeca et dodeca tungstosilicates et germanates isomeres," *J. Inorg. Nucl. Chem.*, vol. 39, no. 6, pp. 999–1002, 1977, doi: 10.1016/0022-1902(77)80251-0.

[15] G. Hervé and A. Tézé, "Study of α-and β-Enneatungstosilicates and -germanates," *Inorganic Chemistry*, vol. 16, no. 8. American Chemical Society, pp. 2115–2117, 1977, doi: 10.1021/ic50174a060.

[16] H. T. Brown and J. C. W. Frazer, "Mixed Heteropoly Acid Catalysts for the Vapor Phase Air Oxidation of Naphthalene," *J. Am. Chem. Soc.*, vol. 64, no. 12, pp. 2917–2920, 1942, doi: 10.1021/ja01264a056.

[17] C. Rocchiccioli-Deltcheff, R. Thouvenot, and R. Franck, "Spectres i.r. et Raman d'hétéropolyanions α - $XM_{12}O40_n^-$ de structure de type Keggin (X = B^{III}, Si^{IV}, Ge^{IV}, P^V, As^V et M = W^{VI} et Mo^{VI})," *Spectrochim. Acta Part A Mol. Spectrosc.*, vol. 32, no. 3, pp. 587–597, 1976, doi: 10.1016/0584-8539(76)80121-3.

[18] A. J. Bridgeman, "Density functional study of the vibrational frequencies of α-Keggin heteropolyanions," *Chem. Phys.*, vol. 287, no. 1–2, pp. 55–69, 2003, doi: 10.1016/S0301-0104(02)00978-3.

[19] A. J. Bridgeman, "Computational study of the vibrational spectra of α- and β-Keggin," *Chem. - A Eur. J.*, vol. 10, no. 12, pp. 2935–2941, 2004, doi: 10.1002/chem.200305781.

[20] A. Ishii and T. Ozeki, "Crystal structure of a mixed-metal β-Keggin molybdotungstosilicate, K4[A-β-SiMo3W9O40] ·9H2O," *Polyhedron*, vol. 24, no. 15, pp. 1949–1952, 2005, doi: 10.1016/j.poly.2005.06.015.

[21] M. Muñoz *et al.*, "Synthesis and spectroscopic ^{27}Al NMR and Raman characterization of new materials based on the assembly of $[AlO_4Al_{12}(OH)\ 24(H_2O)_{12}]^{7+}$ isopolycation and Co-Cr and $[AlMo_6O_{24}H_6]^{3-}$ Anderson heteropolyanions," *J. Mol. Struct.*, vol. 841, no. 1–3, pp. 96–103, 2007, doi: 10.1016/j.molstruc.2006.11.067.

[22] L. Catita, A. A. Quoineaud, D. Espinat, C. Pichon, and O. Delpoux, "Application of Magnetic Resonance Imaging and Raman Imaging to study the impact of phosphorus in impregnation of hydrotreatment catalysts," *Appl. Catal. A Gen.*, vol. 547, pp. 164–175, 2017, doi: 10.1016/j.apcata.2017.08.039.

[23] L. Le Bîhan, P. Blanchard, M. Fournier, G. Blot, and E. Payen, "Raman spectroscopic evidence for the existence of 6-molybdoalonminate entities on an Mo/Al_2O_3 oxidic precursor," *J. Chem. Soc. - Faraday Trans.*, vol. 94, no. 7, pp. 937–940, 1998, doi: 10.1039/a706359h.

[24] X. Carrier, J. F. Lambert, and M. Che, "Ligand-promoted alumina dissolution in the preparation of $MoO(x)/\gamma\text{-}Al_2O_3$ catalysts: Evidence for the formation and deposition of an Anderson-type alumino heteropolymolybdate," *J. Am. Chem. Soc.*, vol. 119, no. 42, pp. 10137–10146, 1997, doi: 10.1021/ja971981r.

[25] P. Raybaud and H. Toulhoat, *Catalysis by Transition Metal Sulphides - From Molecular Theory to Industrial Application*. Paris: Editions Technip, 2013.

[26] P. Hartel, H. Rose, and C. Dinges, "Conditions and reasons for incoherent imaging in STEM," *Ultramicroscopy*, vol. 63, no. 2, pp. 93–114, 1996, doi: 10.1016/0304-3991(96)00020-4.

[27] P. P. Minaev, P. A. Nikulshin, M. S. Kulikova, A. A. Pimerzin, and V. M. Kogan, "$NiWS/Al_2O_3$ hydrotreating catalysts prepared with 12-tungstophosphoric heteropolyacid and nickel citrate: Effect of Ni/W ratio," *Appl. Catal. A Gen.*, vol. 505, pp. 456–466, 2015, doi: 10.1016/j.apcata.2015.05.012.

[28] R. Thomas, E. M. van Oers, V. H. J. de Beer, J. Medema, and J. A. Moulijn, "Characterization of γ-alumina-supported Molybdenum oxide and tungsten oxide; reducibility of the oxidic state versus hydrodesulfurization activity of the sulfided state," *J. Catal.*, vol. 76, no. 2, pp. 241–253, Aug. 1982, doi: 10.1016/0021-9517(82)90255-X.

[29] H. Topsøe, B. S. Clausen, and F. E. Massoth, "Hydrotreating Catalysis," *Catalysis*, pp. 1–269, 1996, doi: 10.1007/978-3-642-61040-0_1.

[30] M. Nikulshina *et al.*, "Genesis of active phase in MoW/Al_2O_3 hydrotreating catalysts monitored by HAADF and in situ QEXAFS combined to MCR-ALS analysis," *Appl. Catal. B Environ.*, vol. 269, no. February, p. 118766, 2020, doi: 10.1016/j.apcatb.2020.118766.

[31] R. Huirache-Acuña, B. Pawelec, E. M. Rivera-Muñoz, R. Guil-López, and J. L. G. Fierro, "Characterization and HDS activity of sulfided Co-Mo-W/SBA-16 catalysts: Effects of P addition and Mo/(Mo+W) ratio," *Fuel*, vol. 198, pp. 145–158, 2017, doi: 10.1016/j.fuel.2016.09.042.

[32] H. Wang *et al.*, "Optimizing MoS_2 Edges by Alloying Isovalent W for Robust Hydrogen Evolution Activity," *ACS Catal.*, vol. 8, no. 10, pp. 9529–9536, 2018, doi: 10.1021/acscatal.8b02162.

Chapter 3

Ni-promoted MoWS hydrotreating catalysts supported on alumina

3.1 Introduction

Previous results have shown that the use of mixed $SiMo_nW_{12-n}$ HPAs makes it possible to increase the activity of MoW/Al_2O_3 catalysts through the formation of a mixed $MoWS_2$ phase (chapter 2). However, the industry mainly uses promoted systems for the hydrotreating of real feedstock. Based on the literature review [1–3], it was shown that the promotion of bimetallic MoW catalysts by cobalt atoms is less effective than the promotion by nickel due to the higher binding energy metal-sulfur. Therefore, this chapter is devoted to the study of Ni promoted MoW catalysts supported on alumina, to investigate if the mixed phase observed on MoW catalysts is maintained in Ni promoted solids and could contribute to improved catalytic performance. The effect of Mo/W ratio between 1/11 and 9/3 on activity will also be considered.

The $NiMo_nW_{12-n}/Al_2O_3$ samples were tested in model reactions (HDS, HYD and HDN), as well as in the hydrotreating of straight-run gas oil (SRGO) of West Siberian oil with boiling range 180-360°C, to evaluate the efficiency of catalysts on real feedstock. The inhibitory effect of nitrogen-containing compounds on a model mixture (DBT + naphthalene + quinolone) and real feed was also investigated. Prior analysis and catalytic evaluations, all catalysts were sulfided at hydrogen pressure by a mixture of dimethyl disulfide (DMDS) (6 wt. % of sulfur) in toluene. The catalysts were fully characterized by transmission electron microscopy (TEM) and X-ray photoelectron spectroscopy (XPS). For a more detailed study of the composition and structure of the active phase of the Ni-promoted systems, high angle annular dark field imaging (HAADF) and Quick X-ray absorption spectroscopy (XAS) were also used on selected systems.

All the obtained results were presented in an article published in the Journal of Catalysis (DOI: 10.1016/j.jcat.2021.02.019).

3.2 Synthesis of NiMo(W)/Al_2O_3 catalysts

Catalysts with fixed surface density of metals *d*(Mo+W) equal to 4 at nm^{-2} and Ni/(Mo+W) ratio equal to 0.5 were synthesized by simultaneous impregnation of alumina [γ-Al_2O_3, specific area: 240 $m^2\ g^{-1}$, pore volume: 0.9 mL g^{-1}] *via* the wetness impregnation method using aqueous solution of HPAs, citric acid (CA) and nickel carbonate (CA/Ni molar ratio equal to 1:1). Four trimetallic catalysts were prepared using mixed HPAs (hereafter $NiMo_nW_{12-n}/Al_2O_3$, n = 1, 3, 6 and 9). Trimetallic reference samples with a Mo/W ratio corresponding to the composition of the mixed $SiMo_nW_{12-n}$ HPAs were synthesized using a mixture of monometallic Mo and W HPAs, and will be denoted $Ni(Mo_n+W_{12-n})/Al_2O_3$. The bimetallic catalysts based on monometallic $H_4[SiMo_{12}O_{40}]$ and $H_4[SiW_{12}O_{40}]$ HPAs were prepared for comparison and denoted as $NiMo_{12}/Al_2O_3$ and NiW_{12}/Al_2O_3, respectively. After maturation, the oxidic catalysts were dried at 60°C (4 h), 80°C (2 h) and 100°C (4 h) in air atmosphere without further calcination. The metal compositions in the solids were obtained using an EDX800HS Shimadzu X-ray fluorescence analyzer and are given in **Table 3.1**.

Table 3.1. Composition of the dried solids and textural characteristics of sulfided NiMo(W)/Al_2O_3 catalysts.

Catalyst	Content (wt. %)			Textural characteristics		
	Mo	W	Ni	S_{BET} ($m^2\ g^{-1}$)	V_p ($cm^3\ g^{-1}$)	*D* (nm)
NiW_{12}	-	20.8	3.3	240	0.58	8.4
$NiMo_1W_{11}$	0.9	19.0	3.4	202	0.47	8.4
$NiMo_3W_9$	2.8	15.9	3.4	233	0.49	8.4
$NiMo_6W_6$	5.5	10.5	3.4	205	0.48	8.2
$NiMo_9W_3$	8.4	8.7	3.5	225	0.48	8.4
$Ni(Mo_1+W_{11})$	0.9	19.0	3.4	230	0.51	8.4
$Ni(Mo_3+W_9)$	2.8	15.9	3.4	210	0.48	8.4
$Ni(Mo_6+W_6)$	5.5	10.5	3.4	216	0.50	8.4
$Ni(Mo_9+W_3)$	8.4	8.7	3.5	233	0.53	8.6
$NiMo_{12}$	12.0	-	3.7	236	0.42	8.4

3.3 Characterization of sulfided NiMo(W)/Al_2O_3 catalysts

For further investigation, all catalysts were sulfided with the same protocol than prior the catalytic test, at 3.0 MPa of hydrogen, 2 h^{-1} LHSV and a 300 NL L^{-1} volume ratio of hydrogen to feed by a mixture of dimethyl disulfide (DMDS) with 6 wt. % of sulfur in toluene at 240°C for 10 h and at 340°C for 8 h. For characterization of the active phase, sulfided catalysts were unloaded from the reactor for analysis in a glove box in an inert gas atmosphere (argon). The samples were transferred to glass vials with n-heptane to avoid reoxidation. The textural properties of the liquid

phase sulfided samples are summarized in **Table 3.1**. All catalysts have close textural characteristics. The surface area varied slightly from 202 to 240 m^2g^{-1} and the average pore volume was about 0.5 cm^3g^{-1}. All catalysts present an average pore size around 8.4 nm.

3.3.1 Transmission electron microscopy (TEM)

Liquid sulfided NiMo(W)/Al_2O_3 catalysts were characterized by HRTEM in order to obtain information about the global dispersion of the active phase particles, without possible discrimination between Mo and W containing particles. Typical micrographs are presented in **Fig. 3.1** and the average values of stacking degree and slab length of active phase particles in **Table 3.2**. For all catalysts, the average length and stacking varied from 3.4 to 4.1 nm and from 1.4 to 2.1, respectively. $NiMo_{12}/Al_2O_3$ had the slabs with the shortest length ~3.4 nm among all studied catalysts and an average stacking number of 1.6, corresponding to high dispersion of the active phase (0.34). NiW_{12}/Al_2O_3 catalyst consisted of slabs with an average length ~ 3.9 nm and stacking number ~ 2.1.

The Mo/(Mo+W) atomic ratio had almost no effect on the geometric characteristics of the active phase. By comparison with the active phase morphology of unpromoted catalysts, promotion of Mo(W)S_2 phase by Ni is reported to decrease the average slab length due to the decorating action of the Ni atoms, which fixed on the edges of Mo(W)S_2 during the formation of the disulfide slabs hindering their further growth [4–6]. However, in our case, the non-promoted were sulfided in gas phase, preventing direct comparison.

Table 3.2. Morphological characteristics of the NiMo(W)S active phase species.

Catalyst	Average length $\bar{L}$ (nm)	Average stacking number $\bar{N}$	Dispersion of NiMo(W)S particles D
NiW_{12}	3.9	2.1	0.30
$NiMo_1W_{11}$	3.9	2.1	0.30
$NiMo_3W_9$	3.6	1.8	0.32
$NiMo_6W_6$	3.7	2.0	0.32
$NiMo_9W_3$	3.6	1.9	0.32
$Ni(Mo_1+W_{11})$	3.7	1.9	0.32
$Ni(Mo_3+W_9)$	3.6	1.4	0.32
$Ni(Mo_6+W_6)$	4.1	1.9	0.29
$Ni(Mo_9+W_3)$	3.8	1.7	0.31
$NiMo_{12}$	3.4	1.6	0.34

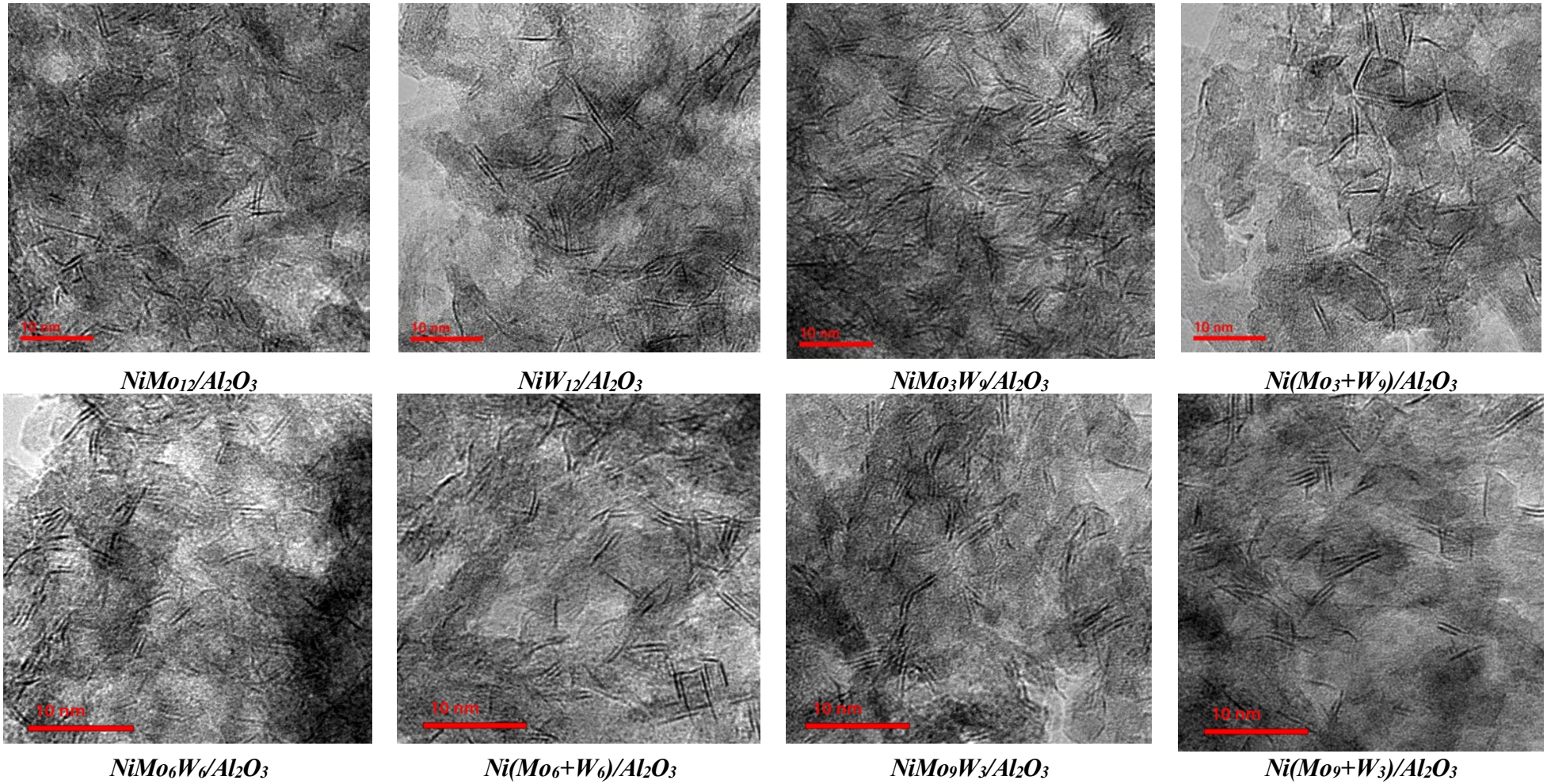

Fig. 3.1 HRTEM micrographs of sulfided NiMo(W)/Al_2O_3 catalysts

3.3.2 X-ray photoelectron spectroscopy (XPS)

The species formed after liquid phase sulfidation on the surface of the synthesized catalysts have been analyzed by XPS and spectra of NiMo(W)/Al_2O_3 samples were decomposed in CasaXPS. Typical spectra of some samples are shown in **Fig. 3.2-3.4** as an example.

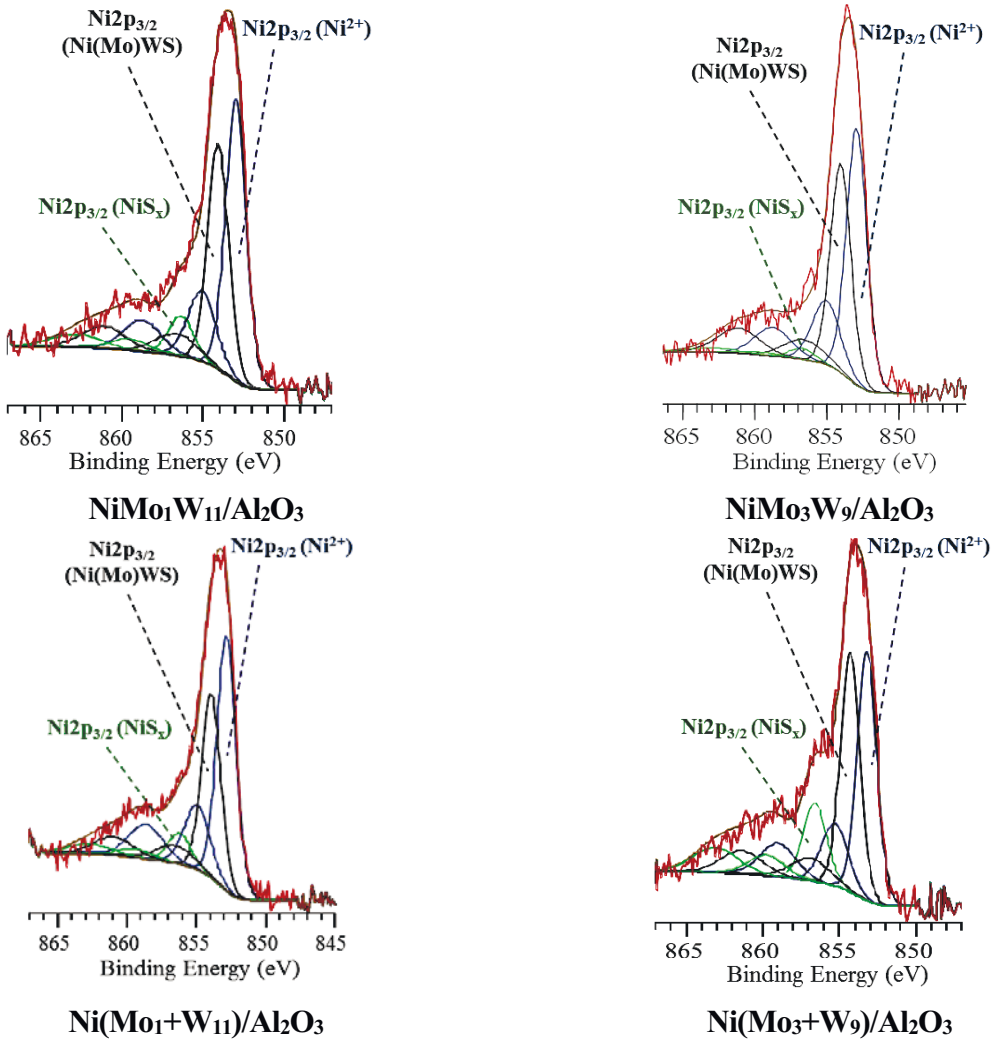

Fig. 3.2 Decomposition of XPS of the Ni2p spectra recorded for the NiMo(W)/Al_2O_3 catalysts; in blue: Ni^{2+}oxide contributions; in green: NiS contributions; in black: Ni(Mo)WS phase contributions.

As already reported for unpromoted catalysts, on the Mo3d spectra, there are three doublets corresponding to Mo^{4+} (MoS_2 species) at 229.0 eV and 232.0 eV, the doublet with binding energies at 230.0 and 233.5 eV is related to oxysulfide species and the signals at 232.5 and 235.7 eV is correlated to Mo^{6+} (oxide species). The W 4f spectra contain three W 4f doublets: the doublet with binding energies at 32.5 and 34.8 eV is associated to W^{4+} species (WS_2 phase), the doublet with binding energies at 33.4 and 35.5 eV to W^{5+} (oxysulfide species), and finally the doublet with binding energies at 36.21 and 38.2 eV to W^{6+} (oxide species). Concerning Ni, the spectral region of Ni2p3/2 contains three peaks with their respective satellites. The peak at a BE of 853.7 eV is related

to Ni(Mo)WS phase. The signals at 852.9 eV and 856.5 eV correspond to the NiS species and Ni^{2+} in an oxidic environment, respectively [7 – 9]. The decomposition of the XPS spectra revealed the relative amounts of nickel, molybdenum and tungsten species present on the surface of the sulfided catalysts, summarized in **Table 3.3**.

The sulfidation degree of Mo, expressed as the percentage of MoS_2, varied from 60 to 74% for all catalysts and almost did not depend on the Mo/(Mo+W) atomic ratio. In mixed HPA based samples, as noted for unpromoted catalysts, Mo and W sulfidation degree appears slightly higher than in the corresponding reference samples, the difference being more significant for W (between 17 and 25%) than for Mo (below 15%). This difference in sulfidation of metals in MoW samples was explained for non-promoted solids by the difference in the sulfidation steps for Mo and W in MoW and Mo+W samples, which could affect the final sulfidation degree of both metals [10, 11]. Shan et al. [12] also prepared $NiMoW/Al_2O_3$ catalysts and observed high sulfidation of metals. They claimed that it was due to the close interaction of Mo and W provided by the hydrothermal deposition method and its ability to generate highly dispersed W/Mo/Ni oxide species easier to reduce and to sulfide. The authors also noted in their work that the precursor has a direct effect on the interaction of metals.

In the trimetallic catalysts, the fraction of Ni species involved in NiMo(W)S active phase increased from 37% to 42 % in $NiMo_1W_{11}$ and $NiMo_3W_9$, respectively and then remains almost constant when increasing the Mo content. For Ni(Mo+W), the NiMoWS phase percentage remains between 35 and 39%. The values are always over that obtained in the NiW sample.

Except for the $NiMo_{12}$ sample, the main species is always NiS (about or more 43% of the Ni relative percentage) together with 5-20% of Ni in oxidic environment. That means that more than 80 % of Ni is sulfided, which may be due to the addition of citric acid introduced in the impregnating solution for the preparation of the oxidic precursors. Citric acid chelates the Ni ions, to improve their dispersion of Ni species on the support, to decrease the interaction of the Ni ions with the support and thus to improve the sulfidation of Ni [6]. However, the excess of Ni that is not used for promotion is present as a pure NiS species that remain at the surface. At the same time, for catalysts based on mixed HPAs, the fraction of bulk nickel sulfide is slightly higher than for samples $Ni(Mo_n+W_{12-n})/Al_2O_3$, which in turn may be associated to an enhancement of the metallic properties of Mo due to the extra electrons that W provides to the unitary cell [13], which is why Ni atoms are more difficult to incorporate into the structure of the active phase. This also confirms the data that the bond between molybdenum and tungsten is retained even during sulfidation [10]. The high proportion of bulk nickel sulfide is also associated to the type of sulfidation. Eijsbouts et al. [14] noted in their work that Ni is more susceptible to segregation into Ni_2S_3 particles under conditions

of liquid-phase sulfidation. At the same time, during gas-phase sulfiding, a smaller proportion of nickel is segregated into bulk sulfide, but larger particles are formed.

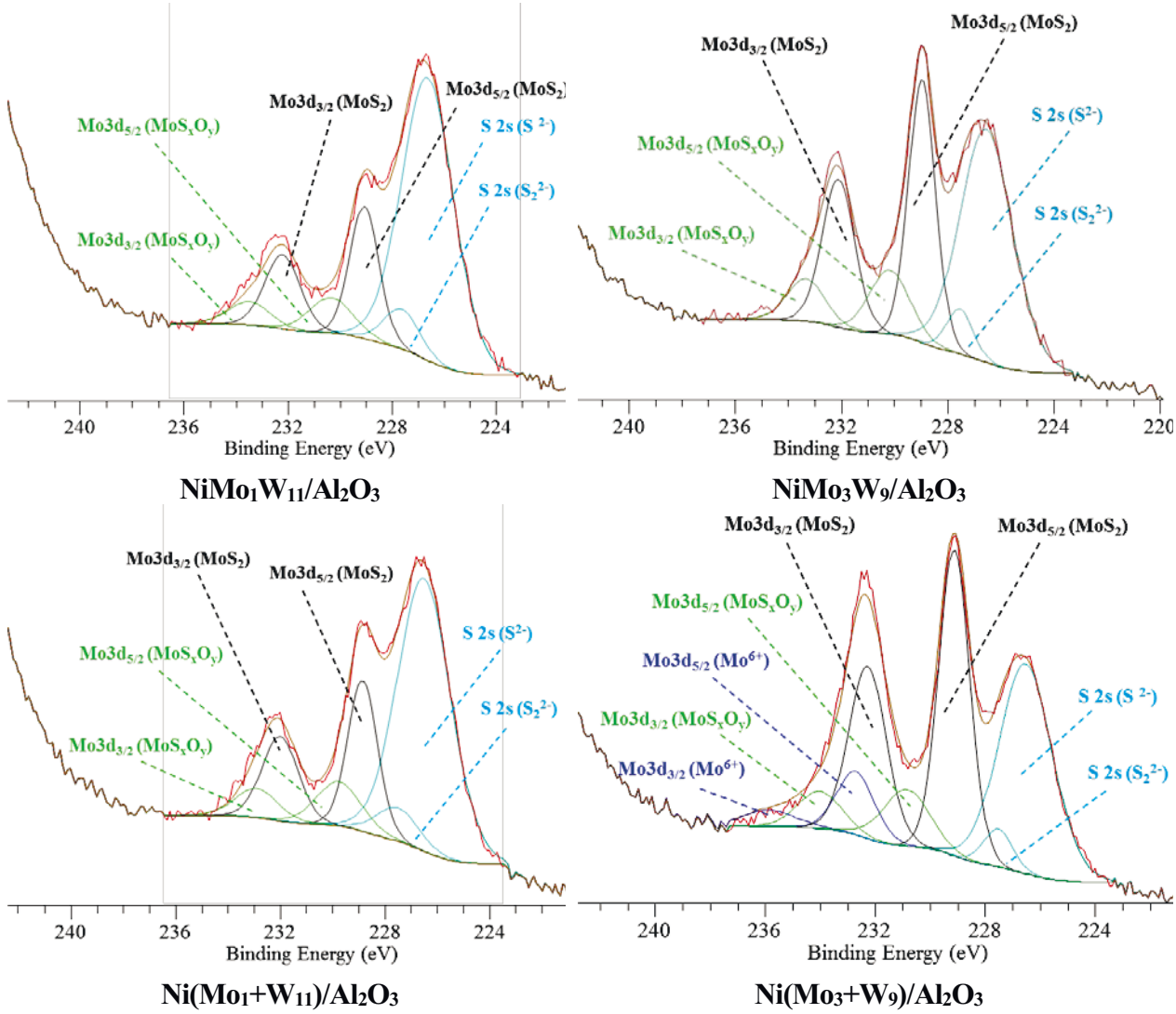

Fig. 3.3 Decomposition of XPS of the Mo3d spectra recorded for the NiMo(W)/Al_2O_3 catalysts; in blue: Mo^{6+} oxide contributions; in green: MoS_xO_y contributions; in black: MoS_2 contributions.

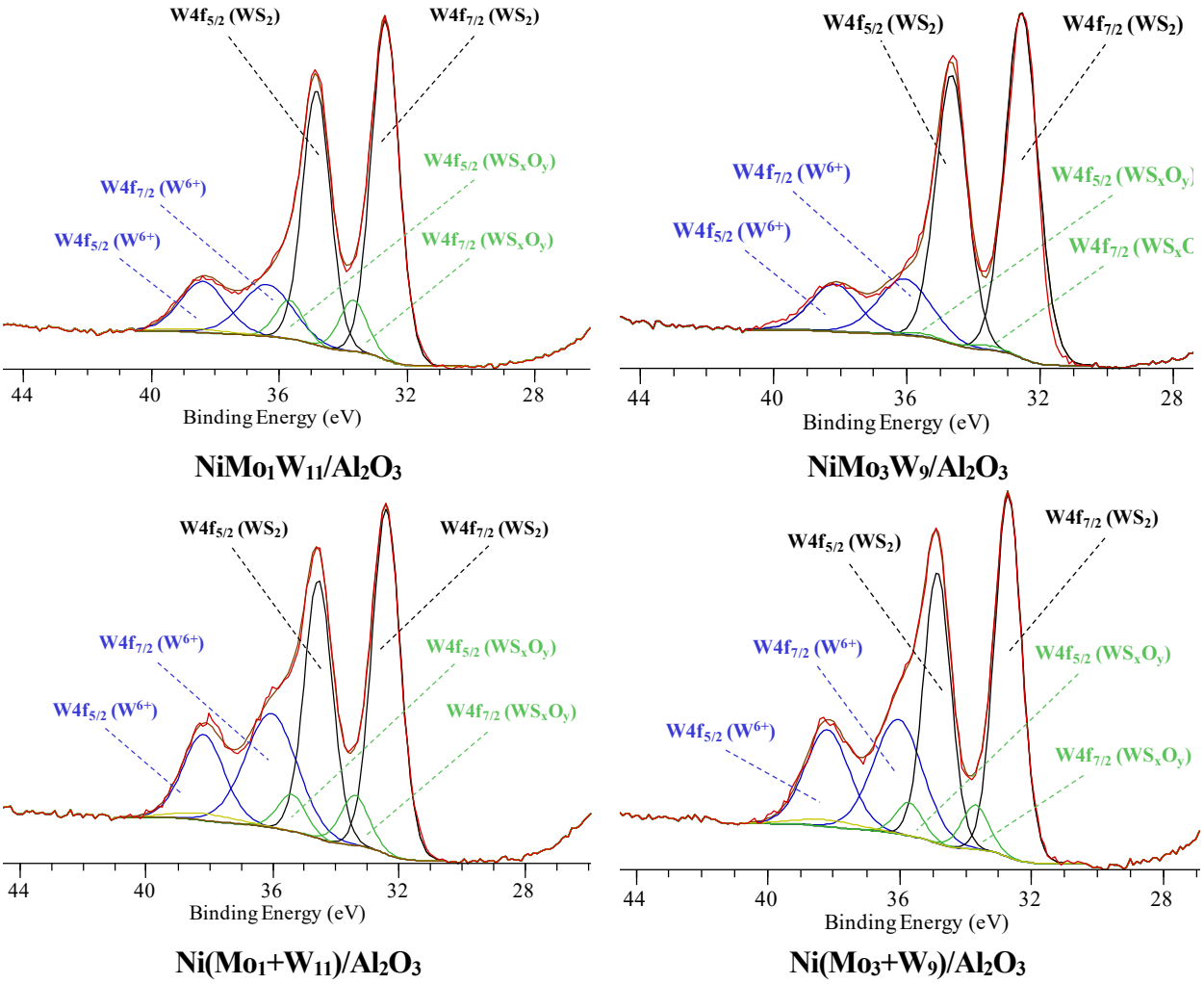

Fig. 3.4 Decomposition of XPS of the W4f spectra recorded for the NiMo(W)/Al_2O_3 catalysts; in blue: W^{6+} oxide contributions; in green: WS_xO_y contributions; in black: WS_2 contributions

Table 3.3. Relative metal fractions measured by XPS for Mo and W species present at the surface of sulfided NiMo(W)/Al_2O_3 catalysts.

Catalyst	Ni percentage (rel. %)			Mo percentage (rel. %)			W percentage (rel. %)			$Ni(Mo+W)_{edge}$
	NiMo(W)S	NiS	Ni^{2+}	MoS_2	MoS_xO_y	Mo^{6+}	WS_2	WS_xO_y	W^{6+}	
NiW_{12}	30	56	14	-	-	-	64	7	29	0.74
$NiMo_1W_{11}$	37	51	12	72	28	0	69	10	21	0.82
$NiMo_3W_9$	42	54	4	74	26	0	74	8	18	0.82
$NiMo_6W_6$	40	50	10	71	26	4	73	7	20	0.88
$NiMo_9W_3$	43	49	8	69	25	6	77	8	15	0.92
$Ni(Mo_1+W_{11})$	35	55	10	70	30	0	59	9	33	0.79
$Ni(Mo_3+W_9)$	36	43	21	67	19	14	59	7	34	0.87
$Ni(Mo_6+W_6)$	37	44	19	63	22	15	61	10	29	0.97
$Ni(Mo_9+W_3)$	39	43	18	60	23	17	64	9	27	0.99
$NiMo_{12}$	62	27	11	73	15	12	-	-	-	0.90

3.4 Determination of the composition and structure of the active phase

Liquid phase sulfidation prior to catalytic tests was chosen to be close to the real conditions of hydrotreating reactions, as a consequence, the same type of activation was used before TEM and XPS analysis. To obtain information about the presence of mixed active phase in the promoted catalysts as observed in non-promoted ones, XAS and HAADF were considered. Unfortunately, at the time of the experiments, no liquid phase sulfidation could be followed by *in situ* XAS on the ROCK beamline at Soleil synchrotron.

We however decided to study selected NiMoW catalysts by this technique and by HAADF after gas phase sulfidation. Indeed, previous work comparing gas and liquid phase sulfidation of non-promoted MoW catalyst [15] evidenced that regardless of the activation type, mixed HPA based catalysts had high amount of mixed $MoWS_2$ clusters, while samples based on a mixture of two monometallic HPAs had predominantly monometallic MoS_2 and WS_2 slabs, the only difference being the arrangement of the Mo and W atoms in the slabs. Based on this result, the main task of HAADF and EXAFS characterization in this part will be to determine how the addition of nickel to MoW systems affected the formation of the active phase, assuming that the effect will be the same whatever the sulfidation procedure.

The following paragraphs thus present the HAADF and XAS analysis of $NiMo_3W_9/Al_2O_3$ and $Ni(Mo_3+W_9)/Al_2O_3$ catalysts after sulfidation in a flow of 10 % H_2S in H_2 at atmospheric pressure with heating from room temperature to 400 °C with a heating rate of 3°C/min followed by a plateau of 2 h.

3.4.1 HAADF characterization of gas phase sulfided Ni(Mo)W/Al_2O_3 catalysts

HAADF technique allows to visualize the sulfide NiMoW slabs with basal planes oriented perpendicularly to the electron beam. HAADF images of sulfided $NiMo_3W_9/Al_2O_3$ and $Ni(Mo_3+W_9)/Al_2O_3$ catalysts are presented in **Fig. 3.5.** The sulfide particles of Ni-promoted catalysts had irregular shapes, as observed in the case of unpromoted samples, which is attributed to the interaction with alumina surface. On HAADF micrographs, Mo and W atoms are easily discriminated due to their Z difference: heavy tungsten atoms are imaged as brighter spots than lighter molybdenum atoms. We can thus see that $NiMo_3W_9/Al_2O_3$ images show the formation of mixed (Ni)MoWS slabs, in which small agglomerates of Mo atoms were surrounded by W ones. Even if mixed MoW slabs are clearly observed in the case of this promoted catalyst, the atomic repartition in a disulfide slab differs from the core-shell structure of unpromoted Mo_3W_9/Al_2O_3 catalyst (sulfided with the same gas phase procedure) containing a whole Mo core [15]. The distribution of Mo and W atoms in the particles of $NiMo_3W_9/Al_2O_3$ is more similar to the one that has been observed for unpromoted Mo_3W_9/Al_2O_3 catalyst sulfided under liquid phase by DMDS

[16]. The active phase of $Ni(Mo_3+W_9)/Al_2O_3$ sulfided under gas phase consisted mainly of homogeneous (Ni)MoS and (Ni)WS slabs (**Fig 3.5**). However, the presence of some mixed (Ni)MoWS slabs was also evidenced. Thus, the structure of sulfide particles in $Ni(Mo_3+W_9)/Al_2O_3$ catalyst is quite similar to the one observed for unpromoted $(Mo_3+W_9)/Al_2O_3$ sample sulfided under gas or liquid phase [15]. Hensen and co-workers [17] found that $NiMo_{0.75}W_{0.25}/Al_2O_3$ catalyst with a random distribution of Mo and W atoms in mixed $MoWS_2$ slabs was formed in liquid phase sulfidation conditions and was more active in the gas oil hydrotreatment compared to $NiMo/Al_2O_3$.

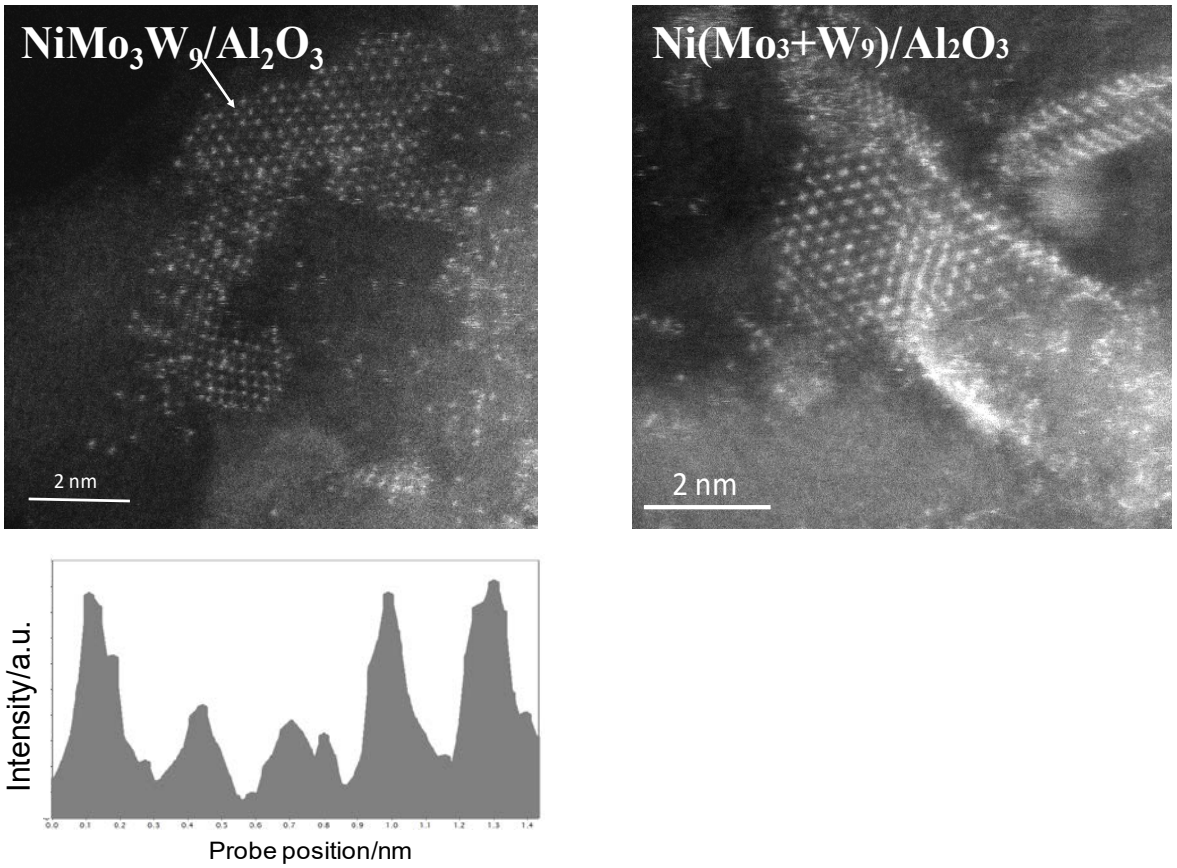

Fig. 3.5 HAADF images of sulfided $NiMo_3W_9/Al_2O_3$ and $Ni(Mo_3+W_9)/Al_2O_3$ catalysts with intensity profiles corresponding to the row of atoms identified by the arrow on $NiMo_3W_9/Al_2O_3$.

3.4.2 EXAFS characterization of gas phase sulfided Ni(Mo)W/Al_2O_3 catalysts

Fig. 3.6 compares the magnitude of k^3-weighted Fourier transformed (FT) EXAFS spectra for bimetallic $NiMo_{12}/Al_2O_3$ (NiW_{12}/Al_2O_3) and trimetallic $NiMo_3W_9/Al_2O_3$, and $Ni(Mo_3+W_9)/Al_2O_3$ catalysts. The best-fit parameters for EXAFS data are gathered in **Table 3.4**. At both Mo *K*- and W L_3-edges, the first FT contribution with a maximum at 2.0 Å (not phase corrected), was attributed to the metal-sulfur first coordination. The coordination numbers of the Mo−S and W−S contributions varied from 5.4 to 5.9 and from 5.6 to 6.1, respectively, thus indicating the high sulfidation degree of metals (**Table 3.4**). In the case of unpromoted catalysts, the coordination

numbers of the Mo−S and W−S were lower and varied from 5.1 to 5.3 and from 4.3 to 4.8, respectively.

The contribution around 2.9 Å (not phase corrected) at both edges was assigned to metal backscatter within Mo(W)S_2 structure. A noticeable decrease can be seen in the second coordination shell when comparing trimetallic samples to bimetallic NiMo and NiW references (**Fig. 3.6**), particularly for mixed HPA based catalyst. The same behavior was already observed for unpromoted samples [11], the second coordination shell was more modified for the catalysts prepared from Mo_3W_9HPA compared to those based on a mixture of two monometallic HPAs. Such decrease in the second shell of the bimetallic MoW catalysts can be caused by the presence of W neighboring atoms with opposite backscattering phases in this shell [10]. In the bimetallic catalysts, the coordination numbers were $N_{Mo\text{-}Mo}$ = 3.7 (at 3.18 Å) for $NiMo_{12}/Al_2O_3$ and $N_{W\text{-}W}$ = 4.3 (at 3.16 Å) for NiW_{12}/Al_2O_3. The higher value for W−W compared to Mo−Mo can be related to larger sulfide particles in NiW_{12} sample, which is in agreement with TEM data.

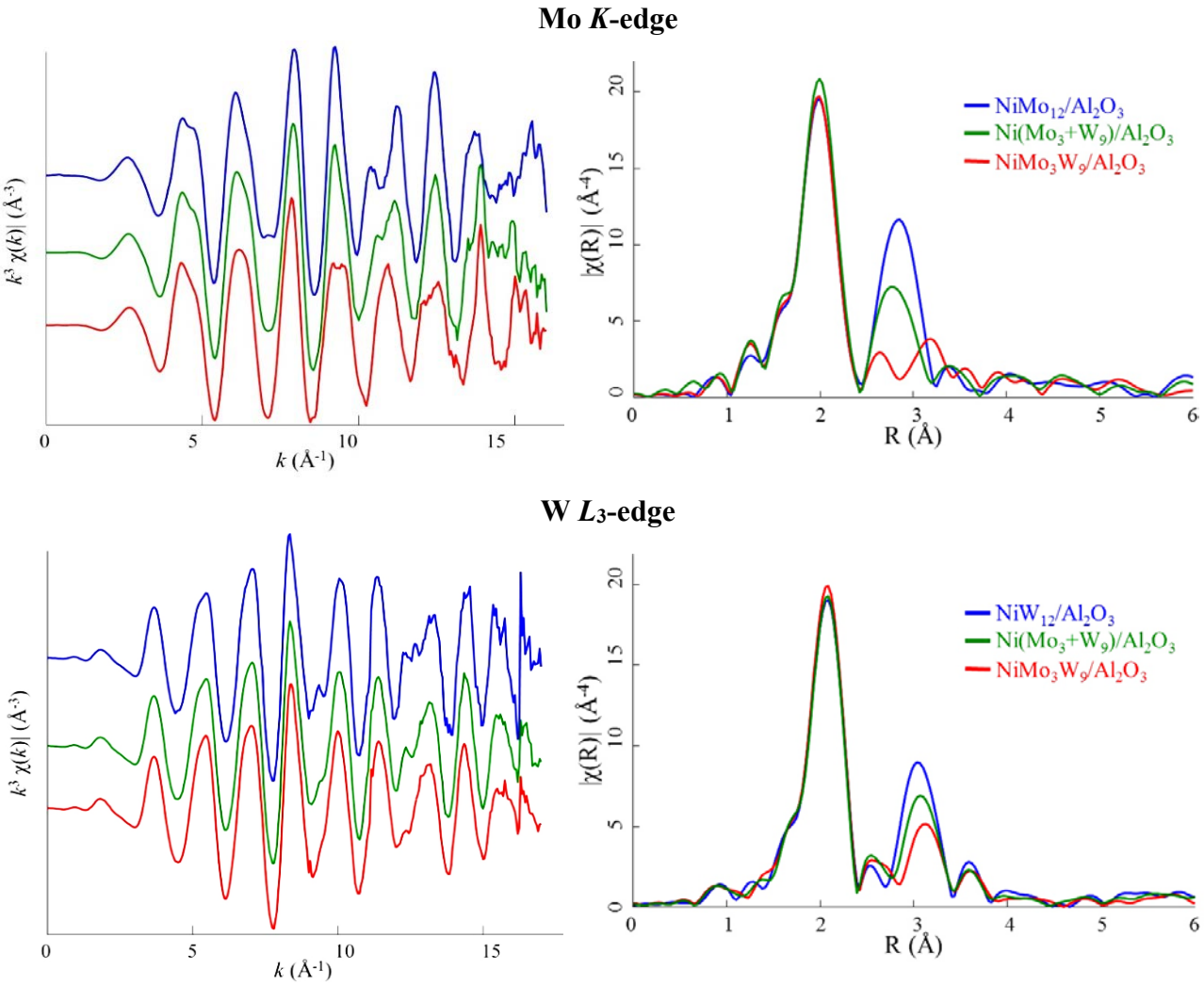

Fig. 3.6 k^3-weighted EXAFS at the Mo *K*-edge and W L_3-edge, and the corresponding Fourier transforms of sulfided NiMo(W)/Al_2O_3 catalysts.

For both trimetallic catalysts, the fit at the Mo *K*-edge was improved when adding a second metal-metal Mo−W contribution in the second coordination shell. The second coordination shell at the Mo *K*-edge in $NiMo_3W_9/Al_2O_3$ consists of a molybdenum atom with N_{Mo-Mo} = 1.5 and a tungsten one with N_{Mo-W} = 2.8, in $Ni(Mo_3+W_9)/Al_2O_3$ with N_{Mo-Mo} = 3.3 and N_{Mo-W} = 1.6 both at 3.19 Å. The simultaneous presence of Mo−Mo and Mo−W contributions indicates the formation of mixed sulfide phase in both NiMoW catalysts. However, the higher contribution of Mo−W path for the second shell in $NiMo_3W_9/Al_2O_3$ indicates the higher concentration of mixed slabs than in its trimetallic $Ni(Mo_3+W_9)/Al_2O_3$ counterpart. Indeed, a comparison of trimetallic catalysts by HAADF shows that both samples contain mixed $MoWS_2$ particles but in $Ni(Mo_3+W_9)/Al_2O_3$ these mixed slabs are much less numerous.

Table 3.4. Structural parameters obtained by multi-edge fitting from the Fourier-analysis of Mo *K*- and W L_3-edges EXAFS spectra of sulfided $NiMo(W)/Al_2O_3$ catalysts.

Scattering path	*N*	*R* (Å)	σ^2 x 10^3 (Å^2)	E_0 (eV)	*R*-factor
$NiMo_{12}/Al_2O_3$					
Mo-S	5.4 ± 0.5	2.41 ± 0.01	3.2 ± 0.7	1.9 ± 0.8	0.0057
Mo-Mo	3.7 ± 0.7	3.18 ± 0.01	4.0 ± 0.9		
NiW_{12}/Al_2O_3					
W-S	5.8 ± 0.7	2.41 ± 0.01	3.0 ± 0.9	7.7 ± 1.6	0.0105
W-W	4.3 ± 1.1	3.16 ± 0.01	4.3 ± 1.0		
$NiMo_3W_9/Al_2O_3$					
Mo-S	5.5 ± 0.5	2.42±0.01	3.3 ± 0.8		
Mo-Mo	1.5 ± 0.6	3.21±0.02	4.8 ± 2.3	3.0±1.0	
Mo-W	2.8 ± 1.2	3.20±0.01	4.8 ± 2.3		0.010
W-S	6.1 ± 0.7	2.41±0.01	3.0± 0.8	9.0 ±1.7	
W-W	2.8 ± 1.6	3.17±0.01	4.8 ± 2.3		
$Ni(Mo_3+W_9)/Al_2O_3$					
Mo-S	5.9 ± 0.9	2.42 ± 0.01	3.4 ± 1.0		
Mo-Mo	3.3 ± 0.8	3.19 ± 0.01	4.4 ± 1.1	2.9 ± 2.0	
Mo-W	1.6 ± 0.8	3.19 ± 0.03	4.4 ± 1.1		0.0058
W-S	5.6 ± 0.4	2.41 ± 0.01	2.9 ± 0.5	9.2 ± 1.3	
W-W	3.5 ± 0.8	3.17 ± 0.01	4.4 ± 1.1		

At the W L_3-edge of trimetallic samples, a lower W−W coordination number is observed, compared to that of NiW_{12} catalyst. The morphology of WS_2 slabs could thus be affected by the

presence of Mo. The same evolution of the coordination numbers was also observed for the corresponding unpromoted catalysts showing that the behavior does not depend on the Ni promotion. The second coordination shell of trimetallic samples contains one heteroatomic metal-metal contribution. It should also be noticed that tungsten concentration was three times higher than molybdenum. Thus, the obtained distribution of the contributions may be indicative of a greater presence of tungsten atoms surrounding small molybdenum islands, which have more W neighbors in this case. That is in agreement with the results of HAADF characterization.

Determination of the local environments of the Ni atoms in the sulfided catalysts from the EXAFS data is hampered. In sulfided catalyst nickel could be part of various compounds, such as Ni_3S_2, NiS_x, and NiMo(W)S phase. Such multicomponent system presents different scattering paths overlapping in the *R*-range, which leads to instability of the fitting procedure and correlations of the fitting parameters.

The Ni *K*-edge XANES and EXAFS spectra of sulfided catalysts are shown in **Fig. 3.7A** and **B**, respectively. For comparison purposes, Ni/Al_2O_3 catalyst was also synthesized using impregnating solutions prepared from a mixture of nickel carbonate and citric acid with molar ratio citric acid/Ni = 1/1. This sample was gas-phase sulfided under the same conditions as $Ni(Mo)W/Al_2O_3$ catalysts and its XAS spectra were also recorded.

All Ni *K*-edge EXAFS spectra are similar in phase (**Fig. 3.7B**). The oscillations of the Ni−S scattering will dominate in the lower *k*-region with a characteristic maximum around 6 $Å^{-1}$ corresponding to the maximum of the scattering amplitude of S backscatters, whereas Mo and W backscatters will contribute at the higher *k*, leading when they are coordinated as second neighbors of promotors to a second relative maximum beyond 10 $Å^{-1}$ [18, 19]. For the bimetallic and trimetallic catalysts, this second relative maximum is observed in agreement with the decoration of the sulfide slabs by nickel atoms. It is noteworthy that both trimetallic catalysts (**Fig. 3.7B (b))** display a maximum at the higher *k*, which is markedly lower in intensity than the ones observed for the bimetallic catalysts (**Fig. 3.7B (a))**. This decrease of signal in the higher *k*-region is in agreement with the simultaneous presence of W and Mo, that is due to the destructive interference of the individual scattering paths of these atoms, which are out of phase [17, 20].

The Ni *K*-edge XANES spectra of the $NiMo(W)/Al_2O_3$ catalysts differ from Ni/Al_2O_3 due to the changes in the electronic structure by the appearance of Mo and/or W neighbors (**Fig. 3.7A (a), (b)**). Spectra of both trimetallic catalysts are close to each other (**Fig. 3.7A (b)**). The spectrum of mixed HPA based sample looks like an intermediate between its trimetallic counterpart and $NiMo_{12}/Al_2O_3$ sample (**Fig. 3.7A (c)**), while $Ni(Mo_3+W_9)/Al_2O_3$ itself is close to the NiW_{12}/Al_2O_3 (**Fig. 3.7A (d)**).

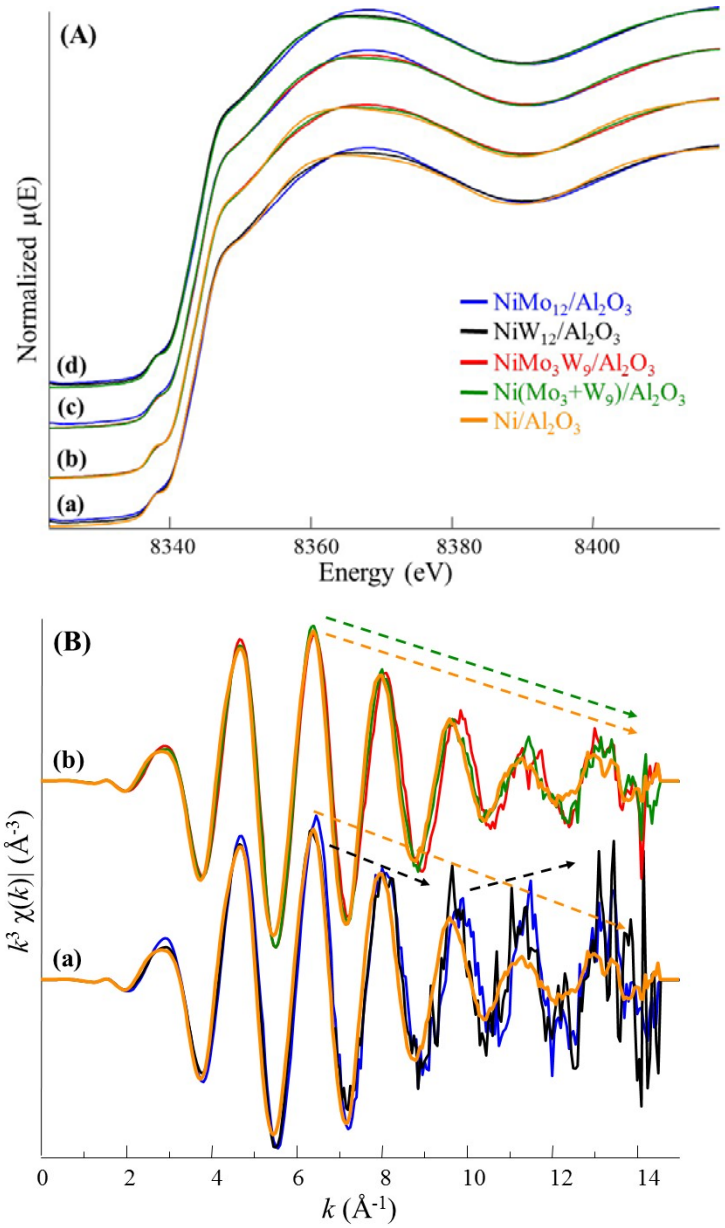

Fig. 3.7 Ni *K*-edge XANES spectra comparison (A): (a) Ni/Al_2O_3 and bimetallic samples, (b) Ni/Al_2O_3 and trimetallic samples, (c) $NiMo_{12}/Al_2O_3$ and trimetallic samples, (d) $Ni(Mo_3+W_9)/Al_2O_3$ and bimetallic catalysts; Comparison of k^3-weighted EXAFS spectra of sulfided catalysts (B): (a) Ni/Al_2O_3 and bimetallic samples, (b) Ni/Al_2O_3 and trimetallic catalysts

Summarizing, the HAADF and XAS data showed that the promotion by Ni did not prevent the formation of mixed $MoWS_2$ slabs during gas-phase sulfiding, and based on previous results for unpromoted systems [15], the same observation is assumed for liquid activation, despite possible differences in the arrangement of Mo and W atoms inside the plates. By HAADF it was visualized that the mixed slabs are formed with small Mo islands surrounded by W atoms under gas phase sulfidation. However, the active phase of the catalyst prepared from separate monometallic HPAs consisted mainly of monometallic sulfide particles. The changes of the Ni *K*-edge XANES spectra confirm the formation of NiMo(W)S phase along with nickel sulfide.

3.5 Catalytic tests in hydrotreating of model and real feeds

All the prepared promoted catalysts have been evaluated in the process of co-hydrotreating of DBT (1000 ppm S) and naphthalene (3 wt. %). Further addition of a nitrogen-containing component (quinoline, 500 ppm N) was considered in order to determine the inhibition effect on trimetallic NiMoW/Al_2O_3 catalysts. To confirm the results obtained in model reactions, the trimetallic NiMoW/Al_2O_3 catalysts were also investigated in the process of hydrotreating of straight-run gas oil (SRGO). West Siberian oil with boiling range 180-360°C was used as feedstock, with a density at 20°C of 0.841 kg/m^3, sulfur and nitrogen contents of 0.815 wt. % and 156 ppm, respectively. The tests were carried out at 340°C, 4.0 MPa of hydrogen, 2 h^{-1} LHSV and a 700 NL L^{-1} volume ratio of hydrogen to feed.

3.5.1 NiMo(W)/Al_2O_3 catalysts in hydrotreating of DBT and naphthalene

Results of the catalytic activities of the sulfided NiMo(W)/Al_2O_3 catalysts in hydrotreating of DBT and naphthalene are presented in **Table 3.5**. DBT HDS and naphthalene HYD conversions varied in a wide range, from 42 to 75% and from 32 to 49 %, respectively. Some catalysts were tested twice, after which the average conversion values of the reagents were calculated. The experiment data show that the accuracy of determining the rate constant is on average 3%.

Table 3.5. Catalytic properties of NiMo(W)/Al_2O_3 catalysts in HDT of a mixture of DBT and naphthalene.

Catalysts	Conversion (%)		$k \times 10^4$ (mol h^{-1} g^{-1})		$S_{HYD/DDS}$
	DBT HDS	Naphthalene HYD	k_{HDS}	k_{HYD}	
NiW_{12} [a]	49.0 ± 1.5	39.6 ± 0.6	16.4 ± 0.7	60.2 ± 2.3	0.32
$NiMo_1W_{11}$ [a]	60.1 ± 1.8	36.8 ± 1.1	22.3± 1.1	56.3 ± 2.1	0.34
$NiMo_3W_9$ [a]	73.2 ± 2.2	38.9 ± 1.2	31.9 ± 2.0	60.2 ± 2.7	0.19
$NiMo_6W_6$	71.6	37.3	30.6	56.8	0.21
$NiMo_9W_3$	75.4	38.9	34.2	60.0	0.24
Ni(Mo_1+W_{11}) [a]	49.0 ± 1.0	35.0 ± 0.7	16.4 ± 0.5	52.5 ± 1.3	0.49
Ni(Mo_3+W_9)	42.0	32.1	13.3	47.0	0.36
Ni(Mo_6+W_6)	60.4	33.0	22.5	48.8	0.24
Ni(Mo_9+W_3)	72.7	37.6	31.6	58.9	0.20
$NiMo_{12}$ [a]	70.8 ± 2.1	49.2 ± 1.4	29.9 ± 1.8	79.2 ± 3.3	0.13

(Test conditions: T=280°C, LHSV= 40 h^{-1}, K_H=500 NL L^{-1}, P = 3.0 MPa)

[a] samples have been tested twice

Fig. 3.8a shows that the HDS rate constants of all trimetallic $NiMo_nW_{12-n}/Al_2O_3$ catalysts based on mixed HPAs are higher than that of their $Ni(Mo_n+W_{12-n})/Al_2O_3$ counterparts and then the values calculated by additive way using the data for $NiMo_{12}/Al_2O_3$ and NiW_{12}/Al_2O_3 samples (dotted line). The most active $NiMo_9W_3$ catalyst even surpasses the $NiMo_{12}$ one. Ni(Mo+W) catalysts show values close to the additive ones. Trimetallic catalysts prepared using mixed SiMoW HPAs show a different behavior: the HDS activity noticeably increases when incorporating one and three Mo atoms in the structure: from 16 mol h^{-1} g^{-1} for NiW_{12} to 22 and 32 mol h^{-1} g^{-1} for $NiMo_1W_{11}$ and $NiMo_3W_9$, respectively, while further increase in molybdenum content resulted in only a very slight increase in performance, with 31 and 34 mol h^{-1} g^{-1} for $NiMo_6W_6$ and $NiMo_9W_3$. $NiMo_3W_9$ catalyst is 2.4 times more active than $Ni(Mo_3+W_9)$, but this difference decreases when increasing the Mo content. When comparing catalysts with equal Mo/W ratio, the percentage of Ni atoms in the NiMoWS phase is slightly higher for the NiMoW catalysts than for their reference counterparts. However, these little differences in promotion of the slabs, that are similar for all MoW and Mo+W solids whatever the Mo/W ratio, cannot explain the observed discrepancies in activity. These results thus highlight the influence of the formation of the mixed phase present in a larger extend in NiMoW catalysts than in Ni(Mo+W) catalysts. On non-promoted catalysts, HDS activity shows a maximum for Mo_6W_6 catalyst, a further increase in molybdenum content leading to a less organized mixed phase that appeared to be less active in HDS. On promoted catalysts, the effect of the mixed nature of the slabs on the activity of the promoted sites is more noticeable at low Mo contents, the largest difference between NiMoW and Ni(Mo+W) catalysts being observed for a ratio Mo/W of 3/9.

The HDS DBT reaction mainly proceeds along the preliminary hydrogenation route for unpromoted catalysts. Promotion by Ni atoms leads to a sharp change in selectivity and shifts the reaction to the path of direct desulfurization (DDS), which also agrees with the literature data [21], [22]. **Fig. 3.8c** shows that the introduction of one molybdenum atom in the catalysts contributes to a shift in the reaction to the route of pre-hydrogenation, particularly sharp in the case of $Ni(Mo_1+W_{11})/Al_2O_3$. With a further increase of the Mo/(Mo+W) atomic ratio from 0.08 to 0.75, a gradual decrease in $S_{HYD/DDS}$ selectivity occurs, except for $NiMo_9W_3/Al_2O_3$ catalyst, showing a slight increase in selectivity. The $NiMo_{12}/Al_2O_3$ catalyst exhibits the lowest $S_{HYD/DDS}$ selectivity.

Regarding hydrogenation, bimetallic $NiMo_{12}/Al_2O_3$ sample was the most active in naphthalene HYD reactions (**Fig. 3.8b**). The conversion of naphthalene HYD almost does not change with an increase in the Mo/(Mo+W) atomic ratio in the catalysts based on mixed HPAs and varies in the range of 37-39 %. The hydrogenating character of Ni seems to level any other effect, while for $Ni(Mo_n+W_{12-n})/Al_2O_3$ catalysts, the activity passes through a minimum at a ratio of 0.25. As in the DBT HDS, mixed $NiMo_nW_{12-n}/Al_2O_3$ catalysts are superior to reference samples prepared from a mixture of monometallic HPAs in HYD of naphthalene. The higher activity of the mixed $NiMo_nW_{12-n}/Al_2O_3$ catalysts in comparison with the samples prepared from the mixture of

monometallic HPAs can be explained by the formation of a mixed NiMoWS active phase, which was confirmed by EXAFS and HAADF.

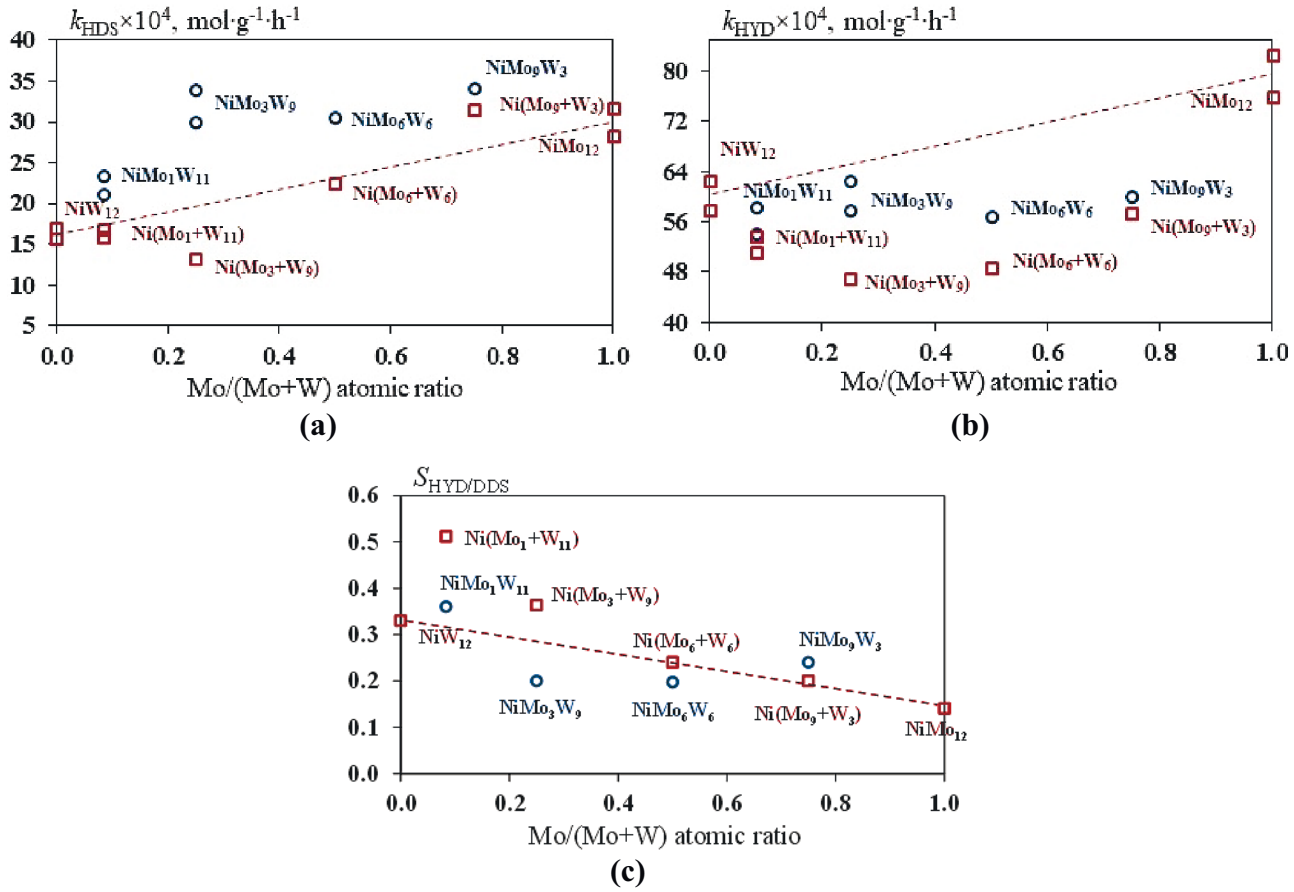

Fig. 3.8 Dependence of reaction rate constants in DBT HDS (a), naphthalene HYD (b) and selectivity route of DBT HDS (c) on Mo/(Mo+W) atomic ratio in NiMo(W)/Al_2O_3 catalysts (circles correspond to $NiMo_nW_{12-n}/Al_2O_3$ catalysts; squares are $Ni(Mo_n+W_{12-n})/Al_2O_3$ catalysts; dotted line indicates additive values between $NiMo_{12}/Al_2O_3$ and NiW_{12}/Al_2O_3).

3.5.2 NiMo(W)/Al_2O_3 catalysts in co-hydrotreating of DBT, naphthalene and quinoline

The catalytic properties of the sulfided NiMo(W)/Al_2O_3 catalysts in co-hydrotreating of DBT, naphthalene and quinoline are given in **Table 3.6**. The DBT and naphthalene conversion during the tests varied from 60.0 to 79.6% and from 4.0 to 14.2%, respectively. A detailed analysis of the reaction products showed that diphenyl was the main reaction product, which means that the direct desulfurization is the preferred reaction route, as evidenced by the selectivity values (**Table 3.6**). The presence of only traces of tetrahydro-, perhydrodibenzothiophenes, as well as cyclohexylbenzene and bicyclohexyl, is due to the strong inhibitory effect of quinoline on the hydrogenation function. In the case of HYD of naphthalene, only tetralin was found in the reaction products. More than 96% of quinoline was converted to tetrahydroquinoline under hydrotreating conditions, the degree of nitrogen removal being only 10.2–21.2%.

Table 3.6. Catalytic properties of NiMo(W)/Al_2O_3 catalysts in HDT of a mixture of DBT, naphthalene and quinoline.

Catalysts	Conversion (%)			$k\times10^4$ (mol·g^{-1}·h^{-1})			$S_{HYD/DDS}$
	DBT HDS	Naphthalene HYD	Quinoline HDN [b]	HDS	HYD	HDN	
NiW_{12} [a]	65.0 ± 2.0	11.0 ± 0.3	10.2 ± 0.4	25.5 ± 1.4	14.2 ± 0.5	2.0 ± 0.1	0.24
$NiMo_1W_{11}$ [a]	77.9 ± 2.3	14.2 ± 0.4	21.2 ± 0.6	36.8 ± 2.7	18.6 ± 0.6	4.4 ± 0.1	0.03
$NiMo_3W_9$ [a]	72.0 ± 2.2	7.2 ± 0.3	19.4 ± 0.7	31.0 ± 1.9	9.1 ± 0.4	4.0 ±0.1	0.02
$NiMo_6W_6$	70.2	6.4	17.0	29.5	8.0	3.4	0.01
$NiMo_9W_3$	73.2	6.0	14.3	32.0	7.5	2.9	0.01
Ni(Mo_1+W_{11}) [a]	70.0 ± 1.4	6.9 ± 0.3	15.0 ± 0.5	29.3 ± 1.1	8.8 ± 0.4	3.0 ± 0.1	0.08
Ni(Mo_3+W_9)	60.0	4.0	14.5	22.3	5.0	2.9	0.05
Ni(Mo_6+W_6)	68.0	4.8	13.8	27.8	6.0	2.7	0.01
Ni(Mo_9+W_3)	71.3	5.4	13.2	30.3	6.7	2.6	0.01
$NiMo_{12}$ [a]	79.6 ± 2.4	6.4 ± 0.3	11.8 ± 0.4	38.8 ± 2.9	8.0 ± 0.3	2.3 ± 0.1	0.09

(Test conditions: T=280°C, LHSV= 40 h^{-1}, K_H=500 NL L^{-1}, P = 3.0 MPa)

[a] samples tested twice;

[b] indicates the depth of nitrogen removal (%).

The maximum activity in all model reactions was observed for the $NiMo_1W_{11}/Al_2O_3$ sample (**Fig. 3.9**), as evidenced by the calculated reaction rate constants. It was previously noted by Lercher and co-workers [23] that the hydrogenating activity correlated with concentration of SH-groups formed due to the dissociative adsorption of H_2 and H_2S. In another work [24], investigating catalytic activity of unsupported trimetallic NiMoW systems with different Mo/W atomic ratios (1:2, 1:1, and 2:1), the authors found by using method of continuous-flow H_2-D_2 scrambling that the concentration of SH-groups directly depends on the tungsten content in mixed NiMoW systems. This can explain the higher HDS, HYD and HDN activities of the $NiMo_1W_{11}/Al_2O_3$. Further increase in the proportion of Mo in the composition of the catalyst leads to a decrease in the catalytic activity in all studied reactions. Moreover, the greatest drop in HDS and HYD activity for mixed $Ni(Mo_nW_{12-n})/Al_2O_3$ is observed when the Mo/(Mo+W) ratio goes from 0.08 to 0.25 **(Fig. 3.9a,b)**. It should be noted that when quinoline was added in the feed, only $NiMo_1W_{11}/Al_2O_3$ sample significantly exceeded the additive values (**Fig. 3.9a**).

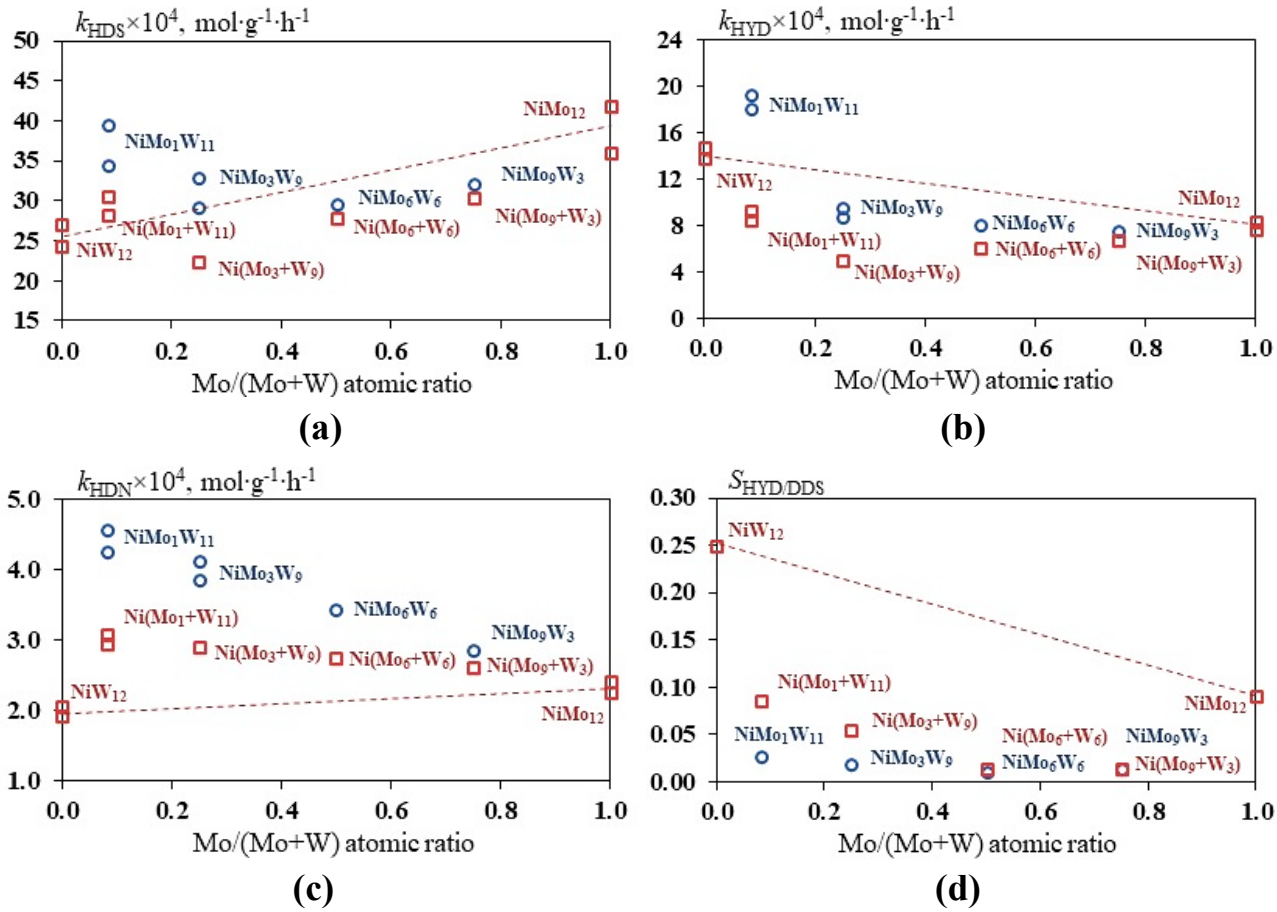

Fig. 3.9 Dependence of reaction rate constants in DBT HDS (a) naphthalene HYD (b), quinoline HDN (c) and selectivity route of DBT HDS (d) on Mo/(Mo+W) atomic ratio in $NiMo(W)/Al_2O_3$ catalysts (circles correspond to $NiMo_nW_{12-n}/Al_2O_3$ catalysts; squares are $Ni(Mo_n+W_{12-n})/Al_2O_3$ catalysts; dotted line indicates additive values between $NiMo_{12}/Al_2O_3$ and NiW_{12}/Al_2O_3).

The values of the degree of inhibition were calculated taking into account the values of the reaction rate constants before and after the addition of quinoline in model feed. The introduction of quinoline into the model mixture promoted a slight increase in HDS activity, as evidenced by the obtained values of the inhibition effect (**Fig. 3.10a**). This effect is pronounced for bimetallic NiW_{12} and trimetallic catalysts with high W percentages in the catalysts. The mechanism of the effect of nitrogen-containing compounds on the hydrogenolysis of DBT was previously described in the literature [25], [26]. It was shown that the tetrahydroquinoline formed as a main product of the reaction, being adsorbed perpendicular to the catalyst surface on one π-active site, leaves the second vacant active site available for anchor σ-adsorption of the DBT molecule, thereby shifting the reaction to the direct desulfurization route and increasing the HDS activity. It should be noted that this effect weakens with an increase in the Mo/(Mo+W) atomic ratio and turns into inhibition on both types of catalysts. The highest inhibiting effect for DBT HDS is manifested for catalysts based on mixed $SiMo_nW_{12-n}$HPAs with Mo/(Mo+W) atomic ratio more than 0.25, but at the same time the $NiMo_nW_{12-n}/Al_2O_3$ catalysts provide a higher DBT conversion. $NiMo_1W_{11}/Al_2O_3$ sample was less sensitive to quinoline, which is typical for NiW_{12}/Al_2O_3 catalyst, but the activity of the bimetallic sample was lower.

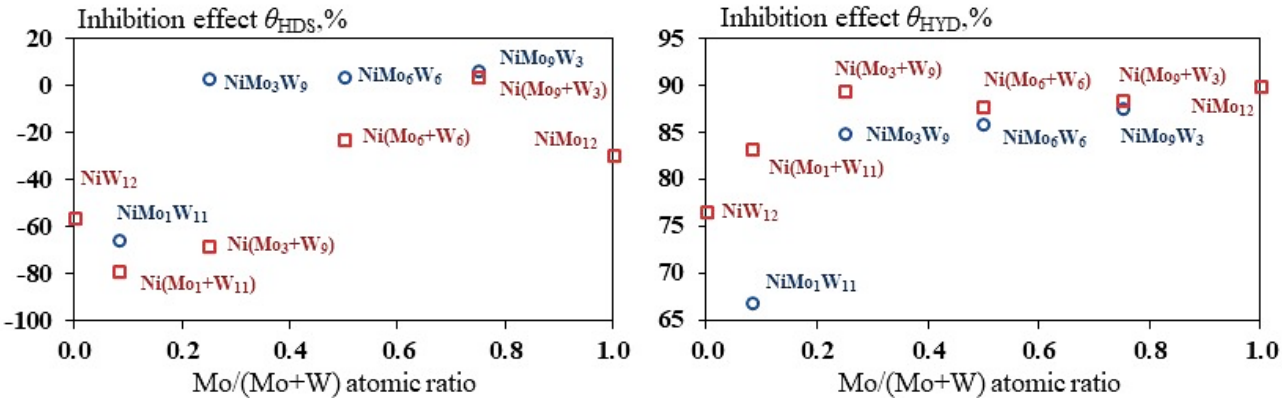

Fig. 3.10 Inhibition effect in the HDS of DBT (a) and naphthalene HYD (b) in presence of quinoline.

The highest selectivity in the DBT HDS is observed on a bimetallic NiW_{12}/Al_2O_3 catalyst due to the lesser susceptibility to the action of quinoline. With the introduction of molybdenum into the structure of the active phase, a sharp decrease in selectivity is observed for both types of trimetallic catalysts. Kinetic studies using model compounds presented in [27, 28] also confirm the assumption that nitrogen-containing heterocyclic compounds inhibit to a greater extent the HYD route of the DBT HDS.

The inhibition of the reaction by the N-containing component is more intense for naphthalene HYD, which is consistent with literature data [29]. The inhibitory effect of naphthalene HYD ranges

from 67 to 90 % **(Fig. 3.10b)**. The catalysts with high content of Mo were the most affected by quinoline inhibition effect. Naphthalene HYD performance of catalysts prepared from a mixture of monometallic HPAs are a little more affected by quinoline than the samples prepared from the mixture of monometallic HPAs. As in the case of the HDS reaction, the inhibition degree in the naphthalene HYD depends on the atomic ratio of the structure-forming metals of the active phase. It should be noted that the increase in the atomic ratio more than 0.25 almost does not change the degree of inhibition, and varies around 1-2%.

3.5.3 Hydrotreating of SRGO

The contents of stable hydrogenation products obtained after hydrotreating of SRGO over NiMo(W)/Al_2O_3 catalysts are shown in **Table 3.7**. The catalytic activity was evaluated by residual sulfur content in the hydrogenated product. All studied catalysts exhibited stable performance during a 48h period. In order to minimize errors in the determination of the rate constants, all catalysts were tested twice, after which the average conversion values of the reagents were calculated. The experiment data show that the accuracy of determining the rate constant is on average 3%. There was no acid component in the catalysts, for this reason no cracking products of model compounds were found in the hydrogenation product. The yield of hydrogenated diesel fraction was close to 96-97 %.

The highest residual sulfur and nitrogen contents were observed over NiW_{12}/Al_2O_3 catalyst. Replacement of only one tungsten atom by molybdenum leads to a decrease in the content of sulfur and nitrogen, by 35% and 28% for S and N contents on $Ni(Mo_1+W_{11})/Al_2O_3$ and by 57% and 46% for S and N contents on $NiMo_1W_{11}/Al_2O_3$.

When increasing the Mo content, performance in HDS and HDN evolve in a similar way. As previously observed in the hydrotreatment of model feeds, mixed HPAs based $NiMo_nW_{12-n}/Al_2O_3$ catalysts demonstrated higher activity during hydrotreating of SRGO than their corresponding counterparts, which can be related to the presence of mixed NiMoWS phase in NiMoW solids. The optimum Mo/(Mo+W) atomic ratio, corresponding to the lowest content of both residual sulfur and nitrogen, corresponds to 0.25 for both types of catalysts (**Fig 3.11**).

The shift in the maximum of HDS activity in comparison with the model feedstock containing quinolone may be associated with a lower nitrogen content (147 ppm versus 500 ppm) in SRGO. As noted earlier in model reactions, quinoline and its by-products can block the HYD centers, thereby opening vacant HDS centers through anchor adsorption. Since the content of quinoline in SRGO was much lower, inhibition affect was to a lesser extent. As a result, the high HYD activity of catalysts with a high molybdenum percentage was observed.

Table 3.7 HDS rate constants (k_{HDS}) and composition of products obtained in the process of SRGO hydrotreating over the synthesized NiMo(W)/Al_2O_3 catalysts

Catalyst	Content of products					Rate constants k_{HDS} (h^{-1} (wt. % S)$^{-0.4}$)
	S (ppm)	N (ppm)	Aromatics (wt. %)			
			mono-	bi-	tri-	
Feedstock	8147	156	31.9	10.03	2.46	-
NiW_{12} [a]	114.1 ± 5.1	42.1 ± 2.6	31.8 ± 0.8	4.02 ± 0.08	0.84 ± 0.02	29.1
$NiMo_1W_{11}$ [a]	48.8 ± 3.0	22.7 ± 1.6	30.7 ± 0.8	3.54 ± 0.07	0.66 ± 0.01	44.8
$NiMo_3W_9$ [a]	40.9 ± 1.9	14.0 ± 0.9	30.9± 0.6	3.35 ± 0.05	0.66 ± 0.01	49.2
$NiMo_6W_6$	45.3	17.0	29.8	3.39	0.63	47.1
$NiMo_9W_3$	52.2	22.2	31.7	3.40	0.70	43.8
$Ni(Mo_1+W_{11})$ [a]	74.5 ± 3.1	30.2 ± 1.1	30.9 ± 0.7	3.66 ± 0.04	0.80 ± 0.02	35.6
$Ni(Mo_3+W_9)$ [a]	46.6 ± 2.6	20.0 ± 1.1	30.4 ± 0.6	3.71 ± 0.06	0.79 ± 0.02	45.9
$Ni(Mo_6+W_6)$	50.1	20.9	31.4	3.40	0.77	44.6
$Ni(Mo_9+W_3)$	58.7	30.3	31.7	3.70	0.74	41.0
$NiMo_{12}$	73.8	25.4	30.6	3.44	0.80	36.5

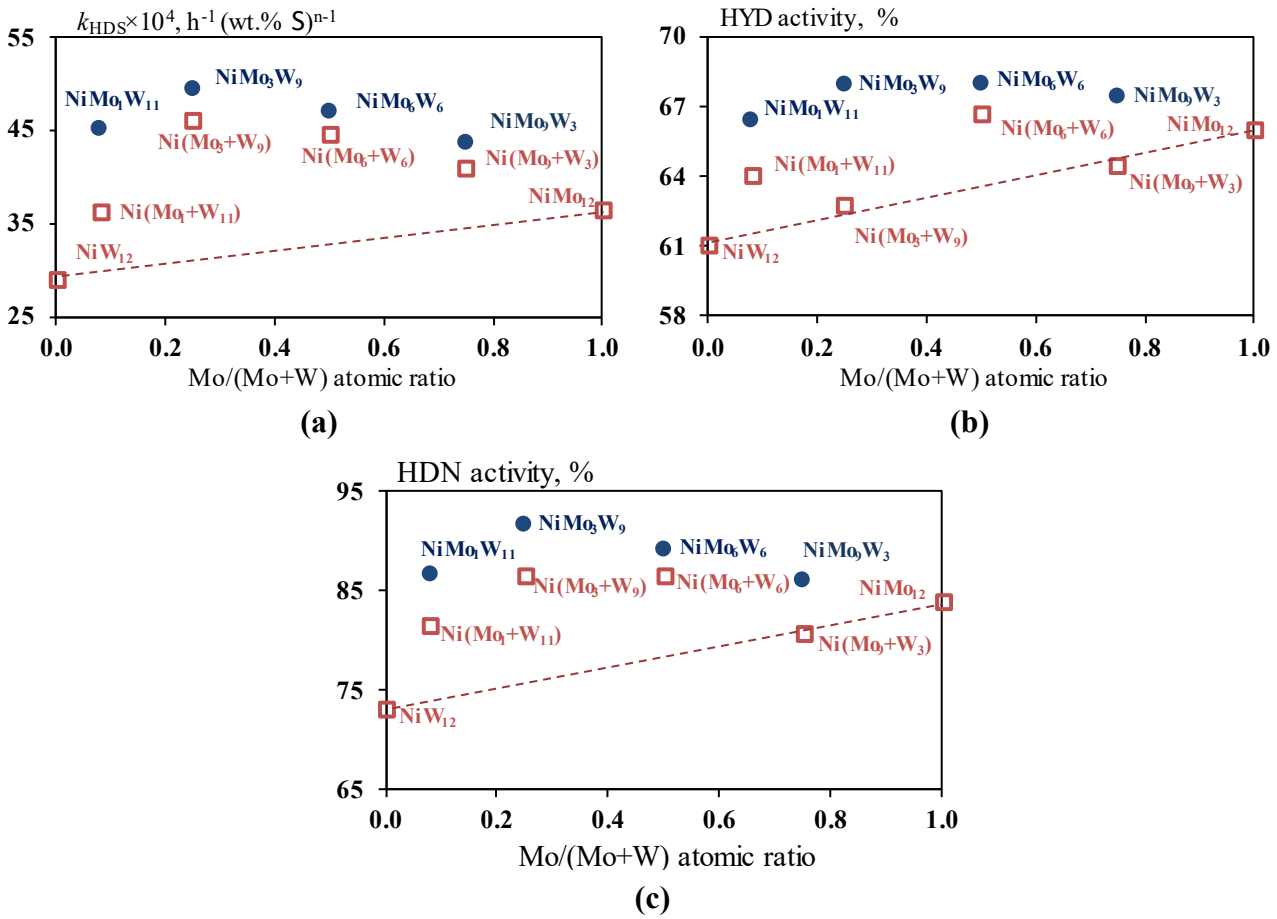

Fig. 3.11 Dependence of reaction rate constants k_{HDS} (a), HYD (b) and HDN (c) activities in HDT of SRGO on Mo/(Mo+W) atomic ratio in NiMo(W)/Al_2O_3 catalysts (dotted line indicates additive values between $NiMo_{12}/Al_2O_3$ and NiW_{12}/Al_2O_3).

In contrast to HDS (**Fig. 3.11a**), the HYD (**Fig. 3.11b)** function did not change significantly with the increase of Mo/(Mo+W) from 0.25 to 1.00 ratio in the catalysts**.** Mixed HPAs based samples exhibited higher HYD activity and, as in model reactions without quinoline, no strong effect on the HYD activity was observed with the increase in the fraction of molybdenum in the catalyst. The most abrupt increase in activity was found when one tungsten atom was replaced by molybdenum, a further increase is noted for $NiMo_3W_9$ but for higher Mo content, the values do not change much. For $Ni(Mo_n+W_{12-n})/Al_2O_3$ catalysts, no clearly pronounced dependence of the HYD activity on the atomic ratio of Mo and W is observed. High-efficiency liquid chromatographic analysis of hydrogenated products showed that only bi- and tricyclic aromatic hydrocarbons are hydrogenated, while monocyclic ones underwent almost no transformation.

It should be noted that the maximum performance in the three reactions HDN, HDS and HYD refers to the $NiMo_3W_9/Al_2O_3$ catalyst.

3.6 Conclusions

In the present chapter, NiMoW catalysts supported on alumina were prepared by co-impregnation of nickel carbonate, citric acid and mixed $SiMo_nW_{n-12}$ (n = 1, 3, 6 and 9) HPAs and characterized by different techniques. Trimetallic reference $Ni(Mo_n+W_{12-n})/Al_2O_3$ catalysts were also synthesized from a mixture of two monometallic $SiMo_{12}$ and SiW_{12} HPAs with the same Mo/W ratio as in the mixed HPAs based catalysts.

HAADF and XAS characterizations performed after gas phase sulfidation of trimetallic solids with a (Mo/Mo+W) ratio equal to 0.25 have allowed to evidence the formation of promoted mixed $MoWS_2$ slabs, where Mo islands are distributed inside the WS_2 slabs for the catalyst prepared from $SiMo_3W_9$ HPA while the active phase of the catalysts based on two separate HPAs consisted mainly of monometallic sulfide slabs. The behavior of the promoted samples towards the formation of the sulfide slabs is similar to that observed with unpromoted ones and presence of nickel does not hinder the formation of mixed clusters in HPA based catalysts.

Liquid sulfided $NiMo(W)/Al_2O_3$ catalysts were characterized by XPS and TEM. The dispersion values obtained by the TEM results indicate that the type of precursor as well as Mo/(Mo+W) ratio does not affect the distribution of the $NiMo(W)S_2$ active phase particles over the support surface. Tungsten and molybdenum sulfidation degrees in the $NiMo_nW_{12-n}/Al_2O_3$ catalysts were higher compared to the corresponding counterparts, which can be related to the simultaneous sulfidation of Mo and W due to their proximity in the initial MoW-heteropolyanion precursor, as observed in the non-promoted solids. Higher quantity of NiMoWS phase was also measured on the $NiMo_nW_{12-n}/Al_2O_3$ catalysts, where the metals thus appear better sulfided and better promoted than in the Ni(Mo+W) catalysts.

Catalytic tests were performed using liquid phase sulfidation in a bench scale flow reactor, for HDS of DBT and HYD of naphthalene with or without quinoline, as well as in the hydrotreating of a real feed (SRGO). In all reactions, mixed HPAs based $NiMo_nW_{12-n}/Al_2O_3$ catalysts presented higher activity than their $Ni(Mo_n+W_{12-n})$ counterparts, which was associated to the presence of mixed promoted $MoWS_2$ slabs as evidenced by EXAFS and HAADF results. As for non-promoted solids, the proximity of Mo and W atoms in the starting material resulted in a synergetic effect between them during sulfidation through the formation of mixed slabs, which higher efficiency was maintained after promotion.

In the presence of quinoline in the model feed, $NiMo_1W_{11}/Al_2O_3$ catalyst was the most active in HDS, HYD and HDN reactions, this catalyst being the less sensitive to the inhibiting effect of quinoline. In SRGO HDT, the optimum Mo/W ratio is shifted to $NiMo_3W_9/Al_2O_3$ sample, this difference being attributed to the lower concentration of N compounds in the SRGO. Enhanced N-

inhibition resistance being observed at a low Mo content, the Mo/(Mo+W) ratio in the catalysts should be selected depending on the content of N-containing compounds in the feed. For petroleum fractions with a high nitrogen content, NiMoW catalysts with a high tungsten content are most preferred due to their higher resistance to inhibition effect.

References

[1] C. Thomazeau, C. Geantet, M. Lacroix, M. Danot, V. Harlé, and P. Raybaud, "Predictive approach for the design of improved HDT catalysts: γ-Alumina supported (Ni, Co) promoted $Mo_{1-x}W_xS_2$ active phases," *Appl. Catal. A Gen.*, vol. 322, pp. 92–97, 2007, doi: 10.1016/j.apcata.2007.01.016.

[2] S. L. Amaya, G. Alonso-Núñez, T. A. Zepeda, S. Fuentes, and A. Echavarría, "Effect of the divalent metal and the activation temperature of NiMoW and CoMoW on the dibenzothiophene hydrodesulfurization reaction," *Appl. Catal. B Environ.*, vol. 148–149, pp. 221–230, 2014, doi: 10.1016/j.apcatb.2013.10.057.

[3] A. V. Mozhaev, M. S. Nikul'shina, C. Lancelot, P. Blanchard, C. Lamonier, and P. A. Nikul'shin, "Trimetallic Hydrotreating Catalysts CoMoW/Al_2O_3 and NiMoW/Al_2O_3 Prepared on the Basis of Mixed Mo-W Heteropolyacid: Difference in Synergistic Effects," *Pet. Chem.*, vol. 58, no. 14, pp. 1198–1205, 2018, doi: 10.1134/S0965544118140104.

[4] N. Frizi *et al.*, "Genesis of new HDS catalysts through a careful control of the sulfidation of both Co and Mo atoms: Study of their activation under gas phase," *Catal. Today*, vol. 130, no. 2–4, pp. 272–282, 2008, doi: 10.1016/j.cattod.2007.10.109.

[5] M. Sun, P. J. Kooyman, and R. Prins, "A high-resolution transmission electron microscopy study of the influence of fluorine on the morphology and dispersion of WS_2 in sulfided W/Al_2O_3 and NiW/Al_2O_3 catalysts," *J. Catal.*, vol. 206, no. 2, pp. 368–375, 2002, doi: 10.1006/jcat.2001.3503.

[6] P. P. Minaev, P. A. Nikulshin, M. S. Kulikova, A. A. Pimerzin, and V. M. Kogan, "NiWS/Al_2O_3 hydrotreating catalysts prepared with 12-tungstophosphoric heteropolyacid and nickel citrate: Effect of Ni/W ratio," *Appl. Catal. A Gen.*, vol. 505, pp. 456–466, 2015, doi: 10.1016/j.apcata.2015.05.012.

[7] J. C. Mogica-Betancourt *et al.*, "Interaction effects of nickel polyoxotungstate with the Al_2O_3-MgO support for application in dibenzothiophene hydrodesulfurization," *J. Catal.*, vol. 313, pp. 9–23, 2014, doi: 10.1016/j.jcat.2014.02.009.

[8] K. Ben Tayeb, C. Lamonier, C. Lancelot, M. Fournier, A. Bonduelle-Skrzypczak, and F. Bertoncini, "Increase of the Ni/W ratio in heteropolyanions based NiW hydrocracking catalysts with improved catalytic performances," *Catal. Letters*, vol. 144, no. 3, pp. 460–468, 2014, doi: 10.1007/s10562-013-1173-5.

[9] L. Coulier, G. Kishan, J. A. R. Van Veen, and J. W. Niemantsverdriet, "Influence of support-interaction on the sulfidation behavior and hydrodesulfurization activity of Al_2O_3-supported W, CoW, and NiW model catalysts," *J. Phys. Chem. B*, vol. 106, no. 23, pp. 5897–5906, 2002, doi: 10.1021/jp0136821.

[10] M. Nikulshina *et al.*, "Genesis of active phase in MoW/Al_2O_3 hydrotreating catalysts monitored by HAADF and in situ QEXAFS combined to MCR-ALS analysis," *Appl. Catal. B Environ.*, vol. 269, no. February, p. 118766, 2020, doi: 10.1016/j.apcatb.2020.118766.

[11] M. S. Nikulshina *et al.*, "Molecular approach to prepare mixed MoW alumina supported hydrotreatment catalysts using $H_4SiMo_nW_{12-n}O_{40}$ heteropolyacids," *Catal. Sci. Technol.*, vol. 8, no. 21, pp. 5557–5572, 2018, doi: 10.1039/c8cy00672e.

[12] S. Shan, H. Liu, Y. Yue, G. Shi, and X. Bao, "Trimetallic WMoNi diesel ultra-deep hydrodesulfurization catalysts with enhanced synergism prepared from inorganic–organic hybrid nanocrystals," *J. Catal.*, vol. 344, pp. 325–333, 2016, doi: 10.1016/j.jcat.2016.09.019.

[13] A. Olivas, D. H. Galván, G. Alonso, and S. Fuentes, "Trimetallic NiMoW unsupported catalysts for HDS," *Appl. Catal. A Gen.*, vol. 352, no. 1–2, pp. 10–16, 2009, doi: 10.1016/j.apcata.2008.09.022.

[14] S. Eijsbouts, L. C. A. Van Den Oetelaar, and R. R. Van Puijenbroek, "MoS2 morphology and promoter segregation in commercial Type 2 Ni-Mo/Al_2O_3 and Co-Mo/Al_2O_3 hydroprocessing catalysts," *J. Catal.*, vol. 229, no. 2, pp. 352–364, 2005, doi: 10.1016/j.jcat.2004.11.011.

[15] M. Nikulshina *et al.*, "Enhancing the hydrodesulfurization of 4,6-dimethyldibenzothiophene

through the use of mixed $MoWS_2$ phase evidenced by HAADF," *Catal. Today*, vol. 329, 2018, pp. 24–34, 2019, doi: 10.1016/j.cattod.2018.11.051.

[16] M. Nikulshina *et al.*, "MoW synergetic effect supported by HAADF for alumina based catalysts prepared from mixed $SiMo_nW_{12-n}$ heteropolyacids," *Appl. Catal. B Environ.*, vol. 224, 2017, pp. 951–959, 2018, doi: 10.1016/j.apcatb.2017.11.049.

[17] L. Van Haandel, M. Bremmer, P. J. Kooyman, J. A. R. Van Veen, T. Weber, and E. J. M. Hensen, "Structure-Activity Correlations in Hydrodesulfurization Reactions over Ni-Promoted $Mo_xW_{(1-x)}S_2/Al_2O_3$ Catalysts," *ACS Catal.*, vol. 5, no. 12, pp. 7276–7287, 2015, doi: 10.1021/acscatal.5b01806.

[18] N. Koizumi, Y. Hamabe, S. Jung, Y. Suzuki, S. Yoshida, and M. Yamada, "In situ observation of Ni-Mo-S phase formed on $NiMo/Al_2O_3$ catalyst sulfided at high pressure by means of Ni and Mo K-edge EXAFS spectroscopy," *J. Synchrotron Radiat.*, vol. 17, no. 3, pp. 414–424, 2010, doi: 10.1107/S0909049510004802.

[19] L. Plais, C. Lancelot, C. Lamonier, E. Payen, and V. Briois, "First in situ temperature quantification of CoMoS species upon gas sulfidation enabled by new insight on cobalt sulfide formation," *Catal. Today*, 2020, doi: 10.1016/j.cattod.2020.06.065.

[20] A. Rochet *et al.*, "Influence of the Preparation Conditions of Oxidic $NiMo/Al_2O_3$ Catalysts on the Sulfidation Ability: A Quick-XAS and Raman Spectroscopic Study," *J. Phys. Chem. C*, vol. 119, no. 42, pp. 23928–23942, 2015, doi: 10.1021/acs.jpcc.5b06219.

[21] H. Topsøe, B. S. Clausen, and F. E. Massoth, "Hydrotreating Catalysis," *Catalysis*, pp. 1–269, 1996, doi: 10.1007/978-3-642-61040-0_1.

[22] A. Cho, J. H. Koh, S. H. Moon, and A. Wang, "Performance of $NiMoS/Al_2O_3$ Catalysts Prepared by the Selective Deposition of Ni on MoS_2/Al_2O_3 in the Hydrodesulfurization of Dibenzothiophenes," *Stud. Surf. Sci. Catal.*, pp. 469–472, 2007, doi: 10.1016/b978-0-444-53202-2.50106-8.

[23] E. Schachtl, E. Kondratieva, O. Y. Gutiérrez, and J. A. Lercher, "Pathways for H_2 Activation on (Ni)-MoS_2 Catalysts," *J. Phys. Chem. Lett.*, vol. 6, no. 15, pp. 2929–2932, 2015, doi: 10.1021/acs.jpclett.5b01217.

[24] S. Albersberger, H. Shi, M. Wagenhofer, J. Han, O. Y. Gutiérrez, and J. A. Lercher, "On the enhanced catalytic activity of acid-treated, trimetallic Ni-Mo-W sulfides for quinoline hydrodenitrogenation," *J. Catal.*, vol. 380, pp. 332–342, 2019, doi: 10.1016/j.jcat.2019.09.034.

[25] V. Lavopa and C. N. Satterfield, "Response of dibenzothiophene hydrodesulfurization to presence of nitrogen compounds," *Chem. Eng. Commun.*, vol. 70, no. 1, pp. 171–176, 1988, doi: 10.1080/00986448808940626.

[26] R. Prins, "Catalytic hydrodenitrogenation," *Adv. Catal.*, vol. 46, pp. 399–464, 2001, doi: 10.1016/s0360-0564(02)46025-7.

[27] M. Egorova and R. Prins, "Mutual influence of the HDS of dibenzothiophene and HDN of 2-methylpyridine," *J. Catal.*, vol. 221, no. 1, pp. 11–19, 2004, doi: 10.1016/S0021-9517(03)00264-1.

[28] G. C. Laredo, A. Montesinos, and J. A. De Los Reyes, "Inhibition effects observed between dibenzothiophene and carbazole during the hydrotreating process," *Appl. Catal. A Gen.*, vol. 265, no. 2, pp. 171–183, 2004, doi: 10.1016/j.apcata.2004.01.013.

[29] M. Egorova and R. Prins, "Competitive hydrodesulfurization of 4,6-dimethyldibenzothiophene, hydrodenitrogenation of 2-methylpyridine, and hydrogenation of naphthalene over sulfided $NiMo/\gamma\text{-}Al_2O_3$," *J. Catal.*, vol. 224, no. 2, pp. 278–287, 2004, doi: 10.1016/j.jcat.2004.03.005.

Chapter 4

Bulk mixed MoWS hydrotreating catalysts

Introduction

In order to explore possible ways of increasing the performance of MoW based catalysts, we studied in the previous chapter the effect of support. In this chapter, we will consider another option, consisting in the removal of the support to obtain mixed bulk catalysts. Recently, there has been an increased interest in the development of bulk hydrotreating catalysts, which contain more than 90% of active phase. This interest is primarily due to the development and introduction into the industry of the bulk NiMoW catalyst (NEBULA and Celestia) by ExxonMobil and Albemarle. Many methods have been proposed for the synthesis of bulk catalysts, only some of them making it possible to obtain bulk MoWS catalysts with a mixed active phase. As already mentioned in the literature review, one of the promising methods for the synthesis of bulk catalysts is the removal of the support by acid HF etching. Moreover, unsupported MoS_2 catalysts synthesized via etching of alumina were found with higher catalytic properties compared to those prepared by other methods, due to high dispersion of active sulfide particles and good accessibility to active sites [25].

This chapter is devoted to the synthesis of mixed MoWS bulk catalysts using previously obtained supported $MoWS/Al_2O_3$ samples based on mixed $H_4SiMo_1W_{11}O_{40}$ and $H_4SiMo_3W_9O_{40}$ in order to produced systems with a previously formed mixed $MoWS_2$ active phase. The effects of catalyst composition on catalytic performance were studied in the co-hydrotreating of DBT and naphthalene. Bulk catalysts were characterized by nitrogen physisorption, powder X-ray diffraction (XRD), extended X-ray absorption fine stricture spectroscopy (EXAFS), transmission electron microscopy (TEM), X-ray photoelectron spectroscopy (XPS) and time-of-flight secondary ion mass spectrometry (ToF-SIMS).

All the obtained results were presented in an article published in the journal Catalysis Today (doi.org/10.1016/j.cattod.2020.07.018).

Catalysis Today xxx (xxxx) xxx–xxx

Contents lists available at ScienceDirect

Catalysis Today

journal homepage: www.elsevier.com/locate/cattod

Bulk hydrotreating $Mo_nW_{12-n}S_2$ catalysts based on $SiMo_nW_{12-n}$ heteropolyacids prepared by alumina elimination method

A. Kokliukhin[a,b,c], M. Nikulshina[a], A. Mozhaev[a,c], C. Lancelot[b], C. Lamonier[b], N. Nuns[d], P. Blanchard[b], A. Bugaev[e,f], P. Nikulshin[a,c,g,*]

[a] Samara State Technical University, 244 Molodogvardiyskaya St., 443100, Samara, Russia
[b] Univ. Lille, CNRS, Centrale Lille, ENSCL, Univ. Artois, UMR 8181–UCCS – Unité de Catalyse et Chimie du Solide, F-59000 Lille, France
[c] Gubkin Russian State University of Oil and Gas, Leninskiy Prospect 65, 119991, Moscow, Russia
[d] Université Lille, CNRS, INRA, Centrale Lille, ENSCL, Univ. Artois, FR 2638 - IMEC - Institute Michel-Eugène Chevreul, F-59000 Lille, France
[e] The Smart Materials Research Institute, Southern Federal University, Sladkova 178/24, 344090, Rostov-on-Don, Russia
[f] Southern Scientific Centre, Russian Academy of Sciences, Chekhova 41, 344006, Rostov-on-Don, Russia
[g] All-Russia Research Institute of Oil Refining, 6 Aviamotornaya st., Moscow, 111116, Russia

ARTICLE INFO

Keywords:
Hydrodesulfurization
Heteropolyanion
$MoWS_2$ catalysts
Unsupported catalyst
DBT
Naphthalene
EXAFS

ABSTRACT

A series of unsupported mono- and bimetallic $Mo_nW_{12-n}S_2$ catalysts were synthesized by alumina elimination from supported $Mo_nW_{12-n}S_2/Al_2O_3$ samples using acid etching. Alumina supported catalysts have been in turn prepared by using monometallic $H_4SiMo_{12}O_{40}$ and $H_4SiW_{12}O_{40}$ heteropolyacids (HPAs), their mixture with Mo/W atomic ratio equal to 1/11 and 3/9, and mixed bimetallic $H_4SiMo_1W_{11}O_{40}$ and $H_4SiMo_3W_9O_{40}$ HPAs. All catalysts were characterized by N_2 adsorption, temperature-programmed reduction (TPR), X-ray photoelectron spectroscopy (XPS), high-resolution transmission electron microscopy (HRTEM), time-of-flight secondary ion mass spectrometry (ToF-SIMS), extended X-ray absorption fine structure (EXAFS) spectroscopy and powder X-ray diffraction (XRD) and their performance were evaluated in simultaneous hydrodesulfurization (HDS) of dibenzothiophene (DBT) and hydrogenation (HYD) of naphthalene. The etching process led to a successful removal of all the support and of the partially sulfided species, with sulfidation degrees of both Mo and W above 90 % on the final bulk solids. The active phase also underwent a rearrangement, as higher average length and stacking were measured on the bulk catalysts than on the original supported ones. Mixed $MoWS_2$ phase was evidenced in all solids, prepared from mixed HPAs ($Mo_nW_{12-n}S_2$) or from the mixture of monometallic HPAs ($RefMo_nW_{12-n}S_2$), by EXAFS and ToF-SIMS, with however a larger quantity on the MoW solids. It seems that the mixed $MoWS_2$ phase observed on the supported MoW catalysts is maintained through the etching process, while on $RefMo_nW_{12-n}S_2$ the mixed phase, observed in a much lesser extent in the corresponding supported catalyst, could result from the aggregation of the monometallic slabs. $Mo_nW_{12-n}S_2$ catalysts were found more effective than the monometallic catalysts and than the corresponding $RefMo_nW_{12-n}S_2$, in both dibenzothiophene hydrodesulfurization and naphthalene hydrogenation, which was related to the presence of the mixed phase maintained through the etching of the support.

1. Introduction

Due to stricter environmental standards, the oil industry is under pressure to provide clean fuels. Therefore, in recent years, special attention has been focused on improving the activity and stability of hydrotreating catalysts for petroleum fractions. Mixed NiMoW sulfides based on alumina [1–4], silica [5] or mesostructured silica [6] demonstrated excellent catalytic activity in hydrodesulfurization (HDS) of sulfur compounds. The superiority of mixed NiMoW systems over traditional bimetallic Ni(Co)Mo(W) catalysts was attributed to the synergistic effect when using Ni, Mo and W. With the density functional theory (DFT) calculations, it was found that NiMoWS catalysts have a more optimal metal-sulfur bond energy compared to NiMoS and NiWS catalysts [2].

The use of Ni(Co)MoWS systems, in which both tungsten and molybdenum atoms are simultaneously present, allowed increasing HDS and HYD activities [1–3,7–10]. Thomazeau et al. [2] reported that the formation of mixed $MoWS_2$ crystallites is possible only from a precursor

* Corresponding author at: Samara State Technical University, 244 Molodogvardiyskaya St., 443100, Samara, Russia.
E-mail addresses: p.a.nikulshin@gmail.com, nikulshinpa@vniinp.ru (P. Nikulshin).

https://doi.org/10.1016/j.cattod.2020.07.018
Received 30 January 2020; Received in revised form 4 June 2020; Accepted 20 July 2020

which contains both closely related metals in the structure at once. The structure of the mixed active phase is greatly influenced by sulfidation conditions. Previously, for unpromoted catalysts based on mixed $H_4SiMo_3W_9O_{40}$ heteropolyacid (HPA), we found that mixed $MoWS_2$ active species with a core-shell structure, in which smaller islands of Mo were surrounded by W atoms, were formed in the gas-phase sulfidation, while in the liquid-phase sulfidation a structure with random distribution of molybdenum and tungsten atoms was formed, as visualized by HAADF [11]. Moreover, it was found that the use of a mixture of two monometallic $H_4SiMo_{12}O_{40}$ and $H_4SiW_{12}O_{40}$ HPAs led to the preferential formation of corresponding monometallic MoS_2 and WS_2 particles. In the co-hydrotreatment of DBT and naphthalene, catalysts with an ordered core-shell structure of the $MoWS_2$ active phase had highest rate constants for both HDS and HYD reactions.

In addition, the possibility of using bulk Mo(W) sulfide catalysts, which do not contain a support, in hydrotreatment processes on stationary catalyst beds is also being investigated. The concentration of active phase in these catalysts can reach 80–100 %. With the same composition of the active phase, the activity of bulk catalysts in hydroprocessing can be 1.5–1.7 times higher than that of their supported analogs. Thus, industrial bulk NiMoW NEBULA catalysts have higher catalytic activity compared to traditional alumina supported catalysts. The increase in catalytic activity can be explained by the formation of highly active trimetallic NiMoW sulfides [12]. In the middle of last year, the ExxonMobil jointly with Albemarle proposed a new catalyst, Celestia™, the successor of the NEBULA catalyst. Industrial implementation makes promising the development of new catalytic systems based on bulk mixed NiMoW sulfides.

Recently, due to the development of technologies for deep hydroconversion of heavy oil residues in three-phase suspension-type reactors (slurry-reactors) [13–16], in which nanoscale (Ni)Mo(W)S_2 particles are formed *in situ* [14–16], the interest to bulk catalysts based on transition metal sulfides, has been increasing.

Various methods for preparing bulk catalysts such as comaceration [17], homogeneous sulfide precipitation [18], thiosalt decomposition [19], hydrothermal [20,21] and solvothermal [22,23] syntheses, as well as the method of fluoric acid (HF) etching of the substrate of supported catalysts [24,25] have been described. Previously, we reported that unsupported catalysts synthesized via etching of alumina support, exhibited higher catalytic properties compared to those prepared by other methods [26], due to high dispersion of active sulfide particles and good accessibility to active sites.

Summarizing the above, it seems appropriate to combine the method of HF etching of a support and the use of mixed MoW oxide precursors to produce mixed bulk catalysts. That will allow purposefully creating catalysts with a given composition of mixed $MoWS_2$ particles. In the present work, mixed MoWS bulk catalysts were synthesized by acid etching of alumina support from supported sulfide catalysts based on mixed $H_4SiMo_1W_{11}O_{40}$ and $H_4SiMo_3W_9O_{40}$ HPAs. Catalysts prepared from mixture of two monometallic $H_4SiMo_{12}O_{40}$ and $H_4SiW_{12}O_{40}$ HPAs with the same Mo/W molar ratio as in corresponding mixed HPAs were used as reference samples. The effects of catalyst composition on catalytic performance were studied in the hydrotreating reactions of DBT and naphthalene. Prepared bulk catalysts were characterized by methods such as nitrogen physisorption, extended X-ray absorption fine stricture spectroscopy (EXAFS), transmission electron microscopy (TEM), X-ray photoelectron spectroscopy (XPS), time-of-flight secondary ion mass spectrometry (ToF-SIMS) and powder X-ray diffraction (XRD). Moreover, a comparison was made with their alumina supported counterparts in order to reveal the effect of the support.

2. Experimental

2.1. Catalyst preparation

A series of bulk $Mo_nW_{12-n}S_2$ hydrotreating catalysts was synthesized by HF etching of alumina from Mo_nW_{12-n}/Al_2O_3 catalysts. First, supported samples were prepared by the incipient wetness method via impregnation of γ-Al_2O_3 extrudates with aqueous solutions of $H_4SiMo_nW_{12-n}O_{40}$ HPAs [4,9–11]. These mixed HPAs are derived from the Keggin-type polyoxometallate $H_4SiW_{12}O_{40}$, consisting of a regular SiO_4 tetrahedron surrounded by 12 WO_6 octaedra, which are connected by shared edges to form trimetallic W_3O_{13} groups joined together by their vertices. Replacement of one or 3 W atoms by Mo led to the formation of α-$H_4SiMo_1W_{11}O_{40}$ and β-$H_4SiMo_3W_9O_{40}$ HPAs, the structure and synthesis methodology of which were described earlier by Nikulshina et al. [9]. Two catalysts were synthesized using mixed Keggin-type α-$H_4SiMo_1W_{11}O_{40}$ and β-$H_4SiMo_3W_9O_{40}$ HPAs (named as $Mo_1W_{11}S_2$ and $Mo_3W_9S_2$, respectively), another two were based on monometallic $SiMo_{12}$ and SiW_{12} HPAs (named as MoS_2 and WS_2, respectively), and finally two more bimetallic MoW reference samples were synthesized from a mixture of monometallic HPAs with Mo/W ratios of 1/11 and 3/9 (denoted Ref$Mo_1W_{11}S_2$ and Ref$Mo_3W_9S_2$, respectively). The oxidic dried samples were sulfided in a fixed-bed reactor at 400 °C for 4 h in a stream of 10 vol.% of H_2S in H_2 under atmospheric pressure. Detailed characterization of the prepared supported catalysts was described in Refs. [9,11]. After sulfidation, the samples were treated by a solution of hydrofluoric acid. A typical HF etching process was carried out as follows [24]: 10 g of sulfided Mo_nW_{12-n}/Al_2O_3 catalyst, 215 g of 45 wt.% HF, and ml of deionized water were added to a plastic beaker. Required amounts of HF were calculated to have a molar ratio HF/ Al_2O_3 of 60. This mixture was kept with magnetic stirring at 40 °C for 4 h to form a black suspension. The solid material was then filtered, washed with 50 ml of deionized water and acetone, dried in rotary evaporator under vacuum. The chemical compositions of the prepared catalysts are given in Table 1. Content of carbon and sulfur was measured using 2400 Series II CHNS elemental analyzer. Amount of metals was determined using EDX-7000P XRF analyzer. Prior the characterization of the active phase of the catalysts and evaluation of their catalytic activities, the solids were sulfided according to the method described above.

Table 1
Composition and textural properties of prepared unsupported $Mo_nW_{12-n}S_2$ catalysts.

Catalyst	Content in the catalyst (wt.%)		Mo/W atomic ratio[a]	S/(Mo + W)	Specific surface area (m^2/g)	Pore volume (cm^3/g)	Average pore diameter (nm)
	C	S					
MoS_2	2.0	35.0	–	1.8	8 / 210[b]	0.04 / 0.57[b]	< 3.8 / 7.2[b]
WS_2	1.2	25.3	–	2.2	14 / 164	0.03 / 0.48	< 3.8 / 7.9
$Mo_1W_{11}S_2$	1.4	27.2	0.15	2.2	5 / 218	0.01 / 0.56	< 3.8 / 6.8
$Mo_3W_9S_2$	1.9	29.4	0.55	2.0	5 / 179	0.01 / 0.51	< 3.8 / 6.8
Ref$Mo_1W_{11}S_2$	1.5	28.1	0.20	2.2	10 / 182	0.03 / 0.51	< 3.8 / 7.2
Ref$Mo_3W_9S_2$	1.0	30.4	0.60	2.1	3 / 190	0.04 / 0.55	< 3.8 / 7.9

[a] XRF analysis.
[b] Values for supported sulfided Mo_nW_{12-n}/Al_2O_3 catalysts.

2.2. Characterization of the catalysts

2.2.1. Textural properties of catalysts

Textural characteristics of the alumina supported sulfides and solids after HF etching were determined by N_2 physisorption at 77 K on a Quantochrome Autosorb-1 adsorption porosimeter. The samples were outgassed under vacuum at 623 K for 6 h prior to the adsorption. Specific surface areas were calculated using the BET method at a relative partial pressure P/P_0 = 0.05–0.3. Total pore volumes were determined by a desorption curve using the BJH model at a relative partial pressure P/P_0 = 0.99. Pore size distributions were calculated using DFT analysis.

2.2.2. TPR

H_2-TPR of the sulfided samples was carried out on a TPDRO 1100 apparatus with the use of a thermal conductivity detector. Analysis was held in a mixture of H_2 and N_2 (5 vol.% of H_2) under the following conditions: volume flow rate of 25 ml/min, temperature range from room temperature to 900 °C, heating rate of 10 °C /min.

2.2.3. HRTEM

The morphology of the prepared samples was investigated by means of HRTEM. HRTEM measurements were performed using a Tecnai G2 20 microscope with a 0.14 nm lattice-fringe resolution and an accelerating voltage of 200 kV. For statistical analysis, slab length and layer stacking of 400 − 600 $Mo_nW_{1-n}S_2$ crystallites were determined for each catalyst.

The average length ($\overline{L}$) was calculated as an arithmetic mean and corresponds to the average dimension of the projection of the slabs parallel to the electron beam [26]. The number of slabs per stack was determined to obtain the average stacking degree ($\overline{N}$):

$$\overline{N} = \frac{\sum_{i=1..t} n_i N_i}{\sum_{i=1..t} n_i} \quad (1)$$

where n_i is the number of stacks with N_i slabs.

The dispersion of Mo(W)S_2 species was evaluated statistically by dividing the total number of Mo(W) atoms on the edge by the total number of Mo(W) atoms using crystallite sizes determined from HRTEM, which is a common method for determining metal sulfides dispersion for supported [27,28] and bulk [29,30] catalysts. It is assumed that during sulfidation ideal hexagonal particles are formed.

2.2.4. Powder XRD

Powder XRD data collection was performed on an ARLX'TRA diffractometer with Cu Kα emission (λ = 1.54056 Å) operating at 43 kV and 38 mA and recorded peaks were identified using standard JCPDS files. The approximate crystallite dimensions of the MoS_2 slabs were calculated using the Debye-Scherrer relation [31]:

$$D_{002} = \frac{k_{002} \cdot \lambda}{\beta_{002} \cdot \cos\theta} \quad (2)$$

where D_{002} is the mean size of ordered (crystalline) domains (Å) along the stacking direction; λ is the X-ray wavelength; θ is the Bragg angle; β_{002} (or FWHM) is the line broadening at half maximum intensity; k_{002} is the dimensionless shape factor. The shape factor k_{002} depends on the crystal shape and is close to 0.9 for WS_2 [32] and to 0.76 for MoS_2 [31]. The average number of layers N was calculated using the equation $N = D_{002}/6.17$, where 6.17 Å corresponds to the value of the interlayer spacing in the 2H-WS_2 structure.

The crystallite size along the basal direction was calculated using the Debye-Scherrer Eq. (2) applied to the broadening of the diffraction peak (110). The same calculation method was previously used by de la Rosa et al. [31] for MoS_2 prepared by HF acid etching of the support. The peak (110) is not affected by imperfect stacking or bending/folding of layers [31,33]. However, Liang et al. [33] found that the shape factor k_{110} depends on the β_{110} angular line width, and this correlation between β_{110} and k_{110} was taken into account. According to the experimental angular line widths, the shape factor k_{110} was equal to 1.49.

2.2.5. XPS

XPS experiments were performed on a KRATOS Axis Ultra spectrometer with a monochromatic Al K_α source ($h\nu$ = 1486.6 eV, 150 W). The binding energy (BE) values were referred to C1s at 284.8 eV to account for charging effects [34]. The spectrum decomposition was carried out using Casa XPS software after applying a Shirley background subtraction and using Gaussian–Lorentzian (30/70) parameters. S2p, Mo3d, W4f, C1s and O1s spectra were collected. The relative concentrations of each species Mo^{6+}, Mo^{5+} (MoS_xO_y), Mo^{4+} (MoS_2) on Mo3d region (analogically for W_{4f}) were determined for all sulfided catalysts. The relative amounts of metal fractions were determined according to previous works [11,35,36].

2.2.6. EXAFS spectroscopy

The Mo K-edge and W $L_{1,2,3}$ -edges EXAFS spectra were collected at BM31 beamline of the ESRF (Grenoble, France) [37]. The sample powder was diluted with boron nitride, pressed into a pellet and sealed with Kapton tape. All spectra were recorded at room temperature in transmission mode with simultaneous collection of molybdenum and tungsten metal foils for energy calibration. The energy was selected with a double-crystal Si (111) monochromator in the continuous scanning mode. EXAFS data analysis (normalization, background removal, energy alignment, extraction of $\chi(k)$ signal and Fourier analysis) was performed in the Demeter software package [38], FEFF6 [39] was used to calculate theoretical phases and amplitudes. The following structural parameters were set as variables during the fit: interatomic distances (R), coordination numbers (N), Debye-Waller factors (σ^2) for Mo–Mo, Mo–S, Mo–W (and W–Mo), W–W, and W–S scattering paths. To reduce the number of variables, R and σ^2 for W–Mo path were set equal to the corresponding values of Mo–W path. The equation $N_{W-Mo} = \frac{N_{Mo-W}}{3}$ was also applied, based on the stoichiometric ratio of the two metals. Two energy shifts (ΔE_0) were used for all paths at Mo K- and L_3-edges The fit was performed in R-space in 1.2–3.4 Å range using a multiple k-weighted data (1,2,3). The Fourier-transformation ranges for Mo K-edge and W L_3-edge were set to Δk_K = 3.5-15.0 $Å^{-1}$, Δk_{L3} = 4.3-16.3 $Å^{-1}$, respectively. Amplitude reduction factors (S_0^2) were obtained by fitting bulk MoS_2 and WS_2 references. For direct comparison, the same fitting strategy was applied for the analysis of the data previously collected for the supported catalysts [9].

2.2.7. ToF-SIMS measurements

ToF-SIMS measurements were performed with a TOF.SIMS 5 spectrometer (ION-TOF GmbH Germany) equipped with a bismuth liquid metal ion gun (LMIG). The compacted samples were bombarded with pulsed Bi_3^+ primary ion beam (25 keV, 0.25 pA) rastered over a 100 × 100 m^2 surface area. With 30 scans and 128 × 128 pixels, the total primary ion dose does not amount up to 1012 ions/cm^2 ensuring static conditions. Charge effects due to primary ion beam were compensated by means of a 20 eV pulsed electron flood gun. Cycle time was fixed at 150 µs in order to detect secondary molecular ions up to 2000 m/z. The mass resolution (m/Δm) measured on our spectra was about 4000 at m/z = 143 for MoO_3^-. This good mass resolution allowed us to identify high m/z ionic fragments by their exact mass and the attribution could be confirmed most of the time by the simulated isotopic pattern.

2.3. Catalytic performances

The HDT activity tests were performed in a bench-scale flow reactor at 320 °C, 3.0 MPa total pressure of hydrogen, with a liquid hourly space velocity (LHSV) of 40 h^{-1} and a 500 NL/L volume ratio of hydrogen to feed. Pre-sulfided $Mo_nW_{1-n}S_2$ catalysts (0.2 g) were diluted with 0.6 cm^3 of low-surface-area carborundum (0.2–0.4 mm) and

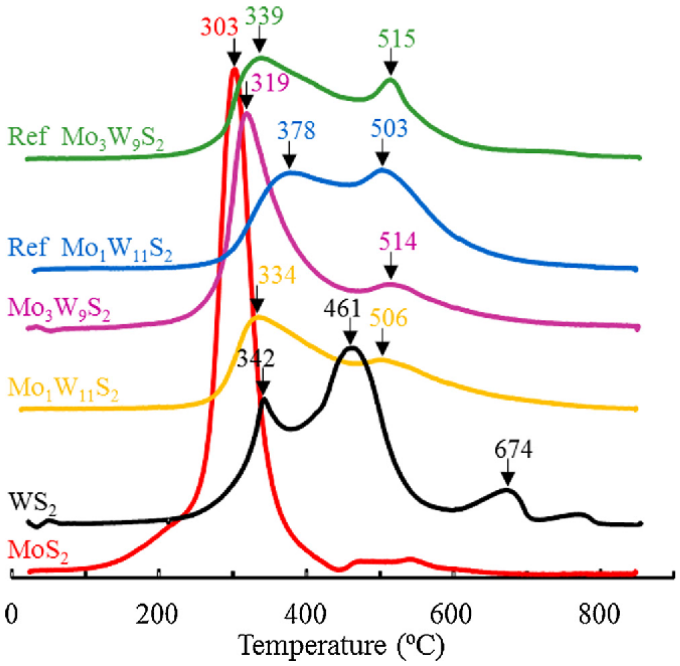

Fig. 1. H_2-TPR profiles for unsupported $Mo_nW_{12-n}S_2$ catalysts.

placed in the center of the reactor with an internal diameter of 0.8 cm. A toluene solution of DBT (Aldrich, 1500 ppm of S), naphthalene (Aldrich, 3 wt.%) and hexadecane (as an internal standard, 1 wt.%) was used as a model feedstock. The liquid product compositions of the samples collected every hour were determined using a Crystall-5000 Gas Chromatograph equipped with a 30 m OV-101 column. The reaction products were identified by matching retention times with those of commercially available standards and by GC/MS analysis using a Finnigan Trace DSQ. All catalysts exhibited stable performance, achieving a steady state after 7–10 h.

The rate constants of the pseudo-first-order reactions of the DBT HDS and naphthalene HYD were determined using the following equations:

$$k_{HDS} = -\frac{F_{DBT}}{W}\ln(1 - x_{DBT}) \text{and} k_{HYD} = -\frac{F_{Naph}}{W}\ln(1 - x_{Naph}), \quad (3)$$

where k_{HDS} and are the pseudo-first-order reaction constants for the DBT HDS and naphthalene HYD (mol g^{-1} h^{-1}), respectively, x_{DBT} and x_{Naph} are the conversions (%) of DBT, and naphthalene, respectively, F_{DBT} and F_{Naph} are the reactant flows in moles (mol h^{-1}) and W is the weight of the catalyst (g).

The HDS products from DBT included biphenyl (BP) via the direct desulfurization (DDS) pathway, as well as cyclohexylbenzene (CHB) and dicyclohexyl (DCH) from the HYD pathway. Only traces of hydrogenated tetrahydro- and hexahydrodibenzothiophenes were observed. The HYD/DDS selectivity was calculated according to the reaction network for DBT HDS:

$$S_{HYD/DDS} = \frac{k_{HYD}}{k_{DDS}} = \frac{C_{CHB} + C_{DCH}}{C_{BP}} \quad (4)$$

where C_{CHB}, C_{BCH} and C_{BP} are the concentrations (mol.%) of CHB, DCH and BP in the reaction products, respectively.

The turnover frequencies (TOF, s^{-1}) normalized on edge sites of $Mo_nW_{12-n}S_2$ slabs for the HDS of DBT, HYD of naphthalene allowed us to get more complete understanding of the catalytic properties of the active phase species. TOF values were calculated using the following equations:

$$TOF_{HDS} = \frac{F_{DBT}\cdot x_{DBT}}{W\cdot\left(\frac{C_{WS_2}}{Ar_W} + \frac{C_{MoS_2}}{Ar_{Mo}}\right)\cdot D\cdot 3600} \text{and} TOF_{HYD} = \frac{F_{Naph}\cdot x_{Naph}}{W\cdot\left(\frac{C_{WS_2}}{Ar_W} + \frac{C_{MoS_2}}{Ar_{Mo}}\right)\cdot D\cdot 3600}, \quad (5)$$

here F_{DBT} and F_{Naph} are the reactant flows (mol h^{-1}), x_{DBT} and x_{Naph} are the conversions (%) of DBT and naphthalene, respectively; W is the weight of the catalyst (g); and are the effective content of W and Mo, respectively, in $Mo_nW_{12-n}S_2$ species (wt.%); D is the dispersion of $Mo_nW_{12-n}S_2$ species; Ar_W and Ar_{Mo} are the standard atomic weights of tungsten (183.9 g/mol) and molybdenum (95.9 g/mol), respectively.

3. Results

3.1. Textural properties of catalysts

The textural properties of the prepared samples are summarized in Table 1. Sulfided alumina-based precursors displayed surface areas in the range of 164 to 218 m^2/g and pore volumes around 0.53 cm^3/g. The alumina removal resulted in a decrease of the surface area to 3 − 14 m^2/g and pore volume to 0.01 − 0.04 cm^3/g. These significant changes in the textural properties are related to the total removal of the porous support. X-ray fluorescence and XPS analysis confirmed the absence of aluminum and silicon in the solids after etching procedure. According to Fig. S1, all materials exhibit adsorption isotherms similar to type I with virtually a non-porous structure. These results are in agreement with those previously reported for bulk catalysts [40–43].

3.2. TPR analysis

Fig. 1 shows the H_2-TPR profiles of the unsupported $Mo_nW_{12-n}S_2$ catalysts and of their references. The reduction of the MoS_2 sample proceeded in the region 100 − 400 °C with a maximum at 303 °C. The TPR profiles of WS_2 displayed two reduction regions: 250 − 400 °C (T_{max} = 342 °C) and 400 − 600 °C (T_{max} = 461 °C). The appearance of a peak in the high-temperature region for WS_2 can be attributed to stronger W−S bond than Mo–S [44]. All bimetallic catalysts also exhibited two main reduction peaks. According to the literature [45–47], the first low-temperature peak corresponds to surface weakly bonded sulfur. Afanasiev et al. [46] believe that after the reduction of surface sulfur, coordinative unsaturated sites (CUS) are formed, which in turn are responsible for the reactions that occur on the surface of the catalyst. This allows to indirectly estimate the possible number of active sites. Lower reduction temperatures of mixed HPA based catalysts are observed compared to that of their corresponding references: 334 and 378 °C for $Mo_1W_{11}S_2$ and its reference, 319 and 339 °C for $Mo_3W_9S_2$ and its reference for the first reduction peak. This can be related to a decrease in the strength of the metal-sulfur bond due to the formation of mixed $MoWS_2$ particles with a more optimal bond energy value [48]. As the molybdenum loading increased, the reducibility of the catalysts was enhanced as indicated by the decrease in the reduction temperature (342 °C for WS_2, 334 °C for $Mo_1W_{11}S_2$, 319 °C for $Mo_3W_9S_2$) and the increase in H_2 consumption (230 mmol/mol for WS_2, 390 mmol/mol for $Mo_1W_{11}S_2$, 640 mmol/mol for $Mo_3W_9S_2$, Table 2). Furthermore, the H_2 consumption was higher for the samples based on MoW HPAs than for their analogs prepared from a mixture of separate HPAs (390 and 367 mmol/mol for $Mo_1W_{11}S_2$ and its Ref, 640 and 450 mmol/mol for $Mo_3W_9S_2$ and its Ref), which indicates that a larger amount of active sites is present in the $Mo_nW_{12-n}S_2$ catalysts.

The maxima temperature of the first reduction peak was lower in the supported catalysts than in the corresponding bulk ones after HF etching. H_2 consumption of all tungsten-containing catalysts was higher than the values of corresponding alumina supported samples (Table 2), which can be related to a larger amount of active sites through increasing the number of Mo(W)S_2 species.

Table 2
Quantitative H_2-TPR results of unsupported $Mo_nW_{12-n}S_2$ catalysts.

Catalyst	1st peak		2nd peak		3rd peak		Total H_2 cons. (mmol/mol M)
	T_{max} (ºC)	H_2 cons. (mmol/mol M)	T_{max} (ºC)	H_2 cons. (mmol/mol M)	T_{max} (ºC)	H_2 cons. (mmol/mol M)	
MoS_2	303 / 343[a]	715 /1453[a]	–	–	–	–	715
WS_2	342 / 259	230 / 99	461	604	674	60	895
$Mo_1W_{11}S_2$	334 / 255	390 / 247	506	232	–	–	622
$Mo_3W_9S_2$	319 / 263	640 / 258	514	174	–	–	813
$RefMo_1W_{11}S_2$	378 / 252	367 / 180	503	379	–	–	746
$RefMo_3W_9S_2$	339 / 269	450 / 330	515	202	–	–	670

[a] Values for supported sulfided Mo_nW_{12-n}/Al_2O_3 catalysts.

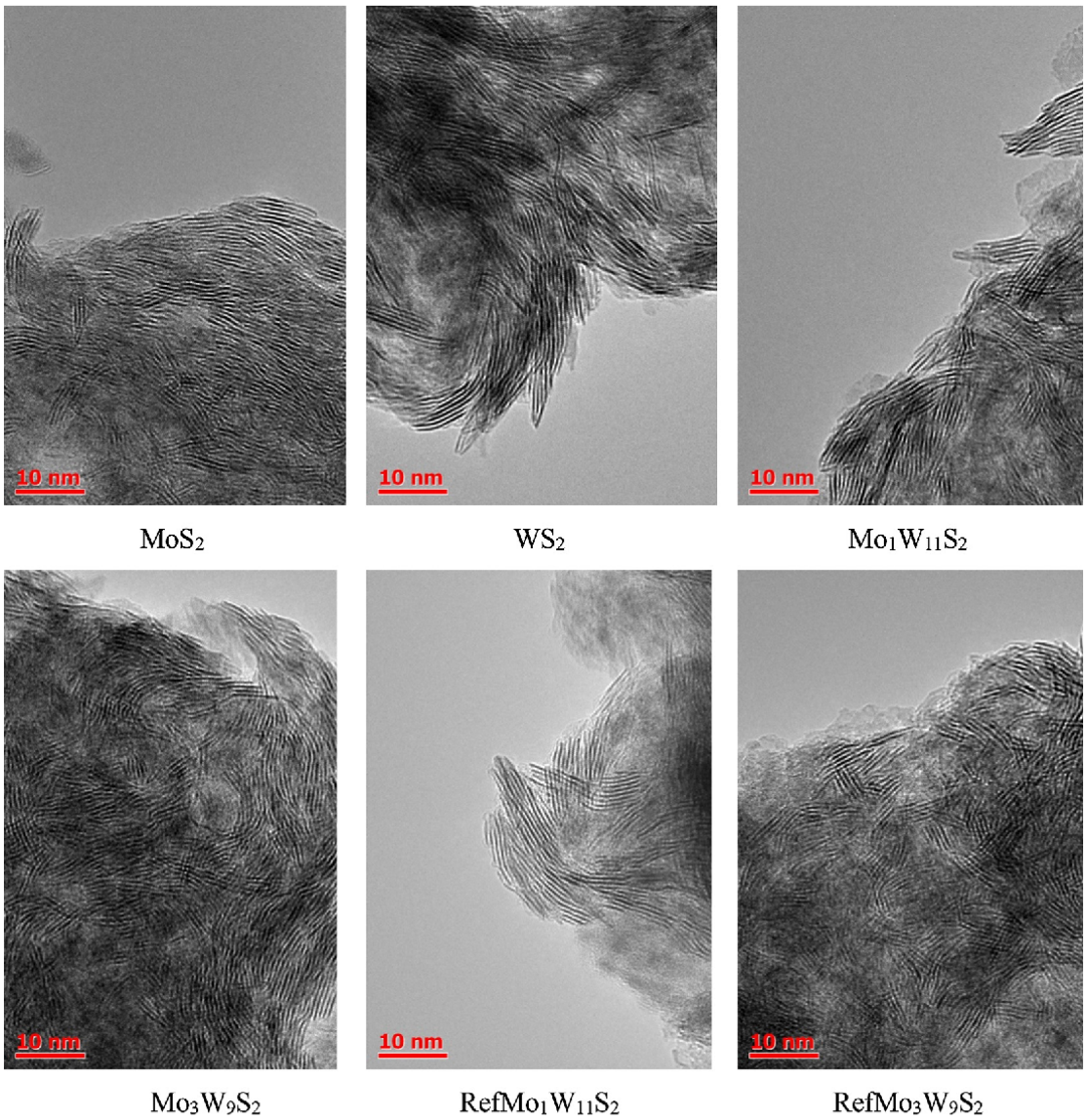

Fig. 2. HRTEM micrographs of unsupported $Mo_nW_{12-n}S_2$ catalysts.

3.3. Morphology of the active phase

Morphology of $Mo_nW_{12-n}S_2$ particles was investigated by HRTEM. Fig. 2 shows representative TEM images taken for bulk samples. Typical fringes of Mo(W)S_2 crystallites with 6.1 Å interplanar distances were observed on micrographs of all sulfided catalysts. Average length and stacking of bulk $Mo_nW_{12-n}S_2$ catalysts are shown in Table 3. Monometallic WS_2 catalyst had the highest average length (6.7 nm) and stacking (3.5) among all the prepared samples. MoS_2 species of pure molybdenum catalyst were shorter (5.2 nm) and a little less stacked than those of pure tungsten disulfide one. Addition of molybdenum atoms in the content of the catalysts resulted in a decrease in size of sulfided slabs. Both bimetallic reference catalysts had almost the same average length despite different Mo contents, while the particles size decreased with the increase of Mo amount in mixed HPAs based catalysts. All bimetallic samples had an average stacking around 3.0, which expectedly exceeded the values for conventional supported catalysts with 1–2 stacking layers [49,50]. Therefore, removing of the alumina support led to agglomeration of Mo(W)S_2 species and to reduction of their dispersion compared to initial supported ones.

Table 3
Morphological characteristics of $Mo_nW_{12-n}S_2$ active phase species calculated from TEM micrographs and XRD.

Catalyst	Average length $\overline{L}$ (nm)		Average stacking number $\overline{N}$		Dispersion of $Mo_nW_{12-n}S_2$ D^b	Distribution of slab length (rel.%)					Distribution of stacking number (rel. %)			
						< 2	2.4	4.6	6.8	> 8	1	2	3	> 3
MoS_2	5.2[a]	6.3[b]	3.3[a]	4.2[b]	0.19	3	34	34	15	14	14	17	25	44
WS_2	6.7	9.6	3.5	4.8	0.13	1	32	23	18	26	6	16	30	48
$Mo_1W_{11}S_2$	5.5	7.8	3.1	4.4	0.16	1	26	37	23	13	11	25	29	35
$Mo_3W_9S_2$	5.2	7.9	3.0	4.5	0.16	4	96	–	–	–	14	29	22	35
$RefMo_1W_{11}S_2$	4.9	7.9	3.0	4.5	0.16	2	32	44	18	4	8	32	26	34
$RefMo_3W_9S_2$	4.8	6.5	3.1	4.2	0.19	3	97	–	–	–	7	29	27	37

[a] Obtained from TEM analysis.
[b] From XRD data.

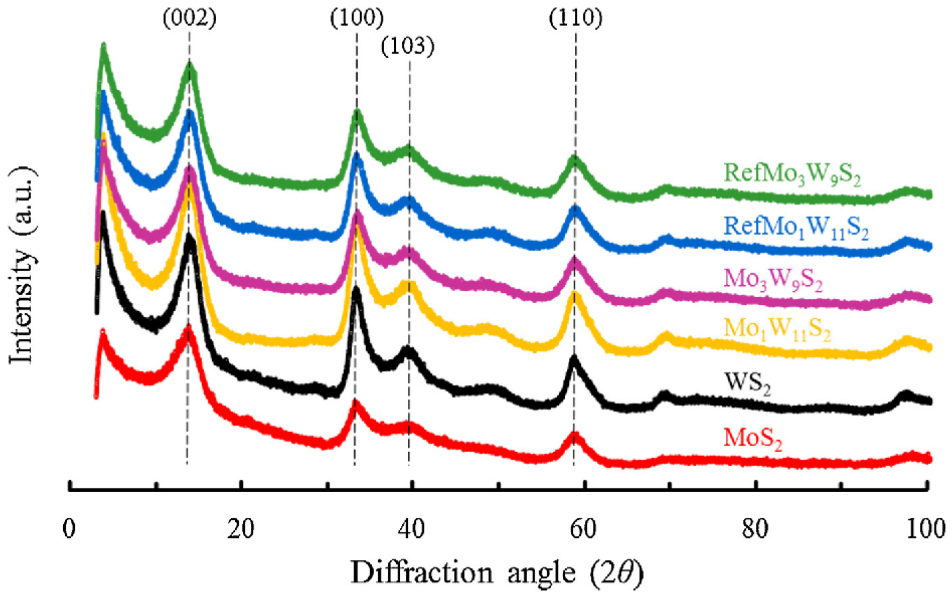

Fig. 3. XRD patterns of unsupported $Mo_nW_{12-n}S_2$ catalysts.

3.4. XRD

The XRD patterns of the prepared $Mo_nW_{12-n}S_2$ catalysts are given in Fig. 3. All samples exhibited several well-resolved XRD peaks at 14 (002), 33 (100), 40 (103), and 59° (110) 2θ corresponding to MoS_2 (WS_2) structure. It can be seen that the results of XRD do not allow to identify a difference in the structure of prepared bimetallic catalysts due to slight shifts of the reflections between MoS_2 and WS_2 phases. Average crystallite sizes were estimated by Debye-Scherrer equation (Table 3). Monometallic references WS_2 and MoS_2 catalysts had the longest and the shortest sulfide slabs, respectively, as observed by HRTEM. Average length and stacking of crystallite in both mixed HPAs based samples and $RefMo_1W_{11}S_2$ were equivalent and less than those of WS_2. In contrast, the values calculated for $RefMo_3W_9S_2$ were close to MoS_2 catalyst. Such decrease of particles size indicated that the sample prepared from two HPAs may have separate monometallic MoS_2 and WS_2 species. In addition, it should be noted that, on the one side, a slight difference in the cell parameters of MoS_2 and WS_2 phases may also result in increasing the width of XRD peaks, leading to an underestimated value of the particle size, and on the other side, TEM results are weighted by the number of particles, while XRD is weighted by particle volume, i.e. larger particles give more contribution.

3.5. Sulfidation of metals evaluated by XPS

Fig. 4 shows examples of decomposition of Mo 3d and W 4f XPS spectra of the sulfided $Mo_nW_{12-n}S_2$ catalysts. The Mo spectra exhibit a Mo $3d_{5/2}$ peak at about 229.0 eV characteristic of MoS_2 [4,34,35,51], the W 4f spectra contain $4f_{5/2}$ peak at about 32.4 eV, associated with WS_2 [4,11,50,52].

Table 4 gives the metal fractions of molybdenum and tungsten species present on the surface of the synthesized $Mo_nW_{12-n}S_2$ catalysts. All studied samples had a high sulfidation degree of metals (92 rel.% and more), corresponding to an increase of around 8 % for Mo and more than 30 % for W compared to supported catalysts [11]. That high amount of metals in the Mo(W)S_2 phase and the near absence of oxide and oxysulfide species is the result of HF etching, where only fully sulfided species were resistant. Surface Mo/W ratios were close to the bulk values determined by XRF analysis due to homogeneous distribution of particles in bulk solids. Higher Mo/W atomic ratios were detected in bulk sulfide solids compared to supported precursors. This result can be explained by the higher percentage of tungsten oxide and oxysulfide species compared to molybdenum ones contained in sulfided Mo(W)/Al_2O_3 catalysts [11], that were completely dissolved during the HF treatment. The S/metal atomic ratios for all catalysts were close to the theoretical value of 2 expected for MoS_2/WS_2.

3.6. EXAFS analysis

Fig. 5 compares the magnitude of k^3-weighted Fourier transformed (FT) EXAFS data for both unsupported and supported [9] $Mo_nW_{1-n}S_2$ catalysts (solid and dashed lines, respectively). The spectra of all catalysts exhibit two main peaks at ca. 2.0 Å and 2.9 Å (phase-uncorrected) corresponding to metal-sulfur (M–S) and metal-metal (M–M) scatterings, respectively. The shape of FT EXAFS spectra of the $Mo_nW_{1-n}S_2$ catalysts depends on the starting oxide precursor. In both Mo *K* and

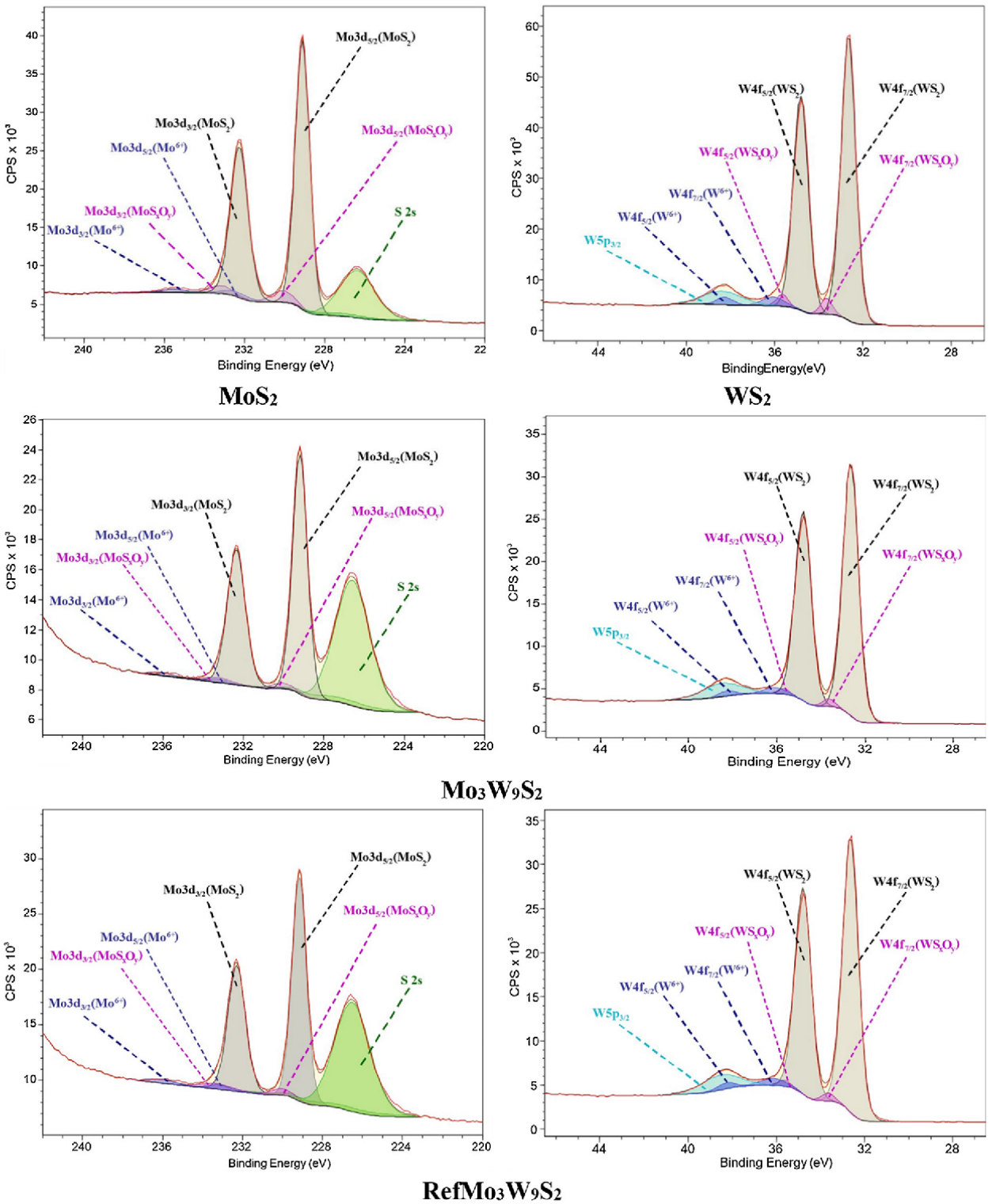

Fig. 4. XPS Mo 3d and W 4f spectra recorded for unsupported $Mo_nW_{12-n}S_2$ catalysts; in blue: $Mo(W)^{6+}$ oxide contributions; in pink: $Mo(W)S_xO_y$ contributions; in gray: $Mo(W)S_2$ contributions (For interpretation of the references to color in this figure legend, the reader should refer to the web version of the article).

W L_3-edge spectra, the highest peak intensity in the region of 3 Å (phase-uncorrected) was observed for monometallic MoS_2 and WS_2 catalysts, while this intensity was lower in bimetallic samples, especially in the case of the catalyst based on the mixed $SiMo_3W_9$ HPA. This fact is indicative of the presence of two different metal-metal contributions (homo- and heterometallic) in the second coordination shell. Indeed, the W–W (Mo–Mo) and W(Mo)–Mo(W) contributions have similar frequencies, but are out of phase and cancel each other, which leads to a decrease in the amplitude of the resulting $\chi(k)$ and $\chi(R)$ signals as shown in Fig. S3. The same effect leads to a high uncertainty in the determination of the total Mo–M and W–M coordination numbers, which was overcome by fixing $N_{W-Mo} = \frac{N_{Mo-W}}{3}$, based on the stoichiometric ratio of the two metals.

The obtained best-fit values are listed in Table 5. All catalysts have relatively high sulfidation degree with N_{M-S} ~5–6 depending on the sample. The second shell of monometallic samples contains one M–M contribution at 3.16 Å: Mo–Mo in MoS_2 (N_{Mo-Mo} = 3.7) and W–W in WS_2 (N_{W-W} = 4.4). The total M-M coordination numbers increase after elimination of the support indicating a larger length of the slabs. The coordination numbers M–M in bimetallic catalysts depend on the initial

Table 4
Metal fractions measured by XPS for molybdenum and tungsten species present in unsupported $Mo_nW_{12-n}S_2$ catalysts.

Catalyst	Mo/ W at. ratio	S/ (Mo + W)	Mo fraction (rel.%)			W fraction (rel.%)		
			MoS_2	MoS_xO_y	Mo^{6+}	WS_2	WS_xOy	W^{6+}
MoS_2	–	1.8	92	5	3	–	–	–
WS_2	–	2.2	–	–	–	92	4	4
$Mo_1W_{11}S_2$	0.16	2.2	98	2	0	92	4	4
$Mo_3W_9S_2$	0.57	2.0	93	3	4	95	2	3
$RefMo_1W_{11}S_2$	0.22	2.2	94	5	1	94	3	3
$RefMo_3W_9S_2$	0.68	2.1	92	4	4	95	2	3

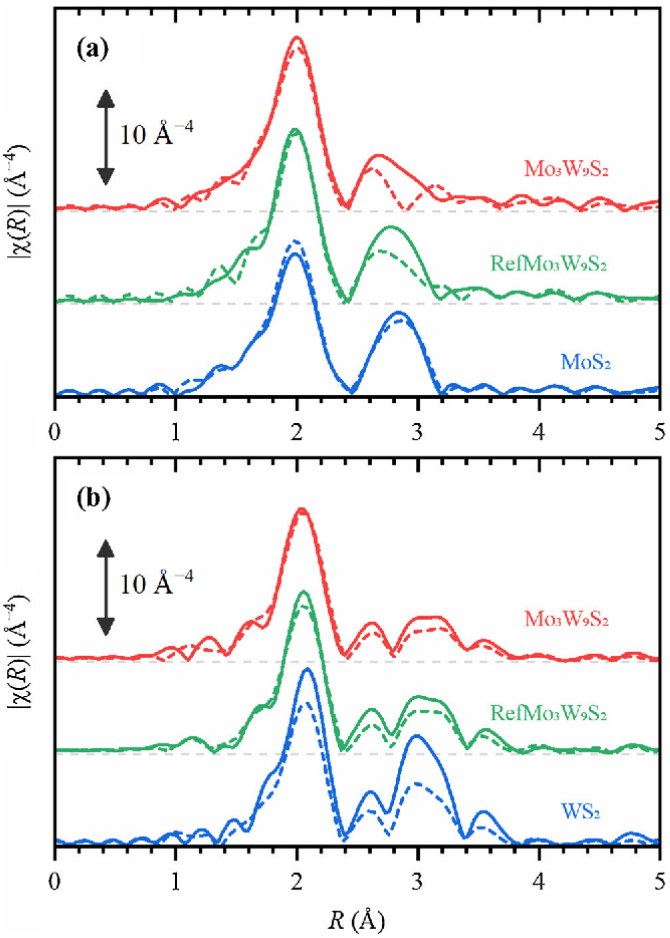

Fig. 5. Phase-uncorrected Fourier transformed Mo *K*- (a) and W L_3- (b) edges k^3-weighted EXAFS data for unsupported monometallic (blue lines) and bimetallic (red lines) catalysts. Green lines correspond to the sample prepared from the mixture of monometallic HPAs. Dashed lines correspond to the data for similar supported catalysts reported in [9]. Corresponding $\chi(k)$ signals are shown in Fig. S2 of the Supporting Information.

precursor. At both Mo *K*- and W L_3-edges, $N_{M1\text{-}M2}$ (where M1 and M2 correspond to different types of metal atom) is higher in the mixed HPA based catalyst than in its bimetallic reference, which evidences the formation of a bimetallic $MoWS_2$ phase. Reference bimetallic samples also contain a mixed M1-M2 contribution, but the corresponding coordination numbers are very close to the experimental uncertainty. To highlight the structural changes induced by the elimination of the support, the corresponding values for the supported catalyst [9] analyzed using the same fitting model are reported in brackets.

3.7. ToF-SIMS analysis

Two zones were analyzed by ToF-SIMS on Mo_1W_{11} and Mo_3W_9 as well as on their reference counterparts $RefMo_1W_{11}S_2$ and $RefMo_3W_9S_2$. This technique allows to investigate possible interaction between Mo and W, as it probes the top layers (1 − 3 nm) of the catalysts and gives molecular information about surface and interfaces. $Mo_xO_yS_z^-$ and $W_xO_yS_z^-$ monometallic fragments were indeed recorded on pure MoS_2 and WS_2 (Fig. 6). On the mixed catalysts, in addition to these monometallic fragments, mixed fragments containing Mo and W are also evidenced (Fig. 6 and Fig. S4). These fragments clearly show that a close interaction exists between Mo and W in the bulk catalysts, indicating that the mixed $MoWS_2$ phase evidenced in the supported catalysts is maintained after etching of the support. The intensity of each identified mixed oxide fragments was normalized in order to compare the four catalysts, as illustrated in Fig. 7. Normalization was performed using fragment intensity of $^{182}WS^-$. If mixed fragments are obtained on all the samples, the intensity of the corresponding peaks is higher on the catalysts prepared from mixed $SiMo_nW_{12-n}$ HPA compared to those prepared from a mixture of monometallic HPAs, as observed on the corresponding supported catalysts.

3.8. Catalytic performances

Catalytic behavior of the synthesized $Mo_nW_{12-n}S_2$ catalysts was evaluated in simultaneous HDT of two model compounds, DBT and naphthalene (Table 6). The results indicated that, under the chosen reaction conditions, substitution of one or three tungsten atoms by molybdenum in the catalyst composition resulted in an increase in HDS as well HYD activities compared to monometallic MoS_2 and WS_2 references, regardless of the precursor type. HDS activities in the two catalysts with Mo/W ratio = 1/11 were close. However, the $Mo_3W_9S_2$ catalyst prepared from the mixed $SiMo_3W_9$ HPA has a twice-higher catalytic activity than its $RefMo_3W_9S_2$ counterpart prepared from mixture of two separate HPAs in both studied reactions (conversions of 50 and 29 % respectively in HDS and conversions of 35 and 18 % respectively in HYD). These results clearly show the advantage of using the mixed $SiMo_3W_9$ HPA as the starting oxidic precursor for the synthesis of bimetallic bulk $MoWS_2$ catalyst.

The detailed analysis of the reaction products shows that for all studied catalysts, the preferential pathway in DBT HDS is pre-HYD. Selectivity HYD/DDS ratio of the prepared catalysts ranges from 1.0 to 2.8.

4. Discussion

In order to gain a better understanding of the synergetic effect between molybdenum and tungsten, the rate constants in HDS and HYD were calculated by additive way based on the results obtained over monometallic MoS_2 and WS_2 references catalysts. Experimental values of the rate constants in DBT HDS and naphthalene HYD over $Mo_1W_{11}S_2$ and $Mo_3W_9S_2$ surpass the theoretical ones by 1.4 and 2.7 times, respectively. Catalytic activities of bimetallic reference samples are also higher than predicted, however, the difference is smaller.

A comparison of catalytic properties of unsupported and alumina based catalysts shows that alumina etching results in an increase of total HDS and HYD activity that can be attributed to the absence of metal-support interaction and, as a consequence, raise of metal sulfidation degree (Fig. 8). It should be noted that in case of bulk catalysts, the WS_2 sample based on monometallic SiW_{12} HPA demonstrated improved catalytic properties compared to monometallic MoS_2 one. We suggest that there are two possible reasons for this effect: (i) more significant concentration of sulfide species (WS_2) in W-based catalyst during support removing due to dissolution of low active in catalysis oxide and oxysulfide particles contained in a larger amount in W-based catalyst compared to Mo-based one; (ii) more covalent W–S strength in bulk WS_2 sample due to the absence of oxysulfide species compared to supported WS_2/Al_2O_3 analog.

HF acid treatment of alumina supported sulfide catalysts leads to an

Table 5
Structural parameters obtained from the Fourier-analysis of Mo *K*- and W L_3-edges EXAFS spectra of unsupported $Mo_nW_{12-n}S_2$ catalysts. The values in brackets correspond to the supported catalysts. The values for W–Mo scattering path given without the uncertainty were linked to the values for Mo–W path.

Scattering path	*N*	*R* (Å)	$\sigma^2 \cdot 10^3$ (Å^2)	ΔE_0 (eV)	*R*-factor
MoS_2					
Mo–S	5.3 ± 0.2	2.41 ± 0.01	4.1 ± 0.3	1.4 ± 0.4	0.0023
	(6.1 ± 0.2)	(2.41 ± 0.01)	(4.3 ± 0.2)	(2.5 ± 0.4)	(0.0016)
Mo–Mo	3.7 ± 0.4	3.16 ± 0.01	4.9 ± 0.5		
	(3.9 ± 0.4)	(3.17 ± 0.01)	(5.3 ± 0.5)		
WS_2					
W–S	5.3 ± 0.4	2.41 ± 0.01	2.4 ± 0.5	8.8 ± 1.0	0.0115
	(4.5 ± 0.3)	(2.41 ± 0.01)	(3.0 ± 0.5)	(8.7 ± 1.1)	(0.0133)
W–W	4.4 ± 1.0	3.16 ± 0.01	3.3 ± 0.7		
	(3.9 ± 0.4)	(3.16 ± 0.01)	(4.0 ± 1.0)		
$Mo_3W_9S_2$					
Mo–S	5.8 ± 0.4	2.41 ± 0.01	3.4 ± 0.6	2.6 ± 1.0	0.0116
	(6.0 ± 0.4)	(2.42 ± 0.01)	(3.8 ± 0.7)	(2.4 ± 1.1)	(0.0063)
Mo–Mo	3.4 ± 1.5	3.16 ± 0.01	4.9 ± 2.6		
	(1.9 ± 1.3)	(3.17 ± 0.02)	(3.9 ± 3.9)		
Mo–W	2.8 ± 2.0	3.17 ± 0.03	6.3 ± 4.2		
	(2.6 ± 1.5)	(3.18 ± 0.02)	(4.6 ± 3.1)		
W–S	5.2 ± 0.4	2.41 ± 0.01	3.1 ± 0.6	8.2 ± 1.2	
	(5.3 ± 0.2)	(2.41 ± 0.01)	(3.7 ± 0.4)	(8.9 ± 0.8)	
W–W	2.8 ± 1.2	3.16 ± 0.01	4.1 ± 1.5		
	(2.4 ± 0.8)	(3.17 ± 0.01)	(4.3 ± 1.1)		
W–Mo	0.9 (0.9)	3.17 (3.18)	6 (5)		
Reference $Mo_3W_9S_2$					
Mo–S	5.8 ± 0.4	2.41 ± 0.01	3.5 ± 0.5	2.5 ± 0.9	0.0148
	(6.0 ± 0.5)	(2.42 ± 0.01)	(3.8 ± 0.8)	(2.9 ± 1.2)	(0.0056)
Mo–Mo	3.6 ± 1.2	3.16 ± 0.01	4.2 ± 1.9		
	(3.0 ± 1.5)	(3.17 ± 0.01)	(4.2 ± 2.9)		
Mo–W	2.0 ± 1.7	3.16 ± 0.03	6.0 ± 5.1		
	(1.6 ± 1.3)	(3.18 ± 0.02)	(3.6 ± 4.0)		
W–S	4.8 ± 0.3	2.41 ± 0.01	2.4 ± 0.5	7.6 ± 1.1	
	(5.1 ± 0.2)	(2.41 ± 0.01)	(3.4 ± 0.4)	(8.8 ± 0.8)	
W–W	2.8 ± 1.0	3.16 ± 0.01	3.6 ± 1.2		
	(2.4 ± 0.7)	(3.17 ± 0.01)	(3.8 ± 1.1)		
W–Mo	0.7 (0.5)	3.16 (3.18)	6 (4)		

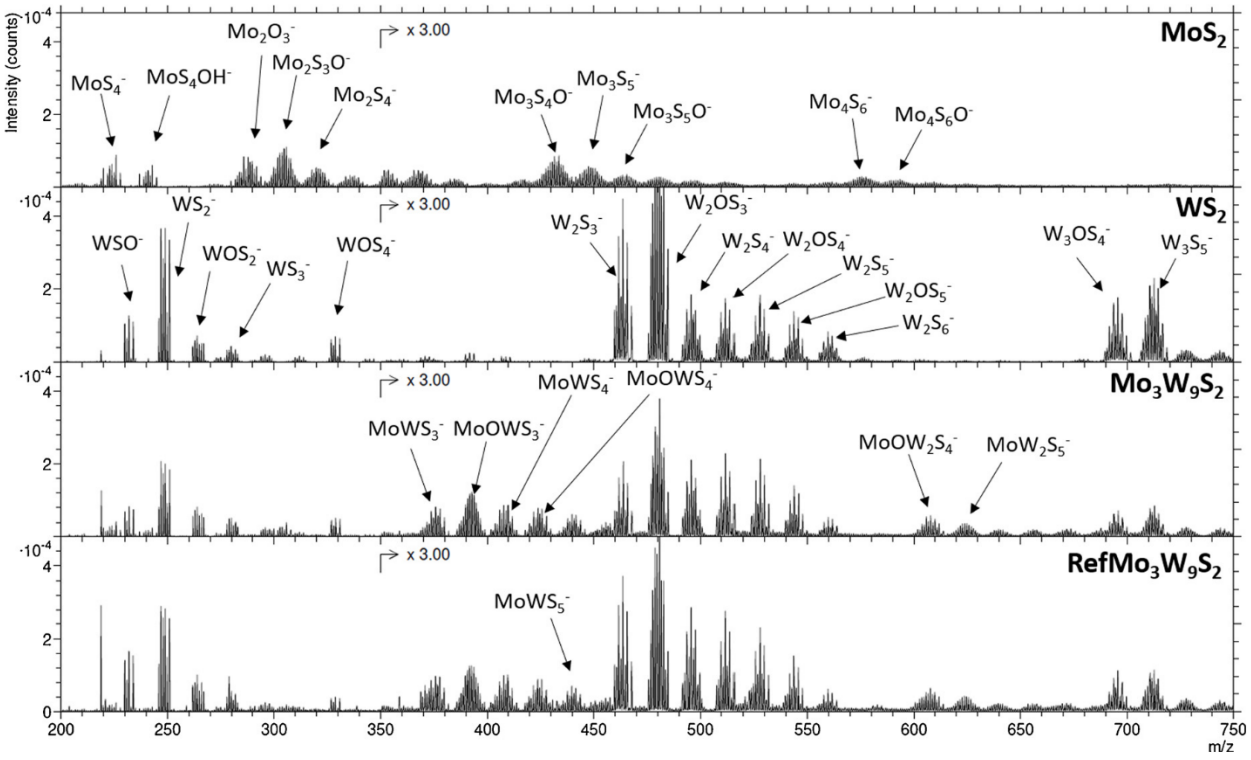

Fig. 6. Mass spectra obtained by TOF-SIMS analysis of unsupported MoS_2, WS_2, $Mo_3W_9S_2$ and $RefMo_3W_9S_2$ catalysts.

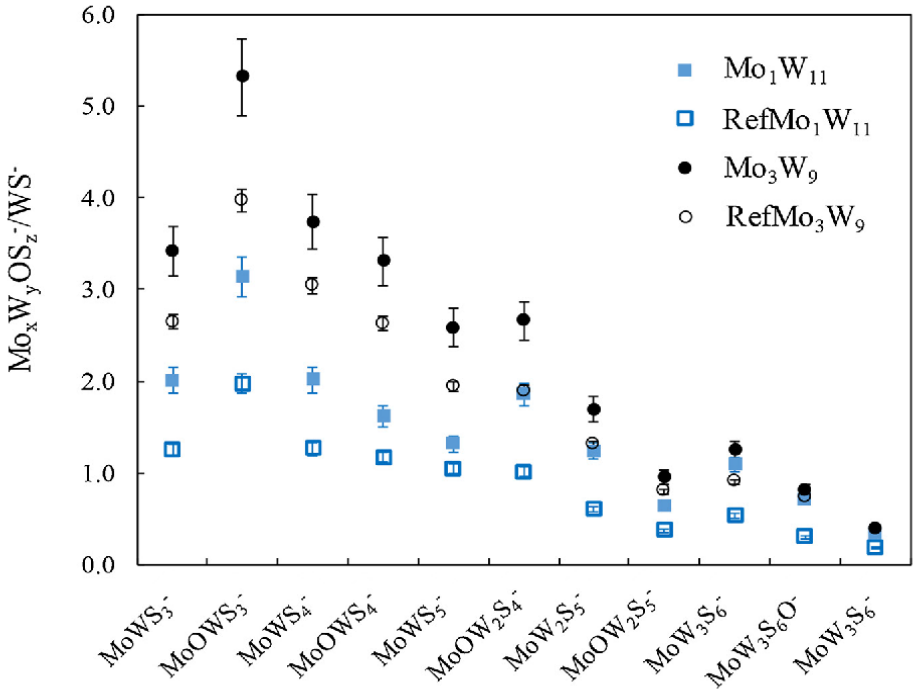

Fig. 7. Fragments contribution on unsupported $Mo_nW_{12-n}S_2$ catalysts.

increase in the linear size and average stacking number of sulfide particles, which is independently confirmed by HRTEM, XRD and EXAFS data. The metal sulfidation degree was also raised especially for tungsten, due to removal of non sulfided species. Moreover, the above results allow us to suppose that the nature of starting oxidic precursor influences the active phase composition and properties. We previously reported the formation of mixed $MoWS_2$ particles with core-shell structure, with Mo atoms predominantly located together in the core region, in Mo_3W_9/Al_2O_3 catalyst during gas phase sulfidation [9,11]. This fact is confirmed by higher total Mo–M coordination numbers in both supported and unsupported catalysts, compared to those for W–M contribution. Moreover, the changes in coordination numbers after the elimination of the support (see Table 5) indicate that the increase in Mo–Mo coordination numbers is more significant than the increase in Mo–W ones, which means that the agglomeration of MoWS slabs preferentially occurs via Mo edges as schematically illustrated in the Fig. 9a. It should be noted, that for unsupported catalyst the total Mo–M coordination numbers are close to 6 as in the bulk samples, suggesting that most of molybdenum is located inside the slabs and not on the edges.

The preferential location of Mo-atoms in the core-region of the slabs is also confirmed by Mo–S coordination numbers close to 6. The lower values obtained for W–S contribution can be explained by the elongation of W–S distances for two sulfur atoms located at M-edge, which may lead to a partial antiphase of the resulting signals, which cannot be reproduced by using a single M–S scattering path. Together with a significant fraction of Mo–W coordination, the obtained results confirm the preservation of mixed $MoWS_2$ active phase in the unsupported $Mo_3W_9S_2$ mixed HPA based catalysts suggesting the structure of the active phase after removal of the support.

The above correlates with the ToF-SIMS analysis. The higher amount of mixed sulfide species in MoW HPA based catalyst explains its almost twice higher activity in DBT HDS and naphthalene HYD compared to the bimetallic references. The small amount of mixed Mo–W phase observed in EXAFS for $RefMo_3W_9S$ sample may be explained by partial connection of monometallic MoS_2 and WS_2 slabs to bimetallic ones as schematically illustrated in Fig. 9b. However, the efficiency of such particles is still lower, compared to those formed from the mixed precursor. That assumption is in line with the calculated TOF values (Table 6) as well as HDS and HYD rate constants which correlated with the relative W–Mo coordination number (Fig. 10). Comparing the sample within one supported or unsupported series of catalysts, it can be seen that catalytic activity was increased with an increase of $N_{W\text{-}Mo}$.

5. Conclusions

We found that the HF etching of the alumina in Mo_nW_{12-n}/Al_2O_3 sulfided catalysts led to successful removal of the support. Further interaction between the particles of the etched sulfide active phase after resulfidation of bulk solids resulted to an increase in the average

Table 6
Catalytic properties of prepared unsupported $Mo_nW_{12-n}S_2$ catalysts in HDT of a mixture of DBT and naphthalene.

Catalyst	Conversion (%)		Selectivity ratio in DBT HDS $S_{HYD/DDS}$	Rate constants ($\times 10^5$ mol g^{-1} h^{-1})		*TOF* values ($\times 10^4$ s^{-1})	
	DBT HDS	Naphthalene HYD		k_{HDS}	k_{HYD}	TOF_{HDS}	TOF_{HYD}
MoS_2	22	14	1.0	60	179	1.5	4.7
WS_2	24	15	1.7	66	198	3.8	12.0
$Mo_1W_{11}S_2$	31	20	2.8	90/65[a]	277/196[a]	3.8/3.6[a]	12.4/11.4[a]
$Mo_3W_9S_2$	50	35	2.6	171/64	523/193	6.0/3.2	20.9/10.2
$RefMo_1W_{11}S_2$	34	18	1.7	100/65	240/196	4.0/3.6	10.6/11.4
$RefMo_3W_9S_2$	29	18	2.6	85 / 64	243/193	2.7/3.2	8.3/10.2

[a] The additive quantities, which were calculated using the values for monometallic MoS_2 and WS_2.

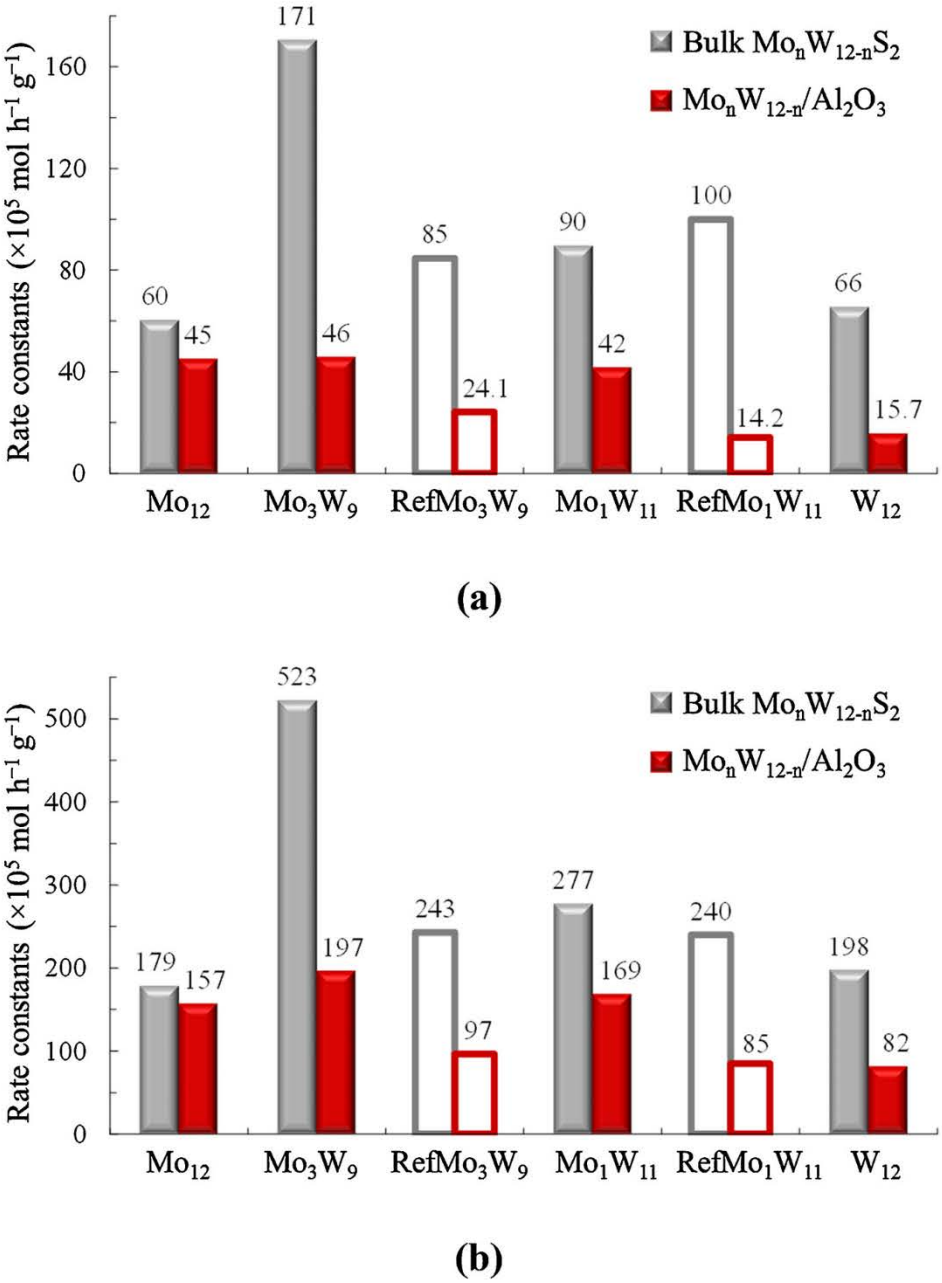

Fig. 8. Rate constants of DBT HDS (a) and naphthalene HYD (b) over unsupported $Mo_nW_{12-n}S_2$ and supported Mo_nW_{12-n}/Al_2O_3 [9] catalysts.

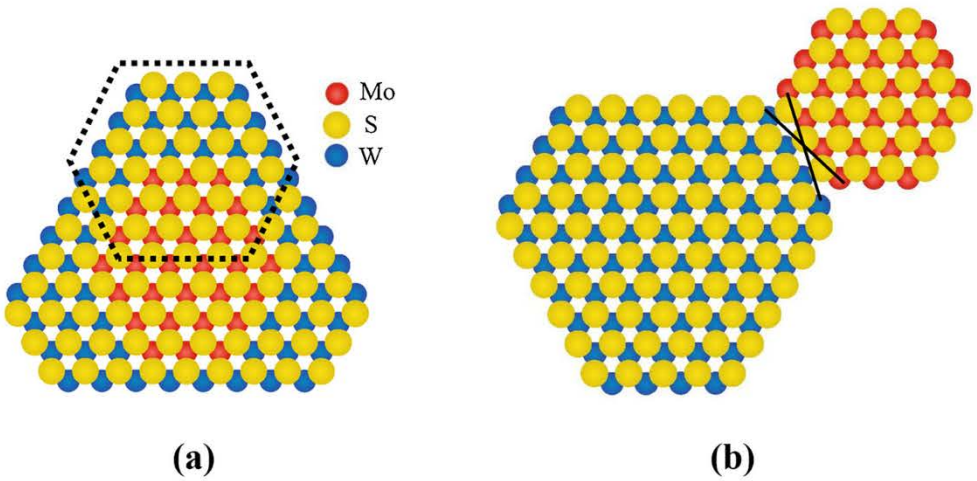

Fig. 9. The possible simplified model of mixed $MoWS_2$ active particles in unsupported $Mo_3W_9S_2$ (a) and $RefMo_3W_9S_2$ (b) catalysts.

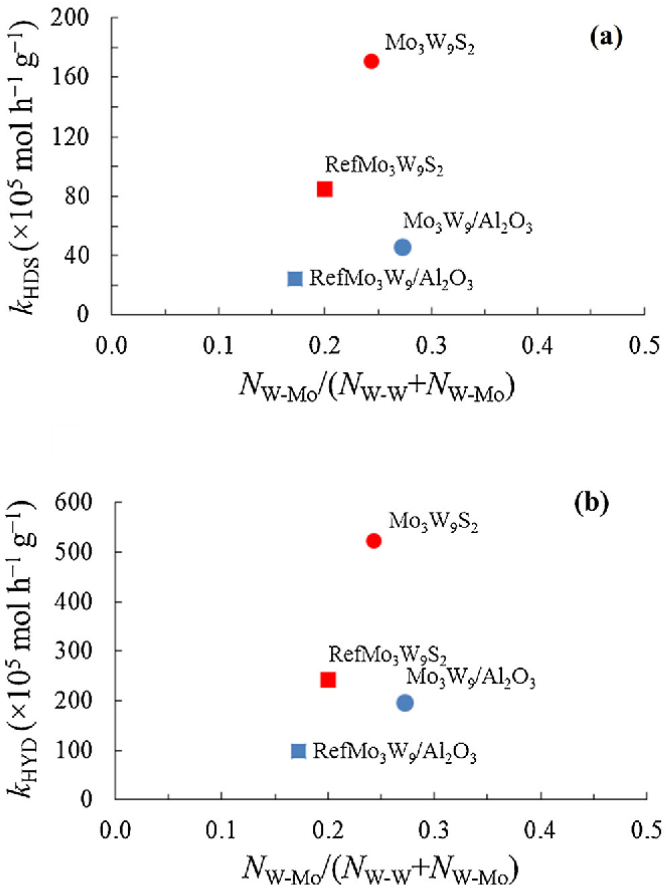

Fig. 10. Activity in DBT HDS (a) and naphthalene HYD (b) over unsupported $Mo_nW_{12-n}S_2$ and supported Mo_nW_{12-n}/Al_2O_3 [9] catalysts depending on the W-Mo coordination number.

particle length and stacking number, which is independently confirmed by HRTEM, XRD and EXAFS data. The metal sulfidation degree was also raised especially for tungsten, due to removal of non sulfided species. The presence of mixed $MoWS_2$ slabs was confirmed by EXAFS and ToF-SIMS analysis.

A beneficial effect in the catalytic activity of bimetallic unsupported $MoWS_2$ catalysts compared to monometallic MoS_2 and WS_2 ones has been shown. Total DBT HDS and naphthalene HYD activities were correlated with the Mo-W contribution. Among the prepared bimetallic catalysts, the $Mo_3W_9S_2$ sample synthesized using $H_4SiMo_3W_9O_{40}$ HPA as starting material demonstrated the highest HDS and HYD activities. Together with a significant fraction of Mo–W coordination, the obtained results confirm the preservation of mixed $MoWS_2$ active phase in unsupported $Mo_3W_9S_2$ mixed HPA based catalysts suggesting the structure of the active phase after removal of the support.

Declaration of competing interest

None.

CRediT authorship contribution statement

A. Kokliukhin: Investigation, Writing - original draft. **M. Nikulshina:** Validation, Writing - original draft. **A. Mozhaev:** Investigation. **C. Lancelot:** Investigation, Writing - review & editing. **C. Lamonier:** Conceptualization. **N. Nuns:** Investigation. **P. Blanchard:** Validation. **A. Bugaev:** Investigation, Methodology. **P. Nikulshin:** Conceptualization, Writing - review & editing.

Acknowledgments

Authors thank Russian Science Foundation for financial support of the investigation by Grant No. 17-73-20386. Chevreul Institute (FR 2638), Ministère de l'Enseignement Supérieur et de la Recherche, Région Nord – Pas de Calais and FEDER are acknowledged for supporting and funding partially this work (TEM and ToF-SIMS).

Appendix A. Supplementary data

Supplementary material related to this article can be found, in the online version, at doi:https://doi.org/10.1016/j.cattod.2020.07.018.

References

[1] S. Sigurdson, V. Sundaramurthy, A.K. Dalai, J. Adjaye, J. Mol. Catal. A 291 (2008) 30.
[2] C. Thomazeau, C. Geantet, M. Lacroix, M. Danot, V. Harlé, P. Raybaud, Appl. Catal. A 322 (2007) 92.
[3] H. Yu, S. Li, G. Jin, Energy Fuels 24 (2010) 4419.
[4] M. Nikulshina, A. Mozhaev, C. Lancelot, M. Marinova, P. Blanchard, E. Payen, C. Lamonier, P. Nikulshin, Appl. Catal. B 224 (2018) 951.
[5] D. Liu, L. Liu, G. Li, C. Liu, J. Nat. Gas Chem. 19 (2010) 530.
[6] R. Huirache-Acuña, B. Pawelec, E. Rivera-Muñoz, R. Nava, J. Espino, J.L.G. Fierro, Appl. Catal. B 92 (2009) 168.
[7] J.A. Mendoza-Nieto, O. Vera-Vallejo, L. Escobar-Alarcón, D.A. Solís-Casados, T. Klimova, Fuel 110 (2013) 268.
[8] M.A. Guzmán, R. Huirache-Acuña, C.V. Loricera, J.R. Hernández, J.N. Díaz de León, J.A. de los Reyes, B. Pawelec, Fuel 103 (2013) 321.
[9] M.S. Nikulshina, P. Blanchard, A. Mozhaev, C. Lancelot, A. Griboval-Constant, M. Fournier, E. Payen, O. Mentré, V. Briois, P.A. Nikulshin, C. Lamonier, Catal. Sci. Technol. 8 (2018) 5557.
[10] M.S. Nikul'shina, A.V. Mozhaev, P.P. Minaev, M. Fournier, C. Lancelot, P. Blanchard, E. Payen, C. Lamonier, P.A. Nikul'shin, Kinet. Catal. 58 (2017) 825.
[11] M. Nikulshina, A. Mozhaev, C. Lancelot, P. Blanchard, M. Marinova, C. Lamonier, P. Nikulshin, Catal. Today 329 (2019) 24.
[12] A. Stanislaus, A. Marafi, M.S. Rana, Catal. Today 153 (2010) 1.
[13] S. Zhang, D. Liu, W. Deng, G. Que, Energy Fuels 21 (2007) 3057.
[14] G. Bellussi, G. Rispoli, A. Landoni, L. Millini, D. Molinare, E. Montanari, P. Pollesel, J. Catal. 308 (2013) 189.
[15] G. Bellussi, G. Rispoli, D. Molinari, A. Landoni, P. Pollesel, N. Panariti, R. Millini, E. Montanari, Catal. Sci. Technol. 3 (2013) 176.
[16] M.T. Nguyen, N.T. Nguyen, J. Cho, C. Park, S. Park, J. Jung, C.W. Lee, J. Ind. Eng. Chem. 43 (2016) 1.
[17] G. Hagenbach, Ph. Courty, B. Delmon, J. Catal. 31 (1973) 264.
[18] R. Candia, B.S. Clausen, H. Topsøe, J. Catal. 77 (1982) 564.
[19] M. Zdrazil, Catal. Today 3 (1988) 269.
[20] E. Devers, P. Afanasiev, B. Jouguet, M. Vrinat, Catal. Lett. 82 (2002) 13.
[21] W.J. Li, E.W. Shi, J.M. Ko, Z.Z. Chen, H. Ogino, T. Fukuda, J. Cryst. Growth 250 (2003) 418.
[22] Y. Peng, Z. Meng, C. Zhong, J. Lu, Z. Yang, Y. Qian, Mater. Chem. Phys. 73 (2002) 327.
[23] N. Rueda, R. Bacaud, M. Vrinat, J. Catal. 169 (1997) 404.
[24] Y. Li, A. Li, F. Li, D. Liu, Y. Chai, C. Liu, J. Catal. 317 (2014) 240.
[25] A.N. Varakin, A.V. Mozhaev, A.A. Pimerzin, P.A. Nikulshin, Appl. Catal. B 238 (2018) 498.
[26] S. Kasztelan, H. Toulhoat, J. Grimblot, J.P. Bonnelle, Appl. Catal. 13 (1984) 127.
[27] G. Berhault, M.P. De la Rosa, A. Mehta, M.J. Yácaman, R.R. Chianelli, Appl. Catal. A 345 (2008) 80.
[28] A. Pimerzin, A. Mozhaev, A. Varakin, K. Maslakov, P. Nikulshin, Appl. Catal. B 205 (2017) 93.
[29] S.-H. Kim, K.-D. Kim, Y.-K. Lee, J. Catal. 347 (2017) 127.
[30] C.T. Tye, K.J. Smith, Catal. Today 116 (2006) 461.
[31] M.P. De la Rosa, J. Catal. 225 (2004) 288.
[32] G. Alonso, V. Petranovskii, M. Del Valle, J. Cruz-Reyes, A. Licea-Claverie, S. Fuentes, Appl. Catal. A 197 (2000) 87.
[33] K.S. Liang, R.R. Chianelli, F.Z. Chien, S.C. Moss, J. Non-Cryst. 79 (3) (1986) 251.
[34] B. Guichard, M. Roy-Auberger, E. Devers, C. Pichon, C. Legens, P. Lecour, Catal. Today 149 (2010) 2.
[35] A.V. Mozhaev, P.A. Nikulshin, Al.A. Pimerzin, K.I. Maslakov, A.A. Pimerzin, Catal. Today 271 (2016) 80.
[36] A. Cordova, P. Blanchard, C. Lancelot, G. Frémy, C. Lamonier, ACS Catal. 5 (2015) 2966.
[37] W. van Beek, O.V. Safonova, G. Wiker, H. Emerich, Phase Transit. 84 (2011) 726.
[38] B. Ravel, M. Newville, J. Synchrotron Radiat. 12 (2005) 537.
[39] M. Newville, J. Synchrotron Radiat. 8 (2001) 322.
[40] R. Huirache-Acuña, M.A. Albiter, C. Ornelas, F. Paraguay-Delgado, R. Martínez-Sánchez, G. Alonso-Nuñez, Appl. Catal. A 308 (2006) 134.
[41] L. Alvarez, J. Espino, C. Ornelas, J.L. Rico, M.T. Cortez, G. Berhault, G. Alonso, J. Mol. Catal. A Chem. 210 (2004) 105.
[42] J. Bocarando, G. Alonso-Nuñez, W. Bensch, R. Huirache-Acuña, M. Del Valle,

J. Cruz-Reyes, Catal. Lett. 130 (2009) 301.
[43] L. Álvarez, G. Berhault, G. Alonso-Nuñez, Catal. Lett. 125 (2008) 35.
[44] H. Toulhoat, P. Raybaud, J. Catal. 216 (2003) 63.
[45] F. Labruyère, M. Lacroix, D. Schweich, M. Breysse, J. Catal. 167 (1997) 464.
[46] P. Afanasiev, Appl. Catal. A 303 (2006) 110.
[47] B. Yoosuk, D. Tumnantong, P. Prasassarakich, Chem. Eng. Sci. 79 (2012) 1.
[48] M. Elizabeth, C. Gaxiola, M. Arroyo-Albiter, A. Pérez-Larios, P.B. Balbuena, J. Espino-Valencia, Fuel 113 (2013) 733.
[49] L. Kaluža, M. Zdražil, Catal. Commun. 107 (2018) 62.
[50] J.N. Díaz de León, J. Antunes-García, G. Alonso-Nuñez, T.A. Zepeda, D.H. Galvan, J.A. de los Reyes, S. Fuentes, Appl. Catal. B 238 (2018) 480.
[51] L. Kaluža, M. Koštejn, D. Gulková, Catalysts 9 (12) (2019) 987.
[52] M. Kniazeva, A. Maximov, Catalysts 8 (12) (2018) 644.

Supporting Information for Chapter 5

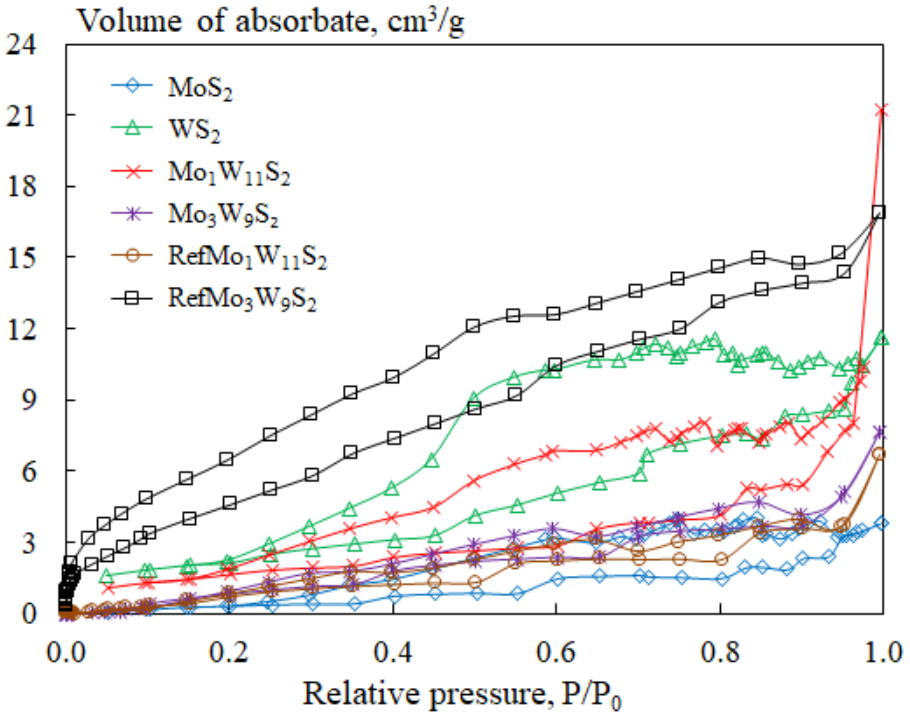

Fig. S1. Low-temperature nitrogen adsorption–desorption isotherms for bulk $Mo_nW_{12-n}S_2$ catalysts

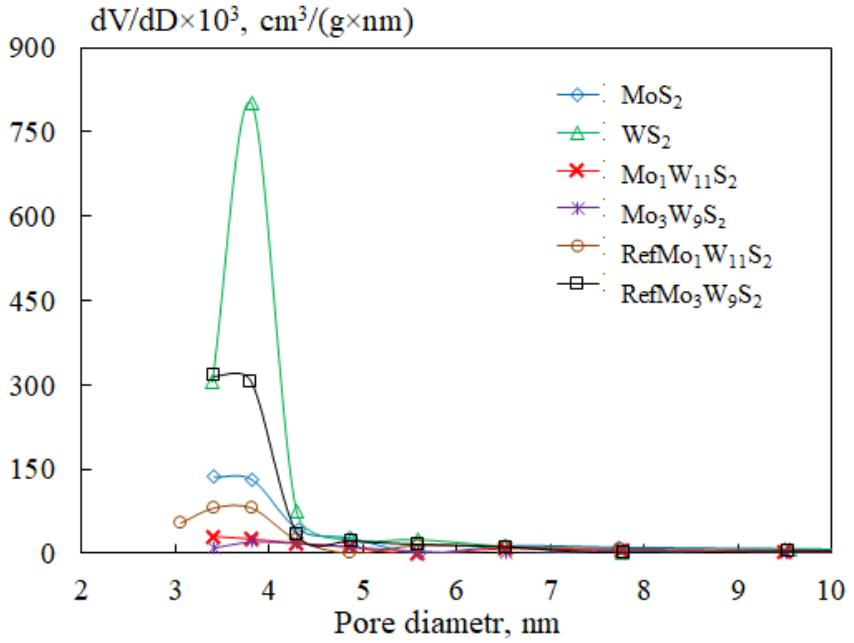

Fig. S2. The pore size distributions for bulk $Mo_nW_{12-n}S_2$ catalysts

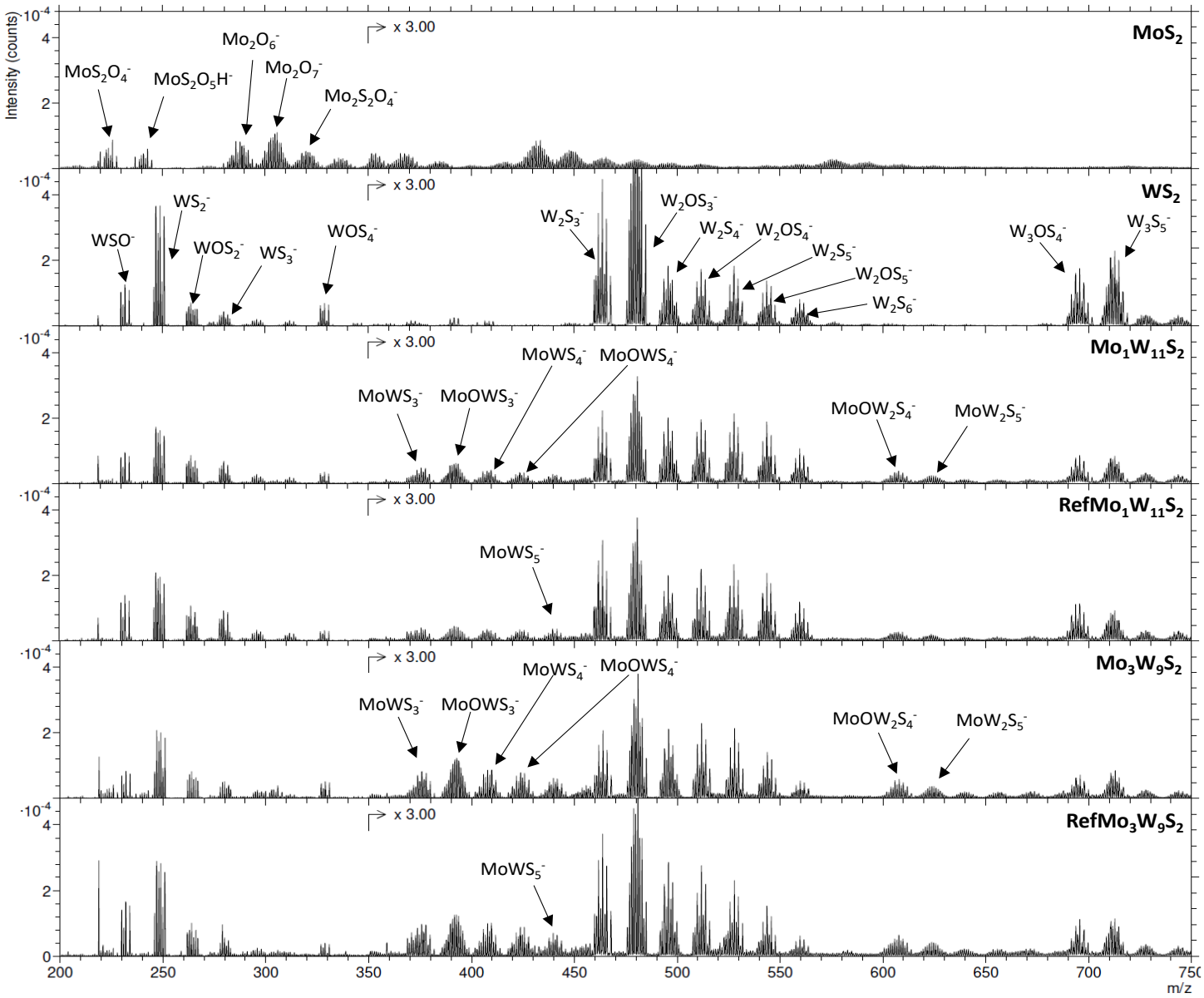

Fig. S3. Mass spectra obtained by TOF-SIMS analysis of $Mo_nW_{12-n}S_2$ catalysts.

Chapter 5

Mixed MoW catalysts supported on mesostructured silica

5.1 Introduction

In the previous sections, (Ni)MoW catalysts supported on alumina, the classical HDT support, were synthesized with different Mo/(Mo+W) atomic ratio, which had a significant effect on activity. The advantage of using mixed $SiMo_nW_{12-n}$HPAs has been demonstrated for these catalysts containing two structure-forming active phase metals in a same molecular precursor. At the same time, it was found that the activity of such catalysts is significantly higher than that of the samples obtained from a mixture of two corresponding monometallic HPA.

In the literature, there are many works in which various other oxides (SiO_2, TiO, MgO, etc) are used as support. One of the promising supports is the mesostructured silica, which differs from traditional alumina by highly developed surface area and specific mesoporosity. Many methods for the synthesis of mesostructured silica have been proposed by many researchers. Using various polymers as a structure-forming material, as well as changing the conditions and temperature of synthesis, it is possible to obtain a support with different textural properties depending on the requirements of the process. There are very few studies related to the influence of the Mo/(Mo+W) ratio on the catalytic performance of catalysts based on mesostructured silica. This chapter deals with MoW mesostructured silica supported catalysts prepared from mixed HPA and corresponding mixture and different Mo/(Mo+W) ratio hoping to keep the beneficial effects observed on alumina-based catalysts.

SBA-15 and COK-12 were chosen as supports. SBA-15 has established itself as a support that can be an excellent replacement for traditional alumina [1–3]. However, it is very difficult to synthesize this material at large scale due to the use of a sol-gel method starting from tetraethylorthosilicate, as the source of silicon. COK-12 is an analogue of SBA-15, a mesostructured silica for which a continuous synthesis method could be developed, COK-12 also presents a platelets morphology avoiding long channels present in SBA-15 [4,5]

Therefore, in this chapter, a comparative analysis of catalysts based on SBA-15 and COK-12 with traditional catalysts supported on alumina was carried out. The samples were investigated in model reactions of HDS DBT and HYD naphthalene.

5.2 Comparison of the catalytic properties of supported mixed catalysts based on alumina and mesostructured silica (SBA-15 and COK-12).

5.2.1 Supports and catalysts preparation

Mesostructured silica COK-12 and SBA-15 were synthesized according to the methods proposed by Jammaer et al. [6] and Stucky et al [7], respectively, using di- and tri-block copolymers as organic structuring agent.

SBA-15: Triblock copolymer Pluronic P123 (M = 5800, EO20PO70EO20, Aldrich) was used as a structure-forming agent and tetraethyl orthosilicate was used as a source of silica. A weighed portion of Pluronic P123 (4 g) was dissolved in water (30 mL) containing 2 M HCl (120 mL) at a temperature of 35°C. The weighed portion of tetraethyl orthosilicate (8.5 g) was added dropwise under vigorous stirring to the obtained solution and the resulting mixture was held for 20 h at 35°C under stirring. After stirring, the solution was transferred to a polypropylene bottle (1000 cm^3) and placed in an oven for 48 h at a temperature of 80°C. The product was cooled to room temperature, filtered, washed with deionized water, dried at 60°C (5h), 80°C (2 h) and 100°C (5 h), and finally calcined at 240°C (4h), then 540°C (6 h).

COK-12: Triblock copolymer Pluronic P123 (4.0 g) was dissolved in distilled water (107.5 mL) and a buffer mixture composed of citric acid (3.68 g) and sodium citrate (2.54 g) were added to buffer the pH of the synthesis at 5. Under stirring 10.4 g of Na_2SiO_3 aqueous solution (NaOH, 10 wt %; SiO_2, 27 wt %; Merck, pH = 11.0 - 11.5) was added dropwise and water (30 mL) was poured through a separating funnel. pH was stabilized within 30 s after the addition and the pH was maintained around 5-5.5. The solution was stirred for 5 min and the resulting mixture was kept at room temperature for 24 h. Synthesis was accompanied by the stage of aging at 90°C (without stirring) to increase the volume and average diameter of pores [6]. The material was isolated from the solution using vacuum filtration, dried at 60°C for 8 h and calcined in an air stream at 300°C for 8 h and at 550°C for the next 8 h with a heating rate of 1°C/min.

The reference support is alumina, which was used in Chapter 2.

Mo_3W_9/Sup (Sup = Al_2O_3, SBA-15 and COK-12) catalysts and the corresponding bimetallic Mo_3+W_9/Sup reference samples were prepared by the single incipient wetness impregnation with the aqueous solution of the $SiMo_3W_9$ heteropolyacid and mixture of $H_4SiMo_{12}O_{40}$ and $H_4SiW_{12}O_{40}$ heteropolyacids, respectively. All catalysts were prepared with the similar loading of metals. After impregnation, all samples were dried at temperatures of 60 (5 h), 80 (2 h), and 100°C (5 h) without calcination. Before physicochemical studies and catalytic tests, oxide samples were sulfided in an H_2S/H_2 flow (10 vol% H_2S), according to the conditions described in Chapter 2.

5.2.2 Characterization of MoW/Sup catalysts

The textural characteristics of the sulfided samples were measured by low-temperature nitrogen adsorption. The specific surface area was calculated according to the Brunauer–Emmett–Teller (BET) model at P/P_0 = 0.05–0.3. The total pore volume and pore size distribution were calculated from the desorption curve and within the framework of the Barrett–Joyner–Halenda model. The Mo and W content and textural properties of the synthesized samples and supports are summarized in **Table 5.1**.

Table 5.1 Metal loadings and textural properties of MoW/Sup catalysts after sulfidation

Catalyst	Content, wt %		d(Mo+W)	Textural characteristics		
	MoO_3	WO_3	at nm^{-2}	S_{BET}[a] ($m^2\ g^{-1}$)	V_p[b] (mL g^{-1})	D[c] (nm)
Al_2O_3	–	–	-	240	0.91	7.6
Mo_3W_9/Al_2O_3	4.2	20.1	3.9	210	0.53	7.6
Mo_3+W_9/Al_2O_3				206	0.53	7.6
COK-12	–	–	-	720	1.27	7.5
Mo_3W_9/COK-12	3.5	16.7	1.2	587	1.02	7.2
Mo_3+W_9/COK-12				523	0.92	7.1
SBA-15	–	–	-	850	1.18	5.6
Mo_3+W_9/SBA-15	4.1	20.7	1.2	452	0.78	5.6
Mo_3W_9/SBA-15				447	0.64	5.6

[a]S_{BET} is the surface area, [b]V_p is the pore volume, and [c]D is the pore diameter.

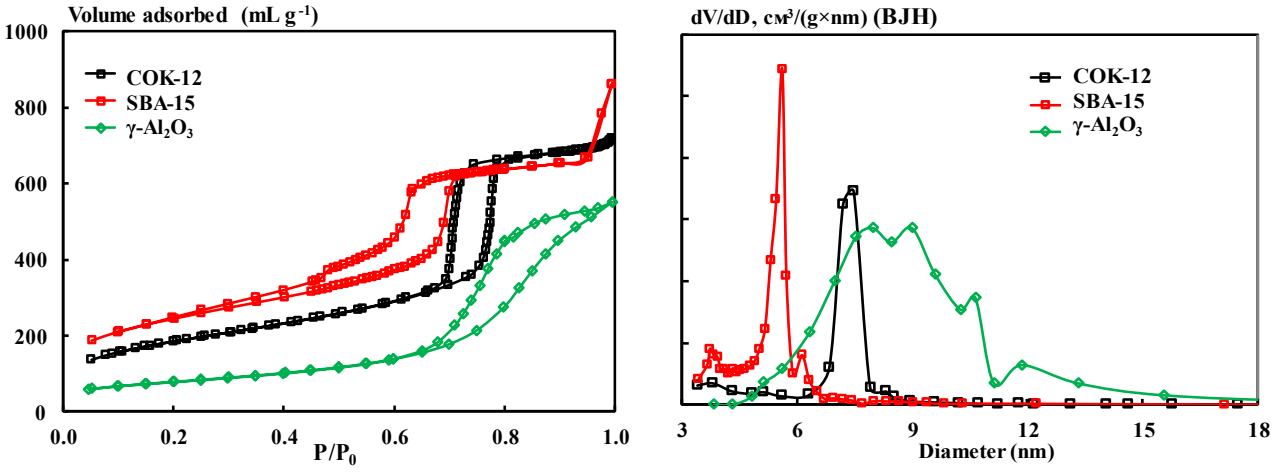

a) **b)**

Fig. 5.1. Nitrogen adsorption/desorption isotherms (a) and pore size distributions (b) of Al_2O_3, SBA-15 and COK-12

Nitrogen sorption curves and pore size distribution are shown in **Fig. 5.1**. Mesostructured silicas demonstrate typical type IV isotherms exhibiting hysteresis loops of type H1, with parallel adsorption and desorption branches due to the regular array of cylindrical pores, according to the classification

proposed by Gregg and Sing [8]. Type IV isotherms exhibiting hysteresis loops of type H1 corresponds to most synthetic mesostructured materials [5,9]. Alumina has a type IV isotherm with a large type H2 hysteresis loop. This type of hysteresis is characteristic of materials with nearly cylindrical channels or consisting of aggregates or agglomerates of spheroidal particles of irregular size or shape. The pore distribution for SBA-15 and COK-12 is monomodal with narrow pore size distribution in agreement with the expected mesoporosity of these supports in the case of alumina, this distribution varies over a wider range from 5 to 11.5 nm.

After impregnation and sulfidation, alumina supported catalysts textural properties remain stable with only a small decrease (less than 10%) of surface area and pore diameter. It indicates the presence of well-dispersed particles at the alumina surface. A significant decrease in pore volume is associated with the deposition of a large amount of the active component inside the pores. COK-12 and SBA-15 present a high specific surface area (720 m^2/g and 850 m^2/g, respectively), related to mesostructured materials [4,10]. However after metal deposition and sulfidation their specific surface area decrease by 300-400 $m^2\ g^{-1}$ together with their pore volume (by 0.25–0.55 mL g^{-1}) due to the partial filling of pores with deposited particles, in agreement with published data [2, 11]. The decrease of the total surface area and the pore volume is more important for SBA-15 supported catalysts presenting the lowest pore size diameter. For the three supports, the average diameter of pores remains stable whatever the sample indicating that a part of the porosity is not affected by metal deposition and sulfidation.

5.2.3 High-resolution transmission electron microscopy (HRTEM)

TEM micrographs are presented in **Fig. 3.2.** Regardless of the type of precursor, the average length of particles on the mesostructured supports (COK-12: 3.7 and 4.0 nm) (SBA-15: 3.9 and 4.1 nm) and deposited on Al_2O_3 (4.0 and 3.6 nm) are very similar, leading to very close dispersion values (*D*). (**Table 5.2**). We can notice a higher average stacking (≥2.3) on mesostructured support compared to alumina (around 2.0/2.3) which is explained by the lack of interaction between the silica supports and the active phase [1].

Table 5.2 Morphological characteristics of MoW/Sup catalysts

Catalyst	Morphological characteristics		
	Average length $\bar{L}$ (nm)	Average stacking number $\bar{N}$	Dispersion of Mo(W)S particles *D*
Mo_3W_9/Al_2O_3	3.8	2.0	0.29
Mo_3+W_9/Al_2O_3	3.5	2.3	0.33
Mo_3W_9/COK-12	3.7	2.3	0.31
Mo_3+W_9/COK-12	4.0	2.5	0.29
Mo_3+W_9/SBA-15	3.9	2.3	0.30
Mo_3W_9/SBA-15	4.1	2.7	0.29

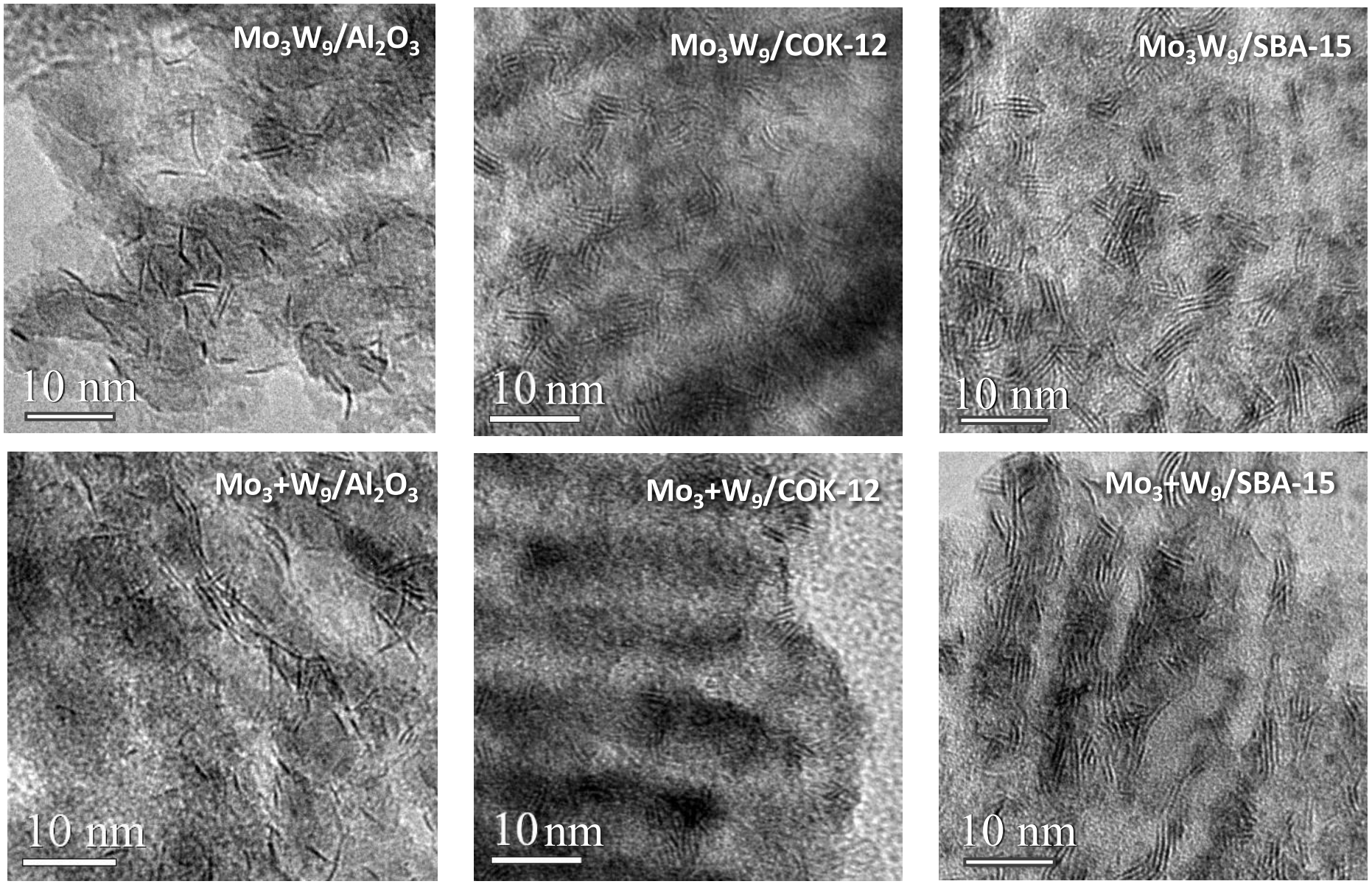

Fig. 5.2. TEM micrographs of sulfided MoW/Sup catalysts

The distribution in length from statistical analysis shows only small differences between supports with sulfide phase predominantly represented by slabs with a length mainly between 2 to 6 nm. A stacking equal to two and three is mainly observed on mesostructured silica, while on alumina, single-layer and two-layer particles slightly predominate (**Fig. 5.3**). Higher stacking number can be explained by an initial weaker oxide-oxide interaction of active-phase precursor particles with the SiO_2 surface than that with the Al_2O_3 surface, as reported for the catalysts supported on SBA-15 [2] and MCM-41 [12]. In our case, same Mo and W loadings have been chosen for the catalyst preparation leading to metallic atomic density d(Mo+W) equal 3.9 and 1.2 at nm^{-2} for alumina and silica respectively, explaining that the support has almost no effect on the dispersion of the active phase, even if a slightly higher stacking is observed for silica-based catalysts.

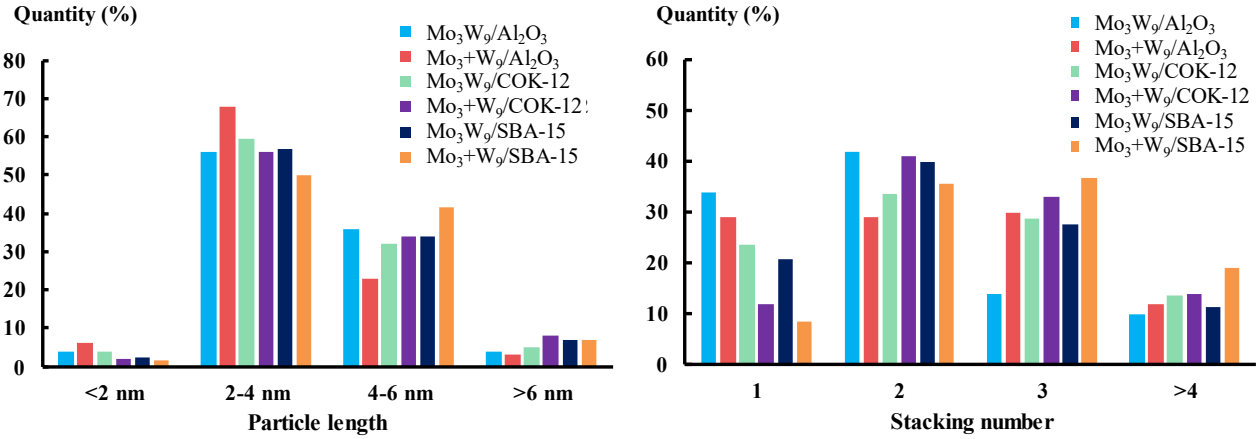

Fig. 5.3 Distribution of slab length (a) and of stacking number (b) (rel. %)

5.2.4 X-ray photoelectron spectroscopy (XPS) of MoW/Sup catalysts

Information about nature and relative amount of Mo and W species on the surface of the synthesized catalysts were obtained by XPS. **Fig. 5.4** shows the decomposition of Mo3d-S2s and W4f photoelectron spectra recorded for Mo_3W_9/Sup and Mo_3+W_9/Sup catalysts. Decomposition of the spectra was performed similarly to Chapter 2 using the appropriate monometallic sulfide catalysts. The results of the XPS decomposition for the metal fractions of molybdenum and tungsten species of the sulfided Mo_3W_9/Sup and Mo_3+W_9/Sup are reported in **Table 5.3**.

In bimetallic catalysts, the sulfidation degree of molybdenum was found higher than 80 rel. % for Mo and 60 rel. % of W, respectively. Similar and high degree of sulfidation of tungsten in Mo_3W_9 and Mo_3+W_9 for a same silica support are observed. Differences in the degree of sulfidation of tungsten depending on the nature of the precursors – mixed $SiMo_nW_{12-n}$ HPA or mixture of $SiMo_{12}$ and SiW_{12} HPAs, which were previously observed in Chapter 2 for catalysts supported on alumina, are not observed for catalysts supported on mesostructured silica.

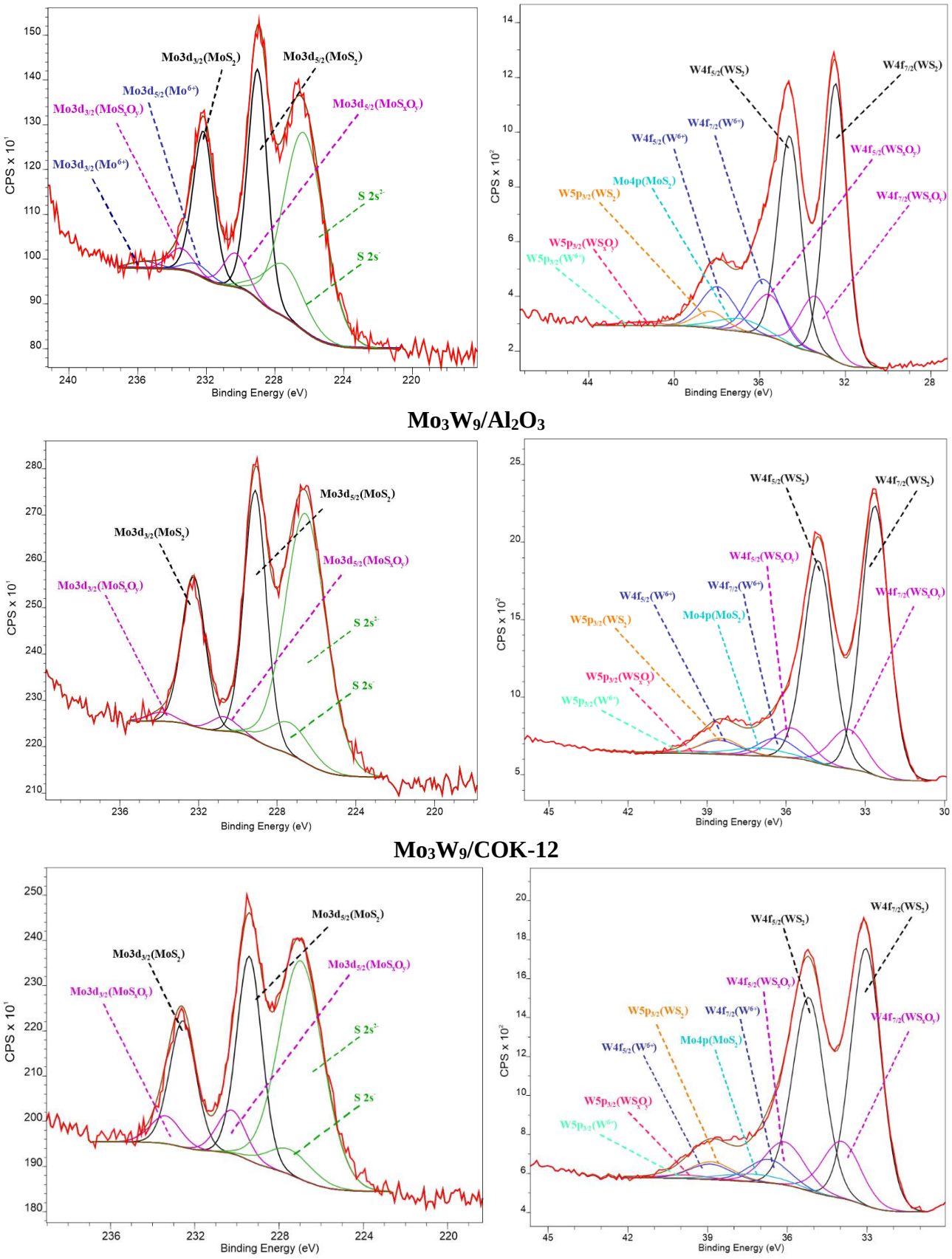

Fig. 5.4 XPS Mo 3d and W 4f spectra recorded for sulfided Mo_3W_9/Sup catalysts; in blue: $Mo(W)^{6+}$ oxide contributions; in pink: $Mo(W)S_xO_y$ contributions; in black: $Mo(W)S_2$ contributions: in green S contributions.

Table 5.3. Metal distribution for Mo and W species present at the surface of sulfided Mo(W) catalysts.

Catalyst	Mo percentage (rel. %)			W percentage (rel. %)		
	MoS_2	MoS_xO_y	Mo^{6+}	WS_2	WS_xO_y	W^{6+}
Mo_3W_9/Al_2O_3	89	2	9	58	8	34
Mo_3+W_9/Al_2O_3	90	8	2	77	11	12
Mo_3W_9/COK-12	94	6	0	78	15	7
(Mo_3+W_9)/COK-12	99	1	0	83	9	8
Mo_3W_9/SBA-15	80	20	0	71	20	9
(Mo_3+W_9)/SBA-15	82	18	0	75	18	7

The sulfidation degrees of metals in COK-12 supported catalysts are the highest with values close to 100% for Mo and 80% for W, and turns out to be higher than with SBA-15. A detailed analysis of the global XPS survey reveals the presence of sodium atoms (0.4 wt. %) in the catalysts based on COK-12, which presumably remained in the structure of the support during its synthesis, since the source of silicon oxide is an aqueous solution of sodium silicate. According to the literature [14–16], the presence of alkali metals in small amounts could contribute to an increase in the degree of sulfidation. A high amount of alkali atoms (K(Na)/Mo > 2) could contribute to the formation of two types of molybdenum disulfide (MoS-1T and MoS-2H) [16] but in our case, the remaining amount is too low to form 1T MoS_2 phase. These results show that the washing of the material after filtration did not completely remove the inhibitor atoms.

5.2.5 MoW/Sup catalysts in hydrotreating of mixture of DBT and naphthalene.

The catalytic properties of the synthesized catalyst samples were studied in the co-hydrotreating of DBT and naphthalene under microflow unit conditions. The degree of conversion of dibenzothiophene and naphthalene varied from 22.4 to 52.7 % (**Table 5.4**) with a mass of 0.6 g for alumina-based catalysts and 0.4 g for the silica ones. In order to better compare the catalysts, the reaction rate constants were calculated per gram of catalyst corresponding to the same amount of Mo and W.

The activity of the catalysts supported on COK-12 is much inferior to the SBA-15 and alumina supported samples. As noted earlier, the structure of COK-12 contains sodium atoms, which are known to have a very high inhibitory activity. The presence of alkali metals in the composition of hydrotreating catalysts primarily affects the hydrogenation function, as evidenced by the low values of selectivity. For catalysts for the hydrotreating of FCC naphtha, this approach is used to selectively

reduce the hydrogenation function of the catalysts in order to maintain a high olefin content [13], [14]. In the present study, inhibition is not wanted and then completely negative.

The catalysts based on SBA-15 demonstrate the highest performances in both naphthalene hydrogenation (230.8 and 214.1 mol h^{-1} g^{-1} for Mo_3W_9/SBA-15 and Mo_3+W_9/SBA-15 respectively) and dibenzothiophene hydrodesulfurization (64.6 and 56.9 mol h^{-1} g^{-1} for Mo_3W_9/SBA-15 and Mo_3+W_9/SBA-15 respectively). These two catalysts are more efficient than the best catalyst supported on alumina prepared from the mixed HPA. It is noticeable that no significant difference is observed between the catalyst prepared from mixed HPAs and one obtained from a mixture of two monometallic HPAs for SBA-15 based catalysts, as noted in the alumina supported ones. Moreover, these alumina catalysts presented very different $S_{HYD/DDS}$ selectivity ratio showing that preliminary hydrogenation route compared with direct desulfurization was largely favored when using Mo_3W_9/Al_2O_3. This behavior together with best catalytic results were related to the mixed sulfide phase $MoWS_2$ formation starting from mixed HPA, as demonstrated in Chapter 2. This hydrogenation performance was also reflected by efficiency in naphthalene hydrogenation. For SBA-15 supported catalysts, such a behavior is not observed with also quite similar values for $S_{HYD/DDS}$.

Table 5.4. Catalytic properties of MoW/Sup catalysts in hydrotreating of DBT and naphthalene.

Catalyst	Conversion (%)		$k \times 10^5$ (mol h^{-1} g^{-1})		$S_{HYD/DDS}$
	DBT HDS	Naphthalene HYD	DBT HDS	Naphthalene HYD	
Mo_3W_9/Al_2O_3*	52.9	47.5	46.1	195.4	3.18
Mo_3+W_9/Al_2O_3*	32.1	27.3	24.2	97.1	1.76
Mo_3W_9/COK-12	23.4	17.1	14.8	52.3	1.53
Mo_3+W_9/COK-12	22.4	14.6	14.1	44.0	1.32
Mo_3W_9/SBA-15	52.2	40.9	64.6	230.8	2.48
Mo_3+W_9/SBA-15	47.8	38.6	56.9	214.1	2.78

(Test conditions: T=320°C, LHSV= 10 h^{-1}, K_H=500 NL L^{-1}, P = 3.0 MPa, m_{cat} = 0.4 (0.6) g)*

These observations lead to propose that the use of SBA-15 support does not allow to form the mixed $MoWS_2$ phase even when starting from the mixed Mo_3W_9 HPA and then the active phase could be constituted mainly with separate MoS_2 and WS_2 phases. Nevertheless, improved catalytic results are obtained for both types of precursors.

Better catalytic results with high hydrogenating activity of MoW/SBA-15 catalysts compared to that of Mo_3+W_9/Al_2O_3 could be explained by different quality of MoS_2 and WS_2 active sites keeping in mind that similar active phase morphology and sulfidation rates were observed for these catalysts. It could be related to a weaker interaction of sulfide particles with SBA-15 support and as

a result a better mobility of SH groups responsible for the hydrogenating function. Mesostructured silica is then a promising replacement for traditional alumina support.

5.3 Influence of the Mo/W ratio on the catalytic activity of mixed SBA-15 based catalysts

5.3.1 Preparation and characterization of the Mo(W)/SBA-15 catalysts

The bimetallic Mo_nW_{12-n}/SBA-15 catalysts with surface density of metals *d*(Mo+W) equal to 1.2 at nm^{-2} were prepared by using the corresponding mixed $H_4[SiMo_nW_{n-12}O_{40}]$ HPAs, n = 0, 3, 6, 9, 12. Reference catalysts were also prepared using the impregnating solutions obtained by mixing $SiMo_{12}$ and SiW_{12} in an aqueous solution with the same Mo/W ratio than the corresponding mixed HPAs and were denoted as Mo_n+W_{12-n}/Al_2O_3. The catalysts supported on SBA-15 were prepared by incipient wetness impregnation of prepared support fraction (0.5-0.25 mm). The oxidic catalyst precursors after maturation were dried at 60°C (4 h) 80°C (2 h) and 100°C (4 h) in air atmosphere without further calcination. The catalysts were activated in gas phase sulfidation. The compositions of oxidic and textural characteristics of sulfided samples are given in **Table 5.5**.

All the obtained samples had approximately the same textural characteristics, regardless of the type of precursor. After impregnation and sulfidation, the surface area decreased by more than 40%, while the specific pore volume also decreased, which indicates that the active components are blocking partially the pores. The average pore diameter remained almost unchanged, which indicates that the pores are available for internal diffusion of molecules to active sites.

5.3.2 Transmission electron microscopy (TEM)

All catalysts were characterized by TEM. Morphological information of SBA-15 based catalysts, through the distributions in stacking degree and length of the $Mo(W)S_2$ slabs, presented together with the corresponding average values are reported in **Table 5.5**.

The average particle length and stacking number ranged from 3.0 to 4.4 nm and from 2.0 to 2.7, respectively. Monometallic W_{12}/SBA-15 sample has the highest particle length and stacking number as a consequence of the lowest dispersion of the active phase, which is typical for a tungsten-based catalyst. The simultaneous presence of Mo and W leads to lower average particles length comparing to those of the monometallic samples and taking into account their relative amounts. It can be noted that the greatest dispersion (0.38 and 0.37) of the active phase is achieved at Mo/W ratio of 0.5 due to the smallest particle length, regardless of the type of precursor. Changing of Mo/(Mo+W) ratio has the same effect on the average particle length and stacking of both types of catalysts regardless of the type of precursor. A similar behavior was also reported for alumina with close morphology of MoW catalysts at a given Mo/(Mo+W) ratio. As previously observed for Mo/(Mo+W) ratio equal to 0.25, the stacking of catalysts on SBA-15 is higher than that of samples supported on alumina.

Table 5.5. Composition, textural characteristics and morphology of sulfide particles of prepared Mo(W)/SBA-15 catalysts

Catalyst	Content, wt. %.		Textural characteristics			Morphological characteristics		
	MoO_3	WO_3	S_{BET}[a] ($m^2\ g^{-1}$)	V_p[b] ($cm^3\ g^{-1}$)	D[c] (nm)	Average length $\bar{L}$ (nm)	Average stacking number $\bar{N}$	Dispersion of Mo(W)S_2, D
SBA-15	–	–	850	1.18	5.6	-	-	-
W_{12}/SBA-15	–	26.4	453	0.55	5.6	4.4	2.6	0.27
Mo_3W_9/SBA-15	4.2	20.1	452	0.78	5.6	3.9	2.3	0.30
(Mo_3+W_9)/SBA-15	4.2	20.1	447	0.64	5.6	4.1	2.7	0.29
Mo_6W_6/SBA-15	9.1	14.7	424	0.61	5.4	3.0	2.0	0.38
(Mo_6+W_6)/SBA-15	9.1	14.7	469	0.69	5.6	3.1	2.1	0.37
Mo_9W_3/SBA-15	14.1	7.6	450	0.66	5.6	3.4	2.1	0.34
(Mo_9+W_3)/SBA-15	14.1	7.6	455	0.65	5.7	3.2	2.1	0.36
Mo_{12}/SBA-15	18.1	–	492	0.68	5.6	4.1	2.7	0.29

5.3.3 X-ray photoelectron spectroscopy (XPS)

The results of the XPS decomposition for the metal fractions of molybdenum and tungsten species of the sulfided Mo_nW_{12-n}/SBA-15 and Mo_n+W_{12-n}/SBA-15 are reported in **Table 5.6.** In all bimetallic catalysts, the sulfidation degree of molybdenum was found higher than in the monometallic Mo_{12} sample: from 74% in Mo_{12} to higher than 80% in all bimetallic samples. The introduction of tungsten increases the degree of sulfidation of molybdenum. The highest sulfidation degree of molybdenum (86-88 rel.%) was obtained on catalysts with a low tungsten content; a further increase in the content led to a slight decrease sulfidation of molybdenum. In the case of tungsten, no trend can be proposed. The highest sulfidation degree of tungsten, exceeding the value for the monometallic W_{12}/SBA-15 sample, was obtained at a Mo/(Mo+W) ratio equal to 0.25. However, the type of precursor does not have a definite effect on the W sulfidation contrary to the case of alumina-based compounds where all the catalysts prepared from mixed HPA presented better W sulfidation rate than their counterpart highlighting different sulfidation behaviors attributed to mixed $MoWS_2$ phase formation.

Table 5.6. Metal distribution for Mo and W species present at the surface of sulfided Mo(W) catalysts.

Catalyst	Mo percentage (rel. %)			W percentage (rel. %)		
	MoS_2	MoS_xO_y	Mo^{6+}	WS_2	WS_xO_y	W^{6+}
W_{12}/SBA-15				61	14	25
Mo_3W_9/SBA-15	80	20	0	71	20	9
(Mo_3+W_9)/SBA-15	82	18	0	75	18	7
Mo_6W_6/SBA-15	83	17	0	69	16	15
(Mo_6+W_6)/SBA-15	84	14	2	57	24	19
Mo_9W_3/SBA-15	86	12	2	55	28	17
(Mo_9+W_3)/SBA-15	88	8	4	62	13	25
Mo_{12}/SBA-15	74	13	13			

5.3.4 Mo(W)/SBA-15 catalysts in hydrotreating of DBT and naphthalene

A series of SBA-15 based catalysts, similar to the samples presented in Chapter 2, was obtained to determine the optimal atomic ratio Mo/(Mo+W). Catalysts were tested in co-hydrotreatment of the mixture of DBT with naphthalene and toluene (as a solvent). Experimental conditions are similar to those described in Chapter 2. The conversion varied from 24.6 to 60.8% for DBT and from 19.5 to 54.9% for naphthalene, respectively (**Table 5.7**) showing large effect of the Mo/(Mo+W) ratio.

Table 5.7. Catalytic properties of Mo(W)/SBA-15 catalysts in hydrotreating of DBT and naphthalene.

Catalyst	Conversion (%)		Reaction rate constant ($\times 10^5$ mol h^{-1} g^{-1})		$S_{HYD/DDS}$
	DBT HDS	Naphthalene HYD	k_{HDS}	k_{HYD}	
W_{12}/SBA-15	24.6	19.5	24.7	95.2	2.66
Mo_3W_9/SBA-15	52.2	40.9	64.6	230.8	2.48
(Mo_3+W_9)/SBA-15	47.8	38.6	56.9	214.1	2.78
Mo_6W_6/SBA-15	55.9	50.1	71.6	305.1	2.52
(Mo_6+W_6)/SBA-15	57.5	51.2	74.9	314.9	2.82
Mo_9W_3/SBA-15	58.3	52.3	76.5	324.9	1.92
(Mo_9+W_3)/SBA-15	60.8	54.9	82.0	349.5	2.12
Mo_{12}/SBA-15	49.3	39.7	57.7	222.0	1.10

Based on the conversions obtained, the reaction rate constants were calculated and are reported in **Fig. 5.5**. In both reactions, all the MoW catalysts present improved catalytic performances by comparison with the monometallic ones showing a clear synergetic effect between Mo and W whatever the Mo/(Mo+W) ratio. Moreover, the maximum activity is achieved at Mo/(Mo+W) atomic ratio equal to 0.75 corresponding to Mo/W = 9/3 in both reactions. It is noticeable that for a same metallic ratio, rate constants of catalysts prepared by mixed HPA and mixture of HPA are similar in both reactions. At the same time, similar selectivity $S_{HYD/DDS}$ are also reported (**Fig. 5.5c**)

For comparison purposes, catalytic results of alumina supported MoW studied in Chapter 2 have been plotted on the same figure. Both types of catalysts possess the same percentage of metals. SBA-15 supported catalysts are more efficient than the alumina ones whatever the Mo/(Mo+W) ratio and a same trend is observed for the evolution of the rate constant with the Mo/(Mo+W) ratio.

Nevertheless, as showed in Chapter 2, the alumina-based catalysts obtained by using mixed HPAs are significantly superior to the samples prepared from a mixture of two HPAs showing a different behavior between alumina and SBA-15 catalysts. On alumina, the improved performances were attributed to the formation of a mixed $MoWS_2$ active phase, which produces an increased hydrogenating activity letting again to think that this mixed phase does not form on SBA-15.

Indeed, the use of mesostructured silica made it possible to significantly improve the catalytic activity of Mo_nW_{12-n} and Mo_n+W_{12-n} bimetallic catalysts, but at the same time deprives the advantages of using mixed HPAs, which may indicate that during sulfidation, a mixed active phase is not formed on SBA-15, due different support interaction by comparison with alumina. As noted earlier, on Mo_n+W_{12-n}/Al_2O_3 catalysts, after impregnation and drying, $SiMo_{12}$HPA interacts with the support transforming into $AlMo_6$ Anderson species, due to which the sulfidation of molybdenum passes

through other intermediates, and as a result, affects the heat of sulfidation of molybdenum. In the case of SBA-15, we see that, for all the studied ratios of metals, the degree of sulfidation does not depend on the type of precursor, which may indicate that the $SiMo_{12}$ HPA structure is retained after impregnation and drying.

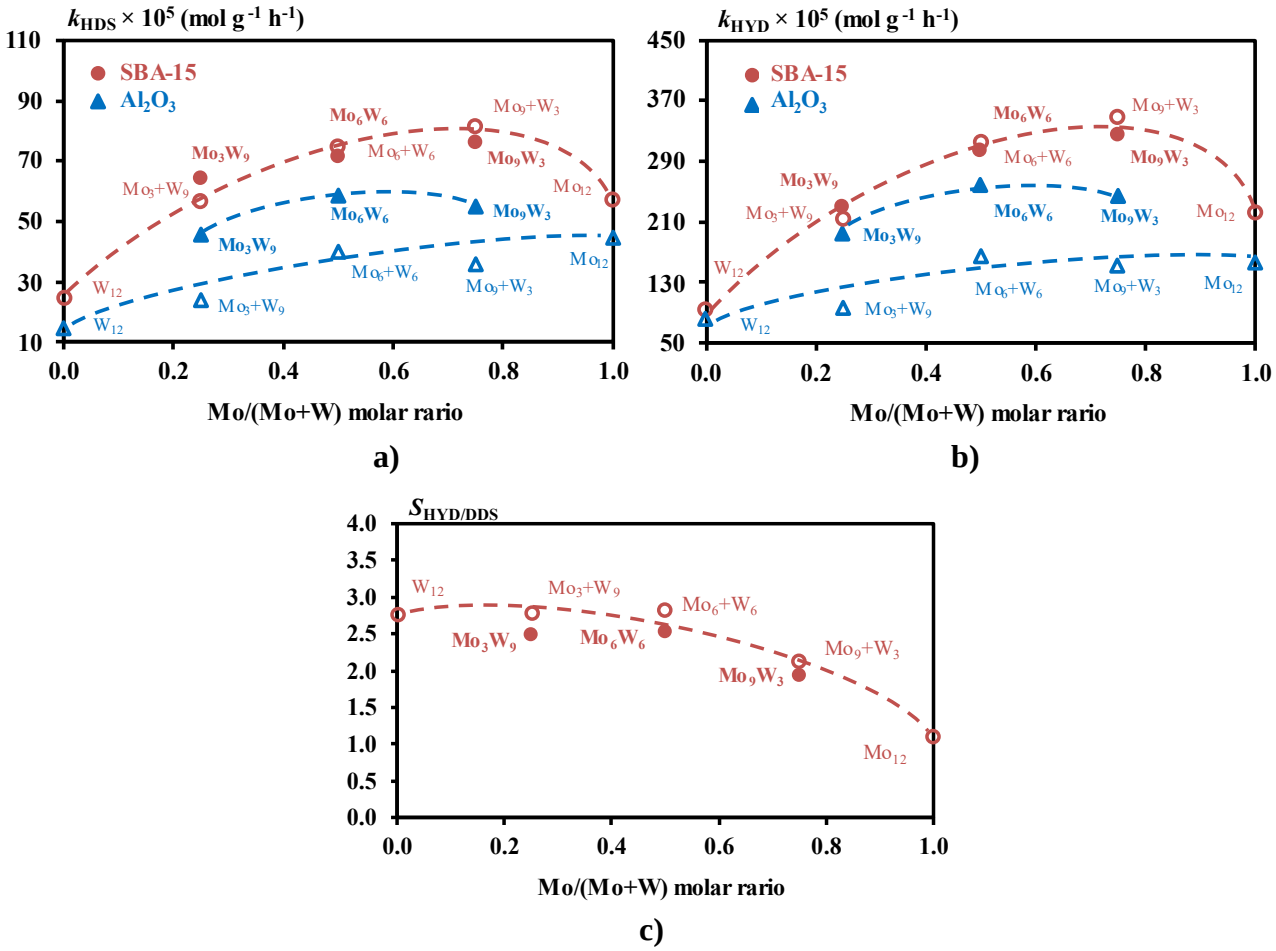

Fig. 5.5 Dependence of reaction rate constants in DBT HDS (a), naphthalene HYD (b), and selectivity route of DBT HDS (c) on Mo/(Mo+W) atomic in MoW/SBA-15 (circle) and MoW/Al_2O_3 (triangle) catalysts (filled dots correspond to mixed MoW catalysts prepared from mixed $SiMo_nW_{12-n}$HPA; open dots correspond to mixed Mo+W catalysts prepared from a mixture of $SiMo_{12}$ and SiW_{12}HPAs.).

Fig. 5.6 shows plots of k_{HYD} and the contribution of the HYD pathway to DBT HDS versus the relative amounts of the sulfide phase. The content of the active phase on the surface of SBA-15 was calculated on the basis of XPS data. The obtained data on the hydrogenating activity are linearly correlated with the content of the active phase (**Fig. 5.6**). It was found that the highest content of the active phase is formed at the Mo/(Mo+W) ratio equal to 0.75 for Mo_n+W_{12-n}/SBA-15, 0.5 and 0.75 for Mo_nW_{12-n}/SBA-15. The selectivity of DBT HDS increased almost linearly from 0.70 to 1.96 with increasing tungsten content. A similar trend is observed whatever the precursors, indicating again that a similar active phase with separate MoS_2 and WS_2 is formed on SBA-15 from different types of precursors.

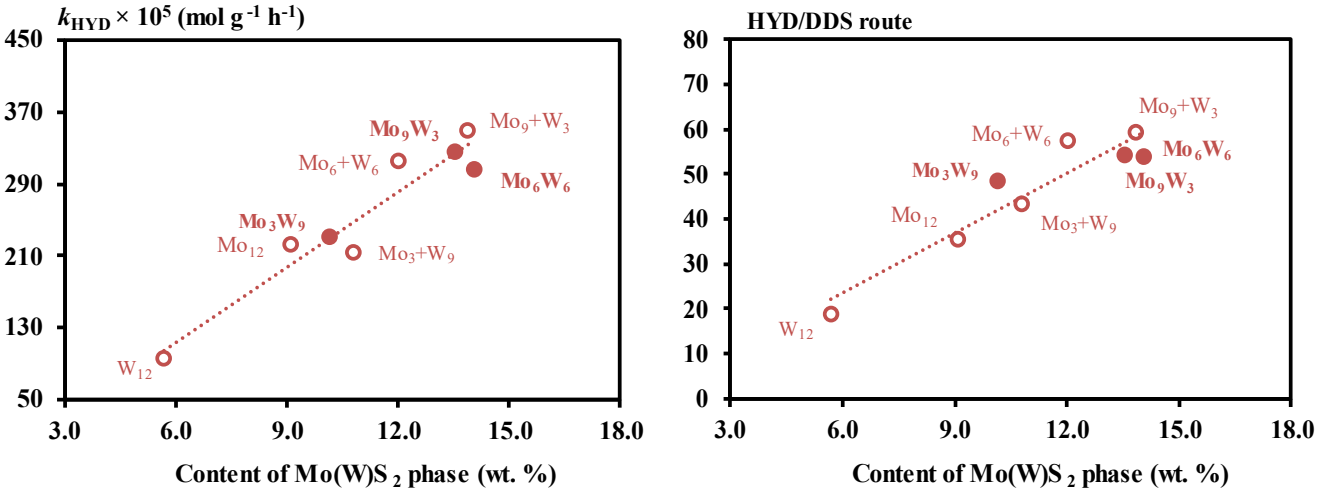

Fig. 5.6 Dependence of the hydrogenating activity on content of Mo(W)S_2 active phase of Mo(W)/SBA-15 catalysts

Even if the use of mixed MoW HPA as precursor is not favorable compared to conventional ones, the simultaneous presence of Mo and W in the catalysts appears to lead to higher catalytic performance than those of monometallic catalysts, as it provides catalysts with a higher content of active phase due to a higher degree of sulfidation of metals.

5.4 Conclusions

In this section, mesostructured silica (SBA-15 and COK-12) supports were synthesized and used as an alternative replacement for traditional alumina. Comparative analysis of bimetallic Mo_3W_9/Sup and Mo_3+W_9/Sup systems in HDS DBT and HYD naphthalene showed that not all types of mesostructured silica supports are suitable for the preparation of catalysts. It was found that the use of sodium silicate as a source of silicon in COK-12 negatively affects the activity due to the presence of sodium atoms in the structure. SBA-15 showed significantly higher reaction rate constants both in the HDS of DBT and HYD of naphthalene whatever the type of precursors used, which is in agreement with the literature data [17–19].

The study of the influence of the Mo/(Mo+W) atomic ratio and the type of precursor on the catalytic activity of catalysts supported on SBA-15 showed that the type of precursor has almost no effect on catalytic activity, as evidenced by the close values of the reaction rate constants. However, it was found that the ratio Mo/(Mo+W) of metals has an effect on the amount of the active phase, and as a result on catalytic activity with better values obtained at high Mo content.

Comparative analysis of the activities of the catalysts supported on SBA-15 and Al_2O_3 showed that the catalysts supported on mesostructured silica for all studied metal ratios are superior to that on alumina-based samples. At the same time, the synergistic effect provided from the use of mixed HPAs on sulfidation degree and rate constants was not evidenced on SBA-15. Almost the same characterization results for both types of catalysts also permit to rule out the possibility to have in both cases the mixed-phase on SBA-15 support. To confirm this assumption deduced from similar catalytic behavior and Mo sulfidation rate for both type of precursors, additional advanced characterization (HAADF, ToF-SIMS) of SBA-15 sulfide catalysts would be required as previously done for alumina-based catalysts.

References

[1] L. Lizama, . Pérez, and T. lim ova, “ o mparison study of NiW and NiPW hydro-desulfurization catalysts supported on SBA-15 and alumina,” *Stud. Surf. Sci. Catal.*, vol. 174, pp. 1251–1254, 2008, doi: 10.1016/S0167-2991(08)80115-2.

[2] A. Kokliukhin, M. Nikulshina, A. Sheldaisov-Meshcheryakov, A. Mozhaev, and P. Nikulshin, “ o o Hydrotreating atal ysts Supported on l $_2O_3$, SiO_2 and SBA-15 Prepared from Single Co_2Mo_{10}-Heteropolyacid: In Search of Self-Promotion Effect,” *Catal. Letters*, vol. 148, no. 9, pp. 2869–2879, 2018, doi: 10.1007/s10562-018-2480-7.

[3] L. Vradman *et al.*, “High loading of short WS_2 slabs inside SBA-15: Promotion with nickel and performance in hydrodesulfurization and hydrogenation,” *J. Catal.*, vol. 213, no. 2, pp. 163–175, 2003, doi: 10.1016/S0021-9517(02)00012-X.

[4] . Vialpando, . erts , J. Persoons, J. ar tens, and G. Van Den oot er, “Evaluation of ordered mesoporous silica as a carrier for poorly soluble drugs: Influence of pressure on the structure and drug release,” *J. Pharm. Sci.*, vol. 100, no. 8, pp. 3411–3420, 2011, doi: 10.1002/jps.22535.

[5] L. M. Henning *et al.*, “High specific surface area ordered mesoporous silica -12 with tailored pore size,” *Microporous Mesoporous Mater.*, vol. 280, pp. 133–143, 2019, doi: 10.1016/j.micromeso.2019.01.050.

[6] J. Jammaer, . erts , J. D’Haen, J. W. Seo, and J. . artens, “ onv enient synthesis of ordered mesoporous silica at room temperature and quasi-neutral pH,” *J. Mater. Chem.*, vol. 19, no. 44, pp. 8290–8293, 2009, doi: 10.1039/b915273c.

[7] D. Zhao *et al.*, “Triblock copolymer syntheses of mesoporous silica with periodic 50 to 300 angstrom pores,” *Science (80-.).*, vol. 279, no. 5350, pp. 548–552, 1998, doi: 10.1126/science.279.5350.548.

[8] S. G. Gregg and K. S. V Sing, *Adsorption, Surface Area and Porosity (2nd end.) Academic Press*. London: A Subsidiary of Harcourt Brace Jovanovich, 1982.

[9] T. enamor , L. Vidal, . Lebeau, and . ar ichal, “Influence of synthesis parameters on the physico-chemical characteristics of SBA-15 type ordered mesoporous silica,” *Microporous Mesoporous Mater.*, vol. 153, pp. 100–114, 2012, doi: 10.1016/j.micromeso.2011.12.016.

[10] S. S. im, . arkam kar, T. J. Pinnavaia, . ruk, and . Jaroniec, “Synthesis and characterization of ordered, very large pore MSU-H silicas assembled from water-soluble silicates,” *J. Phys. Chem. B*, vol. 105, no. 32, pp. 7663–7670, 2001, doi: 10.1021/jp010773p.

[11] . Høj, . Linde, T. . Hansen, . rors on, . D. Jensen, and J. D. Grunwaldt, “Flame spray synthesis of o o/ l2 3 hydrotreating catalysts,” *Appl. Catal. A Gen.*, vol. 397, no. 1–2, pp. 201–208, 2011, doi: 10.1016/j.apcata.2011.02.034.

[12] . Taguchi and F. Schüth, “ rde red mesoporous materials in catalysis,” *Microporous and Mesoporous Materials*, vol. 77, no. 1. pp. 1–45, 2005, doi: 10.1016/j.micromeso.2004.06.030.

[13] D. Ishutenko, Y. nash kin, and P. Nikulshin, “The effect of carrier in KCoMoS-supported catalysts for hydro-upgrading of model F gasoline,” *Appl. Catal. B Environ.*, vol. 259, Dec. 2019, doi: 10.1016/j.apcatb.2019.118041.

[14] S. runet, D. ey, G. Pérot, . ouchy, and F. Diehl, “ n the hydrodesulfurization of FCC gasoline: review,” *Applied Catalysis A: General*, vol. 278, no. 2. pp. 143–172, 2005, doi: 10.1016/j.apcata.2004.10.012.

[15] D. Ishutenko *et al.*, “Potassium effect in -Ni(Co)PW/Al_2O_3 catalysts for selective hydrotreating of model F gasoline,” *Appl. Catal. B Environ.*, vol. 203, pp. 237–246, 2017, doi: 10.1016/j.apcatb.2016.10.043.

[16] . ordova, P. lancha rd, . Lancelot, G. Frémy, and . Lamonier, “Probing the nature of the active phase of molybdenum-supported catalysts for the direct synthesis of methylmercaptan from syngas and H_2S,” *ACS Catal.*, vol. 5, no. 5, pp. 2966–2981, 2015, doi: 10.1021/cs502031f.

[17] R. Huirache- cuña *et al.*, “S -15 Mesoporous Silica as Catalytic Support for Hydrodesulfurization Catalysts—Review,” *Materials (Basel).*, vol. 6, no. 9, pp. 4139–4167,

2013, doi: 10.3390/ma6094139.

[18] J. A. Mendoza-Nieto, F. Robles- én dez, and T. E. lim ova, “Support effect on the catalytic performance of trimetallic NiMoW catalysts prepared with citric acid in HDS of dibenzothiophenes,” *Catal. Today*, vol. 250, pp. 47–59, 2015, doi: 10.1016/j.cattod.2014.05.002.

[19] L. Lizama and T. lim ova, “Highly active deep HDS catalysts prepared using o and W heteropolyacids supported on SBA-15,” *Appl. Catal. B Environ.*, vol. 82, no. 3–4, pp. 139–150, 2008, doi: 10.1016/j.apcatb.2008.01.018.

General conclusions

General conclusions

Due to the constant growth in demand for liquid fuels, and in particular diesel fuel, as well as the deterioration of the quality of raw materials and the introduction of new, more stringent environmental standards, researchers are forced to develop new, highly active catalytic systems. Analysis of the literature data showed that more and more attention of researchers is directed to the creation of polymetallic bulk and supported catalytic systems, in which two structure-forming active phase metals (Mo and W) are present at once. This trend is due to the higher activity of these systems in comparison with traditional catalysts, as well as their high resistance to the inhibitory effect of nitrogen-containing compounds, according to many studies. A particularly important factor in the preparation of such catalysts is the presence of a mixed active phase, which ensures high activity.

It was noted that the formation of a mixed MoWS active phase is facilitated by the use of mixed oxidic precursors, in the molecule of which Mo and W atoms are already in chemical interaction. Mixed heteropolyacids (HPAs), and in particular Keggin-type $SiMo_nW_{12-n}$HPA, are a promising precursor of the active phase. The use of HPAs with different structure and composition as a precursor provides a higher degree of sulfidation and a uniform distribution of the active phase over the support surface as compared to traditional ammonium heptamolybdate (AHM) and ammonium metatungstate (AMT) precursors. A series of works devoted to the study of $SiMo_3W_9$ HPA showed a number of advantages of this precursor, the main of which is the formation of a mixed MoW active phase on alumina supported catalysts regardless of the type of sulfidation. Comparative analysis with $SiMo_1W_{11}$ HPA showed that an increase in the content of molybdenum in mixed HPAs promotes an increase in HDS and HYD activity due to a higher degree of sulfidation of metals. DFT calculations reported in literature also indicate an optimal bond energy between metal and sulfur at higher molybdenum contents. The aim of this work is then the study of MoW catalysts supported on alumina with a larger range of Mo/W content, up to 9/3 starting from mixed MoW Keggin HPA. However, in the literature, there were no established protocols for the synthesis of HPA with a high content of molybdenum. In fact, $SiMo_1W_{11}$ HPA, like $SiMo_3W_9$ HPA, were obtained from the corresponding lacunar salts, which was not possible for HPA with higher Mo content. The primary objective of this study was thus the development of a new method for the synthesis of mixed $SiMo_nW_{12-n}$ HPA with a high molybdenum content for the development of highly active mixed catalysts for deep hydrotreating of oil fractions. In Chapter 2 of the thesis, a new synthesis protocol was developed, which made it possible to obtain mixed $SiMo_nW_{12-n}$HPA with Mo/W ratio of 6/6 and 9/3, the composition and structure of which were confirmed by Raman and IR spectroscopy, as well as single-crystal XRD. The new protocol makes it possible to obtain mixed HPAs in one step, without preparation of corresponding lacunar salts, which greatly facilitates the synthesis. This made it possible to supplement the previous results of the study of the effect of using mixed Keggin-type HPAs for the synthesis of unpromoted alumina supported mixed catalysts, as well as to determine the effect of the

ratio of structure-forming metals of the active phase on the composition and structure of the active phase and its activity in the reactions of HDS DBT and HYD naphthalene. The composition and structure of the active $MoWS_2$ phase in MoW/Al_2O_3 catalysts obtained by gas-phase sulfidation were studied by TEM, XPS, and HAADF. It has been found that the use of new $SiMo_6W_6$HPA and $SiMo_9W_3$HPA also allows the production of highly active mixed $MoWS_2$ phase. Higher activity in the reaction of HDS DBT and HYD naphthalene was measured compared to monometallic catalysts and bimetallic references obtained from the corresponding monometallic $SiMo_{12}$ and SiW_{12} HPAs with the corresponding Mo/W ratio. It was shown that Mo/(Mo+W) atomic ratio affects not only the activity of mixed catalysts, but also affects the structure of the active phase itself. HAADF analysis showed that an ordered core-shell structure is formed at Mo/W metal ratios equal to 3/9 and 6/6. A further increase in the proportion of molybdenum led to disordering of the structure, which had a negative effect on the activity in the DBT HDS and naphthalene HYD. However, the mixed Mo_9W_3/Al_2O_3 catalyst remained more active than the sample prepared from a mixture of two monometallic heteropolyacids with a corresponding metal ratio.

The introduction of promoters into the composition of the catalyst has a huge effect on the activity. According to literature data, the synergistic effect from the use of two structure-forming metals of the active phase (Mo and W) is preserved when Ni is used as a promoter. This effect was not observed for Co-promoted systems. The question of the formation of a mixed NiMoWS active phase for alumina supported catalysts based on mixed $SiMo_nW_{12-n}$HPAs has not been studied in detail. For this reason, Chapter 3 examined the effect of using mixed HPAs and of the Mo/(Mo+W) ratio on the formation and structure of the active NiMoWS phase, as well as on the catalytic activity in HDS of DBT and HYD of naphthalene with or without quinoline, as well as in the hydrotreating of a real feed (SRGO) under liquid-phase sulfidation conditions. By EXAFS and HAADF it was shown that the behavior of the promoted samples towards the formation of the sulfide slabs is similar to that observed with unpromoted ones and that the presence of nickel does not hinder the formation of mixed clusters in HPA based catalysts. In contract, the active phase of $Ni(Mo_n+W_{12-n})/Al_2O_3$ sulfided under gas phase consisted mainly of monometallic slabs, as previously observed for non-promoted catalysts. In all reactions, mixed HPAs based $NiMo_nW_{12-n}/Al_2O_3$ catalysts presented higher activity than their $Ni(Mo_n+W_{12-n})$ counterparts, which was associated to the presence of mixed promoted $MoWS_2$ slabs as evidenced by EXAFS and HAADF results. In the presence of quinoline in the model feedstock, the $NiMo_1W_{11}/Al_2O_3$ catalyst was the most active in the HDS, HYD, and HDN reactions, due to its higher resistance to the inhibitory effect of quinoline. In SRGO HDT, the optimal Mo/W ratio is shifted to the $NiMo_3W_9/Al_2O_3$ sample, which is explained by the lower concentration of N compounds in SRGO. Increased resistance to nitrogen inhibition is observed at low Mo content, however, the Mo/W ratio in the catalysts should be selected depending on the content of nitrogen-containing compounds in the feed. For petroleum fractions with a high nitrogen content,

NiMoW catalysts with a high tungsten content are most preferred due to their higher resistance to inhibitory effect.

Due to the increased interest in bulk catalytic systems in Chapter 3, unsupported samples were obtained by acid (HF) etching of alumina support. The samples obtained had an active phase concentration of more than 90% with high dispersion of nanoparticles by XRD and TEM results. The use of mixed $SiMo_nW_{12-n}$HPAs as starting material contributed to an increase in the content of mixed sulfides compared to their counterparts, which was confirmed by the results of EXAFS and TOF-SIMS. Total DBT HDS and naphthalene HYD activities were correlated with the W–Mo coordination number. According to the catalytic tests, it was found that the catalyst based on the mixed $SiMo_3W_9$HPA is more active in model reactions due to the high concentration of the mixed $MoWS_2$ active phase.

Another strategy to increase catalytic performance is to explore the effect of support. Mesostructured silica was thus chosen instead of alumina and it was found to promote an increase in the activity of bimetallic MoW catalysts in the reactions of HDS of DBT and HYD of naphthalene due to the weaker interaction of the active phase with the support. At the same time, it was found that the use of mixed HPAs compared to separate precursors did not lead to an increase in activity, as was observed for catalysts supported on alumina. It was assumed that on supported SBA-15 catalysts, a mixed active phase was not formed on the catalyst; nevertheless, whatever the precursors, the activity of bimetallic samples was higher than that of monometallic catalysts due to the high degree of sulfidation of metals and good dispersion of the active phase.

Thus, within the framework of this Ph.D. thesis, new Keggin-type $SiMo_nW_{12-n}$ HPA with high Mo content, not previously described in the literature, were presented. The use of these compounds as precursors made it possible to fully reveal their prospects. The data obtained for Ni-promoted catalysts can be further used to create industrial catalysts for hydrotreating for each type of feedstock, varying Mo/W ratio. The combination of bulk and supported catalysts further facilitates the production of ultrapure fuels. Layered loading of catalysts, as has already been implemented for the NEBULA catalysts, will allow the catalysts to be adapted to the selected process. The use of acid etching of the support opens up the possibility of using already spent catalysts that cannot be regenerated to obtain a highly active MoW bulk catalyst with good dispersion of the active phase. Mesostructured silica as a catalyst support also opens up additional opportunities in the development of hydrotreating catalysts. Their high hydrogenation capacity will provide a lower PAH content, which is regulated by current standards. However, this direction of development needs additional research. Increasingly, researchers are combining such materials with aluminum to provide even greater gains in activity. Perhaps this approach will reveal the additional potential of using mixed heteropolyacids.

Annex

1. Physicochemical methods of analysis

1.1 Raman spectroscopy

Raman spectroscopy is a molecular spectroscopy technique based on irradiation on the sample surface by monochromatic light, the main part of the light is elastically scattered with the same frequency (Rayleigh diffusion). When scattering, two more types of phonon can be observed: (i) when the molecule can go into a phonon state and release a photon with a lower energy compared to the incident photon (Stokes shift of the Raman distribution). (ii) when the molecule is in the phonon state, is excited and goes into a virtual state, then returns to the ground state and emits a photon with a higher energy than the incident light photon (anti-Stokes Raman distribution) (**Fig. 1**).

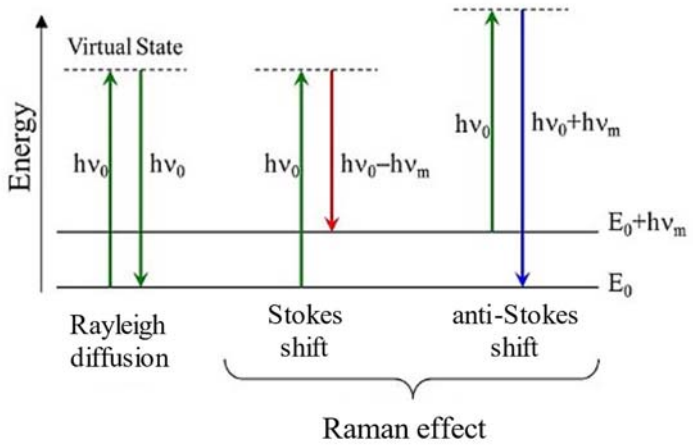

Fig. 1 Processes of energy state change under Rayleigh and Raman distributions

Compared to other vibrational spectroscopy methods, for example, Fourier-transform infrared spectroscopy (FTIR) and near-infrared spectroscopy NIR spectroscopy, Raman spectroscopy has several advantages. They are due to the fact that the Raman effect is observed in the scattered light from the sample, and not in the absorption spectrum of the sample of light. Therefore, Raman spectroscopy does not require special sample preparation and is insensitive to absorption bands. This property of Raman spectroscopy facilitates the process of direct measurement in solid, liquid and gaseous media, as well as measurements through transparent materials such as glass, quartz, plastic. This method of characterization is important for catalysts from the impregnation solution to the sulfided state.

The Raman spectra of the HPAs and oxidic samples were recorded at RT using an Infinity XY Horiba Jobin-Yvon Raman microprobe equipped with a photodiode array detector. The excitation laser source was the 532.16 nm line of a Nd-YAG laser. The wavenumber accuracy was 4 cm^{-1}.

1.2 IR- spectroscopy

IR spectroscopy is a method for the analysis of chemical compounds in which the energy of the infrared region of electromagnetic radiation is absorbed. The absorbed energy causes transitions between vibrational and rotational levels of molecules. The set of spectral bands characterizes the studied molecular structure rather completely.

In the region of near-infrared radiation (12500 - 4000 cm^{-1}), many bands usually appear, corresponding to the overtones of fundamental or composite vibrations. For medium IR radiation, the group frequency region (4000 - 1300 cm^{-1}) and the fingerprint region (1300 - 650 cm^{-1}) are distinguished. In the first region, group vibrations ascribed to some pairs of atoms of the molecule appear: from 4000 to 2500 cm^{-1} - vibrations with the participation of hydrogen atoms, from 2500 to 2000 cm^{-1} - vibrations of triple bonds, from 2000 to 1540 cm^{-1} - vibrations double bonds. In the area of fingerprints, there are deformation and skeletal vibrations of polyatomic systems [1].

IR spectra of $H_4[SiMo_nW_{n-12}O_{40}]$ HPAs (as KBr pellets) (400–4000 cm^{-1}) were measured on a Shimadzu IR Prestige-21 FT-IR spectrophotometer.

1.3 Single-crystal X-ray diffraction (XRD)

Single-crystal X-ray Diffraction (XRD) is a method for studying the crystal structure of a substance to determine the symmetry of the crystal, the amount and content of symmetry elements in it. Moreover, it is used for determination of the unit cell dimensions, bond-lengths, bond-angles and details of site-ordering [2]. Single-crystal XRD is a non-destructive analytical technique based on constructive interference of monochromatic X-rays and a crystalline sample (Fig 2).

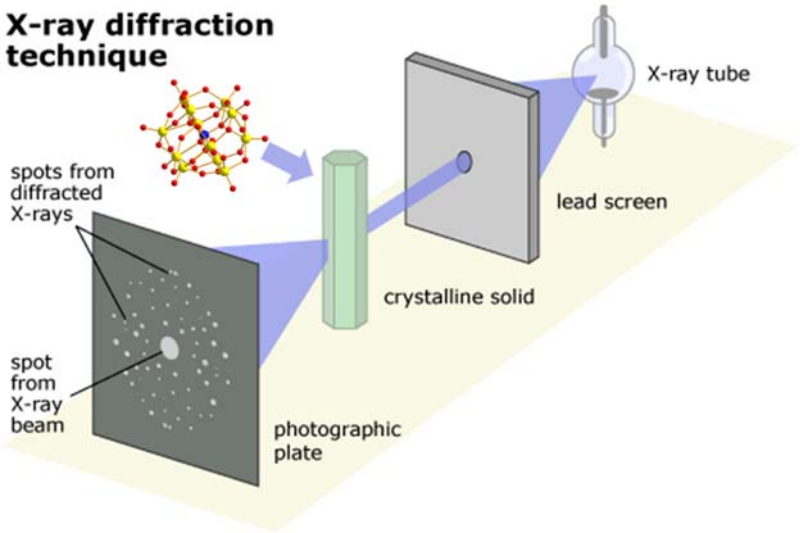

Fig. 2 Schematic single-crystal X-ray diffraction technique

The interaction of the incident rays with the sample produces constructive interference (and a diffracted ray). Based on Bragg's law (**Fig. 3**), knowing the glancing angle and the intensity of the diffracted rays, it is possible to create a three-dimensional picture of the electron density in the crystal.

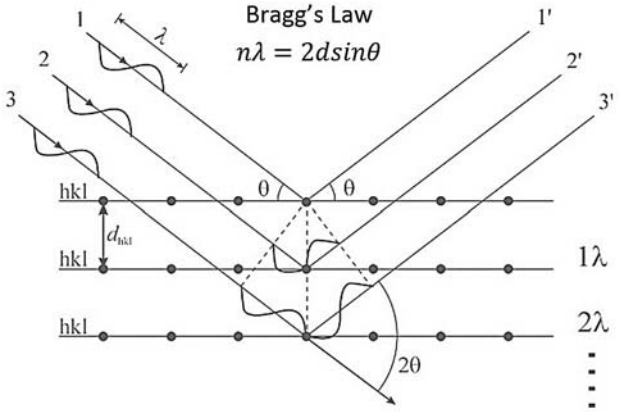

Fig. 3 Bragg diffraction.

A diffraction pattern is obtained by measuring the intensity of scattered waves as a function of scattering angle. Very strong intensities known as Bragg peaks are obtained in the diffraction pattern at the points where the scattering angles satisfy Bragg condition.

Single crystal XRD data for $H_4[SiMo_6W_6O_{40}]\cdot 36H_2O$ and $H_4[SiMo_9W_3O_{40}]\cdot 36H_2O$ have been collected using a Bruker Apex Duo diffractometer with a Mo-IμS microfocus tube (λ=0.71073 Å). It should note that the poor stability of the crystals in air at ambient temperature, even more pronounced for the $H_4[SiMo_6W_6O_{40}] \times 36H_2O$, polycation for which a single crystal had to be isolated very rapidly and collected at 100K in a cold nitrogen flow to prevent from degradation by moisture into an amorphous solid. For the $H_4[SiMo_9W_3O_{40}]$ hydrate a simple protection of the crystals by vacuum grease allows full data collection at room temperature. The intensity data have been extracted and corrected from Lorentz Polarization using the program SAINT-Plus 8.27b. Multiscan absorption correction was applied using SADABS [3]. The structure was solved using Superflip [4] and refined using Jana 2006 [5]. Specificities for each collection and refinement are given in the crystal structure dedicated sections.

1.4. Powder XRD

Powder X-ray diffraction (XRD) is a method for studying the structural characteristics of a material using X-ray diffraction (X-ray structural analysis) on a powder, the result of which is the dependence of the intensity of scattered radiation on the scattering angle.

The main difference between powder XRD and single-crystal XRD is the degree of texturing of the material. Single crystals have the maximum texture and are considered anisotropic, while in powder diffraction the samples are considered isotropic (every possible crystal orientation is represented in the same way). Powder XRD operates on the assumption that the sample is randomized, which follows that a statistically significant amount of each plane of the crystal structure will have the correct orientation for X-ray diffraction and each plane will be represented in the signal.

In practice, it is sometimes necessary to rotate the orientation of the sample to eliminate texturing effects and achieve true randomness [6].

In contrast to a single crystal, in the analysis of which the scattered radiation is collected on a flat plate detector as discrete Laue spots, in the case of a powder rotational averaging leads to smooth diffraction rings around the beam axis (Debye–Scherrer rings). The angle between the ring and the axis of the beam is called the scattering angle and is denoted as 2θ. According to Bragg's law, the reciprocal lattice vector G corresponding to each ring of the sample is determined by the equation (1) [7]:

$$\vec{G} = q = 2k\sin(\theta) = \frac{4\pi}{\lambda}\sin(\theta) \quad (1)$$

where $\vec{G}$ is the reciprocal lattice vector, q is the length of the reciprocal lattice vector, k is the momentum transfer vector, θ is half of the scattering angle, and λ is the wavelength of the source.

Powder XRD data collection was performed on the ARLX'TRA diffractometer with Cu Kα emission (λ = 1.54056 Å) operating at 43 kV and 38 mA and identified using standard JCPDS files. The approximate crystallite dimensions of the MoS_2 slabs was calculated using the Debye-Scherrer relation [8]:

$$D_{002} = \frac{k_{002}\cdot\lambda}{\beta_{002}\cdot\cos\theta} \quad (2)$$

where D_{002} is the mean size of ordered (crystalline) domains (Å) along the stacking direction; λ is the X-ray wavelength; θ is the Bragg angle; β_{002} (or FWHM) is the line broadening at half maximum intensity; k_{002} is the dimensionless shape factor. The shape factor k_{002} depends on the crystal shape and is close to 0.9 for WS_2 [9] and to 0.76 for MoS_2 [8]. The average number of layers N was calculated using the equation $N = D_{002}/6.17$, where 6.17 Å corresponds to the value of the interlayer spacing in the 2H-WS_2 structure.

The crystallite size along the basal direction was calculated using the Debye-Scherrer equation (2) applied to the broadening of the diffraction peak (110). The same calculation method was previously used by de la Rosa et al. [8] for MoS_2 prepared by HF acid etching of the support. The peak (110) is not affected by imperfect stacking or bending/folding of layers. However, Liang et al. [10] found that the shape factor k_{110} depends on the β_{110} angular line width, and this correlation between β_{110} and k_{110} was taken into account. According to the experimental angular line widths, the shape factor k_{110} was equal to 1.49.

1.5 Low-temperature adsorption of nitrogen

The method of low-temperature adsorption of nitrogen is designed to determine the specific surface area by the BET method; it is measured at the boiling point of liquid nitrogen (77 K) and a partial pressure p/p_0 = 0.05 - 0.35. These conditions favoring polymolecular adsorption can be

regarded as intermediate between the conditions of monomolecular adsorption (according to Langmuir) and the conditions of condensation of saturated vapor.

The main quantity that allows calculating the specific surface area is the monolayer capacity (or maximum adsorption), which is equal to the number of adsorbate molecules in a completely filled monolayer on the adsorbate surface. In practice, when nitrogen adsorption is carried out, monomolecular adsorption according to the Langmuir theory is not realized, and the surface filling is not limited to a monolayer. In this case, the Brunauer, Emmett, Teller (BET) method is used to calculate the specific surface area [11]. This method is an extension of Langmuir's theory of monomolecular adsorption to the case of polymolecular adsorption.

The BET method is based on the following provisions:

- all adsorption centers on the surface of a solid are energetically identical;
- only one adsorbate molecule can be adsorbed on one adsorption center;
- gas molecules can be adsorbed on the surface of a solid in the form of layers, the number of which is not limited and the filling of the layers does not necessarily occur uniformly;
- there is no interaction between any adjacent adsorbed molecules;
- Langmuir's theory of monomolecular adsorption is valid for the first adsorption layer;
- the second and subsequent layers are formed due to gas condensation;
- gas adsorption proceeds in equilibrium.

The BET equation is

$$\frac{p}{v(p_0-p)} = \frac{p}{v_m c} + \frac{c-1}{v_m c} \cdot \frac{p}{p_0} \quad (3)$$

where p and p_0 are the equilibrium and the saturation pressure of adsorbates, respectively, v_m is the volume adsorbed in one complete monomolecular layer, and c is the BET constant ($e^{\frac{E_1+E_L}{RT}}$).

The specific surface area (SSA) can be calculated by the equation:

$$S = \frac{v_m \cdot a \cdot N_a}{m \cdot 22400} \quad (4)$$

where a is effective cross-sectional area of one adsorbate molecule (m^2) for nitrogen is 0.162 nm^2, N is Avogadro constant (6.022×10^{23} mol^{-1}), m is mass of test powder (g).

The Barrett-Joyner-Halenda (BJH) method was originally developed for relatively wide pore adsorbents with a wide pore size distribution. However, it has been repeatedly shown that this method can be successfully applied to almost all types of porous materials. The model is based on the assumption of the cylindrical shape of the pores and the fact that the pore radius is equal to the sum of the Kelvin radius and the thickness of the film adsorbed on the pore wall (capillary condensation) [12]. The desorption branch of the isotherm is used as the initial data for calculations by the BJH method (although the use of the adsorption branch is also possible) in the pressure range p/p_0 = 0.4 - 0.967. In this calculation, pores with a diameter of more than 60 nm are not taken into account.

The textural characteristics of the catalysts were measured on a Quantachrome Autosorb-1 adsorption porosimeter by low-temperature nitrogen adsorption at 77 K. Before analysis, the samples were outgassed under vacuum (< 10^{-1} Pa) at 300°C for 3 h. The specific surface area (SSA) was calculated using the BET method at relative partial pressures (p/p_0) ranging from 0.05 to 0.3. Total pore volume (at p/p_0 of 0.99) and pore size distribution were obtained using the desorption curve and the BJH model.

1.6 High-resolution transmission electron microscopy (HRTEM)

HRTEM works on the principle of transmitted electron beams, in contrast to the metallographic light microscope, in which the image is formed by reflected light beams. The light source in the electron microscope is replaced by an electron source (gun), instead of glass optics, electromagnetic lenses are used (to refract electron beams) (**Fig. 4**) [13].

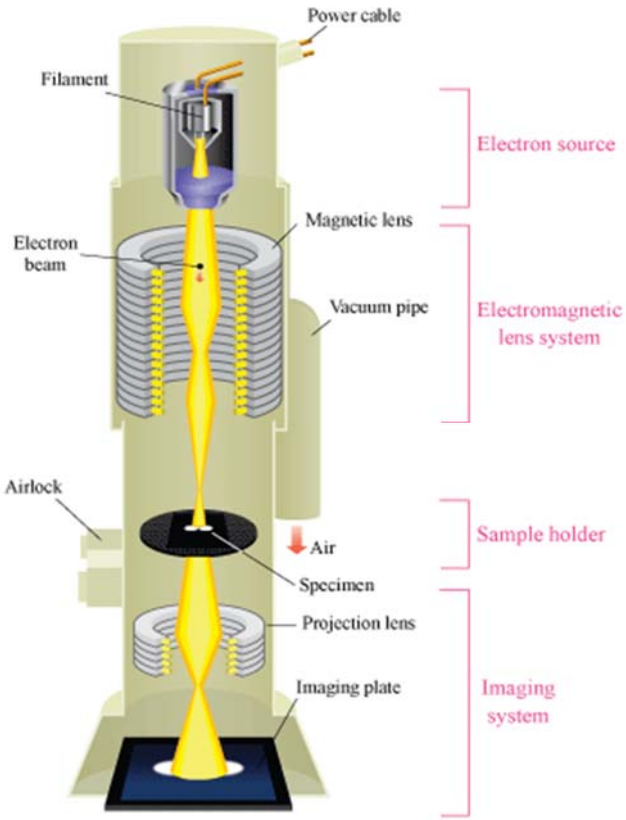

Fig. 4 Scheme of transmission electron microscope

The electron source (gun) creates a stream of electrons that passes through the electromagnetic lens of the capacitor to form an electron beam that illuminates the sample. The beam strikes the specimen and a part of it gets transmitted through it. This transmitted beam is focused by the objective lenses into an image, which is then fed down the column through the projector lenses enlarging the image, depending upon the set magnification. Electrons going through thicker areas of the material or material with higher Z undergo more scattering and the corresponding areas in the sample therefore appear darker in the image, while thinner areas or lighter elements allow more electrons to pass through and appear lighter.

HRTEM was carried out using a Tecnai G2 20 electron microscope with LaB_6 cristal with a 0.19 nm lattice-fringe resolution and an accelerating voltage of 200 kV. The samples were dispersed in ethanol. The suspension was collected on carbon films supported on copper grids and 10 – 15 representative micrographs were obtained for each catalyst in high–resolution mode. Typically, the length and the stacking of at least 500 slabs were measured for each catalyst. ImageJ free software developed for direct qualitative analysis of images. The distribution in length and the stacking of the

slabs was determined. To measure the extent of the Mo(W)S_2 dispersion, the average fraction of Mo(W) atoms at the Mo(W)S_2 edge surface (D) was calculated, assuming that the Mo(W)S_2 slabs were perfect hexagons [14]. Mo(W)S_2 dispersion (D) was statistically evaluated by dividing the total number of Mo(W) atoms at the edge surface (W_e), including corner sites (W_c), by the total number of Mo(W) atoms (W_T) using the slab sizes measured in the TEM micrographs:

$$D = \frac{W_e + W_c}{W_T} = \frac{\sum_{i=1..t} 6n_i - 6}{\sum_{i=1..t} 3n_i^2 - 3n_i + 1}, \quad (5)$$

where n_i is the number of Mo(W) atoms along one side of the Mo(W)S_2 slab, as determined by its length, and t is the total number of slabs in the TEM micrograph.

The number of slabs per stack was determined to obtain the average stacking degree ($\overline{N}$):

$$\overline{N} = \frac{\sum_{i=1..t} n_i N_i}{\sum_{i=1..t} n}, \quad (6)$$

where n_i is the number of stacks in N_i layers.

1.7. High resolution high-angle annular dark-field scanning transmission electron microscopy (HR HAADF-STEM)

One of the types of TEM is scanning transmission electron microscopy (STEM), the main feature of which is that the electron beam is focused into a thin spot (with a typical spot size of 0.05 - 0.2 nm), which is then scanned on a sample in a raster illumination system built in this way that the sample is illuminated at each point using a beam parallel to the optical axis.

High-angle annular dark-field imaging (HAADF) is a STEM technique where only electrons scattered at high angles are collected to build the image [15]. This technique is highly sensitive to variations in the atomic number of atoms in the sample (Z-contrast images). Higher Z elements scatter more electrons at larger angles due to greater electrostatic interaction between the nucleus and the electron beam, which makes the HAADF detector pick up a stronger signal from atoms with high Z [16], making these atoms appear brighter in the image (**Fig. 5**). But high-resolution scanning transmission electron microscopes require extremely stable room conditions. To obtain atomic-resolution images in STEM, vibration, temperature fluctuations, electromagnetic and acoustic waves must be avoided in the room in which the microscope is located [17].

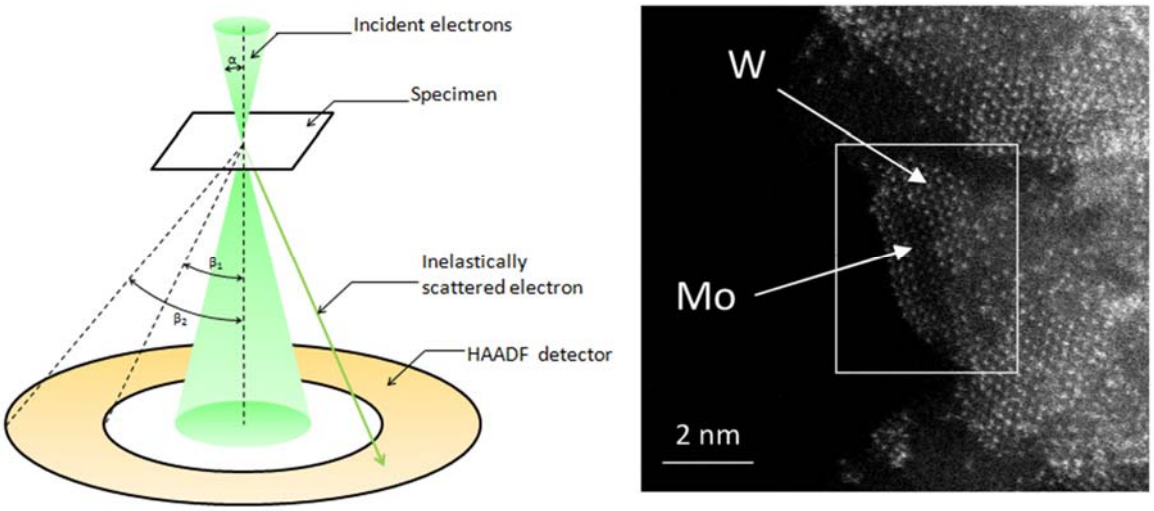

Fig. 5 HAADF-STEM scheme with an example of a photomicrograph of $MoWS_2$ (the intensity between Mo and W is proportional to $Z^{1.7}$).

HAADF-STEM analyses have been performed using a FEG TEM/STEM system (Titan Themis FEI) operated at 300 kV, equipped with a monochromator and a probe Cs corrector. For HAADF acquisition, the spot size was 9 (probe size of the order of 500 pm) with a screen current of ~50 pA and collection angles for the HAADF detector of ~50 and ~200 mrad, respectively. The probe semi-convergence angle has been 21 mrad. All samples were ground under an inert atmosphere. In order to avoid contamination, the samples have been deposited in the form of dry powder, without solvents, on cupper grids with the lacey carbon film.

1.8 X-ray photoelectron spectroscopy (XPS)

X-ray photoelectron spectroscopy (XPS) is a widely used method of chemical surface analysis. This method can be applied to a wide range of applications, from identifying surface contamination to characterizing materials as process control or as a method for characterizing new materials in a research environment. More detailed analysis may require visualization of the sample or depth profiles, and the use of numerical techniques such as curve fitting, layer-by-layer modeling, or linear least squares fit to more accurately describe the material. XPS is based on measuring the energy of photoelectrons knocked out from different energy levels of atoms when a substance is irradiated with X-ray radiation. Under the action of a quantum of light, electrons are knocked out of the substance, the energy of the quantum $h\nu$, in accordance with the energy conservation law, is spent on the ionization energy E_b and the transfer of kinetic energy to this electron ($E_{kin} = mv^2/2$). In the case of a metal, the Fermi level is at the upper point of the filled valence band and is separated from the vacuum level by the potential of the work function φ. If the absorption of a photon occurs at the internal level, the binding energy of the electron is E_b. The emitted electron is recorded with kinetic energy:

$$E_b = h\nu - (E_{kin} + \varphi) \quad (7)$$

where E_b is the electron binding energy, $h\nu$ is the energy of the exciting photon, E_{kin} is the kinetic energy of an electron recorded in the experiment, φ is the work function of the spectrometer.

In the method of X-ray photoelectron spectroscopy (XPS), an X-ray tube with one anode with a wide range of operating energies (from 0 (Fermi level) to 1250 eV and more) is used as a radiation source, and covers almost all electronic levels of chemical elements [18]. This allows to: carry out a qualitative analysis, determine the composition of the surface, establish the valence of elements and study the electronic structure of valence states close to the Fermi level [19].

The spectra were recorded on a Kratos Axis Ultra DLD spectrometer using a monochromatic Al Kα source (hν = 1486.6 eV, 150 W). The samples were mounted on a holder using double-sided adhesive tape. For the non-conductive samples, the Kratos charge neutraliser system was used and the spectra were charge-corrected to provide the C 1s spectral component of adventitious carbon (C–C, C–H) at 284.8 eV. In addition to the survey photoelectron spectra, narrow spectral regions (Al 2p, S 2p, Mo 3d, W 4f, C 1s and O 1s) were recorded. The binding energy (BE) scale of the spectrometer was preliminarily calibrated using the position of the peaks for the Au $4f_{7/2}$ (83.96 eV) and Cu $2p_{3/2}$ (932.62 eV) core levels of pure metallic gold and copper. The pass energy of the analyser was 160 eV for the survey spectra and 40 eV for the narrow scans. The individual spectral regions were analysed to determine the BE of the peaks, identify the chemical state of the elements and calculate the relative ratios of the elements on the catalyst surface.

The collected spectra were analysed using the CasaXPS software program (Version 2.3.16) after applying a Shirley background subtraction. Gaussian (30%) – Lorentzian (70%) peaks were used for spectra decomposition. All XPS spectra were carefully decomposed according to previous works [20], [21].

1.9 ToF-SIMS measurements

Time of flight secondary ion mass spectrometry (Tof SIMS) is based on the measurement of charged particles emitted from a surface as a result of bombardment with high-energy ions (such as Ga^+, In^+, Ar^+, O_2^+, Cs^+, SF^{5+}, Au_x^+, Bi_x^{2+}, and C_{60}^+). When a primary ion collides with the surface of a solid, its kinetic energy is scattered by the solid through cascades of collisions in the near-surface region. As a result, bonds near the impact site are broken, and fragments, which are atoms, molecular fragments and molecules, are ejected from the upper one to three atomic layers (**Fig. 6**). Most discarded species have no net charge. However, a small fraction of these species will be either positively or negatively charged and only these species (ions) are detected by the mass spectrometer [22].

Modern spectrometers are equipped with two ion beams at once, since difficulties often arise in the analysis of dielectric structures, as well as thin-film poorly conducting structures on dielectric substrates. The dual sputter beam completely neutralizes the charge caused by the analyzing ion beam with a low current value. To compensate for the charge caused by sputtering ion beams with a much higher current (hundreds of nA), additional time delays are introduced in the "sputtering-analysis" sequence in a very wide range from a few microseconds to several seconds.

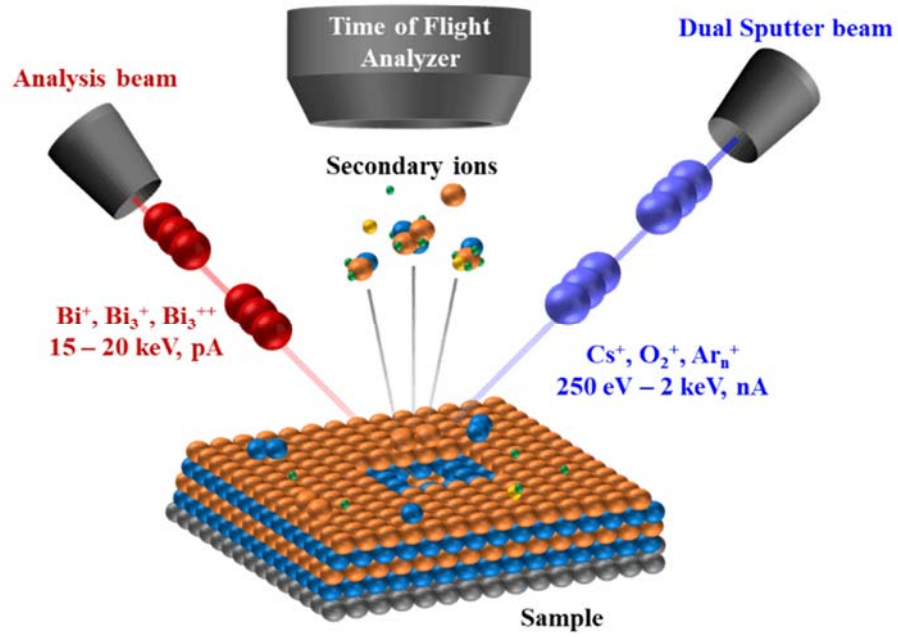

Fig. 6 Schematic ToF-SIMS analysis [23].

In a TOF spectrometer analyzed ions with a charge q are subjected to an extraction field (V_e) of several thousand volts, imparting each ion with a fixed kinetic energy (E_k). The kinetic energy is given by the expression $E_k=qV_e$, which is also equal to $1/2mv^2$, where m is the mass of the ion and v is the velocity of the ion [22]. Since the kinetic energy is constant for all ions, the speed of each ion is inversely proportional to its mass. The heavier the ions, the slower their speed in the extraction field. Consequently, for a given flight length l, the flight time t is shorter for lighter ions $t = l/v$. Thus, the mass of any ion with a unit charge can be determined from the flight time:

$$m = 2qV_et^2/l^2 \quad (8)$$

This method of analysis is of great importance in determining the composition of the active phase of mixed MoW catalysts and makes it possible to analyze not only the composition of the supported catalyst, but is also suitable for the analysis of bulk samples. Moreover, it allows you to quantify the content of mixed MoW sulfides.

ToF-SIMS measurements were performed with a TOF.SIMS 5 spectrometer (ION-TOF GmbH Germany) equipped with a bismuth liquid metal ion gun (LMIG). The compacted samples were bombarded with pulsed Bi^{3+} primary ion beam (25 keV, 0.25 pA) rastered over a 100 × 100 m^2 surface area. With 30 scans and 128x128 pixels, the total primary ion dose does not amount up to 1012

ions/cm^2 ensuring static conditions. Charge effects due to primary ion beam were compensated by means of a 20 eV pulsed electron flood gun. Cycle time was fixed at 150 µs in order to detect secondary molecular ions up to 2000 m/z. The mass resolution (m/Δm) measured on our spectra was about 4000 at m/z = 143 for MoO_3^-. This good mass resolution allowed us to identify high m/z ionic fragments by their exact mass and the attribution could be confirmed most of the time by the simulated isotopic pattern.

1.10 EXAFS spectroscopy

XAFS spectroscopy consists in studying the X-ray absorption fine structure (XAFS) that appears in the X-ray absorption spectra near the absorption edges of the atoms constituting the substance. The study of the short-range fine structure in the energy range extending from the absorption edge to an energy of about 30 eV above it (XANES region) (**Fig. 7**) makes it possible to determine the valence of atoms, the distribution of electron density on them and the structure of electronic bands; this information is of fundamental importance for studies of superconductivity, catalysis and other phenomena. The study of an extended fine structure extending in the energy range from 30 to ~1500 eV above the absorption edge (EXAFS region) makes it possible with a sufficiently high accuracy to determine the distances, coordination numbers and the type of atoms in the local environment of atoms, at the absorption edge of which the studies are carried out.

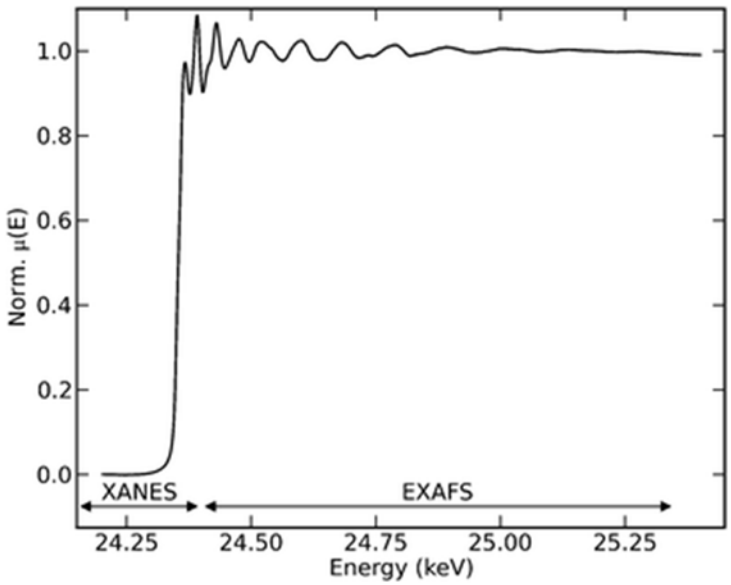

Fig. 7 Normalized XAS Spectrum of Pd foil, E_o = 24.350 keV [24]

The main advantage of EXAFS is the ability to determine the atomic structure of the environment of only one chemical element in a crystal lattice of almost any complexity. As the energy of the incoming X-ray increases, the photo-excited electron has sufficient energy to escape the atom. The outgoing photo-electron has a wavelength, determined by its kinetic energy, and is scattered by

the electrons of neighboring atoms. The outgoing photoelectron wave will be reflected from a neighboring atom, thereby creating an incoming electron wave. The final state is the sum of the outgoing and all incoming waves, one from each neighboring atom [25]. Depending on the type of neighboring atoms and the degree of their remoteness, the amplitude and frequency of sinusoidal oscillations μ vs E. The EXAFS function, χ (k), is described by the following formula [25]:

$$\chi(k) = \sum_j N_j S_i(k) F_j(k) e^{-2\sigma_j^2 k^2} e^{-2r_j/\lambda_j(k)} \frac{\sin(2kr_j + \phi_{ij}(k))}{kr_j^2} \quad (9)$$

where $S_i(k)$ is the amplitude reduction factor due to many-body effects such as shake up/off processes at the central atom (denoted by *i*), *F*j (*k*) is the backscattering amplitude from each of the *N*j neighboring atoms of the j^{th} type with a Debye-Waller factor of σ_j (to account for thermal vibration (assuming harmonic vibration) and static disorder (assuming Gaussian pair distribution) and at a distance between the absorbing atom and a neighbor r_j away), $\phi_{ij}(k)$ is the total phase shift experienced by the photoelectron, and e^{-2r_j/λ_j} is due to inelastic losses in the scattering process (due to neighboring atoms and the medium in between) with $\lambda_j(k)$ – the photoelectron mean free path.

The Mo *K*-edge and W $L_{1,2,3}$ -edges EXAFS spectra for bulk MoWS catalysts were collected at BM31 beamline of the ESRF (Grenoble, France) [26]. The sample powder was diluted with boron nitride, pressed into a pellet and sealed with Kapton tape. All spectra were recorded at room temperature in transmission mode with simultaneous collection of molybdenum and tungsten metal foils for energy calibration. The energy was selected with a double-crystal Si (111) monochromator in the continuous scanning mode. EXAFS data analysis (normalization, background removal, energy alignment, extraction of $\chi(k)$ signal and Fourier analysis) was performed in the Demeter software package [27], FEFF6 [28] was used to calculate theoretical phases and amplitudes. The following structural parameters were set as variables during the fit: interatomic distances (*R*), coordination numbers (*N*), Debye-Waller factors (σ^2) for Mo–Mo, Mo–S, Mo–W (and W–Mo), W–W, and W–S scattering paths. To reduce the number of variables, *R* and σ^2 for W–Mo path were set equal to the corresponding values of Mo–W path. The equation $N_{\mathrm{W-Mo}} = \frac{N_{\mathrm{Mo-W}}}{3}$ was also applied, based on the stoichiometric ratio of the two metals. Two energy shifts (ΔE_0) were used for all paths at Mo *K*- and L_3-edges The fit was performed in *R*-space in 1.2 - 3.4 Å range using a multiple *k*-weighted data (1,2,3). The Fourier-transformation ranges for Mo *K*-edge and W L_3-edge were set to Δk_{K} = 3.5-15.0 Å^{-1}, Δk_{L3} = 4.3-16.3 Å^{-1}, respectively. Amplitude reduction factors (S_0^2) were obtained by fitting bulk MoS_2 and WS_2 references. For direct comparison, the same fitting strategy was applied for the analysis of the data previously collected for the supported catalysts [29].

For NiMoW/Al_2O_3 catalysts, quick XAS was employed to follow *in situ* sulfidation of Mo, W and Ni in alumina supported trimetallic hydrotreating catalysts. XAS measurements were carried out

at the ROCK beamline at the SOLEIL synchrotron [30]. Oxide catalysts were ground and loaded in the cell [31], where they were gas-phase sulfided *in situ*. Spectra were recorded in transmission mode. The use of the remotely-controlled edge jumping capability of the beamline allows to record XAS spectra alternately at the Ni and Mo *K*-edges and W L_1-, L_2-, L_3-edges on the same sample during one sulfidation procedure [30]. At the end of sulfidation, the cell was cooled down at room temperature and 1180 spectra at each edge for the as-sulfided catalysts were recorded and merged. Extended X-ray absorption fine structure (EXAFS) spectra were background-subtracted with Athena and fitted with Artemis, which is an interface to IFEFFIT [27].

The following structural parameters were determined during the fit: interatomic distances (R), coordination numbers (N), Debye-Waller factors (σ^2) and energy shifts (ΔE_0). To reduce the number of variables, Debye-Waller factor for Mo−Mo, W−W and Mo-W paths were set equal. Furthermore, taking into account the size of sulfide particles, no Mo−Ni or W−Ni path has been used for the fitting because this contribution, if it exists, is in insignificant proportion at the Mo *K*- or W L_3-edges. The Fourier transforms (FT) of the measured spectra were modeled with a k-weight of 1, 2, and 3. Amplitude reduction factors (S_0^2) were obtained by fitting bulk MoS_2 and WS_2 references. The fit range of Mo *K*-edge spectra was Δk = 3-14 $Å^{-1}$ and ΔR = 1.4-3.4 Å and the range of W L_3-edge spectra was Δk = 4.1-14.5 $Å^{-1}$ and ΔR = 1.4-3.43 Å.

1.11 Evaluation of catalytic activities in model reactions

The catalytic activity was determined in a flow high-pressure fixed-bed microreactor (**Fig. 8**). Prior to testing, the catalysts were sulfided in a flow of H_2S/H_2 (10 vol. %) at atmospheric pressure and 400 °C for 2 h. 0.4 g of catalyst (0.25 – 0.50 mm) was diluted with of low-surface-area sieved carborundum (0.2–0.4 mm) in a ratio of one to one and placed in isothermal zone of the reactor. Catalysts were tested under the following conditions: 320°C, 3.0 MPa of hydrogen, 10 h^{-1} liquid hourly space velocity (LHSV) and a 500 NL L^{-1} volume ratio of hydrogen to feed. For evaluation of HDS and hydrogenation performances, a mixture of DBT (1000 ppm S), naphthalene (3 wt. %), hexadecane (as an internal standard, 1 wt. %) and toluene (as a solvent) was used. The liquid product compositions of the samples collected every hour were determined using a Crystall-5000 Gas Chromatograph equipped with a 30 m OV-101 column.

For bulk catalysts the same unit was used. $Mo_nW_{12-n}S_2$ catalysts (0.2 g) were diluted with 0.6 cm^3 of low-surface-area carborundum (0.2–0.4 mm) and placed in the center of the reactor. A toluene solution of DBT (Aldrich, 1500 ppm of S), naphthalene (Aldrich, 3 wt. %) and hexadecane (as an internal standard, 1 wt. %) was used as a model feedstock. The catalytic test was performed under the same conditions as for the supported catalysts but at a higher LHSV (40 h^{-1}), since bulk catalysts are significantly superior in activity.

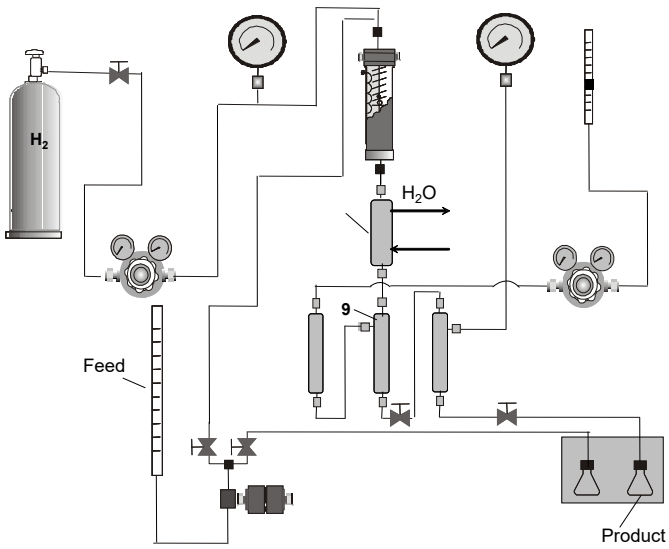

Fig. 8. Scheme of laboratory hydrotreating bench-scale flow unit.

The products of reactions were identified by GC/MS analysis using a Finnigan Trace DSQ. All catalysts exhibited stable performance, achieving a steady state after 7 – 10 h.

A series of catalytic tests of Ni-promoted catalysts was carried out in the process of co-hydrotreating of dibenzothiophene (DBT) (1000 ppm S) and naphthalene (3 wt. %) with the addition of a nitrogen-containing component (quinoline, 500 ppm N) in order to determine the inhibition effect on trimetallic NiMoW/Al_2O_3 catalysts. A mixture of 0.2 g of catalyst (0.25 – 0.50 mm) and low-surface-area sieved carborundum (0.2–0.4 mm) in a ratio of 1:1 was loaded into the isothermal zone of fixed-bed microreactor. Prior to the catalytic activity tests, the catalysts were sulfided by a mixture of DMDS (6 wt.% of sulfur) in toluene sequentially at 240°C for 10 h and at 340°C for 8 h, 3.0 MPa of hydrogen. Catalysts were tested under 280°C, 3.0 MPa of hydrogen, 40 h^{-1} liquid hourly space velocity (LHSV) and a 500 NL L^{-1} volume ratio of hydrogen to feed.

The rate constants of the pseudo-first-order reactions of the DBT HDS and naphthalene HYD were determined using the equations presented in works [32], [33]. The rate constants of were determined using the following equations:

$$k_{HDS} = -\frac{F_{DBT}}{W}\ln(1-x_{DBT}) \text{ and } k_{HYD} = -\frac{F_{Naph}}{W}\ln(1-x_{Naph}), \quad (3)$$

where k_{HDS} and k_{HYD} are the pseudo-first-order reaction constants for the DBT HDS and naphthalene HYD (mol g^{-1} h^{-1}), respectively, x_{DBT} and x_{Naph} are the conversions (%) of DBT, and naphthalene, respectively, F_{DBT} and F_{Naph} are the reactant flows in moles (mol h^{-1}) and W is the weight of the catalyst (g).

The HDS products from DBT included biphenyl (BP) via the direct desulfurization (DDS) pathway, as well as cyclohexylbenzene (CHB) and dicyclohexyl (DCH) from the HYD pathway.

Only traces of hydrogenated tetrahydro- and hexahydrodibenzothiophenes were observed. The HYD/DDS selectivity was calculated according to the reaction network for DBT HDS:

$$S_{HYD/DDS} = \frac{k_{HYD}}{k_{DDS}} = \frac{C_{CHB} + C_{DCH}}{C_{BP}} \quad (4)$$

where C_{CHB}, C_{BCH} and C_{BP} are the concentrations (mol. %) of CHB, DCH and BP in the reaction products, respectively.

The inhibiting factor for the DBT HDS and naphthalene HYD reaction in the presence of quinoline was calculated using the following equations:

$$\theta_{HDS} = \frac{k^0_{HDS} - k_{HDS}}{k^0_{HDS}} \times 100\% \text{ and } \theta_{HYD} = \frac{k^0_{HYD} - k_{HYD}}{k^0_{HYD}} \times 100\% \quad (5)$$

where k^0 is the rate constant (mol $g^{-1}h^{-1}$) in absence of quinoline; k is the rate constant with the addition of quinoline in feedstock (mol $g^{-1}h^{-1}$).

The turnover frequencies (TOF, s^{-1}) normalized on edge sites of $Mo_nW_{12-n}S_2$ slabs for the HDS of DBT, HYD of naphthalene allowed us to get more complete understanding of the catalytic properties of the active phase species. TOF values were calculated using the following equations:

$$TOF_{HDS} = \frac{F_{DBT} \cdot x_{DBT}}{W \cdot \left(\frac{C_{WS_2}}{Ar_W} + \frac{C_{MoS_2}}{Ar_{Mo}} \right) \cdot D \cdot 3600} \text{ and } TOF_{HYD} = \frac{F_{Naph} \cdot x_{Naph}}{W \cdot \left(\frac{C_{WS_2}}{Ar_W} + \frac{C_{MoS_2}}{Ar_{Mo}} \right) \cdot D \cdot 3600}, \quad (6)$$

where F_{DBT} and F_{Naph} are the reactant flows (mol h^{-1}), x_{DBT} and x_{Naph} are the conversions (%) of DBT and naphthalene, respectively; W is the weight of the catalyst (g); C_{WS_2} and C_{MoS_2} are the effective content of W and Mo, respectively, in $Mo_nW_{12-n}S_2$ species (wt. %); D is the dispersion of $Mo_nW_{12-n}S_2$ species; Ar_W and Ar_{Mo} are the standard atomic weights of tungsten (183.9 g/mol) and molybdenum (95.9 g/mol), respectively.

1.12 Evaluation of catalytic activities in hydrotreating of SRGO

For testing on real raw materials, a more modified setup was used (**Fig. 9**). Samples of NiMo(W) catalysts (10 g) with a particle size of 1-3 mm (the bulk density equal to 0.9±0.02 cm^3g^{-1}) and low-surface-area sieved carborundum (0.2–0.4 mm) were loaded into a steel reactor bed at a ratio of 1:2. This loading system with inert material was used to ensure uniform distribution of the feedstock over the catalyst bed.

The tests were carried out at 340°C, 4.0 MPa of hydrogen, 2 h^{-1} LHSV and a 700 NL L^{-1} volume ratio of hydrogen to feed. Before testing, the catalysts had been sulfided according to the procedure described above. SRGO of West Siberian oil with boiling range 180-360°C was used as feedstock with a density at 20°C of 0.841 kg/m^3, the sulfur and nitrogen content are 0.815 wt. % and 156 ppm,

respectively. The content of sulfur and nitrogen in the feedstock and hydrogenated product was determined by elemental analysis on a Multi EA 5000 analyzer (analysis error ± 0.1 ppm), Analytik Jena. The content of mono-, bi- and polycyclic aromatic hydrocarbons was determined by HPLC on an LC-20 Prominence chromatograph, Shimadzu. All catalysts showed steady state activity after 24 h of continuous testing. As mentioned earlier, some samples were also retested under straight run gas oil hydrotreating conditions to confirm the results.

The polycyclic aromatic hydrocarbons (PAH) hydrogenation and hydrodenitrogenation degrees over the catalysts were calculated according to the equations:

$$HYD = \frac{C^0_{PAH} - C_{PAH}}{C^0_{PAH}} \times 100\% \text{ and } HDN = \frac{N_0 - N}{N_0} \times 100\% \quad (7)$$

where C^0_{PAH} and N_0 are PAH and nitrogen content in the feedstock, respectively; C_{PAH} and N are PAH and nitrogen content in the hydrogenation products, respectively.

The apparent HDS reaction order for middle distillates was calculated based on experimental results from [34], [35] according to the following equation:

$$n = 0.2156S_0 + 1.2823 \quad (8)$$

The apparent reaction order in present work was equal to ~1.4 which is typical for a straight-run gas-oils and consistent with the literature data [34], [36], [37].

Apparent HDS rate constant was calculated as follows [35]:

$$k_{HDS} = \frac{LHSV}{n-1}\left[\frac{1}{S^{n-1}} - \frac{1}{S_0^{n-1}}\right] \times 100\% \quad (9)$$

where *LHSV* is the feed hourly space velocity (h^{-1}); n is the apparent reaction order; S^{n-1} and S_0^{n-1} are the concentrations of sulfur in the hydrogenation product and in the initial feedstock (wt. % of sulfur), respectively

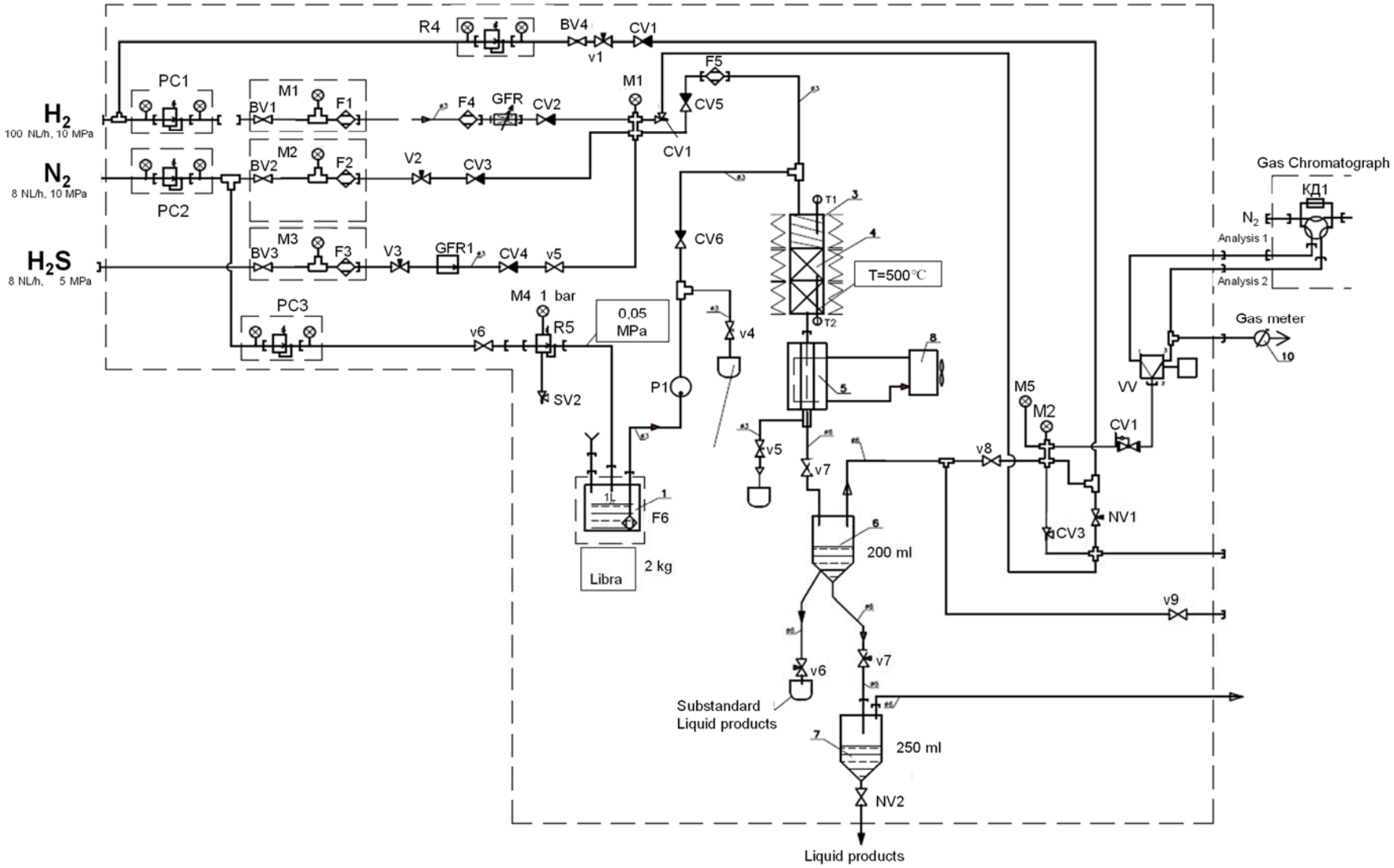

Fig. 9. Scheme of laboratory bench-scale flow unit for hydrotreating of SRGO.

References

[1] J. C. Lindon, G. E. Tranter, and D. W. Koppenaal, *Encyclopedia of Spectroscopy and Spectrometry*. 2016.

[2] C. Kittel, *Introduction to solid state physics*, 8th ed. New York: Wiley, 2005.

[3] G. M. Sheldrick, "SADABS, program for empirical absorption correction," *Univ. Gottingen*, 1996.

[4] L. Palatinus and G. Chapuis, "SUPERFLIP - A computer program for the solution of crystal structures by charge flipping in arbitrary dimensions," *J. Appl. Crystallogr.*, vol. 40, no. 4, pp. 786–790, 2007, doi: 10.1107/S0021889807029238.

[5] V. Petrícek, M. Dušek, and L. Palatinus, "Crystallographic computing system JANA2006: General features," *Zeitschrift fur Kristallographie*, vol. 229, no. 5. R. Oldenbourg Verlag GmbH, pp. 345–352, 2014, doi: 10.1515/zkri-2014-1737.

[6] B. D. Cullity, *Elements of X-ray Diffraction*, Westey Mas. 1978.

[7] K.-D. Liss, A. Bartels, A. Schreyer, and H. Clemens, "High-Energy X-Rays: A tool for Advanced Bulk Investigations in Materials Science and Physics," *Textures Microstruct.*, vol. 35, no. 3–4, pp. 219–252, 2003, doi: 10.1080/07303300310001634952.

[8] M. P. De La Rosa *et al.*, "Structural studies of catalytically stabilized model and industrial-supported hydrodesulfurization catalysts," *J. Catal.*, vol. 225, no. 2, pp. 288–299, 2004, doi: 10.1016/j.jcat.2004.03.039.

[9] G. Alonso, V. Petranovskii, M. Del Valle, J. Cruz-Reyes, A. Licea-Claverie, and S. Fuentes, "Preparation of WS_2 catalysts by in situ decomposition of tetraalkylammonium thiotungstates," *Appl. Catal. A Gen.*, vol. 197, no. 1, pp. 87–97, 2000, doi: 10.1016/S0926-860X(99)00536-0.

[10] K. S. Liang, R. R. Chianelli, F. Z. Chien, and S. C. Moss, "Structure of poorly crystalline MoS_2 - A modeling study," *J. Non. Cryst. Solids*, vol. 79, no. 3, pp. 251–273, 1986, doi: 10.1016/0022-3093(86)90226-7.

[11] S. Brunauer, P. H. Emmett, and E. Teller, "Adsorption of Gases in Multimolecular Layers," *J. Am. Chem. Soc.*, vol. 60, no. 2, pp. 309–319, 1938, doi: 10.1021/ja01269a023.

[12] E. P. Barrett, L. G. Joyner, and P. P. Halenda, "The Determination of Pore Volume and Area Distributions in Porous Substances. I. Computations from Nitrogen Isotherms," *J. Am. Chem. Soc.*, vol. 73, no. 1, pp. 373–380, 1951, doi: 10.1021/ja01145a126.

[13] Shiu-Sing T, "Atomic World - Transmission electron microscope(TEM) - Principle of TEM," *Http://Www.Hk-Phy.Org/Atomic_World/Tem/Tem02_E.Html*. 2020, Accessed: Apr. 17, 2021. [Online]. Available: http://www.hk-phy.org/atomic_world/tem/tem02_e.html.

[14] A. V Mozhaev, P. A. Nikulshin, A. A. Pimerzin, K. I. Maslakov, and A. A. Pimerzin, "Investigation of co-promotion effect in NiCoMoS/Al2O3 catalysts based on Co_2Mo_{10}-heteropolyacid and nickel citrate," *Catal. Today*, vol. 271, pp. 80–90, 2016, doi: 10.1016/j.cattod.2015.11.002.

[15] D. E. Jesson and S. J. Pennycook, "Incoherent imaging of crystals using thermally scattered electrons," *Proc. R. Soc. A Math. Phys. Eng. Sci.*, vol. 449, no. 1936, pp. 273–293, 1995, doi: 10.1098/rspa.1995.0044.

[16] P. D. Nellist and S. J. Pennycook, "The principles and interpretation of annular dark-field Z-contrast imaging," *Adv. Imaging Electron Phys.*, vol. 113, no. C, pp. 147–203, 2000, doi: 10.1016/S1076-5670(00)80013-0.

[17] A. Muller and J. Grazul, "Optimizing the environment for sub-0.2 nm scanning transmission electron microscopy," *J. Electron Microsc. (Tokyo).*, vol. 50, no. 3, pp. 219–226, 2001, doi: 10.1093/jmicro/50.3.219.

[18] D. Briggs and J. T. Grant, *Surface analysis by Auger and XPS*. Manchester: IMPublications, 2003.

[19] P. Beccat, P. Da Silva, Y. Huiban, and S. Kasztelan, "Quantitative Surface Analysis by XPS: Application to Hydrotreating Catalysts," *Oil Gas Sci. Technol.*, vol. 54, no. 4, pp. 487–496, Jul. 1999, doi: 10.2516/ogst:1999042.

[20] M. Nikulshina *et al.*, "Enhancing the hydrodesulfurization of 4,6-dimethyldibenzothiophene through the use of mixed $MoWS_2$ phase evidenced by HAADF," *Catal. Today*, vol. 329, no. September 2018, pp. 24–34, 2019, doi: 10.1016/j.cattod.2018.11.051.
[21] A. Cordova, P. Blanchard, C. Lancelot, G. Frémy, and C. Lamonier, "Probing the nature of the active phase of molybdenum-supported catalysts for the direct synthesis of methylmercaptan from syngas and H_2S," *ACS Catal.*, vol. 5, no. 5, pp. 2966–2981, May 2015, doi: 10.1021/cs502031f.
[22] D. A. Cole and L. Zhang, "Surface Analysis Methods for Contaminant Identification," in *Developments in Surface Contamination and Cleaning - Fundamentals and Applied Aspects*, William Andrew, 2008, pp. 585–652.
[23] "Time-of-Flight Secondary Ion Mass Spectrometry | Time-of-Flight Secondary Ion Mass Spectrometry Laboratory." http://simslab.rice.edu/surface-analysis-lab/teaching-activities-resources/time-of-flight-secondary-ion-mass-spectrometry/ (accessed Apr. 18, 2021).
[24] R. C. Nelson and J. T. Miller, "An introduction to X-ray absorption spectroscopy and its in situ application to organometallic compounds and homogeneous catalysts," *Catalysis Science and Technology*, vol. 2, no. 3. pp. 461–470, 2012, doi: 10.1039/c2cy00343k.
[25] B. K. Teo, *EXAFS: Basic principles and Data Analysis, Springer- Verlag, Heidelberg*, vol. 9, no. 6. Springer Science & Business Media, 1986.
[26] W. Van Beek, O. V Safonova, G. Wiker, and H. Emerich, "SNBL, a dedicated beamline for combined in situ X-ray diffraction, X-ray absorption and Raman scattering experiments," in *Phase Transitions*, 2011, vol. 84, no. 8, pp. 726–732, doi: 10.1080/01411594.2010.549944.
[27] B. Ravel and M. Newville, "ATHENA, ARTEMIS, HEPHAESTUS: Data analysis for X-ray absorption spectroscopy using IFEFFIT," in *Journal of Synchrotron Radiation*, Jul. 2005, vol. 12, no. 4, pp. 537–541, doi: 10.1107/S0909049505012719.
[28] M. Newville, "IFEFFIT: Interactive XAFS analysis and FEFF fitting," *J. Synchrotron Radiat.*, vol. 8, no. 2, pp. 322–324, 2001, doi: 10.1107/S0909049500016964.
[29] M. S. Nikulshina *et al.*, "Molecular approach to prepare mixed MoW alumina supported hydrotreatment catalysts using $H_4SiMo_nW_{12-n}O_{40}$ heteropolyacids," *Catal. Sci. Technol.*, vol. 8, no. 21, pp. 5557–5572, 2018, doi: 10.1039/c8cy00672e.
[30] V. Briois *et al.*, "ROCK: The new Quick-EXAFS beamline at SOLEIL," in *Journal of Physics: Conference Series*, 2016, vol. 712, no. 1, doi: 10.1088/1742-6596/712/1/012149.
[31] C. La Fontaine, L. Barthe, A. Rochet, and V. Briois, "X-ray absorption spectroscopy and heterogeneous catalysis: Performances at the SOLEIL's SAMBA beamline," *Catal. Today*, vol. 205, pp. 148–158, 2013, doi: 10.1016/j.cattod.2012.09.032.
[32] H. Topsøe, B. S. Clausen, and F. E. Massoth, "Hydrotreating Catalysis," *Catalysis*, pp. 1–269, 1996, doi: 10.1007/978-3-642-61040-0_1.
[33] M. Nikulshina *et al.*, "Genesis of active phase in MoW/Al_2O_3 hydrotreating catalysts monitored by HAADF and in situ QEXAFS combined to MCR-ALS analysis," *Appl. Catal. B Environ.*, vol. 269, p. 118766, 2020, doi: 10.1016/j.apcatb.2020.118766.
[34] J. Ancheyta, M. J. Angeles, M. J. Macías, G. Marroquín, and R. Morales, "Changes in apparent reaction order and activation energy in the hydrodesulfurization of real feedstocks," *Energy and Fuels*, vol. 16, no. 1, pp. 189–193, 2002, doi: 10.1021/ef0101917.
[35] J. L. García-Gutiérrez, G. C. Laredo, G. A. Fuentes, P. García-Gutiérrez, and F. Jiménez-Cruz, "Effect of nitrogen compounds in the hydrodesulfurization of straight-run gas oil using a $CoMoP/\gamma\text{-}Al_2O_3$ catalyst," *Fuel*, 2014, vol. 138, pp. 98–103, doi: 10.1016/j.fuel.2014.08.008.
[36] S. K. Bej *et al.*, "Studies on the performance of a microscale trickle bed reactor using different sizes of diluent," *Energy and Fuels*, vol. 14, no. 3, pp. 701–705, 2000, doi: 10.1021/ef990238c.
[37] C. Marín, J. Escobar, E. Galván, F. Murrieta, R. Zárate, and V. Cortés, "NiMo supported on faujasite-modified Al_2O_3 as catalysts for the hydrotreatment of a light cycle oil/straight run gas oil mixture," *Can. J. Chem. Eng.*, vol. 80, no. 5, pp. 903–910, 2002, doi: 10.1002/cjce.5450800513.